

Lecture Notes in Civil Engineering

Roberto Capozucca
Samir Khatir
Gabriele Milani *Editors*

Proceedings of the International Conference of Steel and Composite for Engineering Structures

ICSCES 2022

 Springer

Lecture Notes in Civil Engineering

Volume 317

Series Editors

Marco di Prisco, Politecnico di Milano, Milano, Italy

Sheng-Hong Chen, School of Water Resources and Hydropower Engineering,
Wuhan University, Wuhan, China

Ioannis Vayas, Institute of Steel Structures, National Technical University of
Athens, Athens, Greece

Sanjay Kumar Shukla, School of Engineering, Edith Cowan University, Joondalup,
WA, Australia

Anuj Sharma, Iowa State University, Ames, IA, USA

Nagesh Kumar, Department of Civil Engineering, Indian Institute of Science
Bangalore, Bengaluru, Karnataka, India

Chien Ming Wang, School of Civil Engineering, The University of Queensland,
Brisbane, QLD, Australia

Lecture Notes in Civil Engineering (LNCE) publishes the latest developments in Civil Engineering—quickly, informally and in top quality. Though original research reported in proceedings and post-proceedings represents the core of LNCE, edited volumes of exceptionally high quality and interest may also be considered for publication. Volumes published in LNCE embrace all aspects and subfields of, as well as new challenges in, Civil Engineering. Topics in the series include:

- Construction and Structural Mechanics
- Building Materials
- Concrete, Steel and Timber Structures
- Geotechnical Engineering
- Earthquake Engineering
- Coastal Engineering
- Ocean and Offshore Engineering; Ships and Floating Structures
- Hydraulics, Hydrology and Water Resources Engineering
- Environmental Engineering and Sustainability
- Structural Health and Monitoring
- Surveying and Geographical Information Systems
- Indoor Environments
- Transportation and Traffic
- Risk Analysis
- Safety and Security

To submit a proposal or request further information, please contact the appropriate Springer Editor:

- Pierpaolo Riva at pierpaolo.riva@springer.com (Europe and Americas);
- Swati Meherishi at swati.meherishi@springer.com (Asia—except China, Australia, and New Zealand);
- Wayne Hu at wayne.hu@springer.com (China).

All books in the series now indexed by Scopus and EI Compindex database!

More information about this series at <https://link.springer.com/bookseries/15087>

Roberto Capozucca · Samir Khatir ·
Gabriele Milani
Editors

Proceedings
of the International
Conference of Steel
and Composite
for Engineering Structures

ICSCES 2022

 Springer

Editors

Roberto Capozucca
DICEA
Università Politecnica delle Marche
Ancona, Italy

Samir Khatir
Soete Laboratory, Faculty of Engineering
and Architecture
Ghent University
Ghent, Belgium

Gabriele Milani
Department of Architecture, Built
Environment and Construction Engineering
ABC
Technical University of Milan
Milan, Italy

ISSN 2366-2557 ISSN 2366-2565 (electronic)
Lecture Notes in Civil Engineering
ISBN 978-3-031-24040-9 ISBN 978-3-031-24041-6 (eBook)
<https://doi.org/10.1007/978-3-031-24041-6>

© The Editor(s) (if applicable) and The Author(s), under exclusive license
to Springer Nature Switzerland AG 2023

This work is subject to copyright. All rights are solely and exclusively licensed by the Publisher, whether the whole or part of the material is concerned, specifically the rights of translation, reprinting, reuse of illustrations, recitation, broadcasting, reproduction on microfilms or in any other physical way, and transmission or information storage and retrieval, electronic adaptation, computer software, or by similar or dissimilar methodology now known or hereafter developed.

The use of general descriptive names, registered names, trademarks, service marks, etc. in this publication does not imply, even in the absence of a specific statement, that such names are exempt from the relevant protective laws and regulations and therefore free for general use.

The publisher, the authors, and the editors are safe to assume that the advice and information in this book are believed to be true and accurate at the date of publication. Neither the publisher nor the authors or the editors give a warranty, expressed or implied, with respect to the material contained herein or for any errors or omissions that may have been made. The publisher remains neutral with regard to jurisdictional claims in published maps and institutional affiliations.

This Springer imprint is published by the registered company Springer Nature Switzerland AG
The registered company address is: Gewerbestrasse 11, 6330 Cham, Switzerland

Contents

Solving Engineering Optimization Problems Using Machine Learning Classification-Assisted Differential Evolution	1
Tran- Hieu Nguyen, Huong-Duong Nguyen, and Anh-Tuan Vu	
Damage Detection in Structures Using Strain Measurement	24
Duong Huong Nguyen, Nhu Mai Thi Nguyen, Xuan Hung Doan, Quoc Bao Nguyen, Viet Phuong Nguyen, and Duy Hoa Pham	
Damage Detection in Structures by Wavelet Transforms: A Review . . .	35
Yasin Faghih Larijani, Yaser Rostamian, and Samir Khatir	
Experiences on Anchorage Systems for FRP Rods	48
Roberto Capozucca, Abdelwahhab Khatir, and Erica Magagnini	
Behaviour of Brickwork Masonry Strengthened with B/GFRP Strips . . .	59
Roberto Capozucca, Erica Magagnini, and Giuseppe Pace	
Concrete Plates Reinforced with Embedded CFRP Rods and Carbon/Steel Strips	70
Elisa Bettucci, Roberto Capozucca, Abdelwahhab Khatir, Samir Khatir, and Erica Magagnini	
Structural Health Monitoring for RC Beam Based on RBF Neural Network Using Experimental Modal Analysis	82
A. Khatir, R. Capozucca, E. Magagnini, S. Khatir, and E. Bettucci	
Experimental Acoustic-Wavelet Method for Damage Detection on Laminated Composite Structures	93
Morteza Saadatmorad, Ramazan-Ali Jafari-Talookolaei, Mohammad-Hadi Pashaei, and Samir Khatir	
Damage Identification in Thin Steel Beams Containing a Horizontal Crack Using the Artificial Neural Networks	114
Amirhossein Heshmati, Morteza Saadatmorad, Ramazan-Ali Jafari Talookolaei, Paolo S. Valvo, and Samir Khatir	

Polycarbonate Degradation Under Heat and Irradiation	127
Sonya Redjala, Said Azem, and Nouredine Aït Hocine	
Influence of Decarburization on the Erosion and Corrosion Resistance of a High Chromium Cast Iron	138
ElJersifi Adnane, Chbihi Abdelouahed, Semlal Nawal, Bouaouine Hassan, and Naamane Sanae	
Experimental Research on New Sustainable Geopolymer Mortars Reinforced and Not Reinforced with Natural Fibers	149
Alberto Viskovic, Michał Lach, Łukasz Hojdys, Piotr Krajewski, and Arkadiusz Kwiecien	
Mechanical Performance of Reinforced Pultruded Columns for Curtain Walls	161
Rosa Agliata, Michele Serpilli, and Placido Munafò	
Vibration-Based Damage Assessment in Truss Structures Using Local Frequency Change Ratio Indicator Combined with Metaheuristic Optimization Algorithms	171
Amar Kahouadji, Samir Tiachacht, Mohand Slimani, Amar Behtani, Samir Khatir, and Brahim Benaïssa	
Improved ANN for Damage Identification in Laminated Composite Plate	186
Mohand Slimani, Samir Tiachacht, Amar Behtani, Tawfiq Khatir, Samir Khatir, Brahim Benaïssa, and Mohamed Kamel Riahi	
An Analytical Approach for Describing the Bond Mechanism Between FRP and Curved Masonry Substrate	199
Yu Yuan and Gabriele Milani	
Collapse Analysis of Reinforced Masonry Arches: A Comparison of Associated and Non-associated Sliding	210
Yiwei Hua and Gabriele Milani	
Deep Neural Network and YUKI Algorithm for Inner Damage Characterization Based on Elastic Boundary Displacement	220
Nasreddine Amoura, Brahim Benaïssa, Musaddiq Al Ali, and Samir Khatir	
Energy Dissipation Based Structural Condition Assessment Using Random Decrement Technique	234
Toan Pham-Bao, Thao D. Nguyen, and Nhi Ngo-Kieu	
An Analytical Model for Describing Tensile Behavior of FRCM	244
Yu Yuan and Gabriele Milani	
Simplified Numerical Tool for a Fast Strength Estimation of Squared Masonry Columns Reinforced with FRP Jackets	253
Luis C. M. da Silva, Ernesto Grande, and Gabriele Milani	

Concurrent Multiscale Hybrid Topology Optimization for Light Weight Porous Soft Robotic Hand with High Cellular Stiffness 265
Musaddiq Al Ali, Masatoshi Shimoda, Brahim Benaissa, and Masakazu Kobayashi

Reliability Assessment of Low-Rise Roof Structures Under Wind Loads in the Southern Region of Vietnam 279
Bac An Hoang

A Practical Review of Prairie Dog Optimization Algorithm in Solving Damage Identification Problems in Engineering Structures 296
Lan Ngoc-Nguyen, Hoa-Tran, Samir Khatir, Huu-Quyét Nguyen, Thanh Bui-Tien, and Magd Abdel Wahab

2D Mixed Polygonal Finite Elements for Fluid Computation – An Overview 307
T. Vu-Huu and Thanh Cuong-Le

Author Index. 315



Solving Engineering Optimization Problems Using Machine Learning Classification-Assisted Differential Evolution

Tran- Hieu Nguyen^(✉), Huong-Duong Nguyen, and Anh-Tuan Vu

Hanoi University of Civil Engineering, Hanoi, Vietnam
hieunt2@huce.edu.vn

Abstract. This paper aims to introduce an efficient method called Machine Learning Classification-assisted Differential Evolution (CaDE) for solving engineering optimization problems. In the selection step of the Differential Evolution optimization, an AdaBoost model is employed to classify whether an individual is feasible or not. If the offspring individual is predicted infeasible and its objective function value is greater than that of the parent individual, it will be intermediately discarded. Otherwise, the offspring individual will be evaluated by the true fitness function. The benefit of the proposed technique is to reduce unnecessary fitness evaluations, thereby speeding up the optimization process. The effectiveness of the CaDE is illustrated through five benchmark engineering problems including the welded beam design problem, the tension or compression spring design problem, the pressure vessel design problem, the speed reducer design problem, and the three-bar truss design problem. Additionally, a real-size 30×30 m double-layer grid structure is also optimized using the proposed method to show its applicability in practice. The results show that the CaDE requires from 11% to 55% fewer function calls than the standard Differential Evolution for achieving the same optimal designs. In comparison with other meta-heuristic algorithms, the CaDE has a faster convergence speed with the least number of fitness evaluations.

Keywords: Constrained optimization problem · Differential Evolution · AdaBoost · Machine learning · Surrogate model

1 Introduction

Most engineering design problems can be stated as a constrained optimization problem (COP) in which the best design is found to minimize the objective function while satisfying all design constraints. Over the few past decades, many optimization algorithms have been proposed to solve COPs, in which meta-heuristic algorithms have been received great attention due to their advantages such as no need for gradient information, ability to escape local optima. Among meta-heuristic algorithms, Differential Evolution (DE) proposed by Price and Storn [1] is considered to be one of the most effective optimizers. Since its first introduction in 1995, the DE algorithm has been applied in many engineering fields, for example, aerospace engineering [2], mechanic engineering [3], structural

engineering [4], etc. The main advantages of the DE are simple, robust, and easy to implement without advanced programming ability. However, like other meta-heuristic algorithms, one drawback of the DE is that it requires a lot of fitness evaluations to achieve a sufficiently good solution. For real-world problems, each fitness evaluation often requires computationally expensive simulation, such as finite element analyses in mechanic and structural engineering, or computational fluid dynamic simulation in aerospace engineering. Although each simulation does not take too long when using high-performance computers, the overall computing time is still very large due to a huge number of fitness evaluations. For example, each finite element analysis of a tied-arch bridge takes only 1 min, the optimization process consumes about 133 h with 8000 fitness evaluations [5]. For large-scale structures where each simulation takes hours, the application of meta-heuristic algorithms becomes unrealistic. Despite the fact that using parallel computing can significantly reduce the optimization time, it is still difficult to implement in practice. In such situations, developing techniques to reduce the number of fitness evaluations is a potential solution to tackle this problem.

Recently, numerous studies focusing on surrogate assisted-evolutionary optimization have been carried out [6]. The main idea of these studies is to construct approximate models to quickly evaluate candidates instead of expensive fitness evaluations. Some commonly used approximate models are Kriging [7], Artificial Neural Network (ANN) [8, 9], Support Vector Machine (SVM) [9], k-Nearest Neighbor (kNN) [10, 11]. More detailed, Liu and Sun [10] develop the DE-kNN algorithm which combines the DE with the kNN regression to accelerate the optimization process. In sooner generations, the standard DE is employed with the aim of collecting data. Based on the obtained data, a kNN regression model is built to predict the fitness function. In later generations, all individuals are ranked according to the predictions of the kNN model and then only some of the best individuals are re-evaluated by the true fitness function. In addition, the kNN model continuously updates new data. The advantage of the kNN model is that it stores all samples and defer processing until a prediction is requested, so there is no need to re-train the model when the training data is updated. Following this idea, Park and Lee [11] propose the DE-EkNN algorithm in which a speeded-up variant of the kNN is used instead of the ordinary kNN. Similarly, Pham [12] develop a technique called the nearest neighbor comparison. The proposed technique finds the nearest neighbor of the considered individual in the population based on the Minkowski distance and uses the true fitness function value of this neighbor for comparing with the parent. This technique is then applied to many problems, such as structural optimization [13], engineering optimization problems [14], etc.

Different from all the above-mentioned studies, Lu et al. [15] employ a classification technique instead of regression techniques to identify whether the offspring individual is better than its parent or not. By integrating the classification technique into the optimization process, some worse individuals are discarded without conducting true fitness evaluation. Consequently, the computational cost is greatly reduced. The classification technique used in this study is the SVM. The algorithm is then improved to the classification and regression-assisted DE in which two different types of surrogate models including classification models and regression models are employed simultaneously [16]. Recently, the classification-based surrogate models are utilized for solving

the expensive many-objective optimization [17], in which the feed-forward neural network is built to predict the dominant relationship between offspring and its parent. Based on the predictions, promising candidates are selected to be exactly evaluated.

It can be observed that despite the great efficacy, the number of studies relating to the classification-based surrogate models is still limited. Additionally, ensemble methods such as Random Forest, Adaptive Boosting, Gradient Tree Boosting, etc. have shown good performance in solving classification problems. This paper aims to investigate the ability of an ensemble method called AdaBoost (short for Adaptive Boosting) in reducing fitness evaluations of the DE. In more details, the AdaBoost classification is applied to judge whether the offspring is better than its parent or not. In this way, many useless fitness evaluations are saved. The performance of the proposed method is demonstrated through five engineering problems including the welded beam design problem, the tension/compression spring design problem, the pressure vessel design problem, the speed reducer design problem, and the three-bar truss design problem. Additionally, to showcase the applicability of the proposed method in practice, a real-size double-layer grid structure is also optimized using the CaDE.

The rest of the article is structured as follows. The formulation of COPs and the constraint handling techniques are given in Sect. 2. The DE and the AdaBoost classification are also briefly introduced in this section. The proposed method CaDE is described in Sect. 3. Five benchmark problems are carried out in Sect. 4. The obtained results of the CaDE are compared to those of other state-of-the-art meta-heuristic algorithms. The optimization of a 30×30 m double-layer grid structure using the CaDE is conducted in Sect. 5. Finally, Sect. 6 summarizes the conclusions.

2 Backgrounds

2.1 Constrained Optimization Problems

Generally, a COP is formulated as follows:

$$\begin{aligned}
 &\text{find} && \mathbf{z} = \{z_i | i = 1, \dots, D\} \\
 &\text{to minimize} && f(\mathbf{z}) \\
 &\text{subject to} && g_j(\mathbf{z}) \leq 0, j = 1, \dots, p \\
 &&& h_j(\mathbf{z}) = 0, j = p + 1, \dots, m \\
 &&& z_i^L \leq z_i \leq z_i^U, i = 1, \dots, D
 \end{aligned} \tag{1}$$

where: \mathbf{z} is a vector containing D design variables z_i ; z_i^L and z_i^U are the bounds of z_i , respectively; $f(\mathbf{z})$ is the objective function; $g_j(\mathbf{z}) \leq 0$ is an inequality constraint; $h_j(\mathbf{z}) = 0$ is an equality constraint; p and $m-p$ are the numbers of inequality constraints and equality constraints, respectively.

The equality constraints are often converted to the inequality constraint form as follows:

$$g_j(\mathbf{z}) = h_j(\mathbf{z}) - \varepsilon \leq 0, j = p + 1, \dots, m \tag{2}$$

in which: ε is a very small positive value.

In this way, the COP described in Eq. (1) with both inequality and equality constraints becomes a COP with m inequality constraints. Normally, the COP should be transformed into an unconstrained problem by applying constraint handling techniques. One commonly used technique is the penalty method in which the fitness function $F(\mathbf{z})$ is used instead of the objective function $f(\mathbf{z})$:

$$F(\mathbf{z}) = f(\mathbf{z}) + p(\mathbf{z}) \quad (3)$$

where: $p(\mathbf{z})$ is the penalty function which depends on the constraint violations.

The simplest way is to set $p(\mathbf{z})$ to a very large value if there is any constraint violation. This method, called the “death penalty method”, discards all infeasible individuals during the optimization process. The death penalty method does not need any other parameter, it is therefore preferred in practice. The mathematical form of the death penalty function is as follows:

$$p(\mathbf{z}) = PF \times (1 + cv(\mathbf{z})) \quad (4)$$

where: PF is a very large value; $cv(\mathbf{z})$ is the constraint violation degree that is defined by the sum of all constraints:

$$cv(\mathbf{z}) = \sum_{j=1}^m \max(0, g_j(\mathbf{z})) \quad (5)$$

2.2 Differential Evolution

The DE algorithm was developed in 1995 by Price and Storn [1]. The optimization process starts by initializing a population of NP individuals $P_0 = \{\mathbf{z}_{i,0} \mid i = 1, \dots, NP\}$. Each individual which is a D -dimensional vector $\mathbf{z}_{i,0} = \{z_{i,0,j} \mid j = 1, \dots, D\}$ represents a solution of the problem. At the certain generation g , the current population is $P_g = \{\mathbf{z}_{i,g} \mid i = 1, \dots, NP\}$. The DE employs three operators to improve the current population P_g to P_{g+1} for the next generation. Firstly, the mutation operator creates the mutant vector $\mathbf{x}_{i,g}$ as follows:

$$\mathbf{x}_{i,g} = \mathbf{z}_{r1,g} + F \times (\mathbf{z}_{r2,g} - \mathbf{z}_{r3,g}) \quad (6)$$

Next, the crossover operator produces the trial vector $\mathbf{y}_{i,g}$:

$$y_{i,g,j} = \begin{cases} x_{i,g,j} & \text{if } \text{rand}(0, 1) \leq Cr \text{ or } j = r \\ z_{i,g,j} & \text{otherwise} \end{cases} \quad (7)$$

Then, the selection operator compares between the target vector $\mathbf{z}_{i,g}$ and the trial vector $\mathbf{y}_{i,g}$:

$$\mathbf{z}_{i,g+1} = \begin{cases} \mathbf{y}_{i,g} & \text{if } F(\mathbf{y}_{i,g}) \leq F(\mathbf{z}_{i,g}) \\ \mathbf{z}_{i,g} & \text{otherwise} \end{cases} \quad (8)$$

where: $z_{i,g,j}$, $x_{i,g,j}$, $y_{i,g,j}$ are the j th component of $\mathbf{z}_{i,g}$, $\mathbf{x}_{i,g}$, and $\mathbf{y}_{i,g}$, respectively; $r1 \neq r2 \neq r3 \neq i$ are three random integers in $[1, NP]$; $F > 0$ is called the scale factor; $Cr \in (0, 1)$ is called the crossover rate; r is a random integer in $[1, D]$; $F(\cdot)$ is the fitness function.

Three operators of mutation, crossover, and selection are repeatedly carried out until a stopping condition is met. Normally, the stopping condition is that the pre-defined generation g_{\max} is reached.

2.3 Adaptive Boosting Classification

Adaptive Boosting, as known as AdaBoost, is categorized as an ensemble method in which several weak classifiers are combined to create a strong classifier. The AdaBoost was firstly designed for binary classification problems [18]. It is currently expanded to solve multi-class classification and regression problems. This section gives a brief introduction to the AdaBoost binary classification.

For binary classification problems, the training dataset contains N samples $\{(\mathbf{z}_i, u_i) \mid i = 1, \dots, N\}$ where \mathbf{z}_i is a vector that comprises input features, $u_i \in \{-1, +1\}$ is the output feature. Initially, the AdaBoost assigns a set of the same weights $\mathbf{D}_1 = \{w_{1,i} = 1/N \mid i = 1, \dots, N\}$ to all N samples. A weak classifier called C_1 is then trained by the weighted dataset. The error rate of the weak classifier C_1 is computed as follows:

$$err_1 = \sum_{i=1}^N w_{1,i} I(C_1(\mathbf{z}_i) \neq u_i) \quad (9)$$

where: $I(\cdot)$ is a function that returns 0 if the prediction is correct while 1 if the prediction is wrong.

The weight α_1 of the weak classifier C_1 is determined using the following equation:

$$\alpha_1 = \frac{1}{2} \ln \left(\frac{1 - err_1}{err_1} \right) \quad (10)$$

Next, the weights of samples that are wrongly classified by the C_1 are increased with the aim of getting more attention from the classifier C_2 at the next iteration. The set of weights for the second iteration is $\mathbf{D}_2 = \{w_{2,i} \mid i = 1, \dots, N\}$ where the weight $w_{2,i}$ is calculated as follows:

$$w_{2,i} = \frac{w_{1,i} \exp(\alpha_1 y_i C_1(\mathbf{z}_i))}{\sum_{i=1}^N w_{2,i}} \quad (11)$$

The weak classifier C_2 is then trained by the new weighted dataset. After T iterations, there are totally T weak classifiers that are sequentially trained. The final prediction of the strong classifier H is the weighted sum of the predictions of these weak classifiers:

$$H(\mathbf{z}) = \text{sign} \left\{ \sum_{t=1}^T \alpha_t C_t(\mathbf{z}) \right\} \quad (12)$$

where: $\text{sign}(\cdot)$ is a function that extracts the sign of a real number.

The weak classifier used in the AdaBoost can be any classification algorithm such as ANN, SVM, kNN, in which the classification decision tree is frequently used. The detailed theory of the decision tree is not introduced in this paper because it is out of the scope of the study. Readers can refer to Ref. [19]. The flowchart of the AdaBoost is displayed in Fig. 1.

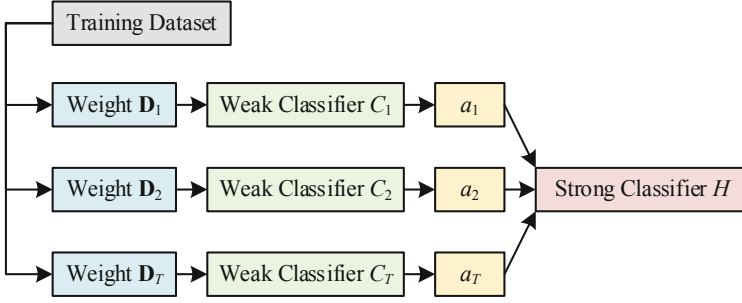


Fig. 1. AdaBoost classification.

3 Classification-Assisted Differential Evolution

In the selection step, the DE adopts a pairwise comparison in which each trial vector is only compared to the corresponding target vector based on the fitness function value. It can be easily observed that if trial vector $\mathbf{y}_{i,g}$ violates any constraint ($cv(\mathbf{y}_{i,g}) > 0$) and its objective function is larger than that of the target vector ($f(\mathbf{y}_{i,g}) > f(\mathbf{z}_{i,g})$), the fitness function of the trial vector is most likely also greater than the target vector's one ($F(\mathbf{y}_{i,g}) > F(\mathbf{z}_{i,g})$). This trial vector has high possibility of losing at the selection step. Conducting true fitness evaluation for these vectors is useless. Additionally, in most real-world optimization problems, the objective function, for example, the weight or the cost of a structure can be quickly calculated. However, the verification of constraints is often time-consuming due to performing computationally expensive simulations. Based on these observations, the main idea behind the CaDE method is to build a classifier that can distinguish whether an individual violates any constraint or not. The classifier is used in conjunction with the computation of objective functions can discard many worse trial vectors without evaluating true fitness functions, thereby, accelerate the convergence. The flowchart of the CaDE algorithm is displayed in Fig. 2.

More specifically, the CaDE method consists of two stages. The first stage performs the standard DE with the aim of collecting data samples. All trial vectors in the first stage are evaluated by the true fitness function. Each trial vector $\mathbf{y}_{i,g}$ will be assigned a label as follows:

$$u_{i,g} = \begin{cases} +1 & \text{if } cv(\mathbf{y}_{i,g}) = 0 \\ -1 & \text{if } cv(\mathbf{y}_{i,g}) > 0 \end{cases} \quad (13)$$

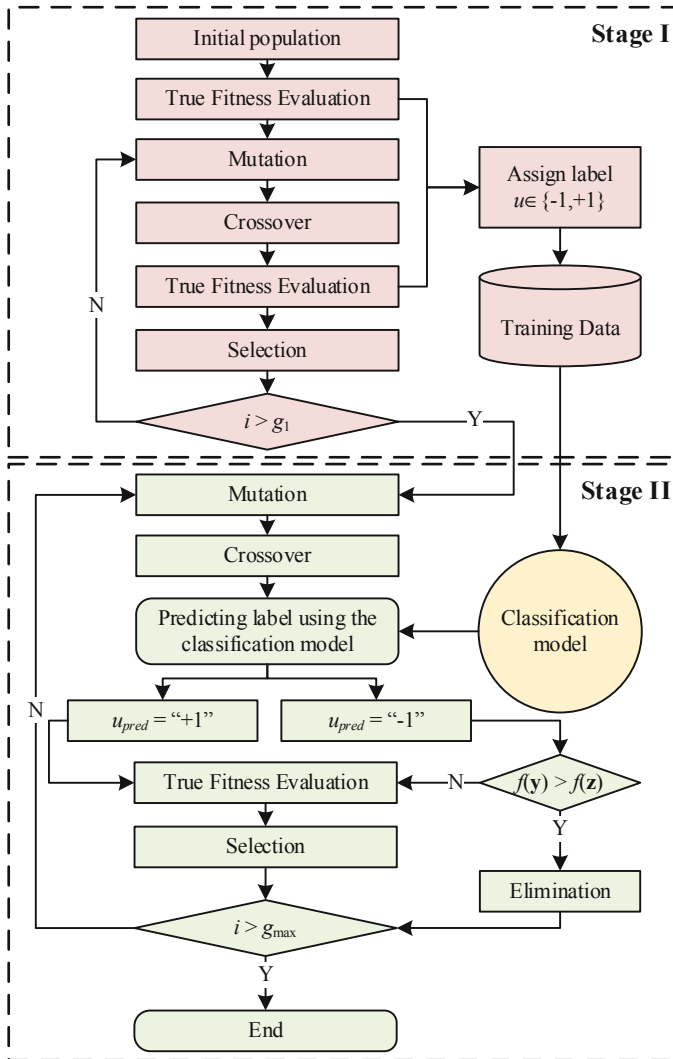


Fig. 2. Classification-assisted Differential Evolution

At the end of the first stage, a machine learning classification model is trained by the collected dataset $(\mathbf{y}_{i,g}, u_{i,g})$. In the second stage, the selection operator is modified as follows. Each trial vector $\mathbf{y}_{i,g}$ will be preliminarily assessed using the classification model. If the predicted label is $u_{pred} = +1$ or the predicted label is $u_{pred} = -1$ and the objective function value of the target vector is smaller than that of the trial vector, the trial vector will be evaluated by the true fitness function. Otherwise, the trial vector will be eliminated. It is apparent that some worse trial vectors are skipped without conducting true fitness evaluations. Consequently, the computation time can be shortened.

The early version of the CaDE was introduced in [20] in which a deep neural network (DNN) model is used to evaluate the trial vector. The DNN model is trained by samples generated by the one-shot Latin Hypercube Sampling at the beginning of the process. The integration of the DNN model helps to reduce about 20% of the number of fitness evaluations. A later research indicated that the AdaBoost model has better performance than the DNN model [21]. Next, the CaDE method has been applied to optimize many truss structures [22, 23]. In improved version of the CaDE method, the training samples are collected during the optimization process, which helps the samples to be distributed near the optimal position, thereby improving the quality of the classification model. In this study, the CaDE method is employed to solve engineering optimization problems.

4 Engineering Optimization Problems

The effectiveness of the CaDE method is investigated through five test problems. Specifically, the CaDE and the standard DE are compared in terms of the objective function values and the required numbers of true fitness evaluations. Moreover, the optimal results found by other meta-heuristic algorithms in the literature are also reported to show the superior of the proposed method.

4.1 Benchmark Problems

Five test problems carried out in this study include the welded beam design problem, the tension/compression spring design problem, the pressure vessel design problem, the speed reducer design problem, and the three-bar truss design problem. They are well-known benchmark problems that are often used to test the behavior and the convergence of a new algorithm [24].

Welded Beam Design Problem. The objective of the first example is to find the main dimensions of a welded beam as shown in Fig. 3 in order to minimize the cost of fabrication while satisfying constraints of the shear stress, the bending stress, the buckling load, and the deflection. Four design variables of this problem are the leg size h ($=z_1$) and the length l ($=z_2$) of the fillet welds as well as the depth t ($=z_3$) and the width b ($=z_4$) of the Beam's cross-section.

The mathematical form of the problem is as follows:

$$\begin{aligned}
 & \text{find: } z = \{z_1, z_2, z_3, z_4\} \\
 & \text{o minimize: } C = 1.10471z_1^2z_2 + 0.04811z_3z_4(14 + z_2) \\
 & \text{subject to:} \\
 & g_1(z) = \tau - \tau_{\max} \leq 0 \\
 & g_2(z) = \sigma - \sigma_{\max} \leq 0 \\
 & g_3(z) = z_1 - z_4 \leq 0 \\
 & g_4(z) = P - P_C \leq 0 \\
 & g_5(z) = \delta - \delta_{\max} \leq 0 \\
 & 0.125 \leq z_1 \leq 10 \\
 & 0.1 \leq z_2, z_3, z_4 \leq 10
 \end{aligned} \tag{14}$$

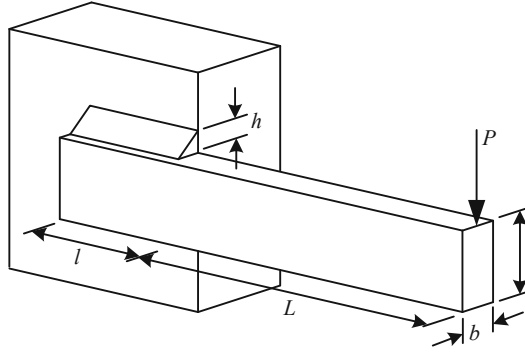


Fig. 3. Welded beam

The shear stresses, the bending stress, the deflection, and the critical buckling load are determined using the following equations:

$$\begin{aligned}\tau &= \sqrt{(\tau')^2 + 2\tau'\tau''\frac{z_2}{2R} + (\tau'')^2} \\ \sigma &= \frac{6PL}{z_4 z_3^2} \\ \delta &= \frac{4PL^3}{E z_4 z_3^3}; \\ P_C &= \frac{4.013E z_3 z_4^3}{6L^2} \left(1 - \frac{z_3}{2L} \sqrt{\frac{E}{4G}} \right)\end{aligned}\quad (15)$$

in which:

$$\begin{aligned}\tau' &= \frac{P}{\sqrt{2z_1 z_2}}; \quad \tau'' = \frac{MR}{J} \\ M &= P\left(L + \frac{z_2}{2}\right); \quad R = \sqrt{\frac{z_2^2}{4} + \left(\frac{z_1 + z_3}{2}\right)^2}; \quad J = 2 \left\{ \sqrt{2} z_1 z_2 \left[\frac{z_2^2}{12} + \left(\frac{z_1 + z_3}{2}\right)^2 \right] \right\}\end{aligned}\quad (16)$$

Other design data of this problem: the applied load $P = 6000$ lb; the length of the beam $L = 14$ in; the modulus of elasticity $E = 30\text{E}+06$ psi; the shear modulus $G = 12\text{E}+06$ psi; the allowable tangential stress $\tau_{\max} = 13,600$ psi; the allowable normal stress $\sigma_{\max} = 30,000$ psi; and the allowable displacement $\delta_{\max} = 0.25$ in.

Tension/Compression Spring Design Problem. The second problem is the optimization of the weight of a coil spring as shown in Fig. 4 subjects to the shear stress constraint, the surge frequency constraint, the displacement constraint. Three design variables considered in this problem $\{z_1, z_2, z_3\}$ denote the diameter d of the wire, the diameter D of the coil, and the number of active coils N of the spring.

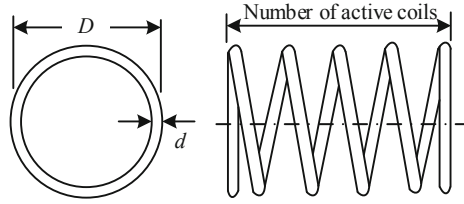


Fig. 4. Tension/Compression Spring

This problem is stated as follows:

$$\begin{aligned}
 &\text{find: } \mathbf{z} = \{z_1, z_2, z_3\} \\
 &\text{to minimize: } C = (z_3 + 2)z_2z_1^2 \\
 &\text{subject to:} \\
 &g_1(\mathbf{z}) = 1 - \frac{z_3^3z_2}{71785z_1^4} \leq 0 \\
 &g_2(\mathbf{z}) = \frac{4z_2^2 - z_1z_2}{12566(z_2z_1^3 - z_1^4)} + \frac{1}{5108z_1^2} \leq 0 \\
 &g_3(\mathbf{z}) = 1 - \frac{140.45z_1}{z_2^2z_3} \leq 0 \\
 &g_4(\mathbf{z}) = \frac{z_1 + z_2}{1.5} - 1 \leq 0 \\
 &0.05 \leq z_1 \leq 2; \quad 0.25 \leq z_2 \leq 1.3; \quad 2 \leq z_3 \leq 15
 \end{aligned} \tag{17}$$

Pressure Vessel Design Problem. This problem is to optimize the manufacturing cost of a compressed air storage tank which consists of a cylindrical shell and two hemispherical heads as displayed in Fig. 5. The manufacturing cost comprises the material cost, the forming cost, and the welding cost. There are totally four design variables in this problem, in which two variables of the thicknesses of the shell T_s ($=z_1$) and the head T_h ($=z_2$) are discrete with the step of 0.0625 in. While two variables of the inner radius R ($=z_3$) and the length L ($=z_4$) of the shell are continuous. The design constraints include the minimum ratios between the thickness and the radius, the minimum volume, and the maximum length of the vessel.

The formulation of this problem is as follows:

$$\begin{aligned}
 &\text{find: } \mathbf{z} = \{z_1, z_2, z_3, z_4\} \\
 &\text{to minimize:} \\
 &C = 0.6224z_1z_3z_4 + 1.7781z_2z_3^2 + 3.1661z_1^2z_4 + 19.84z_1^2z_3 \\
 &\text{subject to:} \\
 &g_1(\mathbf{z}) = 0.0193 - z_1/z_3 \leq 0 \\
 &g_2(\mathbf{z}) = 0.00954 - z_2/z_3 \leq 0 \\
 &g_3(\mathbf{z}) = 1296000 - \pi z_3^2z_4 - (4/3)\pi z_3^3 \leq 0 \\
 &g_4(\mathbf{z}) = z_4 - 240 \leq 0 \\
 &0.06255 \leq z_1, z_2 \leq 5; \quad 10 \leq z_3, z_4 \leq 200
 \end{aligned} \tag{18}$$

Speed Reducer Design Problem. The purpose of this problem is the weight optimization of a speed reducer presented in Fig. 6. Seven design variables of this problem are

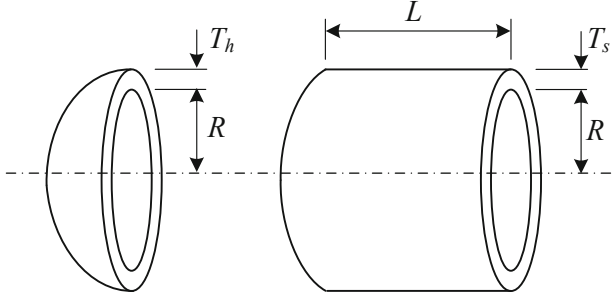


Fig. 5. Pressure vessel

the width of the gear face z_1 , the teeth module z_2 , the number of pinion teeth z_3 , the lengths of the shafts between the bearings z_4 , z_5 , and the diameters of the shafts z_6 , z_7 . This problem is expressed as follows:

$$\begin{aligned} & \text{find: } \mathbf{z} = \{z_1, \dots, z_7\} \\ & \text{to minimize:} \\ & C = 0.7854z_1z_2^2(3.3333z_3^2 + 14.9334z_3 - 43.0934) \\ & - 1.508z_1(z_6^2 + z_7^2) + 7.4777(z_6^3 + z_7^3) + 0.7854(z_4z_6^2 + z_5z_7^2) \end{aligned} \quad (19)$$

Eleven constraints such as teeth stresses, surface stresses, shaft stresses, and deflections are as follows:

$$\begin{aligned} g_1(\mathbf{z}) &= \frac{27}{z_1z_2^2z_3} - 1 \leq 0; \quad g_2(\mathbf{z}) = \frac{397.5}{z_1z_2^2z_3^2} - 1 \leq 0 \\ g_3(\mathbf{z}) &= \frac{1.93z_4^3}{z_2z_3z_6^4} - 1 \leq 0; \quad g_4(\mathbf{z}) = \frac{1.93z_5^3}{z_2z_3z_7^4} - 1 \leq 0 \\ g_5(\mathbf{z}) &= \frac{1}{110z_6^3} \sqrt{\left(\frac{754z_4}{z_2z_3}\right)^2 + 16.9 \times 10^6} - 1 \leq 0 \\ g_6(\mathbf{z}) &= \frac{1}{85z_7^3} \sqrt{\left(\frac{754z_5}{z_2z_3}\right)^2 + 157.5 \times 10^6} - 1 \leq 0 \\ g_7(\mathbf{z}) &= \frac{z_2z_3}{40} - 1 \leq 0; \quad g_8(\mathbf{z}) = \frac{5z_2}{z_1} - 1 \leq 0 \\ g_9(\mathbf{z}) &= \frac{z_1}{12z_2} - 1 \leq 0; \quad g_{10}(\mathbf{z}) = \frac{1.5z_6 + 1.9}{z_4} - 1 \leq 0 \\ g_{11}(\mathbf{z}) &= \frac{1.1z_7 + 1.9}{z_5} - 1 \leq 0 \end{aligned} \quad (20)$$

The bounds on the design variables are:

$$\begin{aligned} 2.6 \leq z_1 \leq 3.6; \quad 0.7 \leq z_2 \leq 0.8; \quad 17 \leq z_3 \leq 18 \\ 7.3 \leq z_4, z_5 \leq 8.3; \quad 2.9 \leq z_6 \leq 3.9; \quad 5 \leq z_7 \leq 5.5 \end{aligned} \quad (21)$$

Three-Bar Truss Design Problem. This problem is to find the members' cross-sectional areas z_1 , z_2 with the objective of minimizing the weight of the truss. The configuration of the truss is displayed in Fig. 7.

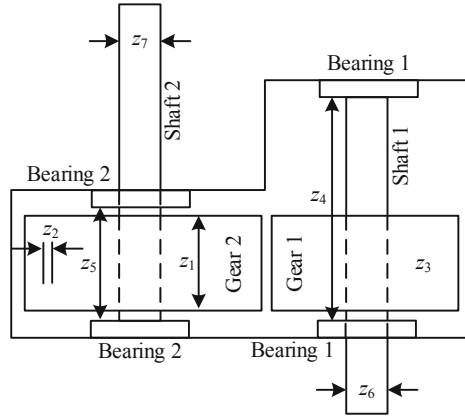


Fig. 6. Speed Reducer

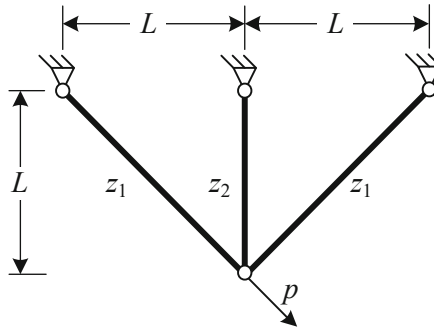


Fig. 7. Three-bar truss

This problem is expressed as follows:

$$\begin{aligned}
 &\text{find: } \mathbf{z} = \{z_1, z_2\} \\
 &\text{to minimize: } W = (2\sqrt{2}z_1 + z_2)L \\
 &\text{subject to:} \\
 &g_1(\mathbf{z}) = \frac{\sqrt{2}z_1 + z_2}{\sqrt{2z_1^2 + 2z_1z_2}} p - \sigma \leq 0 \\
 &g_2(\mathbf{z}) = \frac{z_2}{\sqrt{2z_1^2 + 2z_1z_2}} p - \sigma \leq 0 \\
 &g_3(\mathbf{z}) = \frac{1}{\sqrt{2z_2 + z_1}} p - \sigma \leq 0 \\
 &0 \leq z_1, z_2 \leq 1
 \end{aligned} \tag{22}$$

where: $p = 2 \text{ kN}$; $L = 100 \text{ cm}$; and $\sigma = 2 \text{ kN/cm}^2$.

4.2 Parameter Setting

To exhibit the advantage of the proposed method, the CaDE is compared with the standard DE and other meta-heuristic algorithms collected in the literature. Two metrics used for the comparison are the objective function value and the number of true fitness evaluations (nFE). Each test problem is carried out for 50 independent runs and the obtained results are reported by best, mean, worst, and the standard deviation (SD) values.

Both the standard DE and the CaDE utilize the mutation strategy “DE/target-to-best/1” instead of the original mutation strategy “DE/rand/1”. Two compared algorithms are set with the same parameters as follows: $NP = 20$; $F = 0.8$; $Cr = 0.9$; and $g_{\max} = 300$ for all problems except that for the three-bar truss problem, $g_{\max} = 100$. For the CaDE, the number of iterations for the first stage g_1 is set to 5, which means the number of training samples is 100. The AdaBoost classification model used in all five problems uses the Classification Decision Tree with the maximum depth of 1 as the weak classifier. Each AdaBoost model contains 10 weak classifiers. All codes are written in Python language in which the AdaBoost models are built using the library scikit-learn [25].

4.3 Comparative Results

Tables 1, 2, 3, 4, and 5 report the results obtained by two algorithms implemented in this study and other meta-heuristic algorithms in the literature. The Mine Blast algorithm (MBA) by Sadollah et al. in 2012 [26], the rank-iMDDE by Gong et al. in 2014 [27], the NDE by Mohamed in 2017 [28], the ϵ DEdn by Pham et al. in 2018 [14] are selected for the comparison. It is noted that the bold value denotes that this is the best among the compared values. Five figures from Fig. 8, Fig. 9, Fig. 10, Fig. 11 and Fig. 12 plot the convergence histories of the standard DE and the CaDE on the test problems described above.

Table 1. Comparison of the CaDE with other algorithms for the Welded Beam Problem.

	MBA [26]	rank-iMDDE [27]	NDE [28]	ϵ DEdn [14]	Present work	
					DE	CaDE
z_1	0.205729	–	0.20573	–	0.20573	0.20573
z_2	3.470493	–	3.47049	–	3.47049	3.47049
z_3	9.036626	–	9.03662	–	9.03662	9.03662
z_4	0.205729	–	0.20573	–	0.20573	0.20573
Best	1.724853	1.724852309	1.724852309	1.724852309	1.724852309	1.724852309
Mean	1.724853	1.724852309	1.724852309	1.724852309	1.772538546	1.739730843
Worst	1.724853	1.724852309	1.724852309	1.724852309	3.828706584	2.468469261
SD	6.94E–19	7.71E–11	3.73E–12	3.21E–12	2.95E–01	1.04E–01
nFE	47,340	15,000	8,000	8,000	6,000	4,104

Table 2. Comparison of the CaDE with other algorithms for the Spring Problem

	MBA [26]	rank-iMDDE [27]	NDE [28]	ε DEdn [14]	Present work	
					DE	CaDE
z_1	0.051656	–	0.05169	–	0.05169	0.05169
z_2	0.355940	–	0.35672	–	0.35672	0.35671
z_3	11.344665	–	11.28897	–	11.28897	11.28957
Best	0.012665	0.012665233	0.012665232	0.012665233	0.012665233	0.012665233
Mean	0.012713	0.012665297	0.012668899	0.012665233	0.013061160	0.012825264
Worst	0.012900	0.01266743	0.012687092	0.012665233	0.030814173	0.014545462
SD	6.3E–05	8.48E–07	5.38E–06	3.01E–11	2.54E–03	3.34E–04
nFE	7,650	10,000	24,000	10,000	6,000	2,729

Table 3. Comparison of the CaDE with other algorithms for the Pressure Vessel Problem

	MBA [26]	rank-iMDDE [27]	NDE [28]	ε DEdn [14]	Present work	
					DE	CaDE
z_1	0.7802	–	0.8125	–	0.8125	0.8125
z_2	0.3856	–	0.4375	–	0.4375	0.4375
z_3	40.4292	–	42.0984456	–	42.0984	42.0984
z_4	198.4964	–	176.636596	–	176.6366	176.6366
Best	5889.3216	6059.714335	6059.714335	6059.714335	6059.714335	6059.714335
Mean	6200.64765	6059.714335	6059.714335	6059.714335	6242.519642	6252.993915
Worst	6392.5062	6059.714335	6059.714335	6059.714335	7544.492518	7544.492518
SD	160.34	7.57E–07	4.56E–07	9.46E–13	372.0377519	351.9042002
nFE	50,000	15,000	20,000	10,000	6,000	4,878

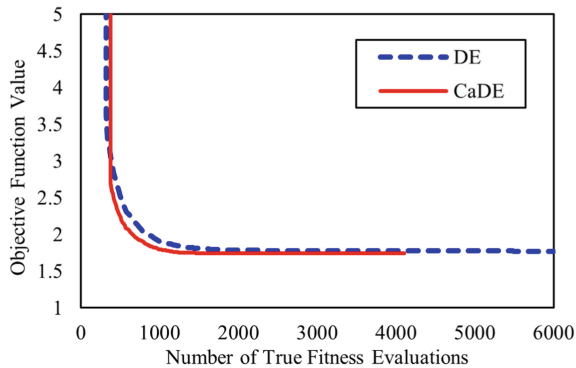
After 50 independent runs, both the DE and the CaDE obtain the same best objective function values on all five test problems. However, the CaDE converges faster than the DE. This conclusion is indicated through the number of true fitness evaluations that are carried by two algorithms. The DE conducts 6000 true fitness evaluations for all problems while the CaDE carries out 4104 evaluations for optimizing the welded beam, 2729 evaluations for optimizing the spring, 4878 evaluations for the pressure vessel problem, 4556 evaluations for optimizing the speed reducer, and 1788 evaluations for optimizing the three-bar truss structure. It is achieved by incorporating the AdaBoost classification model to discard unnecessary fitness evaluation during the DE optimization process. The omitted rates for five test problems are approximately 32%, 55%, 19%, 24%, and 11%, respectively. Additionally, it can be noted that the CaDE is more stable

Table 4. Comparison of the CaDE with other algorithms for the Speed Reducer Problem

	MBA [26]	rank-iMDDE [27]	NDE [28]	ϵ DEdn [14]	Present work	
					DE	CaDE
z_1	3.5	–	3.5	–	3.5	3.5
z_2	0.7	–	0.7	–	0.7	0.7
z_3	17.0	–	17.0	–	17.0	17.0
z_4	7.30033	–	7.3	–	7.3	7.3
z_5	7.715772	–	7.71532	–	7.71532	7.71532
z_6	3.350218	–	3.35021	–	3.35021	3.35021
z_7	5.286654	–	5.28665	–	5.28665	5.28665
Best	2994.482453	2994.471066	2994.4710661	2994.4710661	2994.471066	2994.471066
Mean	2996.769019	2994.471066	2994.4710661	2994.4710661	2994.983502	2994.471066
Worst	2999.652444	2994.471066	2994.4710661	2994.4710661	3019.986324	2994.471067
SD	1.56	7.93E–13	4.17E–12	3.87E–12	3.57E+00	2.23E–07
nFE	6300	19,920	18,000	15,000	6,000	4,556

Table 5. Comparison of the CaDE with other algorithms for the Three-bar Truss Problem

	MBA [26]	rank-iMDDE [27]	NDE [28]	ϵ DEdn [14]	Present work	
					DE	CaDE
z_1	0.7885650	–	0.78868	–	0.78868	0.78868
z_2	0.4085597	–	0.40825	–	0.40825	0.40825
Best	263.8958522	263.8958434	263.8958434	263.8958434	263.8958434	263.8958434
Mean	263.897996	263.8958434	263.8958434	263.8958434	263.8958434	263.8979754
Worst	263.915983	263.8958434	263.8958434	263.8958434	263.8958458	264.0021508
SD	3.93E–03	0.00E+00	0.00E+00	2.44E–13	3.40E–07	1.49E–02
nFE	13,280	4,920	4,000	2,000	2,000	1,788

**Fig. 8.** Comparison of the DE and the CaDE for the Welded Beam Problem

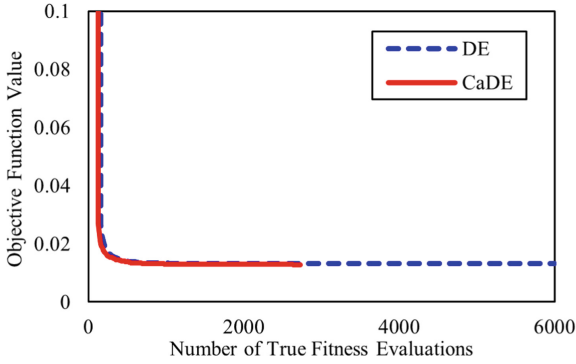


Fig. 9. Comparison of the DE and the CaDE for the Problem

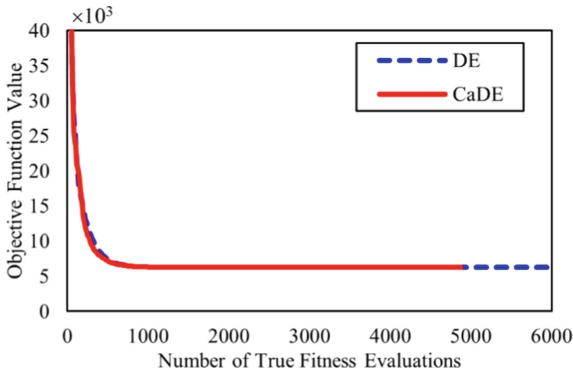


Fig. 10. Comparison of the DE and the CaDE for the Pressure Vessel Problem

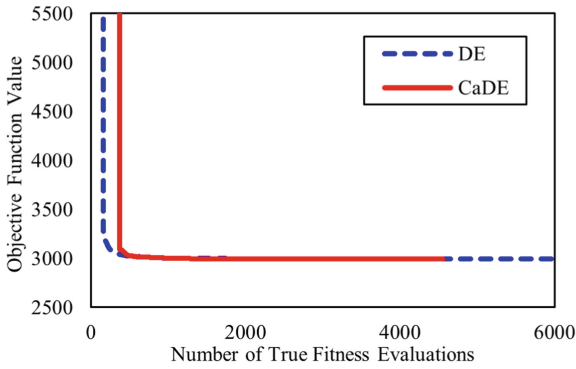


Fig. 11. Comparison of the DE and the CaDE for the Speed Reducer Problem

than the DE indicated by the smaller SD values in all problems except the three-bar truss problem.

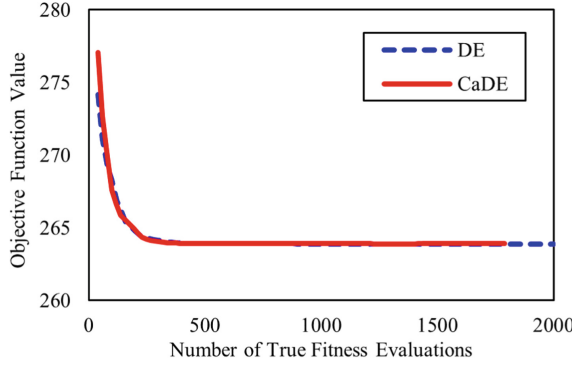


Fig. 12. Comparison of the DE and the CaDE for the Three-bar Truss Problem

In comparison with other meta-heuristic algorithms taken from the literature, the CaDE exhibits superior performance when achieving the same best results but with much fewer evaluations than the remaining ones. However, the larger SD values indicate that the CaDE is less stable than other algorithms.

5 Application to a Real-Size Double-Layer Grid Structure

In this section, the CaDE is employed to optimize the weight of a 30×30 m double-layer grid structure fabricated from the steel grade A992 Gr. 50 with the mechanical properties as follows: the density $\rho = 7850 \text{ kg/m}^3$; the modulus of elasticity $E = 2.1\text{E} + 10 \text{ kg/m}^2$; and the yield strength $F_y = 3.515\text{E} + 07 \text{ kg/m}^2$. This structure consists of 968 members which are divided into 16 section groups as shown in Fig. 13. The depth of the grid structure equals 1.5 m, and the distance between two adjacent nodes is 3.0 m. Table 6 introduces the list of 26 pipe profiles available in this project.

For simplicity, only one load case is considered in this problem in which a uniformly distributed load of 250 kgf/m^2 is applied on the top surface of the grid structure. This structure is designed based on AISC LFRD method [29]. For tension members:

$$P_u \leq \phi_t P_n = \min \left\{ \begin{array}{l} \phi_t F_y A_g \\ \phi F_u A_e \end{array} \right. \quad (23)$$

where: P_u is the required strength; $\phi_t = 0.9$ is the resistance factor for tension; P_n is the nominal strength; F_y is the yield strength; F_u is the tensile strength; A_g is the gross are of member; A_e is the effective net are of member.

For compression members:

$$F_{cr} = \begin{cases} P_u \leq \phi_c P_n = \phi_c F_{cr} A_g \\ \left(0.658^{F_y/F_e} \right) F_y \text{ if } KL/r \leq 4.71 \sqrt{E/F_y} \\ 0.877 F_e \text{ if } KL/r > 4.71 \sqrt{E/F_y} \\ F_e = \frac{\pi^2 E}{(KL/r)^2} \end{cases} \quad (24)$$

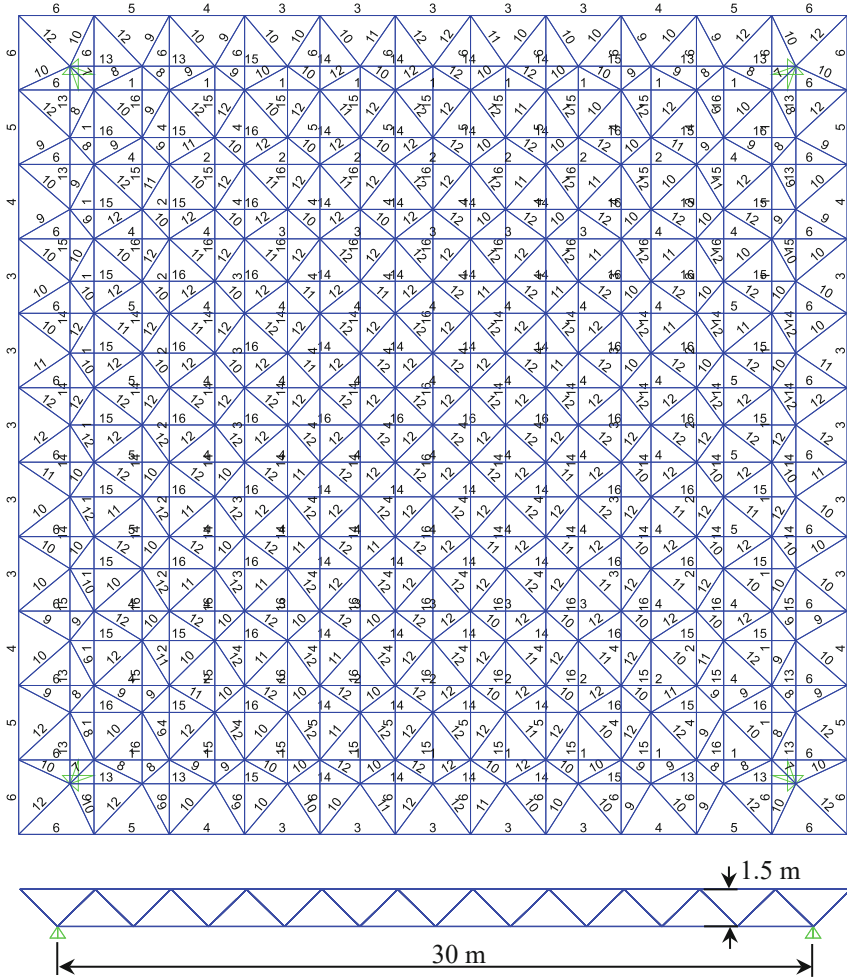


Fig. 13. Configuration of the 30 × 30 m Double-Layer Grid Structure

where: $\phi_c = 0.85$ is the resistance factor for compression; F_{cr} is the critical stress; F_e is the elastic buckling stress; K is the effective length factor which equals 1 in this case; L is the length of the member; and r is the radius of gyration of the member’s cross-section.

Additionally, the slenderness ratio $\lambda = KL/r$ is limited to 200 for compression members while 300 for tension members. The allowable deflection of this truss is $[\delta] = L/120$.

This structure is optimized using the CaDE method with the following parameters: $NP = 50$; $F = 0.8$; $Cr = 0.9$; $g_1 = 10$; $g_{max} = 150$. The AdaBoost model employed in this problem has $T = 50$ weak classifiers. During the optimization process, the grid structure is analyzed using the direct stiffness method. The optimization problem is implemented by Python programming language.

Table 6. List of available pipe profiles

No.	Profile	A (cm ²)	r (cm)	No.	Profile	A (cm ²)	r (cm)
1	φ33.70 × 2.6	2.54	1.1	14	φ159.0 × 4.0	19.48	5.4814
2	φ48.30 × 2.6	3.73	1.62	15	φ168.3 × 4.0	20.65	5.8102
3	φ60.30 × 3.2	5.74	2.02	16	φ193.7 × 4.5	26.75	6.6922
4	φ76.10 × 3.2	7.329	2.5799	17	φ219.1 × 5.0	33.63	7.5716
5	φ82.50 × 3.2	7.972	2.806	18	φ244.5 × 5.4	40.56	8.4557
6	φ88.90 × 3.2	8.616	3.0321	19	φ273.0 × 5.6	47.04	9.457
7	φ101.6 × 3.6	11.08	3.4672	20	φ298.5 × 5.9	54.23	10.3471
8	φ108.0 × 3.6	11.81	3.6934	21	φ323.9 × 5.9	58.94	11.245
9	φ114.3 × 3.6	12.52	3.9161	22	φ355.6 × 6.3	69.13	12.3536
10	φ127.0 × 4.0	15.45	4.3504	23	φ368.0 × 6.3	71.59	12.7895
11	φ133.0 × 4.0	16.21	4.5629	24	φ406.4 × 6.3	79.19	14.1475
12	φ139.7 × 4.0	17.05	4.8004	25	φ419.0 × 7.1	91.88	14.5645
13	φ152.4 × 4.0	18.65	5.2483	26	φ457.2 × 7.1	100.4	15.915

The convergence curve of the CaDE is plotted in Fig. 14 and the statistical results of 30 independent runs are reported in Table 7. Besides, this table also introduces 16 pipe profiles of the best design among 30 designs found by the CaDE. It can be seen that the smallest weight of the grid structure optimized by the CaDE is 24114.2 kg. Remarkable, the CaDE performs only 5735 true fitness evaluation, which is about 76.5% of the number of evaluations required by the standard DE with the same setting.

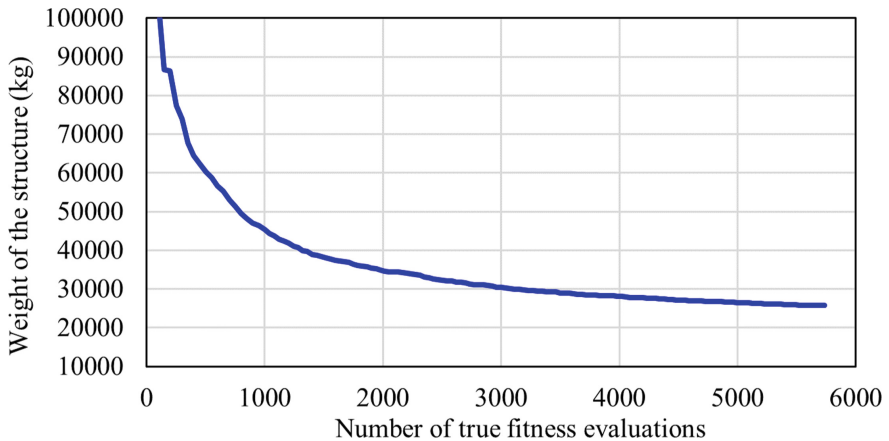
**Fig. 14.** Convergence Curve of the CaDE for the 30 × 30 m Double-Layer Grid Structure

Table 7. Results of the optimization of the 30 × 30 m double-layer grid structure

Best design	Group	Profile	Group	Profile
	1	φ273,0 × 5,6	9	φ108,0 × 3,6
	2	φ168,3 × 4,0	10	φ82,50 × 3,2
	3	φ168,3 × 4,0	11	φ60,30 × 3,2
	4	φ114,3 × 3,6	12	φ60,30 × 3,2
	5	φ88,90 × 3,2	13	φ244,5 × 5,4
	6	φ33,70 × 2,6	14	φ108,0 × 3,6
	7	φ273,0 × 5,6	15	φ60,30 × 3,2
	8	φ152,4 × 4,0	16	φ88,90 × 3,2
Statistical results	Best (kg)			24114.2
	Worst (kg)			30472.4
	Mean (kg)			25723.8
	SD (kg)			1370.8
	<i>nFE</i>			5,735

Figure 15, Fig. 16 and Fig. 17 show the strength ratios, the deflection ratios, and the slenderness ratios for the best design, respectively. It is observed that the maximum strength ratio of members reaches 0.9997 while the maximum deflection ratio is 0.9510 and the slenderness ratio equals 0.9091. Thus, the strength constraint is the design control condition in this case.

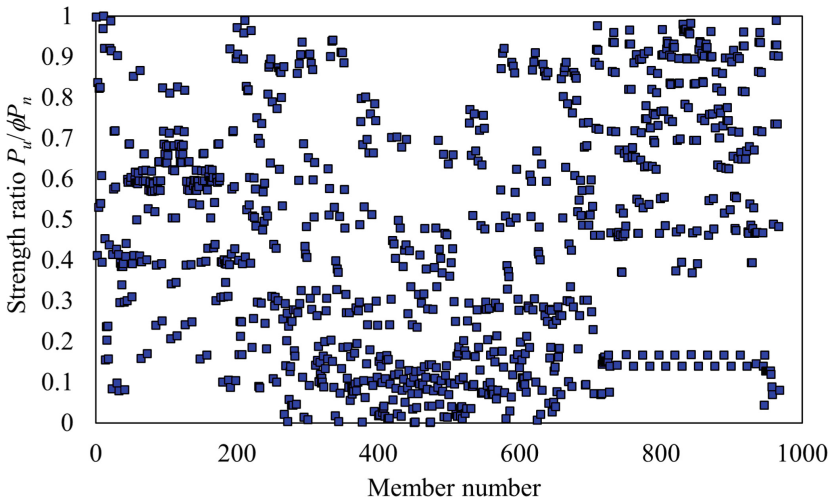


Fig. 15. Strength ratios for the best design

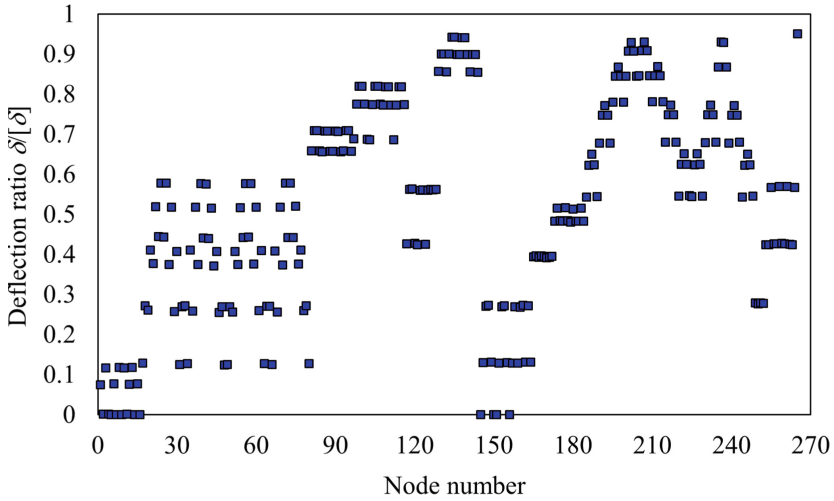


Fig. 16. Deflection ratios for the best design

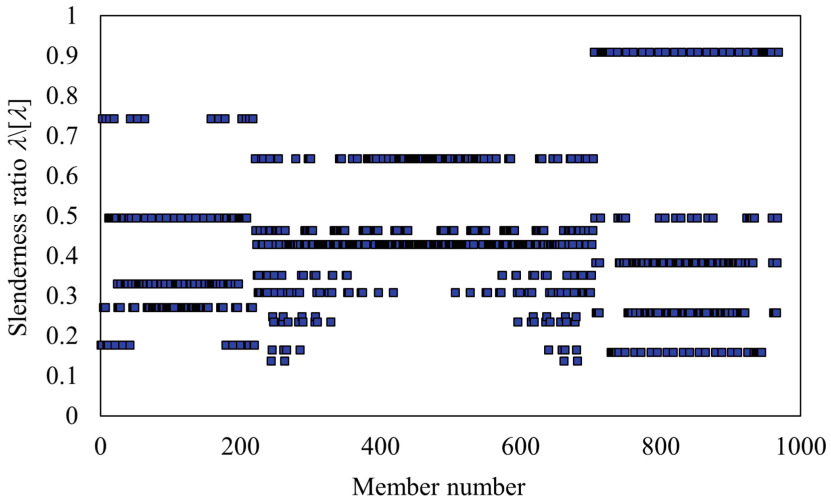


Fig. 17. Slenderness ratios for the best design

6 Conclusions

In this paper, an efficient method called CaDE that integrates the Adaptive Boosting classification technique into the Differential Evolution algorithm is proposed to solve constrained engineering optimization problems. The standard Differential Evolution with four basic operators is employed in the sooner generations with the aim of exploring the design space and collecting training data. The Adaptive Boosting model is trained by the collected data and then utilized to discard worse solutions during later generations.

The proposed method is applied to five benchmark problems and a real-size double-layer grid structure to illustrate its effectiveness. The optimal design found by the CaDE is as good as the results obtained by other optimization algorithms. However, the advantage of the CaDE is the fast convergence speed. This advantage is achieved because the CaDE reduces the number of true fitness evaluations by from 11 to 55% compared to the standard Differential Evolution algorithm.

In the future, extending the application of the machine learning classification model to other optimization algorithms, such as Jaya, Rao, or Yuki [30] is a potential direction. Additionally, the machine learning classification can be used to effectively solve other structural problems, for example, structural health monitoring, etc.

References

1. Storn, R., Price, K.: Differential evolution—a simple and efficient heuristic for global optimization over continuous spaces. *J. Glob. Optim.* **11**(4), 341–359 (1997)
2. Madavan, N.: On improving efficiency of differential evolution for aerodynamic shape optimization applications. In: 10th AIAA/ISSMO Multidisciplinary Analysis and Optimization Conference, p. 4622 (2004)
3. Lampinen, J., Zelinka, I.: Mechanical engineering design optimization by differential evolution. In: *New Ideas in Optimization*, pp. 127–146 (1999)
4. Wang, Z., Tang, H., Li, P.: Optimum design of truss structures based on differential evolution strategy. In: 2009 International Conference on Information Engineering and Computer Science, pp. 1–5. IEEE (2009)
5. Latif, M.A., Saka, M.P.: Optimum design of tied-arch bridges under code requirements using enhanced artificial bee colony algorithm. *Adv. Eng. Softw.* **35**, 102685 (2019)
6. Jin, Y.: A comprehensive survey of fitness approximation in evolutionary computation. *Soft. Comput.* **9**(1), 3–12 (2005)
7. Elsayed, S.M., Ray, T., Sarker, R.A.: A surrogate-assisted differential evolution algorithm with dynamic parameters selection for solving expensive optimization problems. In: 2014 IEEE Congress on Evolutionary Computation (CEC), pp. 1062–1068. IEEE (2014)
8. Jin, Y., Hüsken, M., Olhofer, M., Sendhoff, B.: Neural networks for fitness approximation in evolutionary optimization. In: Jin, Y. (ed.) *Knowledge Incorporation in Evolutionary Computation*. SFSC, vol. 167, pp. 281–306. Springer, Heidelberg (2005). https://doi.org/10.1007/978-3-540-44511-1_14
9. Yan, S., Minsker, B.: A dynamic meta-model approach to genetic algorithm solution of a risk-based groundwater remediation design model. In: *World Water & Environmental Resources Congress 2003*, pp. 1–10 (2003)
10. Liu, Y., Sun, F.: A fast differential evolution algorithm using k-nearest neighbour predictor. *Expert Syst. Appl.* **38**(4), 4254–4258 (2011)
11. Park, S.-Y., Lee, J.-J.: An efficient differential evolution using speeded-up k-nearest neighbor estimator. *Soft. Comput.* **18**(1), 35–49 (2013). <https://doi.org/10.1007/s00500-013-1030-x>
12. Pham, H.A.: Reduction of function evaluation in differential evolution using nearest neighbor comparison. *Vietnam J. Comput. Sci.* **2**(2), 121–131 (2014). <https://doi.org/10.1007/s40595-014-0037-2>
13. Pham, H.A.: Truss optimization with frequency constraints using enhanced differential evolution based on adaptive directional mutation and nearest neighbor comparison. *Adv. Eng. Softw.* **102**, 142–154 (2016)

14. Pham, A. H., Vu, C. T., Nguyen, D. B., Tran, D. T.: Engineering optimization using an improved epsilon differential evolution with directional mutation and nearest neighbor comparison. In: Nguyen-Xuan, H., Phung-Van, P., Rabczuk, T. (eds.) ACOME 2017. LNME, pp. 201–216. Springer, Singapore (2018). https://doi.org/10.1007/978-981-10-7149-2_14
15. Lu, X., Tang, K., Yao, X.: Classification-assisted differential evolution for computationally expensive problems. In: 2011 IEEE Congress of Evolutionary Computation (CEC), pp. 1986–1993. IEEE (2011)
16. Lu, X.F., Tang, K.: Classification-and regression-assisted differential evolution for computationally expensive problems. *J. Comput. Sci. Technol.* **27**(5), 1024–1034 (2012)
17. Pan, L., He, C., Tian, Y., Wang, H., Zhang, X., Jin, Y.: A classification-based surrogate-assisted evolutionary algorithm for expensive many-objective optimization. *IEEE Trans. Evol. Comput.* **23**(1), 74–88 (2018)
18. Freund, Y., Schapire, R.E.: A decision-theoretic generalization of on-line learning and an application to boosting. *J. Comput. Syst. Sci.* **55**(1), 119–139 (1997)
19. Breiman, L., Friedman, J. H., Olshen, R.A., Stone, C.J.: *Classification and Regression Trees*. Routledge, London (2017)
20. Nguyen, T.-H., Vu, A.-T.: Application of artificial intelligence for structural optimization. In: TienKhiem, N., Van Lien, T., Xuan Hung, N. (eds.) *Modern Mechanics and Applications*. LNME, pp. 1052–1064. Springer, Singapore (2022). https://doi.org/10.1007/978-981-16-3239-6_82
21. Nguyen, T.H., Vu, A.T.: Comparison of machine learning classifiers for reducing fitness evaluations of structural optimization. *J. Soft Comput. Civil Eng.* **5**(4), 57–73 (2021)
22. Nguyen, T.H., Vu, A.T.: Weight optimization of steel lattice transmission towers based on differential evolution and machine learning classification technique. *Frattura ed Integrità Strutturale* **16**(59), 172–187 (2022)
23. Nguyen, T., Vu, A.: An efficient differential evolution for truss sizing optimization using AdaBoost classifier. *CMES-Comput. Model. Eng. Sci.* **134**(1), 429–458 (2023)
24. Kumar, A., Wu, G., Ali, M.Z., Mallipeddi, R., Suganthan, P.N., Das, S.: A test-suite of non-convex constrained optimization problems from the real-world and some baseline results. *Swarm Evol. Comput.* **56**, 100693 (2020)
25. Pedregosa, F., et al.: Scikit-learn: machine learning in Python. *J. Mach. Learn. Res.* **12**, 2825–2830 (2011)
26. Sadollah, A., Bahreininejad, A., Eskandar, H., Hamdi, M.: Mine blast algorithm: a new population based algorithm for solving constrained engineering optimization problems. *Appl. Soft Comput.* **13**(5), 2592–2612 (2013)
27. Gong, W., Cai, Z., Liang, D.: Engineering optimization by means of an improved constrained differential evolution. *Comput. Methods Appl. Mech. Eng.* **268**, 884–904 (2014)
28. Mohamed, A.W.: A novel differential evolution algorithm for solving constrained engineering optimization problems. *J. Intell. Manuf.* **29**(3), 659–692 (2017). <https://doi.org/10.1007/s10845-017-1294-6>
29. AISC, Lrfd, Specification: Load and Resistance Factor Design Specification for Structural Steel Buildings. American Institute of Steel Construction, USA (1986)
30. Benaissa, B., Hocine, N.A., Khatir, S., Riahi, M.K., Mirjalili, S.: YUKI algorithm and POD-RBF for elastostatic and dynamic crack identification. *J. Comput. Sci.* **55**, 101451 (2021)



Damage Detection in Structures Using Strain Measurement

Duong Huong Nguyen^(✉), Nhu Mai Thi Nguyen, Xuan Hung Doan,
Quoc Bao Nguyen, Viet Phuong Nguyen, and Duy Hoa Pham

Faculty of Bridges and Roads, Hanoi University of Civil Engineering, Hanoi 100000, Vietnam
duongnh2@huce.edu.vn

Abstract. Vibration-based Structural Health Monitoring (SHM) is a non-destructive method and is widely used in recent years. To measure the vibration response of the structure under impact load, uniaxial/triaxial accelerometers, displacement, and velocity meters are used. Many works use modal parameters extracted from vibration such as frequency, mode shape, and modal curvature to detect damage. Among these parameters, modal curvature is proved very sensitive to damage. Modal strains (or curvatures) can be derived from displacement mode shape using the central difference method, but this procedure may contain cumulative errors. In this paper, direct modal strain measurement will be used. A steel slab equipped with strain transducers is set up in the laboratory. The strain response will be recorded and analysed directly to find the modal strains. From direct modal strain measurements, the damage location will be identified. Two damage scenarios are examined to verify the method.

Keywords: Structural Health Monitoring (SHM) · Strain measurement · Direct modal strain · Curvatures

1 Introduction

Vibration-based SHM relies on the fact that damage will change the modal parameters of a structure. Operational modal analysis (OMA) is known as vibration testing used for Civil engineering structures. OMA testing does not have to measure the input loads that are white noise. Methods are available to estimate modal parameters from the OMA test, such as the stochastic subspace identification (SSI) technique [1] and the frequency-domain decomposition (FDD) [2].

Traditional sensors used in vibration-based SHM are uniaxial/triaxial accelerometers, displacement sensors (LVDT), velocity sensors and strain sensors. Modal parameters of structure such as natural frequencies, mode shapes, and modal curvatures can be estimated by analyzing vibration data and then used in the SHM method. It is suggested that methods from natural frequency shifts are less robust than those based on mode shapes [3, 4]. There are two directions of damage detection methods based on mode shape: the first is directly comparing the mode shape and the second is using mode shape curvature.

The first approach is direct comparing mode shape, Modal Assurance Criterion, MAC [5] and the Coordinate Modal Assurance Criterion, COMAC [6] can be used to measure the resemblance of two mode shapes. If the MAC or COMAC is equal to 1, two mode shapes are perfect fit, and no damage appears. Natural frequencies and MAC, and COMAC indexes are often used in the FE model updating. Tran-Ngoc, Khatir [7] update the FE model of Nam O bridge based on the natural frequencies and mode shapes of the first ten modes. Ho, Khatir [8] successfully obtains the natural frequencies and mode shapes of a cable stayed bridge from accelerometer data. Then the FE model of Kien bridge is updated by using an objective function related to the differences between frequencies, MAC, COMAC and eCOMAC values. Ren and De Roeck [9, 10] verified the damage identification technique using modal data by simulation and testing and concluded that the application for full-scale structure is still a challenge.

The second approach is using mode shape curvatures. The curvatures (or modal strains) have proven more sensitive to local damage than the displacement mode shape [11]. Curvature can be derived from displacement mode shape, but this process may contain many errors. Direct measuring of the modal strain can limit the measurement error and improve the analysis accuracy. In recent years, with the advancement of technology, the dynamic strain could be measured by strain optic FBG distributed strain sensors, and strain transducers. The application of using direct strain data measurement for SHM can be found in many works [12–14]. The influence of modal curvature to evaluate the damage in a prestressed reinforced concrete beam was reported in Ref [15]. The vibration testing using optical Fiber Strain Sensors was performed in Tilff Bridge. Modal parameters of Tilff Bridge were extracted and used for damage identification [16]. Modal curvature coupled with the Convolutional neural network method can detect the damage location of a girder at Bo Nghi bridge [17] and qualified damage in a laboratory beam [18].

The mode shape based damage detection method is very effective in local damage detection. However, the drawback of this method is that it requires a lot of sensors. Different measure setup has to propose in case the number of DOFs are more than the number of sensors. The direct measurement of modal strains will improve the accuracy of methods and can be used to detect damage which is invisible at the surface.

In this paper, the BDI strain transducer is used to collect the dynamic strain of a steel slab in the laboratory. The collected data is analyzed utilizing SSI algorithm. Modal parameters such as natural frequencies and modal curvatures are calculated from the OMA test. The modal parameters changes are used to detect damage in the structure.

2 Modal Curvature Damage Detection Method

For a bending moment $M(x)$ is subjected to a beam cross-section with bending stiffness $EI(x)$ at location x , the modal curvature $\phi''(x)$ is given by:

$$\phi''(x) = \frac{d^2\phi(x)}{dx^2} = -\frac{M(x)}{EI(x)} \quad (1)$$

If one cross-section location has damage, the bending stiffness at this location will reduce leading to the increase of local modal curvature. Therefore, using modal curvature as a damage detection index has proven a sensitive and effective method for local

damage detection [19]. The central difference approximation method is commonly used to calculate the curvature:

$$\phi''_{ij} = \frac{\phi_{(i-1)j} - 2\phi_{ij} + \phi_{(i+1)j}}{\Delta x^2} \quad (2)$$

where: i is the mode shape number and j is the node number, Δx is the distance between two nodes, ϕ is the measure measured displacement mode shape. ϕ can be extracted from the acceleration response measurement of the structure. This method contains large errors because of ‘noisy’ mode shape [20].

The strain transducer can directly measure a structure’s modal curvature. A transducer measures differential axial displacements over a sufficiently long distance during ambient excitation.

The absolute differences in curvature of healthy and damaged structure for each mode is defined as:

$$DI_i = \sum_{j=1}^n \phi''_{ij0} - \phi''_{ijd} \quad (3)$$

where ϕ''_{ij0} , ϕ''_{ijd} are modal curvatures of the intact and damaged structure, respectively. The value of DI_i at the damage location will be higher than other locations and can be used as the damage index. Using this equation, the location of damage can be determined.

3 Experiments and Results

3.1 Strain Transducer

In this project, the ST350 strain transducer produced by Bridge Diagnostics, Inc (BDI) is used as the strain measurement sensor. The BDI ST350 strain transducer belongs to the Wheatstone bridge foil transducer class. ST350 only measures the strain in the axis with which it is aligned. The transducer is connected by bolts to the test structure. For steel members, the most efficient method of mounting an ST350 is using the tab/glue method. First, ST350 rests on positioned tabs by using ST350 Tab Jig. Then the centerline of the gaging area is located in both the longitudinal and transverse directions. The midpoint is located first by drawing two centerlines. The clean metal surface should be prepared. A thin line of adhesive will be applied to the bottom of the tab to mount the sensor in a marked location. It is suggested to mount the sensors quickly. Figure 1 shows the strain transducer installation at the laboratory.

3.2 Finite Element Model

To test the results of the experiment, the FE model of tested slab structures is modelled in Sap2000 (Fig. 2). The slab is 2.5 m long, 0.35 m in width and 0.02 m in depth. The boundary condition of the steel slab is simply-supported. The distance between two supports is 2 m. The steel modulus elasticity and density are $E_s = 200000$ MPa and $\rho = 7820$ kg/m³, respectively. Four first bending mode shapes were identified and shown in Fig. 3.

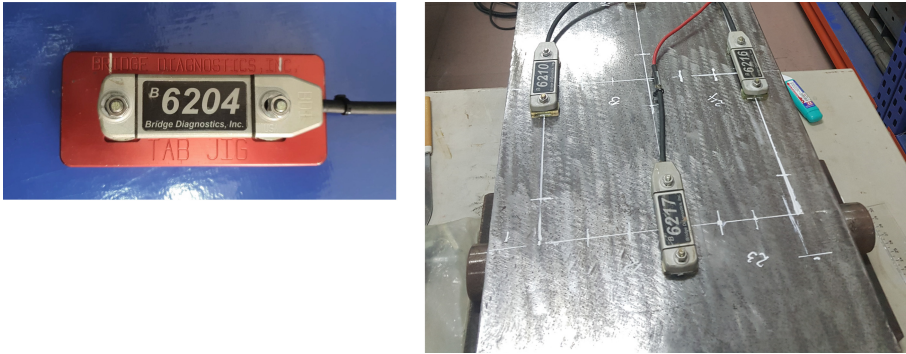


Fig. 1. Strain transducer installation



Fig. 2. FE model of the laboratory slab

3.3 Experimental Setup

A steel slab equipped with ST350 strain transducers is set up in the laboratory. The dimension of the slab is 2.5 m, 0.35 m, 0.02 m in length, width, and depth, respectively. The slab is constructed from steel. The modulus elasticity of steel is $E_s = 200000$ MPa and the density is $\rho = 7820$ kg/m³. Strain transducers were attached to the top of the slab. Damage is presented by adding mass to a specified location (Fig. 6). Because added mass is located at the top, transducers are only attached to the top to measure the modal strain at the top. Analyzing five strain transducers located in the middle, the mode shapes and frequencies can be found for both intact and damaged slabs. Figure 4 and Fig. 5 show the strain transducer installation in the laboratory. Two damage scenarios are labelled D1 and D2 in Fig. 4.

3.4 Results

a. Intact steel slab

A hammer was used to generate excitation loads. The sampling frequency was 200 Hz and the time recording was 300 s. SSI-cov algorithm was used to analyze the strain data. From the stabilization diagram shown in Fig. 7, four modes could be identified in the interval [0:100] Hz. Table 1 shows the frequencies of four identical modes from FE model and experiment. The differences between FE model and experiment are very low, less than 5% for all four modes. These results show that analyzing the strain transducer

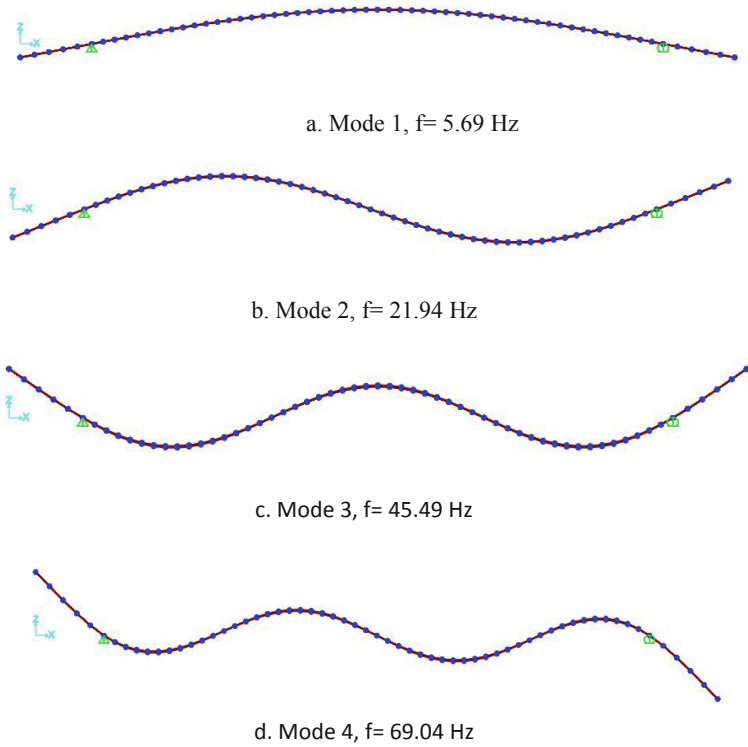


Fig. 3. First four bending mode shape of steel slab



Fig. 4. Strain transducer setup- top view

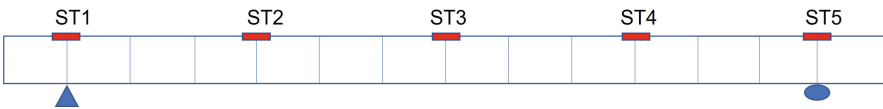


Fig. 5. Strain transducer setup- front view

data can get the correct natural frequencies of the structures. Using SSI-cov algorithms to analyze the strain response of five transducers, the unit normalized modal strain of the top of the slab is identified and shown in Fig. 8. Compared with the mode shape obtained from the FE model shown in Fig. 3, these two modal curvatures are similar. The strain transducer is actually a ‘point’ sensor. In this research, the experimental slab only instrument with five sensors. The modal strain is extracted from only five points

at the strain locations along the slab. Therefore, the experimental modal strain is not smooth.

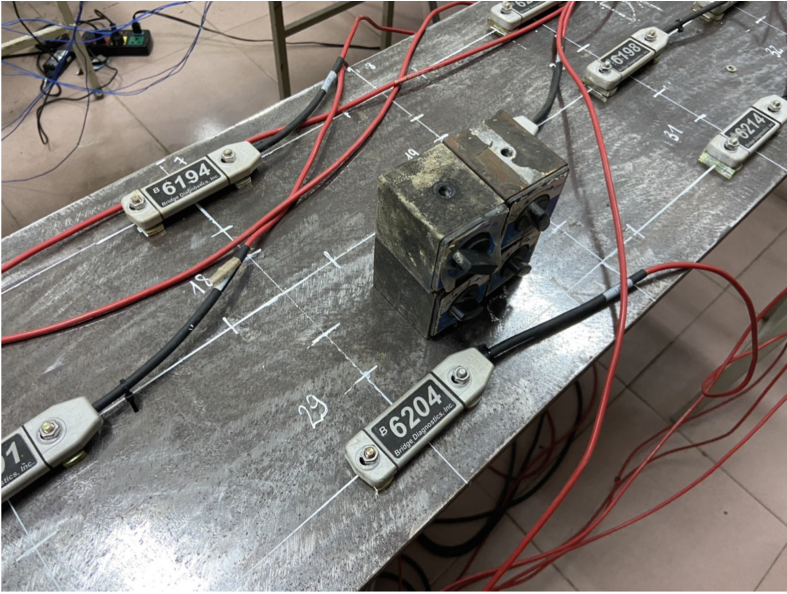


Fig. 6. Added mass on the top of the slab

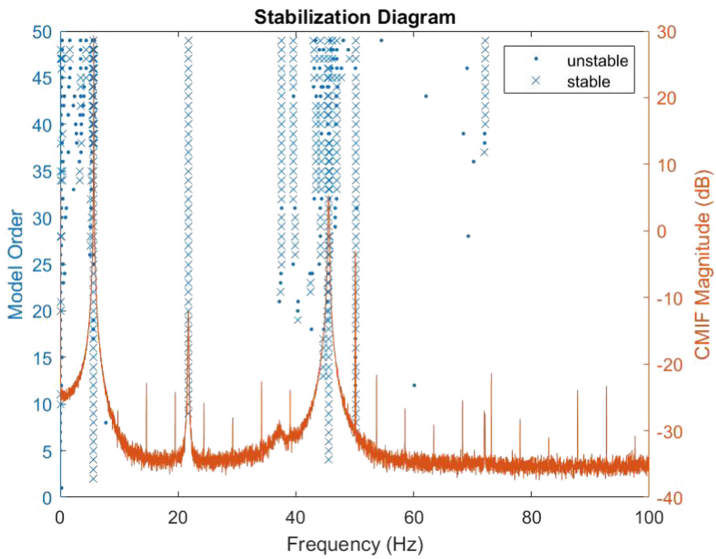


Fig. 7. Stabilization diagram

Table 1. Natural frequencies (Hz) of the steel slab

Mode number	1	2	3	4
Experiment	5.68	21.72	45.19	72.05
FEM	5.69	21.94	45.49	69.04
Differences (%)	0.18	1.01	0.66	-4.18

b. Damaged steel slab

Damage was introduced in the experimental slab by adding mass. Two damage scenarios were invented. There are D1 and D2 with 1.5 kg, and 3 kg added mass, respectively. The location of the D1 and D2 damaged scenarios can be seen in Fig. 4. Table 2 presents natural frequencies extracted from experimental data. For D1 and D2 damaged scenarios, the frequencies of all four modes are reduced when compared with the intact case. However, the differences between damaged and intact scenarios are small. It indicates that strain measurement data can notice the presence of damage in the structure.

The modal curvature damage detection method is proposed to find out the damage location in the structure. Equation (3) is used to calculate the differences between the modal curvature of intact and damaged steel slabs. The value of the damage index for two damage scenarios is shown in Fig. 9. ST3, which is in the middle of the slab, has the highest value for both scenarios. Then the second high value is in the location of ST2 for D1 and ST4 for D2. This means the damage location in D1 is predicted to be between ST2 and ST3 for D1 and between ST3 and ST4 for D2. Therefore, based on the damage indexes calculated from direct strain measurements, the location of the damage could be found.

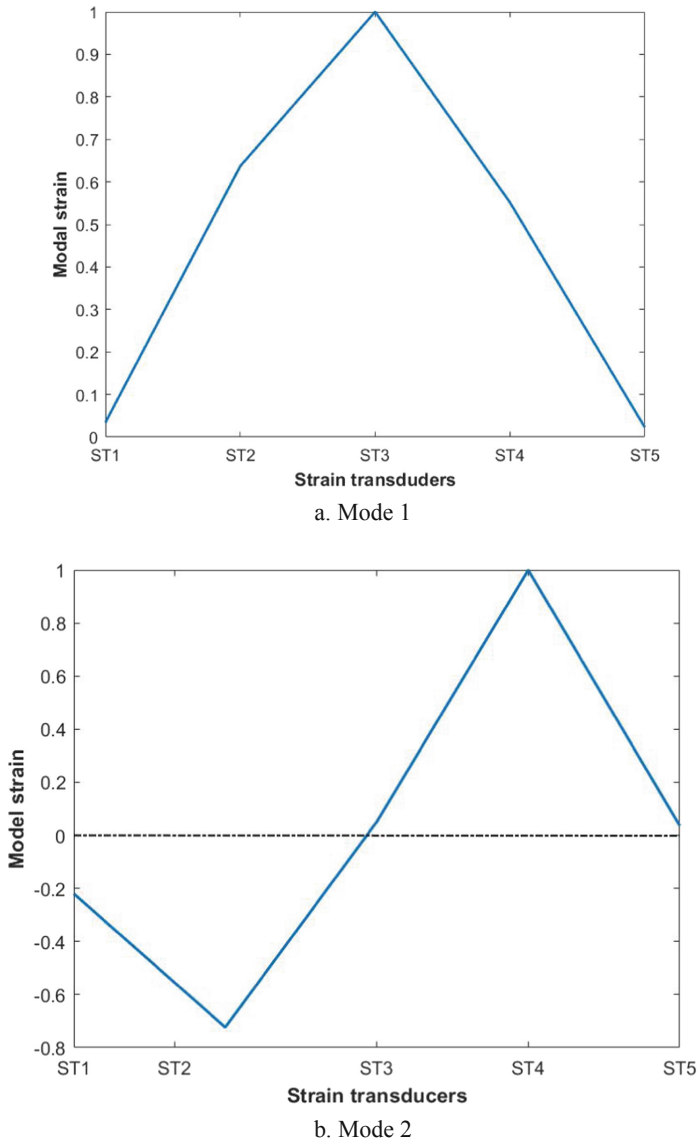
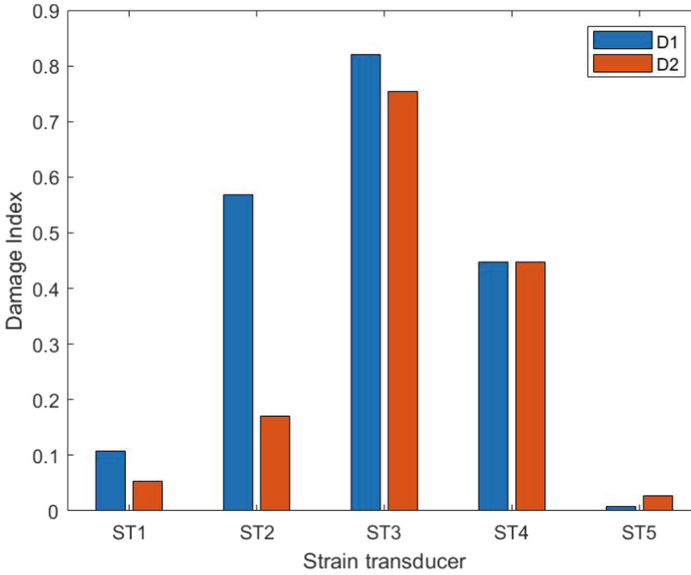


Fig. 8. The normalized modal strain of mode 1 and mode 2 from experiment data

Table 2. Natural frequencies (Hz) from experimental data

Mode number	1	2	3	4
Intact	5.68	21.72	45.19	72.05
D1	5.66	21.52	45.16	72.00
D2	5.54	21.35	43.59	70.64

**Fig. 9.** Damage index calculated from experimental data

4 Conclusion

The modal curvature damage detection method has been demonstrated in many works about its robustness and sensitivity to damage location. The modal strain can be obtained from the displacement mode shape. However, this process contains error in measurement and calculation. The distance between two accelerometers affects the results also. Direct measuring the modal curvature improves the accuracy and potential for application. Modal strains can be added to the objective function of the FE model updating problem then can enhance the damage recognition process.

In this paper, strain transducers are attached to the top of the steel slab and directly measure the strain. Natural frequencies and mode shapes of the steel slab can be found correctly by analyzing the strain response data. Two damage scenarios were set up in the laboratory to verify the method. Applying modal curvature damage detection for direct modal strain measurement, the assumed damage location could be found.

Acknowledgements. Duong Huong Nguyen was funded by the Postdoctoral Scholarship Programme of Vingroup Innovation Foundation (VINIF), code VINIF.2022.STS.54.

References

1. Van Overschee, P., De Moor, B.: Subspace Identification for Linear Systems: Theory—Implementation—Applications. Springer, New York (2012). <https://doi.org/10.1007/978-1-4613-0465-4>
2. Brincker, R., Zhang, L., Andersen, P.: Modal identification from ambient responses using frequency domain decomposition. In: Proceedings of the 18th International Modal Analysis Conference (IMAC), San Antonio, TX, USA (2000)
3. Kim, J.-T., Stubbs, N.: Model-uncertainty impact and damage-detection accuracy in plate girder. *J. Struct. Eng.* **121**(10), 1409–1417 (1995)
4. Shi, Z., Law, S., Zhang, L.: Damage localization by directly using incomplete mode shapes. *J. Eng. Mech.* **126**(6), 656–660 (2000)
5. Allemang, R.J.: A correlation coefficient for modal vector analysis. In: Proceedings of 1st International Modal Analysis Conference (1982)
6. Lieven, N., Ewins, D.: Spatial correlation of mode shapes, the coordinate modal assurance criterion (COMAC). In: Proceedings of the 6th International Modal Analysis Conference, Kissimmee Florida, USA (1988)
7. Tran-Ngoc, H., et al.: Model updating for Nam O bridge using particle swarm optimization algorithm and genetic algorithm. *Sensors* **18**(12), 4131 (2018)
8. Ho, V.L., et al.: Finite element model updating of a cable-stayed bridge using metaheuristic algorithms combined with Morris method for sensitivity analysis. *Smart Struct. Syst.* **26**(4), 451–468 (2020)
9. Ren, W.-X., De Roeck, G.: Structural damage identification using modal data. I: simulation verification. *J. Struct. Eng.* **128**(1), 87–95 (2002)
10. Ren, W.-X., De Roeck, G.: Structural damage identification using modal data. II: test verification. *J. Struct. Eng.* **128**(1), 96–104 (2002)
11. Yam, L., et al.: Theoretical and experimental study of modal strain analysis. *J. Sound Vib.* **191**(2), 251–260 (1996)
12. Schulz, W.L., Conte, J.P., Udd, E.: Long-gage fiber optic Bragg grating strain sensors to monitor civil structures. In: Smart Structures and Materials 2001: Smart Systems for Bridges, Structures, and Highways. SPIE (2001)
13. Casas, J.R., Cruz, P.J.: Fiber optic sensors for bridge monitoring. *J. Bridg. Eng.* **8**(6), 362–373 (2003)
14. Phares, B.M., et al.: Bridge load rating using physical testing. In: Proceedings of the 2003 Mid-Continent Transportation Research Symposium, Iowa State University (2003)
15. Unger, J.F., Teughels, A., De Roeck, G.: Damage detection of a prestressed concrete beam using modal strains. *J. Struct. Eng.* **131**(9), 1456–1463 (2005)
16. Reynders, E., et al.: Damage identification on the Tilff Bridge by vibration monitoring using optical fiber strain sensors. *J. Eng. Mech.* **133**(2), 185–193 (2007)
17. Nguyen, D.H., et al.: Damage detection in girder bridges using modal curvatures gapped smoothing method and convolutional neural network: application to Bo Nghi bridge. *Theoret. Appl. Fract. Mech.* **109**, 102728 (2020)

18. Nguyen, H.D., et al.: Damage detection in structures using modal curvatures gapped smoothing method and deep learning. *Struct. Eng. Mech.* **77**(1), 47–56 (2021)
19. Carden, E.P., Fanning, P.: Vibration based condition monitoring: a review. *Struct. Health Monit.* **3**(4), 355–377 (2004)
20. Philips Adewuyi, A., Wu, Z., Kammrujaman Serker, N.: Assessment of vibration-based damage identification methods using displacement and distributed strain measurements. *Struct. Health Monit.* **8**(6), p. 443–461 (2009)



Damage Detection in Structures by Wavelet Transforms: A Review

Yasin Faghieh Larijani¹, Yaser Rostamian¹ (✉), and Samir Khatir²

¹ Department of Mechanical Engineering, Sari Branch, Islamic Azad University, Sari, Iran
yasser.rostamiyan@iausari.ac.ir

² Soete Laboratory, Ghent University, Ghent, Belgium

Abstract. Wavelet transform is a mathematical technique with many applications in signal processing. Anomaly and faults in signals can be detected using wavelet transform due to their sensitivity to local discontinuity and singularity. One of the most important applications in signal processing through wavelet transform is damage detection in structures. In this paper, a comprehensive literature review is performed on notable works about damage detection in structures by wavelet method to introduce various applications of the wavelet transforms for detecting damages in different structures. Depending on the type of signal acquired from the structures, two types of wavelet analysis can be performed: one-dimensional wavelet transform and two-dimensional wavelet transform. This paper describes one-dimensional wavelet transform analyses to clarify how the wavelet analysis may be helpful for damage detection in structures.

Keywords: Damage detection · Wavelet transforms · Signal processing · Anomaly detection · Damaged structures

1 Introduction

Analysis of damaged structure, from nano size to macro size, is an interesting topic for researchers [1–4]. Generally, damaged structures can be analyzed using two approaches: forward analysis and inverse analysis. In forward analysis, the damage is modeled, and modal characteristics of the structure are determined. In inverse analysis, the damage is determined using the modal characteristics of the structure [5, 6]. For many decades, damage detection techniques have been investigated by many researchers [7–11]. The researchers have been used different strategies for damage detection of the structures.

Some strategies are optimization-based methods and an objective function is set to be minimized or maximized in order to localize damage [12–15]. Dinh-Cong et al. [16] employed the Jaya optimization algorithm to localize damages in plates. Gomes et al. [17] used the SFOA algorithm to detect damages in laminate composites. Mishra et al. [18] proposed the ALO algorithm for identifying damages via vibration data. Maity et al. [19] suggested the GA algorithm for detecting damages of structures via shifts in natural frequencies. They demonstrated that the GA algorithm could localize damage with high precision. Also, Alexandrino et al. [20] proposed a multiobjective optimization plan to

identify damages to the plates. This optimization method revealed that using the multi-objective method, artificial neural networks (ANNs) and fuzzy inference systems can act as a proper means to identify damages. In [21], the effectiveness of the PSO and ACO algorithms to localize damages in 3D trusses was considered. The objective function suggested was established using mode shapes and corresponding natural frequencies. Gerist et al. [22] employed the IC optimization Algorithm to localize damage in engineering structures based on a novel objective function. In [23], the DE optimization algorithm was used to determine the damage's location and severity in structures.

Also, many techniques have been created in the inverse analysis in the research. One of the most contemporary inverse methods is the artificial neural network (ANN) for localizing damage's location and severity [24]. ANN is a superior means for localizing damages in the structures. Investigators usually utilized modal characteristics such as natural frequency and mode shape as the input of ANNs to identify the level of damage in various structures [25–28].

Another method of damage detection in structures is signal processing-based methods. In these methods, signals are decomposed to detect the damage's location and level using the existed information in the signal acquired for the damaged structure [29]. Wavelet transform is a signal processing-based method. In this method, a signal is transformed into sub-signals to show the damaged signal's discontinuity [30]. The singularities and discontinuities detected by wavelet transform in signals indicate damages in a specific location or time [31]. Yang et al. utilized two-dimensional wavelets for detecting damage of laminate composites [32]. Cao et al. proposed a new approach named integrated wavelet transforms to detect damages on composite beams. This method combined the continuous wavelet transforms (CWTs) and stationary wavelet transforms (SWTs) to create a powerful wavelet-based damage detection model [33]. Sohn et al. presented a wavelet-based approach for detecting delaminations [34]. Mitra et al. introduced an element-based model combined with wavelet transform to detect damages on composite beams [35]. The reviewed investigations on wavelet-based damage detection methods show that they are the simple and effective methods for damage detection in various structures since they only need signals. In this paper, Damage detection in engineering structures by wavelet transforms for various structures are reviewed.

2 One Dimensional Continuous Wavelet Transforms (1D-CWT)

The signals obtained for cables, bars, beams, and all beam-like structures are one-dimensional; therefore, a one-dimensional wavelet transform is applied to decompose these signals. Wavelet transform can be continuous or discrete. Assume the one-dimensional signal $A(t)$ having a subtle discontinuity or damage. In order to identify this discontinuity, it is required to transform its values into another coordinate system using a wavelet function called $\psi(t)$. The following expression indicates a family of wavelets [23]:

For a signal $f(x)$, , family of wavelets in real space at the Hilbert space $(\psi(x) \in L^2(\mathbb{R}))$ is defined as follows:

$$\psi(x)_{u,s} = \frac{1}{\sqrt{s}} \psi\left(\frac{x-u}{s}\right) \quad (1)$$

where x indicates the space variable related to the original signal $f(x)$, u is the shifting factor, and s denotes the scaling factor. The continuous wavelet coefficients $C(u, s)$ can be calculated as follows [36]:

$$C(u, s) = \langle f, \psi(x)_{u,s} \rangle = \frac{1}{\sqrt{s}} \int_{-\infty}^{+\infty} f(x) \psi\left(\frac{x-u}{s}\right) dx \tag{2}$$

$$C(u, s) = \frac{s^n}{\sqrt{s}} \int_{-\infty}^{+\infty} f(x) \frac{d^n}{dx^n} \theta\left(\frac{-(u-x)}{s}\right) dx = \frac{s^n}{\sqrt{s}} \frac{d^n}{du^n} f * \theta\left(\frac{-u}{s}\right) = s^n \frac{d^n}{du^n} (f * \theta_s)(u) \tag{3}$$

Figure 1 shows an example of a one-dimensional signal obtained from a beam structure and its continuous wavelet transform.

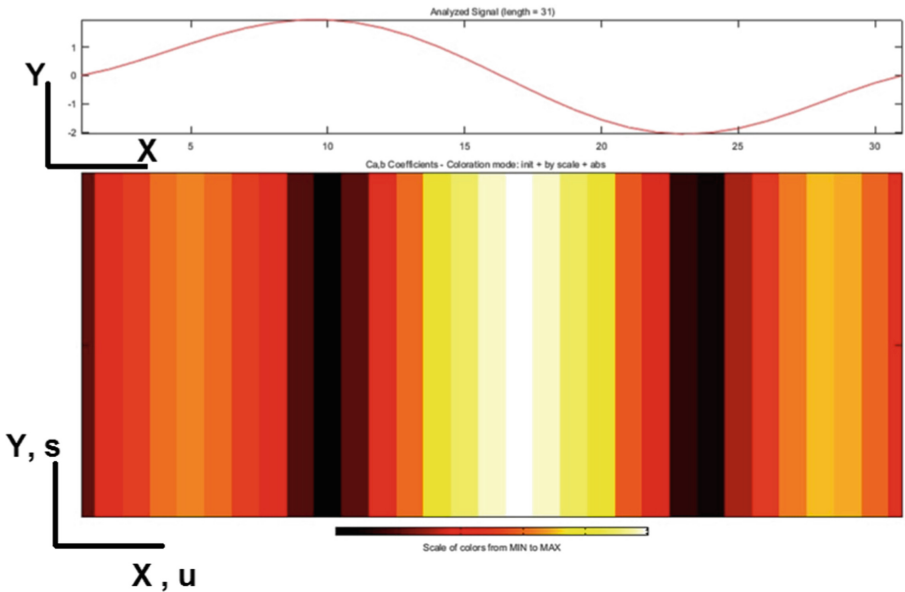


Fig. 1. An example of a one-dimensional signal obtained from a beam structure and its continuous wavelet transform.

In the continuous wavelet transform results, the brightest position horizontal axis of the wavelet coefficients diagram shows the location of the damage. Therefore, the damage is located at $X = 17$.

Janeliukstis et al. [37] conducted an experimental study for damage localization in beam-like structures based on spatial mode shape signals. Montanari et al. [38] used continuous wavelet transform for detecting cracks in beam structures. Rucka et al. [39] investigated the application of one-dimensional wavelet transforms for damage detection of beams.

Figure 1 shows the continuous wavelet transform created from the signal obtained from the finite element method; however, the number of data points in experimental

data is high. Figures 2 and 3 indicate the continuous wavelet transform created from the experimental velocity signals of an intact structure and a damaged structure, respectively. Figures 4 and 5 show the continuous wavelet transform created from the experimental displacement signals of an intact structure and a damaged structure, respectively.

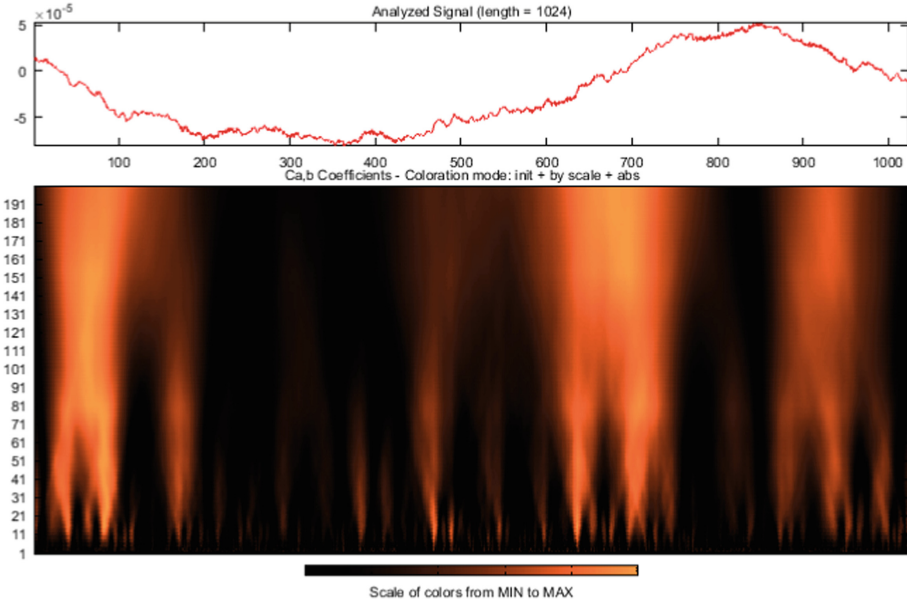


Fig. 2. Experimental velocity signal for an intact structure and its continuous wavelet transform

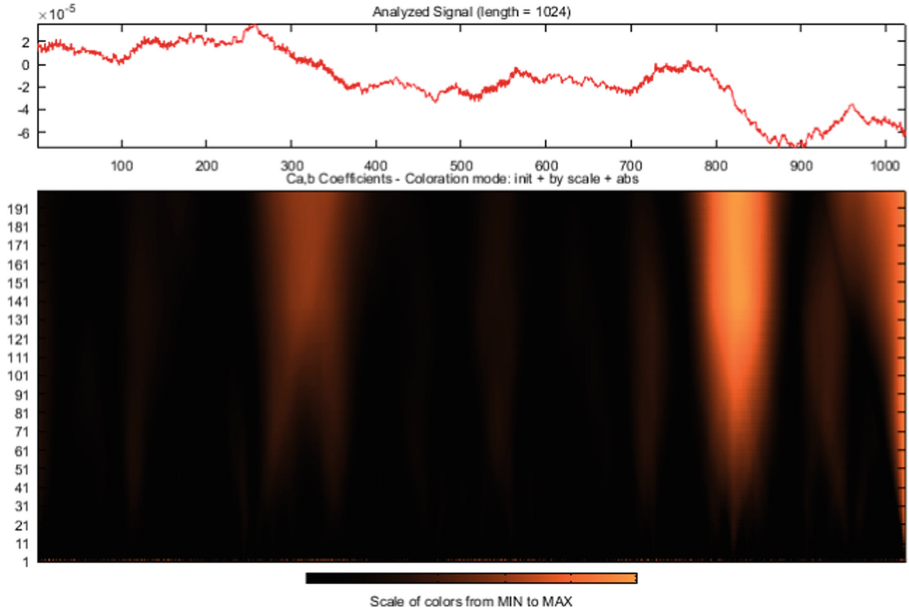


Fig. 3. Experimental velocity signal for a damaged structure and its continuous wavelet transform

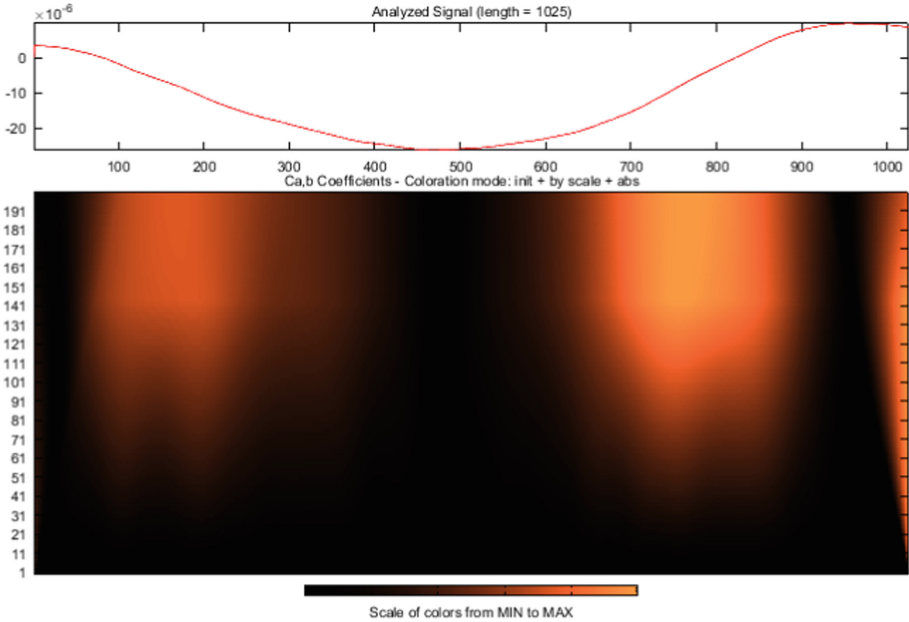


Fig. 4. Experimental displacement signal for an intact structure and its continuous wavelet transform

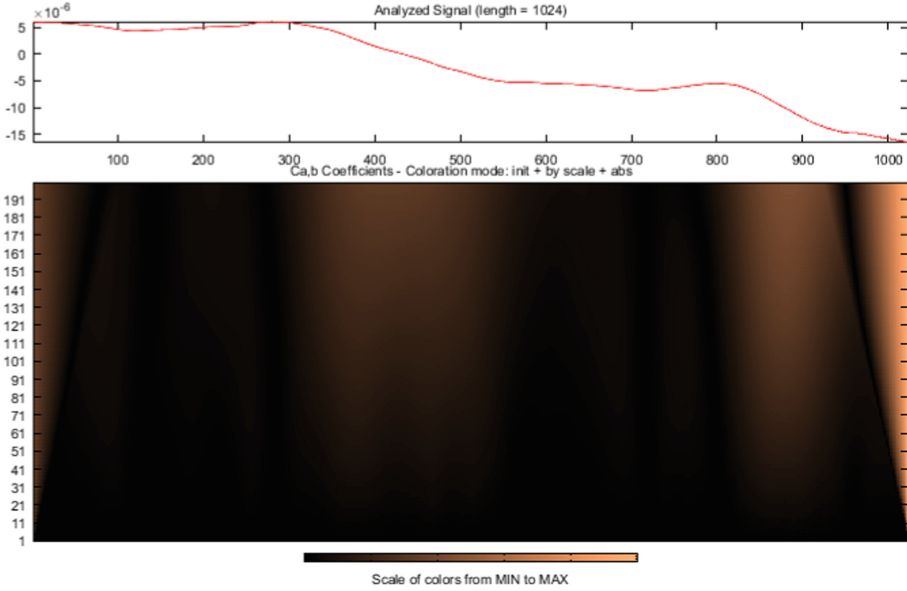


Fig. 5. Experimental displacement signal for a damaged structure and its continuous wavelet transform

3 One Dimensional Discrete Wavelet Transforms (1D-DWT)

Another type of wavelet transform is one-dimensional discrete wavelet transform. The 1D-DWT for a signal $f(x)$ is defined as follows [40]:

$$f(x) = A_j(x) + \sum_{j < J} D_j(x) \tag{4}$$

where A_j are approximation signals at level j , D_j show detail signals at level j .

The approximation signals at level j are calculated as follows:

$$A_j(x) = \sum_{k=-\infty}^{+\infty} cA_{j,k} \phi_{j,k}(x) \tag{5}$$

where $cA_{j,k}$ indicate approximation coefficients at level j . $\phi_{j,k}(x)$ are scaling functions at level j .

The detail signals at level j are expressed as follows:

$$D_j(x) = \sum_{k \in Z} cD_{j,k} \psi_{j,k}(x) \tag{6}$$

where $cD_{j,k}$ denote detail coefficients at level j . $\psi_{j,k}(x)$ indicate wavelet functions.

Figure 2 shows an example of a one-dimensional signal obtained from a delaminated composite beam structure and its discrete wavelet transform. Note that damage causes

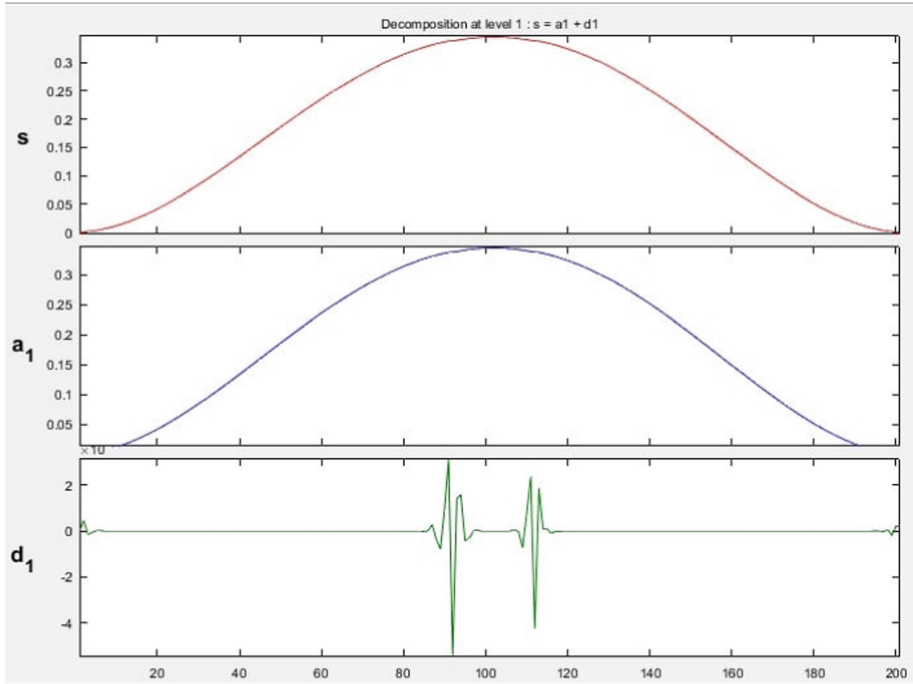


Fig. 6. An example of a one-dimensional signal obtained from a beam structure and its discrete wavelet transform.

a local jump in the signal; therefore, damage can be detected in the detail signal. As shown in Fig. 2, two jumps are observed in the detail signal. These two jumps are the boundaries of the damage delamination in a laminated composite beam.

Along with this, there are many types of research; for instance, Yang et al. [41] identified a crack in aluminum beams using discrete wavelet transform. The experimental findings showed that the suggested discrete wavelet transform could effectively determine the damage locations and be applied to more complicated structures.

Figure 6 shows the discrete wavelet transform created from the signal obtained from the finite element method; however, as mentioned, the number of data points in experimental data is high. Figures 7 and 8 indicate the discrete wavelet transform created from the experimental velocity signals of an intact structure and a damaged structure, respectively. Figures 9 and 10 show the discrete wavelet transform created from the experimental displacement signals of an intact structure and a damaged structure, respectively.

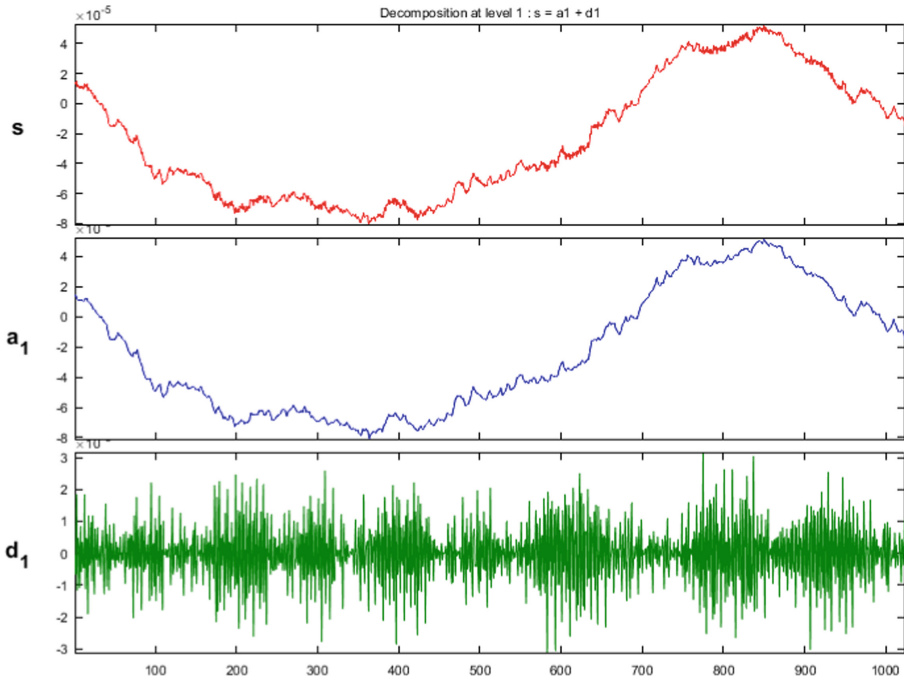


Fig. 7. Experimental velocity signal for an intact structure and its discrete wavelet transform

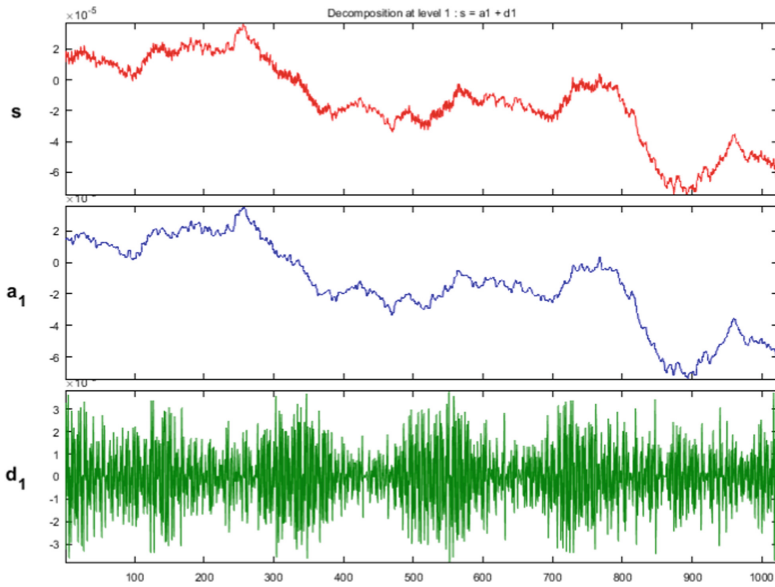


Fig. 8. Experimental velocity signal for a damaged structure and its discrete wavelet transform

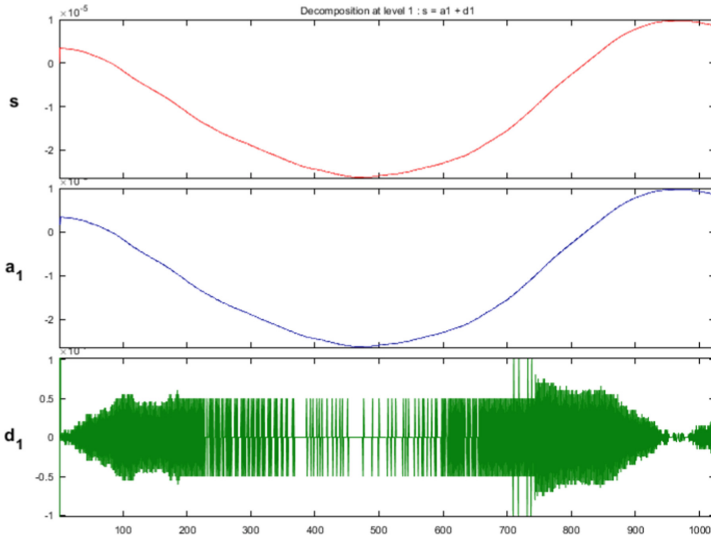


Fig. 9. Experimental displacement signal for an intact structure and its discrete wavelet transform

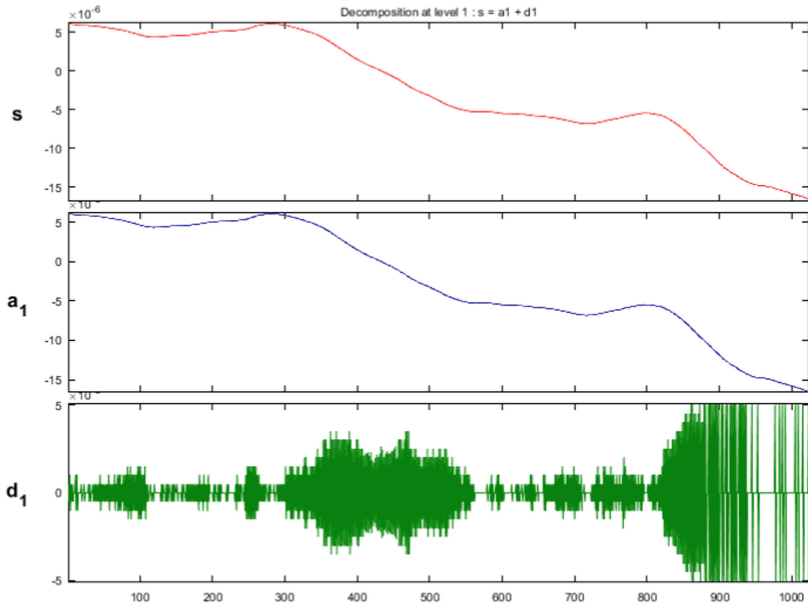


Fig. 10. Experimental displacement signal for a damaged structure and its discrete wavelet transform

4 Discussion

Damage detection using one-dimensional wavelet transform is a powerful and proper method based on the structure's signal. There is no need for having other modal characteristics such as natural frequencies. Signals from structures such as cables, bars, and beams are one-dimensional signals. Thus, these structures can be detected by the one-dimensional wavelet transforms. The one-dimensional continuous wavelet transforms (1D-CWT) and one-dimensional discrete wavelet transforms are two main types of one-dimensional wavelet transforms. These two different methods decompose the original signals using two different ways. The 1D-CWT shifts and scales the original signal at various continuous levels, and the 1D-DWT decomposes the original signals into approximation and detail sub-signals at various discrete levels. Both methods are powerful tools for detecting damages and faults in one-dimensional signals.

5 Conclusions

In this study, a review of damage detection methods in structures is performed. The emphasis of the research is on the introduction of one-dimensional damage detection methods using wavelet transform. Two common types of one-dimensional wavelet transform are introduced. Their formulation and how to evaluate the results of these two continuous and discrete types of damage detection based on one-dimensional wavelet transform are discussed. It has been proven that damage detection by the one-dimensional wavelet transform method can be a powerful tool for locating damage in cable structures, rods, isotropic beams, and laminated composite beams.

Acknowledgement. The first three authors acknowledge the funding support of Babol Noshirvani University of Technology through Grant program No. BNUT/965919012/99.

References

1. Mofidian, R., Barati, A., Jahanshahi, M., Shahavi, M.H.: Fabrication of novel Agarose–Nickel Bilayer composite for purification of protein nanoparticles in expanded bed adsorption column. *Chem. Eng. Res. Des.* **159**, 291–299 (2020)
2. Shahavi, M.H., Selakjani, P.P., Abatari, M.N., Antov, P., Savov, V.: Novel biodegradable poly (lactic acid)/wood leachate composites: investigation of antibacterial, mechanical, morphological, and thermal properties. *Polymers* **14**(6), 1227 (2022)
3. JafariTalookolaei, R.A., Abedi, M., Kargarnovin, M.H., Ahmadian, M.T.: Dynamic analysis of generally laminated composite beam with a delamination based on a higher-order shear deformable theory. *J. Compos. Mater.* **49**(2), 141–162 (2015)
4. Khalili, M., Razmjou, A., Shafiei, R., Shahavi, M.H., Li, M.C., Orooji, Y.: High durability of food due to the flow cytometry proved antibacterial and antifouling properties of TiO₂ decorated nanocomposite films. *Food Chem. Toxicol.* **168**, 113291 (2022)
5. Jafari-Talookolaei, R.A., Abedi, M.: Analytical solution for the free vibration analysis of delaminated Timoshenko beams. *Sci. World J.* (2014)

6. Saadatmorad, M., Siavashi, M., JafariTalookolaei, R.-A., Pashaei, M.H., Khatir, S., Thanh, C.-L.: Genetic and particle swarm optimization algorithms for damage detection of beam-like structures using residual force method. In: Bui, T.Q., Cuong, Le Thanh, Khatir, Samir (eds.) *Structural Health Monitoring and Engineering Structures*. LNCE, vol. 148, pp. 143–157. Springer, Singapore (2021). https://doi.org/10.1007/978-981-16-0945-9_12
7. Wahab, M.A., De Roeck, G.: Damage detection in bridges using modal curvatures: application to a real damage scenario. *J. Sound Vib.* **226**(2), 217–235 (1999)
8. Saadatmorad, M., JafariTalookolaei, R.A., Pashaei, M.H., Khatir, S.: Damage detection on rectangular laminated composite plates using wavelet based convolutional neural network technique. *Compos. Struct.* **278**, 114656 (2021)
9. Khatir, S., Tiachacht, S., Le Thanh, C., Ghandourah, E., Mirjalili, S., Wahab, M.A.: An improved artificial neural network using arithmetic optimization algorithm for damage assessment in FGM composite plates. *Compos. Struct.* **273**, 114287 (2021)
10. Saadatmorad, M., Talookolaei, R.A.J., Pashaei, M.H., Khatir, S., Wahab, M.A.: Pearson correlation and discrete wavelet transform for crack identification in steel beams. *Mathematics* **10**(15), 2689 (2022)
11. Tiachacht, S., Khatir, S., Le Thanh, C., Rao, R.V., Mirjalili, S., Wahab, M.A.: Inverse problem for dynamic structural health monitoring based on slime mould algorithm. *Eng. Comput.* 1–24 (2021)
12. Behtani, A., Bouazzouni, A., Khatir, S., Tiachacht, S., Zhou, Y.L., Abdel Wahab, M.: Damage localization and quantification of composite beam structures using residual force and optimization. *J. Vibroeng.* **19**(7), 4977–4988 (2017)
13. Khatir, S., Wahab, M.A., Benaissa, B., Köppen, M.: Crack identification using eXtended IsoGeometric analysis and particle swarm optimization. In: Abdel Wahab, M. (ed.) *FFW 2018*. LNME, pp. 210–222. Springer, Singapore (2019). https://doi.org/10.1007/978-981-13-0411-8_21
14. Kang, F., Li, J.J., Xu, Q.: Damage detection based on improved particle swarm optimization using vibration data. *Appl. Soft Comput.* **12**(8), 2329–2335 (2012)
15. Wei, Z., Liu, J., Lu, Z.: Structural damage detection using improved particle swarm optimization. *Inverse Probl. Sci. Eng.* **26**(6), 792–810 (2018)
16. DinhCong, D., VoDuy, T., HoHuu, V., Nguyen-Thoi, T.: Damage assessment in plate-like structures using a two-stage method based on modal strain energy change and Jaya algorithm. *Inverse Probl. Sci. Eng.* **27**(2), 166–189 (2019)
17. Gomes, G.F., da Cunha, S.S., Ancelotti, A.C.: A sunflower optimization (SFO) algorithm applied to damage identification on laminated composite plates. *Eng. Comput.* **35**(2), 619–626 (2018). <https://doi.org/10.1007/s00366-018-0620-8>
18. Mishra, M., Barman, S.K., Maity, D., Maiti, D.K.: Ant lion optimisation algorithm for structural damage detection using vibration data. *J. Civ. Struct. Heal. Monit.* **9**(1), 117–136 (2019)
19. Maity, D., Tripathy, R.R.: Damage assessment of structures from changes in natural frequencies using genetic algorithm. *Struct. Eng. Mech.* **19**(1), 21–42 (2005)
20. Alexandrino, P.D.S.L., Gomes, G.F., Cunha Jr., S.S.: A robust optimization for damage detection using multiobjective genetic algorithm, neural network and fuzzy decision making. *Inverse Probl. Sci. Eng.* 1–26 (2019)
21. Barman, S.K., Maiti, D.K., Maity, D.: Damage detection of truss employing swarm-based optimization techniques: a comparison. In: Venkata Rao, R., Taler, J. (eds.) *AEOTIT 2018*. AISC, vol. 949, pp. 21–37. Springer, Singapore (2020). https://doi.org/10.1007/978-981-13-8196-6_3
22. Gerist, S., Maheri, M.R.: Structural damage detection using imperialist competitive algorithm and damage function. *Appl. Soft Comput.* **77**, 1–23 (2019)

23. Kim, N.I., Kim, S., Lee, J.: Vibration-based damage detection of planar and space trusses using differential evolution algorithm. *Appl. Acoust.* **148**, 308–321 (2019)
24. Bakhary, N., Hao, H., Deeks, A.J.: Damage detection using artificial neural network with consideration of uncertainties. *Eng. Struct.* **29**(11), 2806–2815 (2007)
25. Mehrjoo, M., Khaji, N., Moharrami, H., Bahreininejad, A.: Damage detection of truss bridge joints using artificial neural networks. *Expert Syst. Appl.* **35**(3), 1122–1131 (2008)
26. Rosales, M.B., Filipich, C.P., Buezas, F.S.: Crack detection in beam-like structures. *Eng. Struct.* **31**(10), 2257–2264 (2009)
27. Saadatmorad, M., JafariTalookolaei, R.-A., Pashaei, M.-H., Khatir, S., Abdel Wahab, M.: Adaptive network-based fuzzy inference for damage detection in rectangular laminated composite plates using vibrational data. In: Abdel Wahab, M. (ed.) *SDMA 2021. LNCE*, vol. 204, pp. 179–196. Springer, Singapore (2022). https://doi.org/10.1007/978-981-16-7216-3_14
28. Saadatmorad, M., JafariTalookolaei, R.-A., Pashaei, M.-H., Khatir, S., Abdel Wahab, M.: Application of multilayer perceptron neural network for damage detection in rectangular laminated composite plates based on vibrational analysis. In: Abdel Wahab, M. (ed.) *SDMA 2021. LNCE*, vol. 204, pp. 163–178. Springer, Singapore (2022). https://doi.org/10.1007/978-981-16-7216-3_13
29. Staszewski, W.J.: Intelligent signal processing for damage detection in composite materials. *Compos. Sci. Technol.* **62**(7–8), 941–950 (2002)
30. Kim, H., Melhem, H.: Damage detection of structures by wavelet analysis. *Eng. Struct.* **26**(3), 347–362 (2004)
31. Hou, Z., Noori, M., Amand, R.S.: Wavelet-based approach for structural damage detection. *J. Eng. Mech.* **126**(7), 677–683 (2000)
32. Yang, C., Oyadji, S.O.: Delamination detection in composite laminate plates using 2D wavelet analysis of modal frequency surface. *Comput. Struct.* **179**, 109–126 (2017)
33. Cao, M., Qiao, P.: Damage detection of laminated composite beams with progressive wavelet transforms. In: *Nondestructive Characterization for Composite Materials, Aerospace Engineering, Civil Infrastructure, and Homeland Security 2008*, vol. 6934, p. 693402. International Society for Optics and Photonics, March 2008
34. Sohn, H., Park, G., Wait, J.R., Limback, N.P., Farrar, C.R.: Wavelet-based active sensing for delamination detection in composite structures. *Smart Mater. Struct.* **13**(1), 153 (2003)
35. Mitra, M., Gopalakrishnan, S.: Wavelet based spectral finite element modelling and detection of de-lamination in composite beams. *Proc. Roy. Soc. A Math. Phys. Eng. Sci.* **462**(2070), 1721–1740 (2006)
36. Rucka, M., Wilde, K.: Application of continuous wavelet transform in vibration based damage detection method for beams and plates. *J. Sound Vib.* **297**(3–5), 536–550 (2006)
37. Janeliukstis, R., Rucevskis, S., Wesolowski, M., Chate, A.: Experimental structural damage localization in beam structure using spatial continuous wavelet transform and mode shape curvature methods. *Measurement* **102**, 253–270 (2017)
38. Montanari, L., Spagnoli, A., Basu, B., Broderick, B.: On the effect of spatial sampling in damage detection of cracked beams by continuous wavelet transform. *J. Sound Vib.* **345**, 233–249 (2015)
39. Rucka, M.: Damage detection in beams using wavelet transform on higher vibration modes. *J. Theor. Appl. Mech.* **49**(2), 399–417 (2011)
40. Puchala, D., Stokfiszewski, K.: Highly effective GPU realization of discrete wavelet transform for big-data problems. In: Paszynski, M., Kranzlmüller, D., Krzhizhanovskaya, V.V., Dongarra, J.J., Sliot, P.M.A. (eds.) *ICCS 2021. LNCS*, vol. 12742, pp. 213–227. Springer, Cham (2021). https://doi.org/10.1007/978-3-030-77961-0_19
41. Yang, J.M., Hwang, C.N., Yang, B.L.: Crack identification in beams and plates by discrete wavelet transform method. *Chuan Bo Li Xue/J. Ship Mech.* **12**(3), 464–472 (2008)

42. Guminiak, M., Knitter-Piątkowska, A.: Selected problems of damage detection in internally supported plates using one-dimensional Discrete Wavelet Transform. *J. Theor. Appl. Mech.* **56** (2018)



Experiences on Anchorage Systems for FRP Rods

Roberto Capozucca^(✉), Abdelwahhab Khatir, and Erica Magagnini

Structural Section DICEA, Polytechnic University of Marche, Ancona, Italy
r.capozucca@staff.univpm.it

Abstract. In recent years, investigation on FRP rods for prestressing tendons both for high strength and high resistance to corrosion, lightweight, nonconducting, and nonmagnetic properties is increasing. Anchorage systems are often not completely reliable because the characteristic of orthotropic material of FRP with high strength for loads parallel to the axis while a low capacity in normal direction to axis doesn't allow to use anchorage systems typically used for steel. This paper presents experimental experiences on anchorage systems for FRP rods. Firstly, the behaviour of anchorages with metallic tubular and filled resin around the FRP rod, adopted in tensile tests of Carbon and Glass FRP rods is investigated. Then, anchorage for prestressing FRP rods with experimental tests on clamp and split wedge anchorage types is analysed. Results of experimental campaign are shown and discussed with the aim to provide recommendations for the future research.

Keywords: Anchorage system · Carbon-Glass FRP Rods · Tensile test · Prestressing

1 Introduction

The use of Fibre Reinforced Polymers (FRPs) is increasing in civil engineering especially in the rehabilitation of damaged RC beams or to retrofit RC elements [1–3]. FRPs are available in lamina, strips, tendons, reinforcing bars and meshes. One between techniques usually adopted in the RC concrete elements like beams and columns consist in the use of near surface mounted (NSM) FRP rods/strips inserted into grooves in the cover of sections [4–6]. NSM technique is usually based on FRP rods with or without pretension as a strengthening of damaged reinforced concrete (RC) beams and slab of bridges often subjected to process of corrosion. Corrosion of steel reinforcing and prestressing steel tendons cause reduction of ductility of structural elements with dangerous effect on the safety. In recent years as an emerged alternative to steel is the use of FRP composites also for prestressing tendons [7] due to high strength and high resistance to corrosion, lightweight, nonconducting, and nonmagnetic properties. FRP anchoring systems is one of main topic that was studied and investigated [8] although some aspect should be deeply developed. First research on prestressing FRP rods started in Germany at the end of seventy years of last century; next in Japan and USA extensive studies and experimental research have been developed [9, 10] on Glass-FRP tendons and anchorages. The characteristic of orthotropic material for FRP with high strength for loads

parallel to the axis while a low capacity in normal direction to axis doesn't allow to use anchorage systems typically used for steel because they would crush transversally the FRP rods. Recently, innovative technique based on soft computing have been adopted to civil engineering problems [11, 12]. New frontiers of research about anchor systems for FRP are focused on the implementation of artificial neural network (ANN) models for the anchorage reliability assessment [12].

The anchorage system and orthotropic material are two aspects that must be taken in account also in the investigation of FRP rods under tensile tests to obtain correct results about ultimate strength, f_t , Young's modulus, E , and develop of strains, ε .

The first part of this paper deals about anchorages with metallic tubular and filled resin around the FRP rod, adopted in tensile tests of Carbon/Glass-FRP rods. The second part of this paper is focused on the anchorage for prestressing CFRP rods with experimental tests on split wedge and clamp anchorages [8].

2 Anchorage Systems for FRP Rod Under Tensile Load and Tests

IN This Paper, FRP Rods Made with an Epoxy Matrix Reinforced with Unidirectional Fibers Are Analyzed. With the Aim to Evaluate the Ultimate Tensile Strength and the Elastic Modulus of FRP Rods, the Test Methods Indicated by the American ACI [13] and Italian CNR [14] Codes of Practice Were Taken as Reference.

The anchorage system is of fundamental importance and can seriously affect the test's performance even if many factors can contribute to changing the results of the tests. For example, the gripping system of the test machine can influence the experimental campaign, since if the lateral pressure applied is not high enough, the specimen may slip during the tore phase, while an excessive pressure can cause premature rupture of the sample.

The anchoring system adopted for this experimental campaign is shown in Fig. 1. The design of the anchorage was done with reference to the suggestions reported in [13, 14]. The rods have been inserted into steel tubes filled with epoxy resin. The minimum anchor length, l_a , is set as 15 times the diameter of the rod, d_b . The overall length of the steel tube, however, has been extended by 1 cm, to allow the insertion of rubber caps to prevent the resin from leaking. The total rod's length, l_p , was determined by referring to the greater of the two relations defined in the considered standards [13, 14]:

$$l_p \geq 100 + 2 \cdot l_a; \quad l_p \geq 40 \cdot d_b + 2 \cdot l_a. \quad (1)$$

2.1 Tensile Test for G/CFRP Rods

CFRP and GFRP rods, with a nominal diameter, respectively, of 8 mm and 9 mm, with high resistance and high glass transition temperature, were subjected to tensile tests. The rods had a special superficial treatment to improve adhesion, obtained by surface sandblasting of spheroidal quartz and helical winding in carbon/glass threads (Fig. 2). Tables 1 and 2 show the mechanical and geometric characteristics, provided by the manufacturer.



Fig. 1. Manufacturing of GFRP and CFRP rods samples.

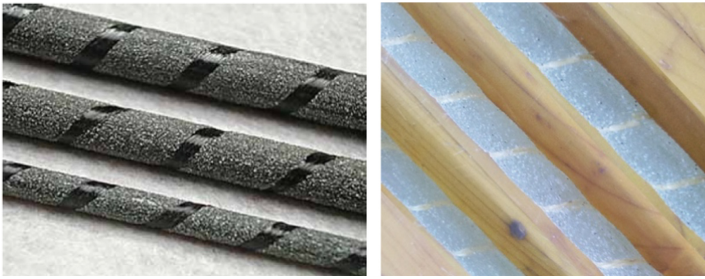


Fig. 2. CFRP and GFRP rods adopted for experimental tensile tests.

The two-component epoxy resin with high adhesion was used for the application of the tubular metallic socket. Table 3 shows the dimensional characteristics of the samples, depending on the nominal diameter of the tested rod.

The specimens were subjected to an increased tensile load under displacement control. A strain gauge was placed on the middle section of rod to record the evolution of axial strain during tests. Glass fiber specimens showed an explosive failure, with the detachment of the fibers in the classic “brush” way but without the complete disintegration (Fig. 3). According to the ASTM notation, this failure can be classified in both cases as XGM (Explosive, Gage, Middle). For carbon fiber rods, failure was reached only for a single specimen and it was localized near the anchor (Fig. 3). In this case, failure can be classified as a LAB type (Linear A, at Grip, Bottom) e XMV (Explosive Multiple Various). Main results of uniaxial tensile tests are shown in Fig. 4. Results of the tensile tests confirm the reliability of the anchoring system adopted, with resistance values of tested specimens higher than those declared by the manufacturer (Table 4).

Table 1. Mechanical characteristics of tested CFRP rods by the manufacturer*.

CFRP rods	
Nominal section [mm ²]	50
Nominal diameter [mm]	8
Characteristic tensile strength, f_{tk} , ASTM D 3039 [MPa]	1800
Average tensile Young's modulus, ASTM D 3039 [GPa]	130
Average ultimate tensile strain, ASTM D 3039 [%]	1.8
Glass transition temperature, ASTM 1356 [°C]	> 250

* BASF Construction Chemicals Italia S.p.A.

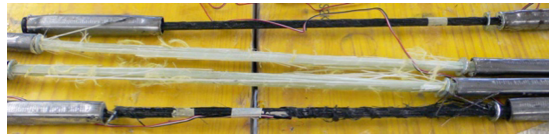
Table 2. Mechanical characteristics of tested CFRP rods by the manufacturer*.

GFRP rods	
Nominal section [mm ²]	71.26
Nominal diameter [mm]	9.53
Characteristic tensile strength, f_{tk} , ASTM D 3039 [MPa]	760
Average tensile Young's modulus, ASTM D 3039 [GPa]	40.80

* Mapei S.p.A.

Table 3. Geometrical characteristics of tested specimens.

Material	Specimen	Nominal diameter	Nominal area	Outside diameter of steel tube, d	Bond length l_a	Length of steel tube l_{tube}	Free length l	Length of specimen l_p
		[mm]	[mm ²]	[mm]	[mm]	[mm]	[mm]	[mm]
CFRP	CB1, CB2	8.0	50.27	25	150	160	380	690
GFRP	GB1, GB2	9.53	71.26	25	120	130	320	570

**Fig. 3.** Failure of tested specimens.

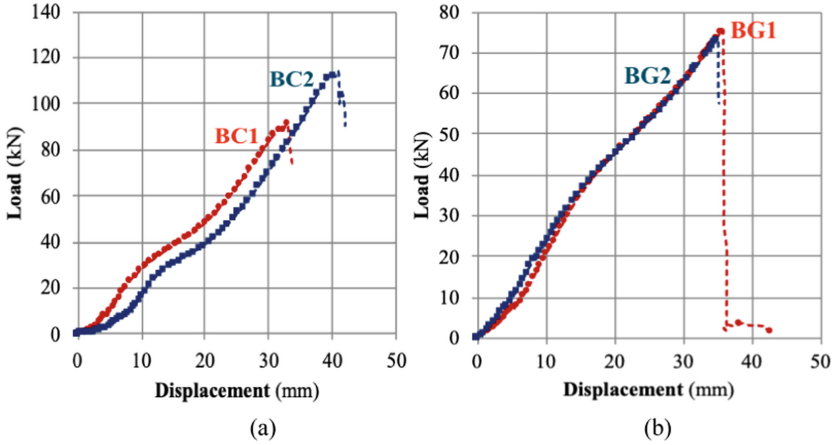


Fig. 4. Exp. Diagram load, kN, vs displacement for tested (a) CFRP and (b) GFRP rods.

Table 4. Experimental mechanical parameters of CFRP and GFRP rod.

Material	Specimen	F_{max}	A_b	f	E	Type of failure
		[N]	[mm ²]	[N/mm ²]	[GPa]	
CFRP	BC1	91904	50.27	1828.37	–	LAB
CFRP	BC2	114316	50.27	2274.24	157.21	XMV
GFRP	BG1	75470	71.26	1059.08	–	XGM
GFRP	BG2	73630	71.26	1033.26	33.59	XGM

3 Anchor Systems for Prestressed CFRP Rod

An experimental campaign on anchor systems for prestressing FRP rods was carried out. The anchoring technique analyzed was the split wedge developed by Täljsten (2009) [15], for the anchor of CFRP rod. This anchor was subjected to short-term tensile strength tests using, for the other end of the cable, a clamp anchorage. This anchorage has the function of creating a firm locking of the cable, to contrast the prestressing force applied to the split wedge anchorage and transmitted along the entire cable (Fig. 6).

With the aim to focus attention on the behavior of the split wedge anchorage, the anchorage at the opposite end must ensure the absence of sliding and negligible deformations. A mechanical clamped anchorage was chosen for this function, consisting of 2 steel plates with longitudinal semicircular cavity on both. These plates are locked around the cable by means of 6 bolts with a diameter of 16 mm, through a thin aluminum interface sleeve (Figure 5). Figure 6 shows the executive drawings of the cylinder and the wedge and the completed pieces. The mechanical properties of each anchorage component are summarized in Table 5.

First, the aluminum wedge was inserted inside the external steel cylinder. The specimen was then placed in a vertical position on the universal tensile testing machine. The

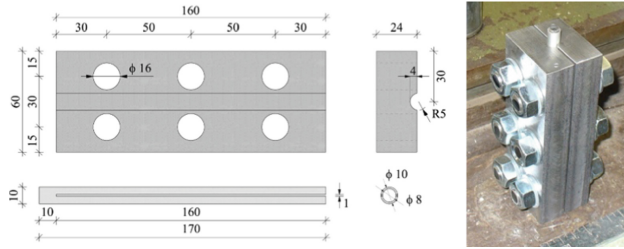


Fig. 5. Geometrical dimension of clamp anchorage.

mechanical clamp anchor was then positioned in the free end, paying attention to the bolts' clamping [16]. During this first phase, the aluminum wedge was pushed inside the steel cylinder, in order to block the CFRP cable and inhibit much of the sliding during the subsequent pretension of rod. The wedge insertion procedure was carried out thanks to a hydraulic jack, contrasted by a frame specially made in laboratory. The force was applied on the wedge, by means of an interface cylinder 60 mm long, made by high resistance steel, with an internal diameter of 12 mm, greater than that of the cable, and an external diameter of 22 mm, smaller than the internal diameter of the cylinder. In Fig. 7(a) the phases of the procedure are schematized, while in Fig. 7(b) the positioning of the interface cylinder on the anchor is shown. The result that occurs after this preliminary operation is the complete locking of the only open slot of the wedge, which results in a shrinkage of the internal diameter of the wedge itself with consequent clamping of the CFRP cable. Regarding the pre-tensioning operation of the cable and therefore the execution of the experimental test, a small frame was created specifically for the purpose of this test, which consists of two steel plates of $225 \cdot 204 \cdot 20$ dimensions, connected with 4 threaded bolted bars having a diameter of 24 mm (Fig. 8).

The insertion of this small frame on the test machine is of fundamental importance in order to create a contrast to the anchorage, and, above all, to recreate the conditions of contrast and constraint that are likely to be realistic.

Once the additional frame was positioned, it was possible to arrange the CFRP rod cable equipped with the previously locked wedge anchorage. Once the specimen was positioned, the mechanical clamp anchorage was placed in the free upper end, paying attention to the tightening of the bolts (Fig. 8(a)).

The tensile force was applied by vertical upward displacement of the machine's upper structure, with which the mechanical clamp anchorage also moved, while the wedge anchorage remained fixed in its original position. At both ends of the cable, the portions of the protruding cable were preliminary measured, in order to evaluate, at the end of the test, the actual sliding of the cable itself, with respect to the anchor.

Three short-term tensile tests were carried out with increasing monotonic load. The load speed was 1 N/mm^2 per second. A strain gauges was positioned at the middle of the CFRP cable to record the evolution of strain with a frequency of 2 Hz.

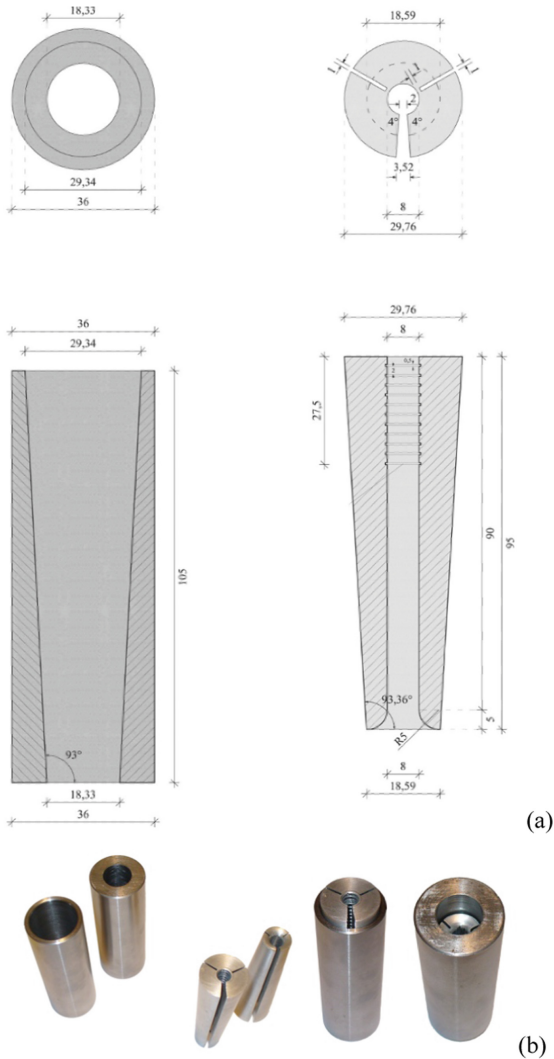


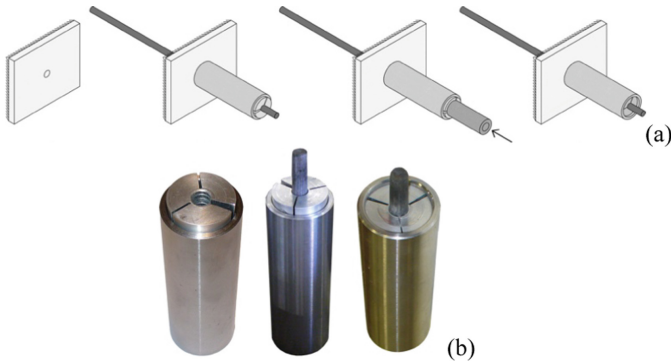
Fig. 6. (a) Technical drawings of split wedge anchorage; (b) components of anchorage.

3.1 Results of Experimental Tests

The first experimental test was interrupted at a load value of 21.9 kN due to sliding along the cable-wedge interface for about 15 mm. In Fig. 9, it can be seen the residues of fibers accumulated near the end of the anchorage, as evidence of a flaking of the hollow lateral surface. On the contrary, no sliding occurred in the mechanical clamp anchor. The split wedge anchorage was then modified by adding a two-component resin in the cable-wedge interface. However, the test was very similar to the previous one. In this case the sliding occurred at a load of 21 kN, in the mechanical clamp anchorage, for an amount equal to 10 mm. The split wedge anchorage equipped with resin, on the

Table 5. Mechanical properties of each anchorage components.

Components	Material	Yielding strength f_y (MPa)	Ultimate strength f_u (MPa)	Young's modulus E (GPa)
Cable	CFRP	–	1800	130
Wedge	Alluminium 6262-T9	400	430	70
Conical socket	Steel C40	450	700	210
Sleeve	Alluminium 6060-T6	200	230	70
Slabs	Steel S355	355	510	210
Bolts	Steel	640	800	210

**Fig. 7.** (a) Wedge insertion's procedure; (b) positioning of the interface cylinder on the anchor.

other hand, has not undergone any sliding. In the third experimental test, however, the mechanical clamp anchorage was modified, by inserting a double interface aluminum sleeve, formed by two completely separate half-cylinders, in order to increase the radial compression tensions and therefore the friction load in the wedge-cable interface.

This modification was made on the same CFRP cable as the second specimen, using the same wedge anchor with additional resin. Result of tensile test did not allow to reach the maximum value of the resistant capacity of the CFRP rod but allowed to reach a value of 40% of the maximum expected failure load without any sliding of the anchorages. The split wedge anchorages did not undergo any sliding and an elastic modulus of 130 GPa was evaluated with reference to the tension of about 430 N/mm². The experimental values of the modulus of elasticity, in agreement with that declared by the supplier, confirmed the validity of the project path carried out up to this point (Fig. 10).

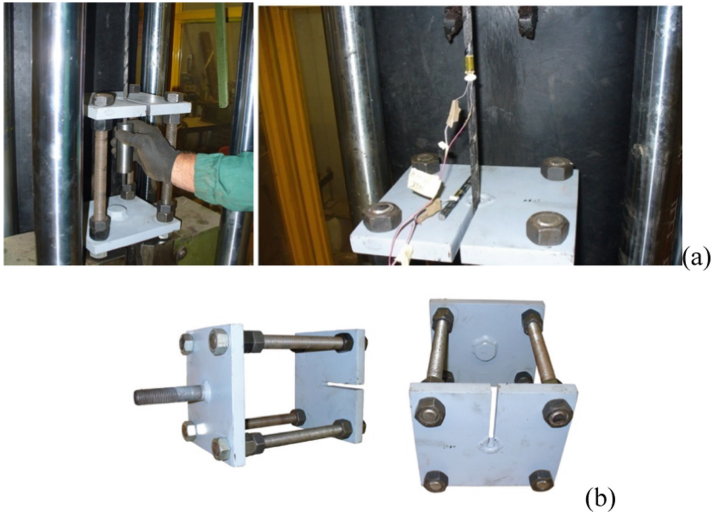


Fig. 8. (a) Set-up of tensile tests with (b) steel frame built for test.



Fig. 9. Residues of fibers accumulated near the end of the anchorage, after cable's slip.

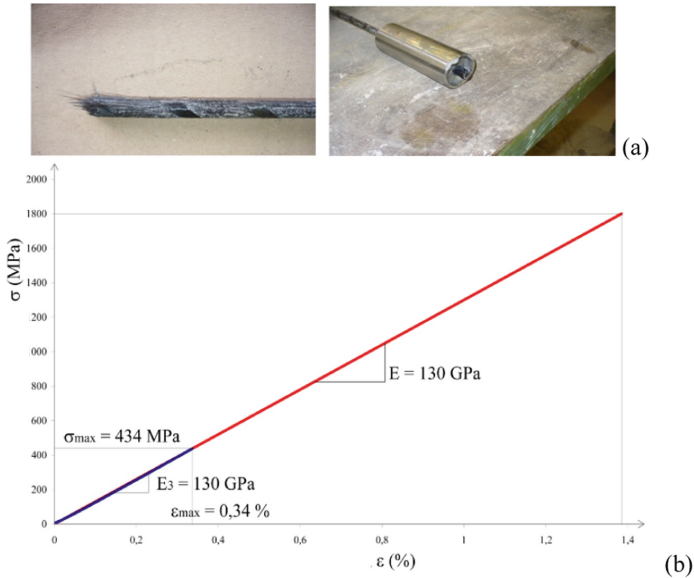


Fig. 10. (a) Failure mode after third test; (b) strain-stress diagram for the third specimen (in blue), in comparison with the one declared by the manufacturer (in red).

4 Conclusion

This paper presents experimental experiences on anchorage systems for FRP rods. Firstly, the behaviour of anchorages adopted in tensile tests of Carbon and Glass FRP rods is investigated. Then, anchorage for prestressing FRP rods is analysed. Main results of experimental campaign, that can be considered as the first phase of a wider future work, are synthesized as follows:

- Results of tensile tests on CFRP and GFRP rods, confirm the reliability of the anchoring system adopted, with resistance values of tested specimens higher than those declared by the manufacturer.
- Results tensile test on pre-tensioned CFRP rod underline that the split wedge anchor without resin, was not able to cope with the slow sliding of the cable, which certainly represents the biggest obstacle for these systems.
- Regarding the split wedge anchor's design, it is necessary to concentrate in the development of further experimental tests, regarding the dynamic and long-term behavior, with tests of resistance to cyclic load and fatigue.
- The effect of thermal expansion on the anchoring elements and the scalability of the anchoring for cables of different diameters are some of the aspects that further require an in-depth research and experimentation program.

Acknowledgments. The Authors wish to thank all the technicians and students who worked to carry out the experimental tests. The experimental research was developed through funds provided by Polytechnic University of Marche, Italy.

References

1. Täljsten, B.: Strengthening concrete beams for shear with CFRP sheets. *Constr. Build. Mater.* **17**, 15–26 (2003)
2. Michaluk, C.R., Rizkalla, S.H., Tadros, G., Benmokrane, B.: Flexural behaviour of one-way concrete slabs reinforced by fibre reinforced plastic reinforcements. *ACI Struct. J.* **95**(3), 353–365 (1998)
3. Capozucca, R., Magagnini, E.: RC beam models damaged and strengthened with GFRP strips under bending loading and free vibration. *Compos. Struct.* **253**, 112730 (2020)
4. Capozucca, R., Magagnini, E., Vecchiotti, M.V.: Experimental static and dynamic response of RC beams damaged and strengthened with NSM GFRP rod. *Composites Structures* **241**, 112100 (2020)
5. Capozucca, R., Magagnini, E.: Vibration of RC beams with NSM CFRP with unbonded/notched circular rod damage. *Composites Structures* **144**, 108–130 (2016)
6. Capozucca, R.: Assessment of CFRP Strengthened RC beams through dynamic tests. *Comp. Part. B: Eng.* **46**, 69–80 (2013)
7. Kim, Y.J., Green, M.F., Gordon Wight, R.: 2 - Prestressed fiber-reinforced polymer (FRP) composites for concrete structures in flexure: fundamentals to applications. In: Kim, Y.J. (eds.) *Advanced Composites in Bridge Construction and Repair*, Woodhead Publishing, pp. 30–60 (2014)
8. Schmidt, J.W., Täljsten, B., Bennitz, A., Pedersen, H., Goltermann, P.: Mechanical anchorage of FRP tendons – A literature review. *Constr. Build. Mater.* **32**, 110–121 (2012)
9. Iyer, S.L., Kumaraswamy, C.: Performance evaluation of glass fiber composite cable for prestressing concrete units. In: *Proceedings of the Thirty-Eight International SAMPE Symposium*, Anaheim, California (1988)
10. Woff, R., Miessler, H.J.: Experience with glass fiber composite bars as prestressing elements for engineering structures. *ASME Compos Mater Technol* **53**, 95–10 (1993)
11. Ouladbrahim, A., Belaidi, I., Khatir, S., Magagnini, E., Capozucca, R., Wahab, M.A.: Prediction of guron damage model parameters coupled with hardening law identification of steel X70 pipeline using neural network. *Met. Mater. Int.* **28**, 370–384 (2022). <https://doi.org/10.1007/s12540-021-01024-4>
12. Yan, F., Lin, Z.: New strategy for anchorage reliability assessment of GFRP bars to concrete using hybrid artificial neural network with genetic algorithm. *Compos. B Eng.* **92**, 420–433 (2016)
13. *ACI Report on Fiber-Reinforced Polymer (FRP) Reinforcement for Concrete Structures*, ACI 440R-07. American Concrete Institute, Farmington Hills, USCNR (2007)
14. *CNR DT 203/2006 Guide for the Design and Construction of Concrete Structures Reinforced with Fiber-Reinforced Polymer Bars*. (In English)
15. Bennitz, A., Schmidt, J.W., Täljsten, B.: Failure modes of prestressed CFRP rods in a wedge anchored set-up. In: *Advanced Composites in Construction 2009, Conference proceedings*, Vol. 4 (2009)
16. Al-Mayah, A., Soudki, K., Plumtree, A.: Effect of rod profile and strength on the contact behavior of CFRP-metal couples. *Compos. Struct.* **82**, 19–27 (2008)



Behaviour of Brickwork Masonry Strengthened with B/GFRP Strips

Roberto Capozucca^(✉), Erica Magagnini, and Giuseppe Pace

Structural Section DICEA, Polytechnic University of Marche, Ancona, Italy
r.capozucca@staff.univpm.it

Abstract. The response of masonry walls to loading depends to many factors: strength of units, thickness of bed mortar, presence of infilled mortar joints, arrangements of units and joints, and to direction of loads respect to mortar joints. Nowadays, a common method for improving the mechanical tensile strength of masonry is to strengthen old masonry structures in seismic areas with externally bonded (EB) Fiber Reinforced Polymers (FRPs). EB FRP strips are typically used to increase the historic masonry walls' shear capacity under in-plane loading although the response of strengthened walls has not been deeply analysed considering the inclination of FRP strips respect the mortar bed joints. In this work, the strength of brickwork masonry walls strengthened by Basalt FRP and Glass-FRP strips with different strengthening inclinations has been experimentally analysed by diagonal compression tests. Finally, discussion and comparison of results obtained by experimental campaign have been developed to evaluate the efficiency of the different strengthening configurations in terms of strength and mechanism of failure.

Keywords: Brickwork masonry · Diagonal compression tests · Glass-Basalt FRP strips

1 Introduction

The preservation of the cultural heritage of masonry buildings presents one of the most important objectives in civil engineering hard to pursue due to the complexity of the geometry of the structures, the variability of the materials used and the loading history of the buildings [1–4]. In recent decades, especially for reinforced concrete and masonry structures [5–7], the application of FRPs to existing buildings with the primary goal of enhancing tensile strength and, secondarily, of raising collapse displacements has become crucial [8–12].

Externally bonded FRP strips and/or sheets are usually adopted on buildings in seismic areas with the aim to strengthen shear masonry walls. This technology increases the tensile capacity to withstand combined compression and shear stresses induced during an earthquake. For FRP strips bonded on historic clay bricks, many experimental campaigns reported in literature [13–16] underline that a dangerous mechanism of brittle failure is due to delamination, especially when the clay surface is weak. The delamination of

FRP strips or sheets has an influence on the safety of the strengthening of unreinforced masonry shear walls. Recently, innovative technique based on soft computing have been adopted to civil engineering problems [17, 18]. New frontiers of research are focused on the implementation of artificial neural network (ANN) models for predicting debonding strength of retrofitted masonry elements [18]. On the other side a correct location and inclination of glued FRP strips on masonry walls have a relevant influence on the response under combined compression and shear forces [11, 19].

In this paper, diagonal compression tests have been performed with the aim to experimentally analyze the strength of brickwork masonry walls strengthened by Glass-FRP and Basalt-FRP strips with different strengthening inclinations. Finally, discussion and comparison of results obtained by experimental campaign have been developed to evaluate the efficiency of the different strengthening configurations in terms of strength and mechanism of failure.

2 Experimental Diagonal Compression Tests

A strengthened shear wall has to be assessed by both local and global failure modes, which can occur in combination: the cracking of masonry in tension, the crushing of masonry in compression, the shear-sliding of masonry, the failure of the fiber-reinforced composite, and, finally, the delamination of FRP from masonry.

One of main problems in the strengthening of masonry shear wall is to evaluate the location of FRP strips relatively to principal tensile stress and bed mortar joints [20]. The response of wallets with FRP strips under diagonal compression allowed to evaluate the increase of strength in the historic full brickwork masonry and the efficient position of composite strengthening also in relation to the mortar bed joints. The experimental investigation had the aim of studying the influence of FRP fibers direction to achieve the best response of masonry in terms of mechanical resistance. Figure 1 shows the possible dispositions of FRP strips for shear wall models in scale [21] with an inclination of 0° , 30° , 45° , 60° and 90° in relation to the mortar bed joints. These dispositions of FRP strips have been also taken as reference for the investigation with strengthened wallets under diagonal compression tests.

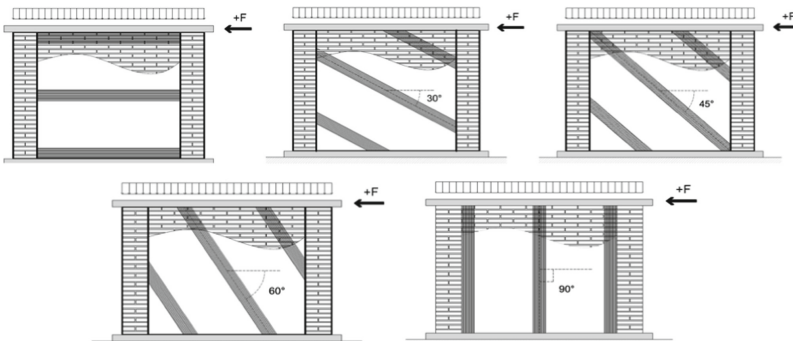


Fig. 1. Strengthening of historic shear wall models with different inclination of FRP strips.

For diagonal compression tests 18 wallets were realized simulating an historic masonry wall made of historic clay bricks and low-quality mortar layers. The wallets were built with historic clay bricks in scale 1:3; the dimension of height and length was equal to 200 mm and thickness of 50 mm. The strengthening of Glass and Basalt FRP strips were used. Table 1 shows the geometrical and mechanical parameters of the soaked unidirectional glass and basalt fibers used for the tests. The specimens were subjected to tensile tests according to ASTM D 3039 [22] and UNI EN ISO 527-1 [23] (Fig. 2).

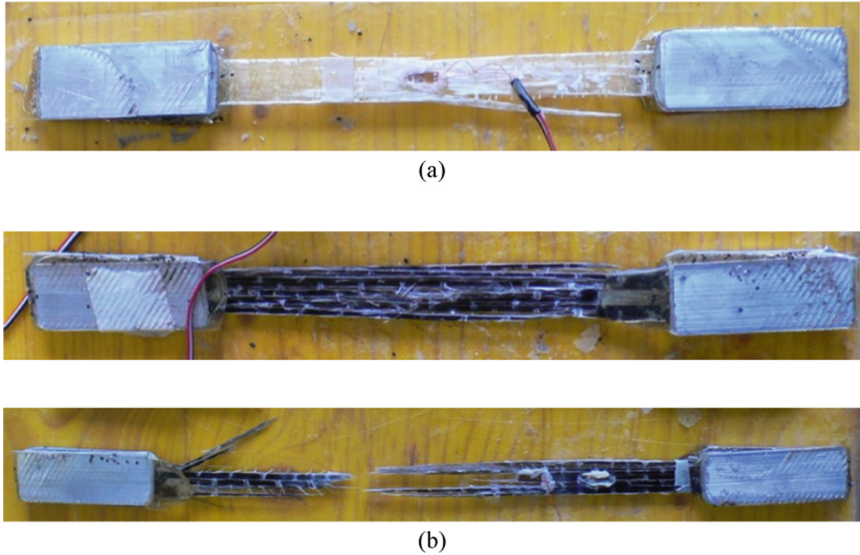


Fig. 2. Failure mode of (a) GFRP specimens - type AGM (Angled, Gage, Middle - ASTM D 3039) and (b) BFRP specimens - type SGM (Long Splitting, Gage, Middle) subjected to tensile tests.

Table 1. Geometrical and mechanical parameters of Glass and Basalt FRP strips.

Fiber	Tensile strength f_{FRP} (N/mm ²)	Young's modulus E_{FRP} (N/mm ²)	Ultimate strain ε_{FRP} (%)	Thickness t (mm)	Density ρ (g/m ²)
GFRP	1273.3	64030	2.0	1.20	300
BFRP	2098.95	84430	2.11	1.20	396

Eight wallets out of eighteen were strengthened with Basalt FRP; the other eight one was strengthened with Glass FRP strips, leaving the last two wallet without strengthening. The inclinations of FRP strengthening considered were: 0°, 45°, 90° in one direction, 30° and 60° in the opposite direction. (Fig. 3).

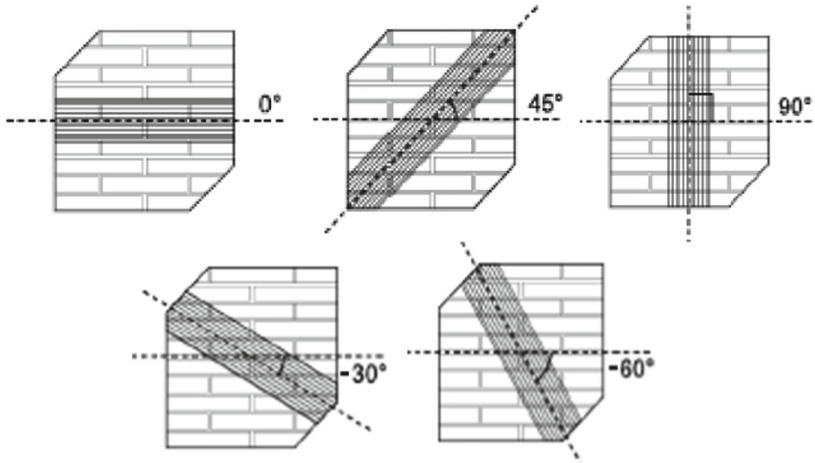


Fig. 3. Masonry wallets strengthened with B-GFRP strips tested by diagonal compression tests.

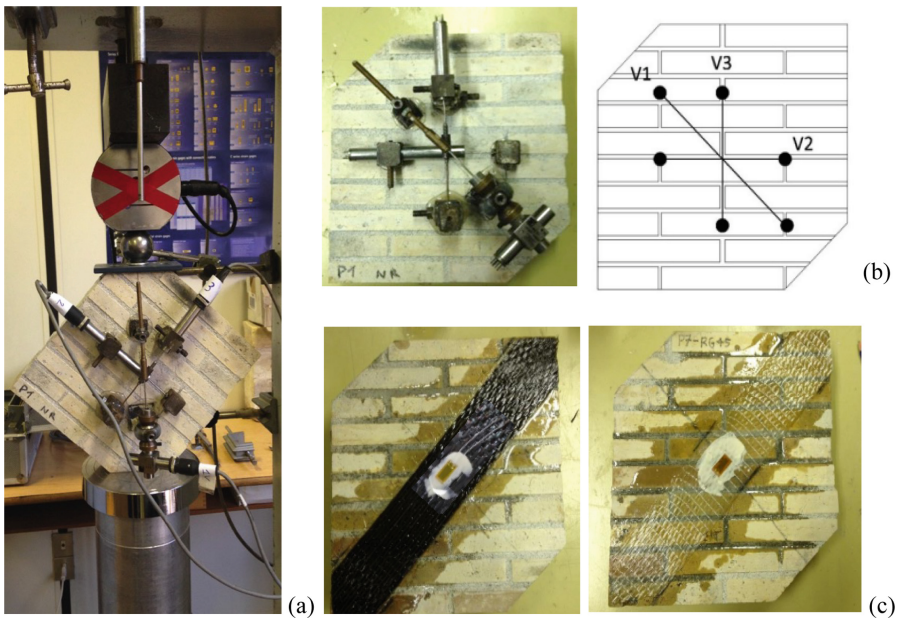


Fig. 4. (a) Set-up for diagonal compression tests; (b) Linear Displacement Transducers LVTD and (c) Strain Gauges on FRP strip surface.

Specimens were initially prepared by cleaning and smoothing their surface; then applying a bi-component primer on the surface of the wallets in order to soak it. Afterwards, epoxy resin was made by mixing two components and then applied along the pre-established directions. FRP strips were applied on the epoxy resin layer just on one surface of each specimen. Diagonal compression tests were realized using a contrast steel frame in order to transfer a diagonal compression load (Fig. 4). Diagonal compression tests were carried out on wallets which were positioned so that the main direction of the mortar layers was always 45° inclined in relation to the load direction. In order to equally transfer the applied load, each specimen was adapted by cutting off two opposite corners; beside a sphere and a 20 mm metallic disc were used in order to uniformly distribute the load (Fig. 4). Measuring equipment foresaw strain-gauges located on the FRP strips in order to evaluate strain values during diagonal compression tests; one load cell for recording of applied diagonal loads; a mechanical transducer (LVTD) in order to measure the vertical displacement of specimens.

Diagonal compression test was chosen to evaluate the response of specimens with and without strengthening although the test creates a biaxial tensile stress uniform just in the center of wallet while results are more complex in the rest of wallet. Main experimental results are presented below. The first experimental test that has been performed is on the two unreinforced specimens. For both specimens, failure occurs with a clear crack along the compressed diagonal at a load value equal to about 16.50 kN. Failure conditions of wallets strengthened with Basalt and Glass FRP strips in different inclination respect the mortar bed joints are shown in Fig. 5.

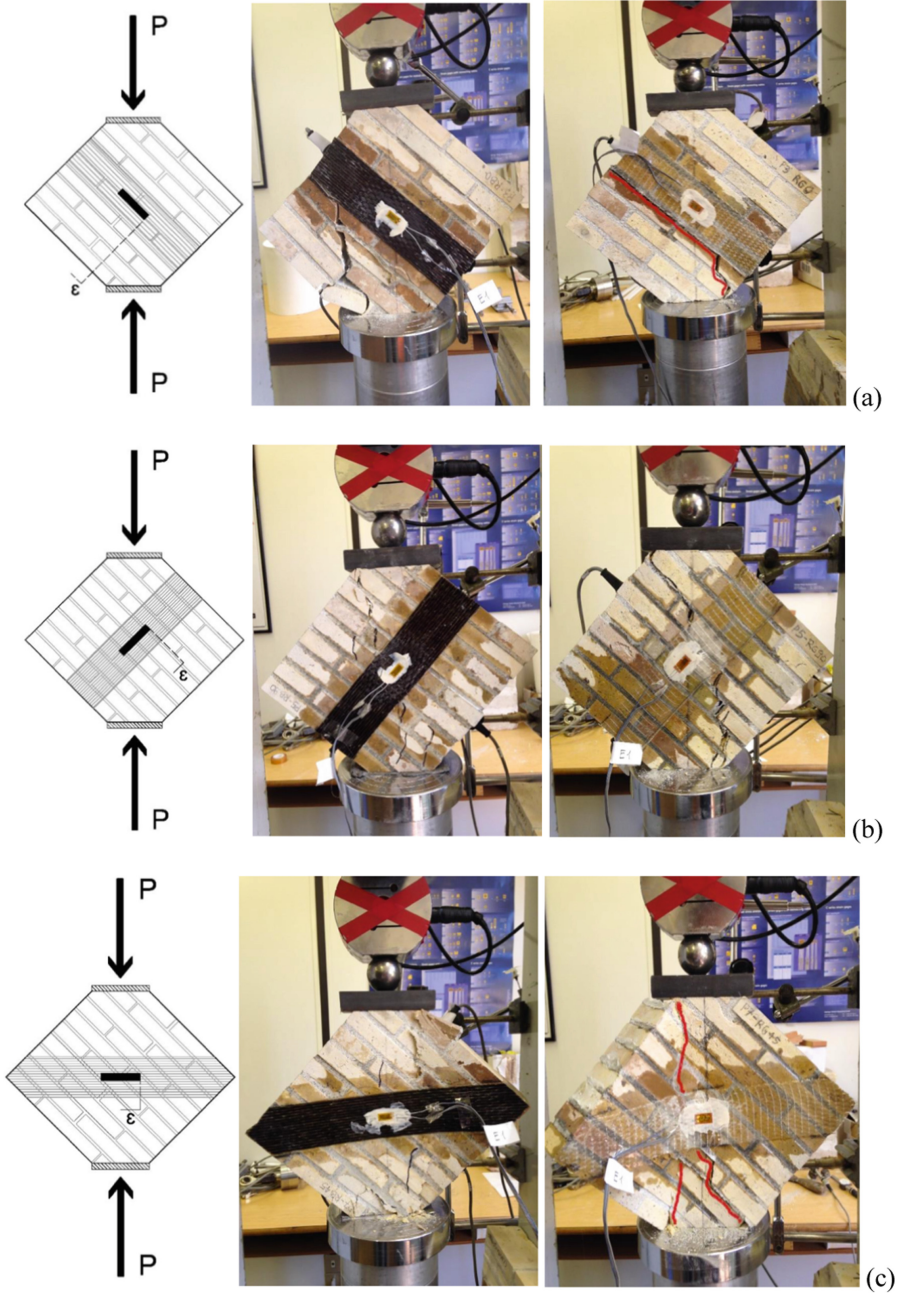


Fig. 5. (a). Failure modes of wallets with different degree inclination of Basalt and Glass FRP strip inclination: (a) 0°; (b) 90°; (c) 45°; (d) -60°; (e) -30°.

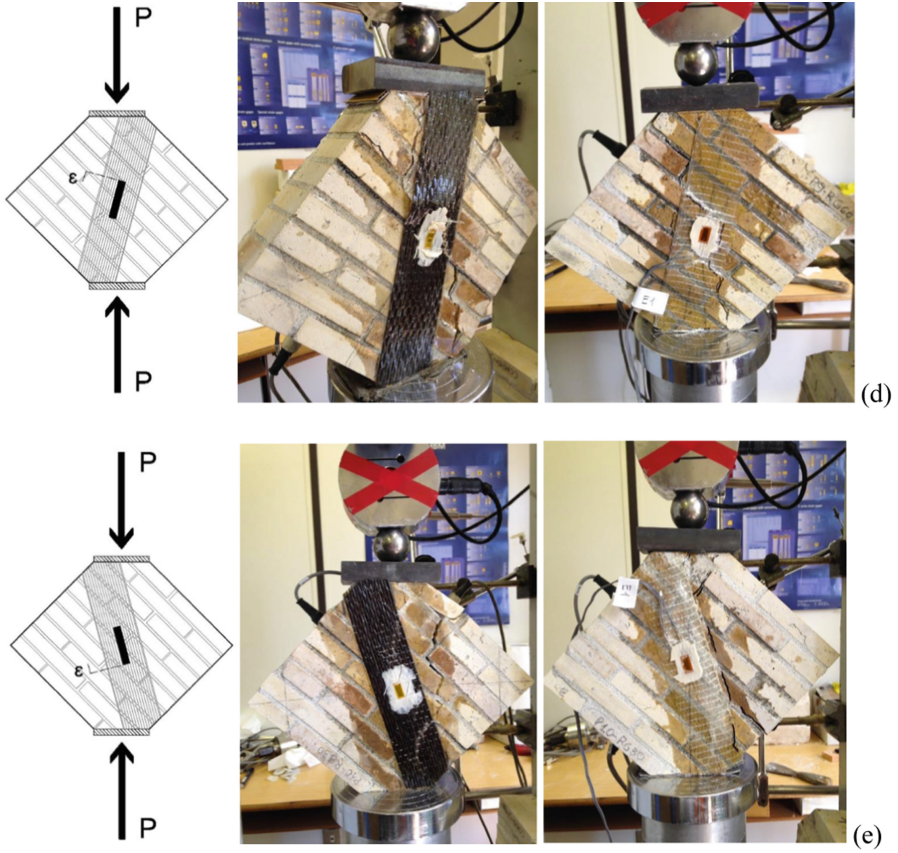


Fig. 5. (continued)

In Table 2 measures obtained at the ultimate load P_u are reported. Results were elaborated following the ASTM E519–81 specifications [24]. Assuming a pure shear stress state at the center of the panel, the value of the average shear stress, τ , equal to the principal tensile stress σ_I , was calculated as (Table 2):

$$\tau = \sigma_I = \frac{0.70P}{A_n}. \quad (1)$$

where P is the diagonal compression load and A_n is the net area of the panel.

Table 2. Measurements obtained by experimental diagonal compression tests at the ultimate load P_u .

Wallets No	Inclination angle of FRP strips	Ultimate Load P_u (kN)	Ultimate Shear stress τ (N/mm ²)	Maximum value of strain on FRP-strip ε_{FRP} (10 ⁻⁶)
BFRP				
1	0°	24.63	1.699	886.80
2	0°	33.5	2.311	1993.44
3	90°	23.2	1.600	1002.48
4	90°	30.5	2.104	117.36
5	45°	31.72	2.188	3562.32
6	45°	25.58	1.765	3996.72
7	-60°	23.7	1.635	-846.48
8	-30°	25.26	1.743	-941.76
GFRP				
1	0°	21.20	1.462	493.92
2	0°	21.25	1.466	121.20
3	90°	17.95	1.238	208.32
4	90°	18.61	1.238	336.72
5	45°	21.87	1.509	2550.48
6	45°	18.53	1.278	1059.12
7	-60°	17.784	1.227	-687.60
8	-30°	16.02	1.105	-468.96

3 Discussion on Experimental Results

In Figs. 6 and 7 the experimental diagrams of the average diagonal load, P , versus average strain, respectively, on BFRP strips, ε_{BFRP} , on GFRP strips, ε_{GFRP} , are presented for the different wallets with various inclinations of GFRP strips in relation to the mortar bed joints.

Experimental results show that maximum resistance is obtained by inclinations of the strengthening of 0° and/or 45° in relation to bed mortar layers. Inclination in positive direction that recorded minimum values of resistance was 90°, with the onset of delamination mechanism.

Therefore, shear resistance of B/GFRP strengthened wallettes, demonstrate the better efficacy of the reinforcement when the inclination ranges from 0° to 45°. Results obtained by shear and compression tests on brickwork wall models confirm that the inclination of the principal tensile strain in relation to mortar layers vary and, generally, it is lower than 45°.

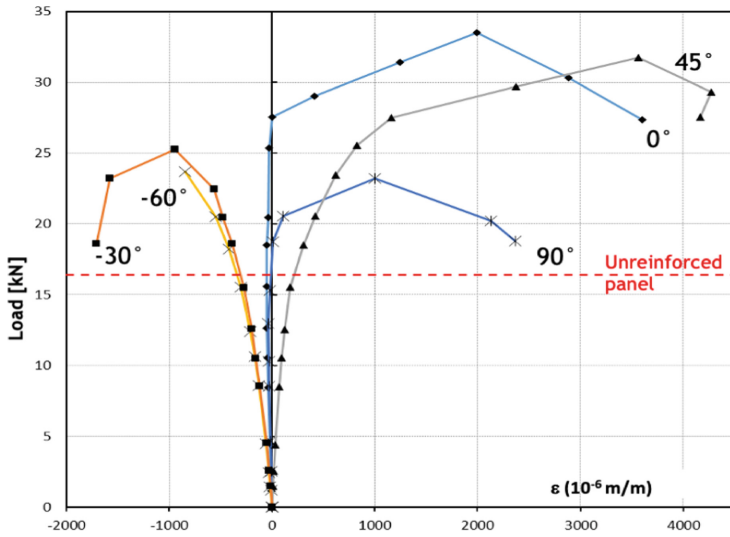


Fig. 6. Experimental average diagrams diagonal load vs strain on BFRP strip.

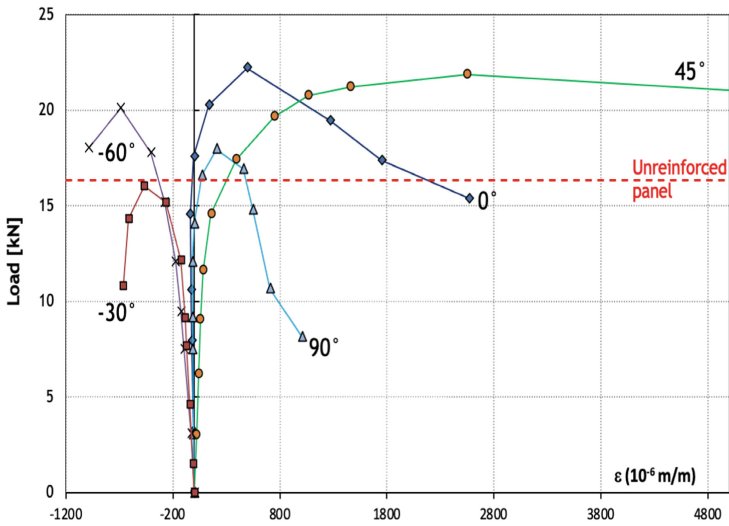


Fig. 7. Experimental average diagrams diagonal load vs strain on GFRP strip.

If we compare the ultimate resistance tests of specimens strengthened with Basalt and Glass FRP, it can be observed that, in all cases investigated, Basalt fibers allow to reach higher maximum loads.

An aspect that needs to be stressed is the behaviour of wallets when the strengthening is placed along the negative direction. In both cases, the strengthening strips were subjected to a compressive stress state; the specimens reached failure for delamination

buckling mechanism. In the case of Glass FRP, delamination buckling mechanism dramatically impairs the resistance capacity of wall, and the specimen showed an ultimate load that was even smaller than the unreinforced case. Instead for Basalt Fiber, the ultimate load was not much affected by this mechanism. In both cases, the deformation capacities were drastically reduced.

4 Conclusion

In this paper an experimental investigation was presented to describe the behaviour of FRP strips used to strengthen historic brickwork masonry. Experimental tests foresaw diagonal compression tests on wallets strengthened with Basalt and Glass FRP strips. Main results are synthesized as follows:

- technique of strengthening by Basalt and Glass FRP strips is convenient to improve the tensile capacity of masonry;
- inclination of FRP strips between $0 \div 45^\circ$ respect to the bed mortar joints permits to obtain high values of capacity maintaining the bond of strengthening;
- inclination of FRP strips between $-30 \div -60^\circ$ leads to a compressive stress state along the FRP strengthening that drastically impairs the resistance and deformation capacities of the system, especially for GlassFRP.

Acknowledgments. The Authors wish to thank all the technicians and students who worked to carry out the experimental tests. The experimental research was developed through funds provided by Polytechnic University of Marche, Italy.

References

1. Magenes, G., Calvi, G.M.: In-plane seismic response of brick masonry walls. *Earthquake Eng. Struct. Dyn.* **26**(11), 1091–1112 (1997)
2. Capozucca, R., Sinha, B.P.: Evaluation of shear strength of historic masonry. In: Proceedings of the 5th International Conference AMCM 2005, Gliwice, Poland (2005)
3. Haach, V.G., Vasconcelos, G., Lourenço, P.B.: Experimentally analysis of reinforced concrete block masonry walls subjected to In-Plane cyclic loading. *Jour. of Struct. Eng.* **136**(4), 452–462 (2010)
4. Salachoris, G.P., Magagnini, E., Clementi, F.: Mechanical characterization of “Scaglia Rossa” stone masonry through experimental and numerical analyses. *Constr. Build. Mater.* **303**, 124572 (2021)
5. Bilotta, A., Ceroni, F., Nigro, E., Pecce, M.: Efficiency of CFRP NSM strips and EBR plates for flexural strengthening of RC beams and loading pattern influence. *Compos. Struct.* **124**, 163–175 (2015)
6. Capozucca, R., Magagnini, E., Vecchiatti, M.V.: Experimental static and dynamic response of RC beams damaged and strengthened with NSM GFRP rod. *Composites Struct.* **241**, 112100 (2020)
7. Capozucca, R., Magagnini, E., Vecchiatti, M.V.: Damaged RC beams strengthened with GFRP. *Procedia Structural Integrity* **11**, 402–409 (2018)

8. Capozucca, R., Magagnini, E.: Experimental response of masonry walls in-plane loading strengthened with GFRP strips. *Compos. Struct.* **235**, 111735 (2020)
9. Gams, M., Tomažević, M., Berset, T.: Seismic strengthening of brick masonry by composite coatings: an experimental study. *Bull. Earthq. Eng.* **15**(10), 4269–4298 (2017). <https://doi.org/10.1007/s10518-017-0136-4>
10. Triantafyllou, T.C.: Strengthening of masonry structures using epoxy-bonded FRP laminates. *Jour. Composites for Construction* **2**(5), 96–104 (1998)
11. Valluzzi, M.R., Tinazzi, D., Modena, C.: Shear behavior of masonry panels strengthened by FRP laminates. *Constr. Build. Mater.* **16**, 409–416 (2002)
12. CNR-DT 200R1/2013. Guide for the design and construction of externally bonded FRP systems for strengthening existing structures. (In English)
13. Aiello, M.A., Sciolti, M.S.: Analysis of bond performance between FRP sheets and calcarenite stones under service and ultimate conditions. *Masonry Intern.* **21**(1), 15–28 (2008)
14. Ceroni, F., Garofano, A., Pecce, M.: Bond tests on tuff elements externally bonded with FRP materials. *Mater. Struct.* **48**(7), 2093–2110 (2014). <https://doi.org/10.1617/s11527-014-0295-6>
15. Oliveira, D.V., Basilio, I., Lourenço, P.B.: Experimental bond behavior of FRP sheets glued on brick masonry. *J. of Composites for Construction* **15**(1), 32–41 (2011)
16. Capozucca, R.: Experimental FRP/SRP-historic masonry delamination. *Compos. Struct.* **92**, 891–903 (2010)
17. Ouladbrahim, A., Belaidi, I., Khatir, S., Magagnini, E., Capozucca, R., Wahab, M.A.: Prediction of guron damage model parameters coupled with Hardening law identification of Steel X70 Pipeline Using Neural Network. *Met. Mater. Int.* **28**, 370–384 (2022). <https://doi.org/10.1007/s12540-021-01024-4>
18. Mansouri, I., Kisi, O.: Prediction of debonding strength for masonry elements retrofitted with FRP composites using neuro fuzzy and neural network approaches. *Compos. B Eng.* **70**, 247–255 (2015)
19. Capozucca, R., Magagnini, E.: Brickwork wall models strengthened with diagonal and horizontal GFRP strips. *Compos. Struct.* **271**, 114062 (2021)
20. Samarasinghe, W.: The in-plane failure of brickwork, Ph. D. thesis, Edinburgh (1980)
21. Benjamin, R., Williams, H.A.: The behaviour of one-story brick shear walls. *J. Struct. Eng. Division ASCE* **84**(1723), 1–30 (1958)
22. ASTM, D. 3039/D3039M-08: Tensile properties of polymer matrix composite materials. Annual book of ASTM: composite materials (2008)
23. UNI EN ISO 527–1 Plastics — Determination of tensile properties — Part 1: General principles (2019)
24. ASTM E519–81 Standard Test Method for Diagonal Tension (Shear) in Masonry Assemblages (2007)



Concrete Plates Reinforced with Embedded CFRP Rods and Carbon/Steel Strips

Elisa Bettucci¹, Roberto Capozucca¹(✉), Abdelwahhab Khatir¹, Samir Khatir²,
and Erica Magagnini¹

¹ Structure Section DICEA, Polytechnic University of Marche, Ancona, Italy
r.capozucca@staff.univpm.it

² Faculty of Civil Engineering, Ho Chi Minh City Open University, Ho Chi Minh City, Vietnam

Abstract. Plates and shells are structural elements present in many civil constructions. These elements are usually built with reinforced concrete or prestressed concrete for considerable plane dimensions. The use of FRP rods during casting instead steel bars may allow to improve the behaviour under high loading and durability avoiding corrosion processes of steel. This work presents an investigation about the behaviour of concrete rectangular plates without steel bars reinforcing in tension. An experimental campaign was carried out on orthotropic and isotropic rectangular concrete plates reinforced, respectively, with carbon fibre polymer (CFRP) rods and carbon/steel fibre (C/SF) strips embedded in concrete in the tensile side. Static load was applied on the centres area of plate models. Evolution of cracking and deflections were monitored during experimental tests and results are shown and discussed.

Keywords: Concrete plate · CFRP rods · Carbon/steel fibres · Bending test

1 Introduction

The use of composite material such as Fibre Reinforced Polymers (FRPs) is growing in civil engineering field especially in the structural rehabilitation of damaged RC beams or to retrofit RC elements [1, 2].

FRPs systems can be found in the form of lamina, strips, reinforcing bars and meshes. The most adopted fibres are Carbon, Glass, Basalt and Aramid; furthermore, in recent years there is an increasing interest in the use of natural fibres for FRPs systems [3].

The main techniques usually adopted in the RC concrete elements like beams and columns consist in the use of FRP lamina/strips glued on the concrete surface or FRP rods/strips inserted into grooves in the cover of sections. This last technique is characterized by near surface mounted FRPs and it represents a convenient method to limit some problems linked to the use of strengthening externally bonded FRP lamina/strips [4–6]. Experimental results confirmed availability of strengthening with FRPs [7–13]. Other investigations analysed the possibility to use fibres embedded in cement matrix [14–17]. Recently, innovative technique based on soft computing have been adopted to

civil engineering problems [18–20]. New frontiers of research are focused on the implementation of artificial neural network (ANN) models for structural behaviour prediction of RC plates strengthened with FRP [20].

This paper describes an experimental investigation carried out to evaluate the bending behaviour of two concrete thin plates reinforced with carbon and steel fibres (C/SF) without use of polymeric matrix. In this way the concrete becomes as matrix for fibres which substitute the steel bars in the tensile zone of plate under loading. Moreover, the bending behaviour of an orthotropic plate consisting of a grid of beams and reinforced with CFRP bars is also analysed.

Two concrete thin plate specimens are reinforced, respectively, with carbon and steel fibres located as a net during the casting of concrete on a plane at 15 mm from concrete surface. The third concrete plate specimen is characterized by two orders of concrete beams in the plane principal directions. Beams are reinforced with CFRP rods, composite material represented by carbon fibres in a polymeric matrix of epoxy resin.

These plates were subjected to a same loading path until failure and experimental results are discussed below.

The behaviour of isotropic plates confirms availability of use of dry fibres as a net in the tensile concrete zone although the bond mechanisms have a great influence on the response.

2 Rectangular Plate Model and Bending Tests Setup

2.1 Isotropic Plate Models

Two concrete thin plate models have been built in laboratory with dimensions 1.0 m·1.0 m in plan and thickness 50 mm (Fig. 1. Rectangular isotropic plate models: (a) plate model with CF strips; (b) plate model with SF strips.) [21]. One of two plates has been reinforced in the tensile side with a net of orthogonal strips of Carbon Fibre (CF) (Fig. 1. Rectangular isotropic plate models: (a) plate model with CF strips; (b) plate model with SF strips.).

CF strips have been located before casting of concrete considering a cover of width about 15 mm. A net of steel bars with a diameter of 5 mm has been positioned at the extrados of the plate. The yield strength of steel bars was equal to $f_y \geq 380 \text{ N/mm}^2$. The average concrete strength for plate model of Fig. 1(a) was about $f_c \cong 20 \text{ N/mm}^2$ and the Young's modulus equal to $E_c \cong 20 \text{ kNmm}^{-2}$. It was evaluated indirectly by the formula $E_c = 4500\sqrt{f_c}$, where f_c is the compressive strength.

The second plate model has been reinforced with strips of steel fibres (SF) embedded in concrete (Fig. 1(b)). Strips have been orthogonally located on a plane at 15 mm from surface with 15 strips each of width 50 mm. The average concrete strength for plate model of Fig. 1(b) was about $f_c \cong 30 \text{ N/mm}^2$. The tensile strength was evaluated experimentally equal to $f_{ct} \cong 3 \text{ N/mm}^2$.

In both plates the area of fibres was about 12 mm^2 for an interval of length of 200 mm. Figure 2 shows carbon and steel fibres used for strengthening the isotropic plates. Steel fibres were characterized by strand with five wires of area 0.096 mm^2 for each wire and about $2.27 \text{ mm}^2/\text{cm}$ and Young's modulus equal to $E_s \cong 206 \text{ kNmm}^{-2}$.

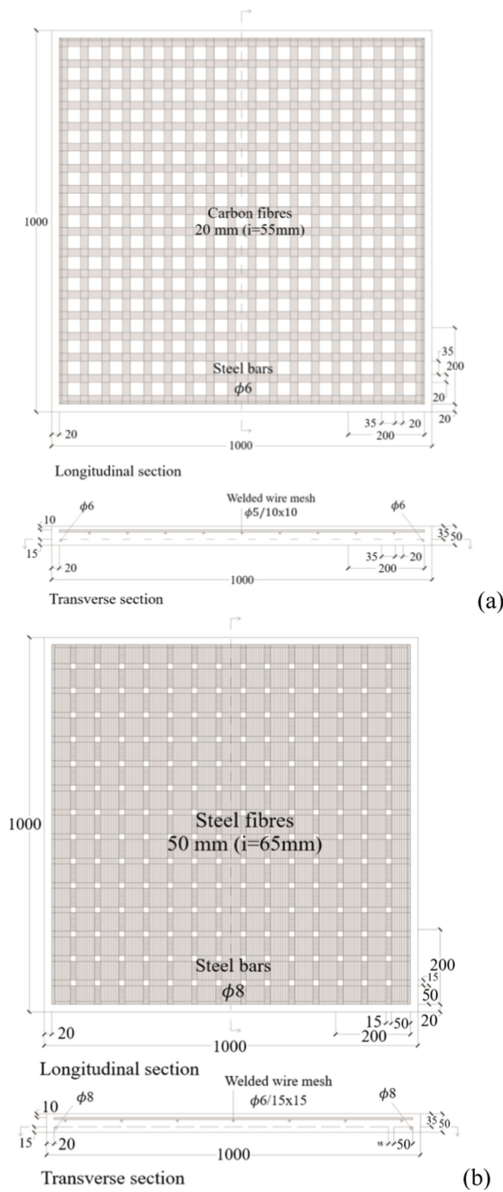


Fig. 1. Rectangular isotropic plate models: (a) plate model with CF strips; (b) plate model with SF strips.

Setup of loading tests for concrete plates is shown in Fig. 3. The plate was disposed in vertical with a contrast due to a steel frame and subjected to loading applied on a central surface by a steel plate connected with a hydraulic jack. The instruments used in the experimental tests were: one loading cell to measure transmitted load, P , on the

central area of the plate of dimensions 300 mm·300 mm; five linear transducers (LVTDs) to measure deflections at five points on the bottom surface of the plate; four strain gauges located at the centre of the plate along both directions and on both concrete plate surfaces to measure strains.

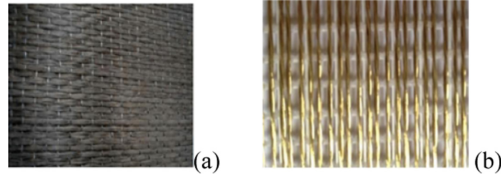


Fig. 2. (a) Carbon fibres; (b) steel fibres.

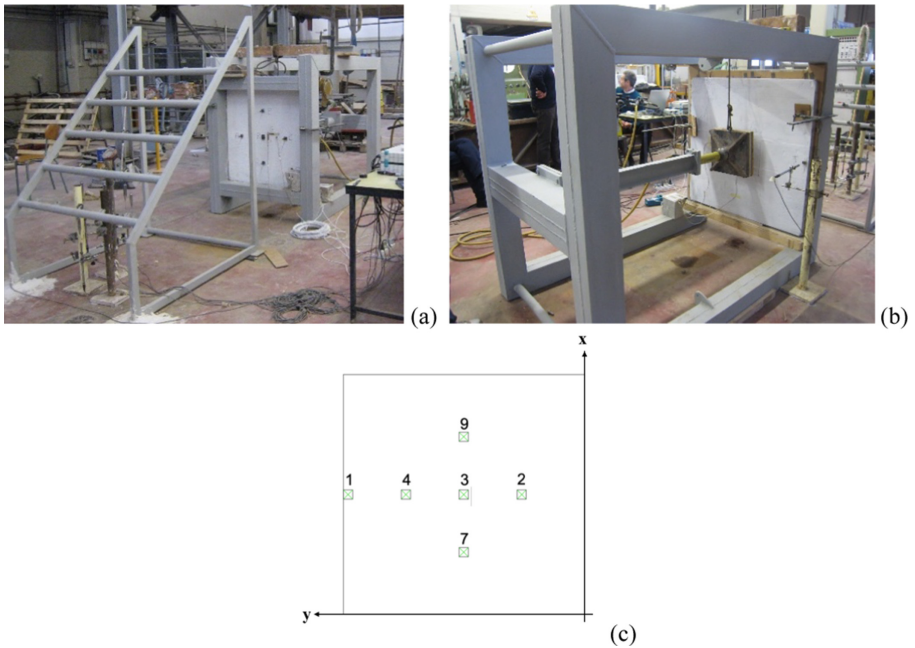


Fig. 3. Setup of tests for isotropic concrete plates: (a) view of intrados and (b) extrados side and (c) (c) points of measure for deflections.

2.2 Orthotropic Plate Model

One concrete orthotropic plate model reinforced with embedded CFRP Rods has been subjected to the same load distributed on a square surface of 300 mm·300 mm on the upper surface of the concrete plate [17].

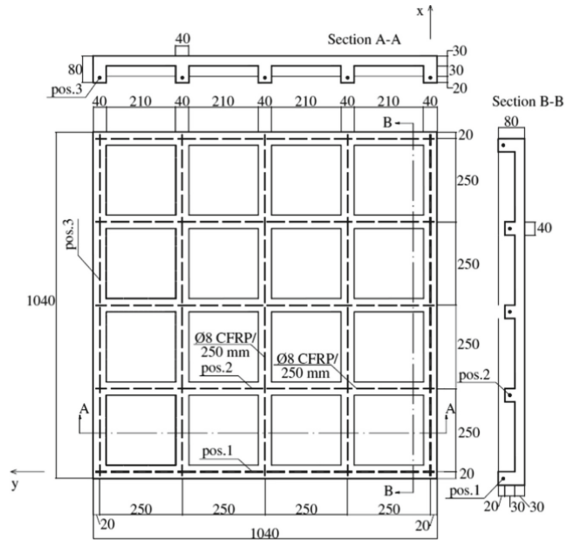


Fig. 4. Rectangular orthotropic plate model with CFRP rods.

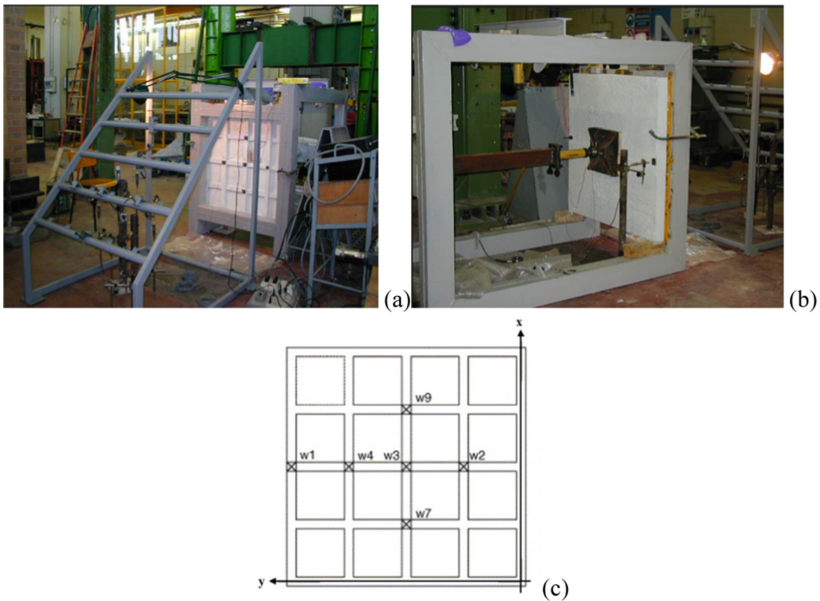


Fig. 5. Setup of tests for orthotropic plate model: (a) view of intrados and (b) extrados side and (c) points of measure for deflections.

This experimental plate model is characterized by two orders of concrete beams in the plane principal directions. The concrete plate measured 1.0 m·1.0 m in plan with a thickness of 30 mm. The dimensions of main ribs section were 40 mm·80 mm and

40 mm-60 mm for perpendicular ribs at constant interval of 250 mm (Fig. 4). The average concrete strength for plate model was about $f_c \cong 20 \text{ N/mm}^2$. Smooth steel bars of diameter 5 mm were arranged in the concrete slab as steel net with 100 mm intervals. The model has been strengthened with CFRP rods of diameter 8 mm in every ribs.

The load was transmitted by a hydraulic controlled jack (Fig. 5). The deflections were measured by six LVTDs: five of them were positioned in the principal concrete ribs and one was positioned in the concrete slab on the upper surface; four strain gauges were located both at the intrados and at the extrados of the concrete slab.

3 Experimental Results

The three concrete plate models were subjected to bending test under an increasing vertical load until failure. The flexural behaviour of the three plates is shown in terms of cracking phases and deflection values.

Isotropic Plates

The isotropic thin plates were subjected under increasing load up to failure. For the plate model reinforced with CF embedded in concrete, first cracks were detected at about $P = 6 \text{ kN}$ during the test, while failure was recorded for a load equal to $P = 26 \text{ kN}$. This failure was associated with an increasing cracking in the bottom surface of the plate (Fig. 6).

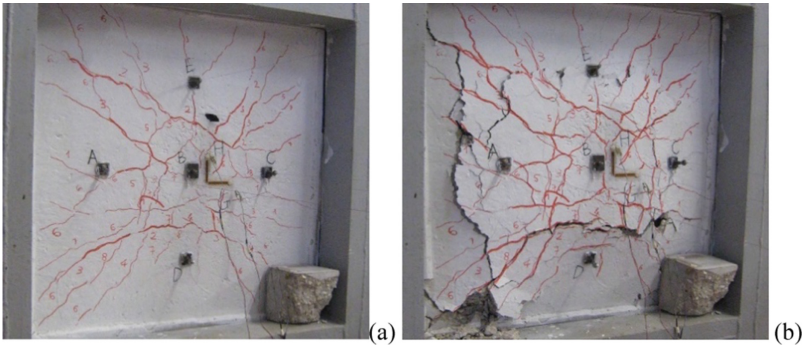


Fig. 6. Cracking at failure of plate with carbon fibres.

Table 1 shows some deflection values of the five control points (Fig. 3(c)) at bottom surface as the vertical load P increases during the bending test.

Table 1. Deflection values at bottom surface of plate with carbon fibres.

P (kN)	w ₂ – A (mm)	w ₃ – B(mm)	w ₄ – C (mm)	w ₇ – D (mm)	w ₉ – E (mm)
0.00	0.000	0.000	0.000	0.000	0.000
6.00	0.209	0.462	0.224	0.415	0.140
10.00	1.573	2.817	1.873	2.842	1.185
16.00	8.877	15.177	10.186	11.936	9.174
18.00	10.380	17.692	11.867	13.667	10.795
20.00	12.968	21.843	14.634	16.597	13.525
24.00	16.774	27.846	18.733	20.783	17.627
26.00	19.764	32.436	22.033	23.955	20.952

**Fig. 7.** Cracking phases of plate with steel fibres: (a) at $P = 26$ kN and (b) at punching failure.

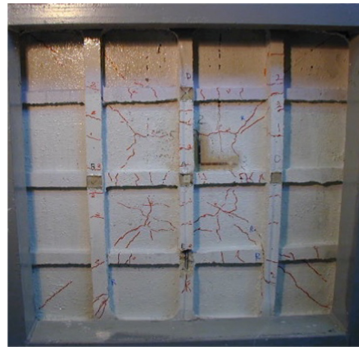
The plate reinforced with steel fibres showed first cracks at about $P = 11$ kN during the test and a diffused cracking phenomenon on the bottom concrete surface for load equal to $P = 26$ kN (Fig. 7(a)). Failure load was equal to about $P \cong 64$ kN with punching (Fig. 7(b)). In Table 2 some deflections values of the five control points (Fig. 3(c)) at the bottom surface are shown.

Orthotropic Plate

For the orthotropic plate model with embedded CFRP rods, the bending test was developed by two cycles of loading: at first, the vertical load was applied until the formation of the first cracks, which were recorded for a load value approximately equal to $P \cong 10.7$ kN; then, at the second cycle, the vertical load was monotonically increased until the failure of experimental model at the value of load equal to $P \cong 30$ kN. At this failure load, cracks totally interested the intrados surface of the concrete plate (Fig. 8). Table 3 shows some deflection values, of the six control points (Fig. 5(c)), recorded for the two phases of loading.

Table 2. Deflection values at bottom surface of plate with steel fibres.

P (kN)	w ₂ – A (mm)	w ₃ – B (mm)	w ₄ – C (mm)	w ₇ – D (mm)	w ₉ – E (mm)
0.00	0.000	0.000	0.000	0.000	0.000
9.006	0.287	0.509	0.387	0.315	0.484
10.006	0.565	0.934	0.659	0.528	0.718
12.012	0.571	1.353	0.909	0.709	0.971
18.060	3.759	6.384	3.828	3.959	4.031
20.026	4.553	7.631	4.559	4.775	4.656
26.012	8.100	12.881	7.834	8.409	7.868
40.038	12.671	19.943	11.550	12.928	11.440
42.197	13.134	20.753	11.937	13.659	11.853
60.017	18.059	28.353	15.640	18.606	15.618
63.892	20.528	33.631	17.178	21.934	17.581

**Fig. 8.** Cracking at failure of orthotropic plate.

4 Discussion

Below are the graphs deduced from the experimental tests related to the three models of concrete plates. Figure 9 shows a comparison between the experimental curves Load, P , versus Deflection, w , of the two models of isotropic concrete plates. Diagrams present the deflection values recorded in three points of the plate where the transducers were placed, points A, C and D respectively. In the experimental curves related to the plate reinforced with CF strips, it is possible to identify a bilinear trend, with two decreases in slope. The first stage describes a linear elastic behaviour up to the value of load corresponding to the cracking of tensile concrete; the second is the inelastic phase, with loss of stiffness and increase of displacement up to failure load.

The experimental diagrams of the plate reinforced with SF strips show a trilinear trend, with a third phase characterized by the resistance of the fibres that determine an

Table 3. Deflection values at bottom surface of orthotropic plate with CFRP rods.

P (kN)	w ₃ – A (mm)	w ₂ – B (mm)	w ₄ – C (mm)	w ₉ – D (mm)	w ₇ – E (mm)	w ₁ (mm)
0.00	0.000	0.000	0.000	0.000	0.000	0.000
1.00	0.037	0.000	0.022	0.053	0.053	-0.003
2.00	0.162	0.034	0.103	0.147	0.162	-0.008
4.00	0.693	0.403	0.566	0.431	0.637	-0.001
7.00	1.743	1.156	1.400	1.087	1.565	0.133
10.70	3.184	2.109	2.422	2.068	2.686	0.454
1.00	1.487	1.153	1.268	0.934	1.384	0.411
2.00	1.671	1.222	1.368	1.072	1.544	0.392
4.00	2.121	1.484	1.650	1.353	1.944	0.414
7.00	2.787	1.881	2.128	1.797	2.468	0.527
13.00	5.006	3.395	3.620	3.262	4.194	0.819
20.00	9.403	6.366	6.556	6.100	7.406	1.026
25.00	12.315	8.496	8.537	7.947	9.844	1.163
30.00	15.256	10.547	10.500	9.810	11.850	1.343

increase in stiffness up to the failure of punching. The plate reinforced with SF strips exhibited widespread cracking for a load value equal to $P = 26$ kN, corresponding to the failure load for the plate reinforced with CF strips. However, from the comparison between the experimental graphs of Fig. 9, at the load $P = 26$ kN, the plate reinforced with SF strips showed deflections about 2.5 times smaller. In Fig. 10 the experimental diagram, Load, P , versus Deflection, w , at the centre of the orthotropic model reinforced with CFRP bars is shown.

From the analysis of the flexural behaviour of the beam grid model in terms of deflections until failure, it can be deduced that three phases describe the response under load of the reinforced plate model: after an un-cracked first phase, up to $P < 4$ kN, the second phase is characterized by an elastic behaviour after cracking of concrete, for load values approximately between 4 and 11 kN; the deflection values increase in the third inelastic phase, for a load value $P > 11$ kN.

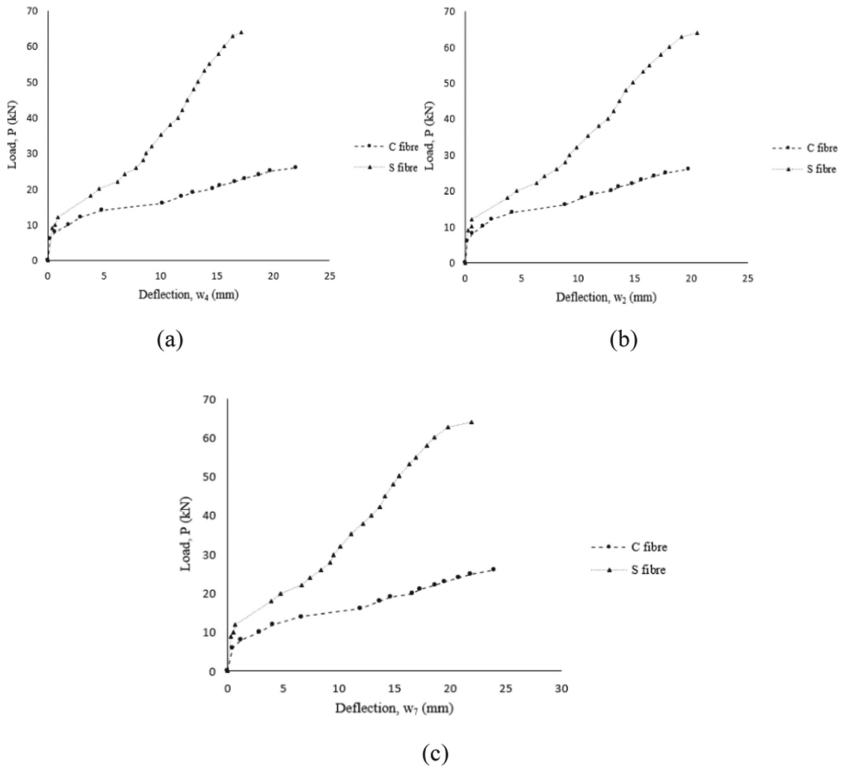


Fig. 9. Comparison of exp. Diagrams load, P , vs. deflection values for isotropic plates, recorded at the points: (a) $w_2 - A$; (b) $w_4 - C$; (c) $w_7 - D$.

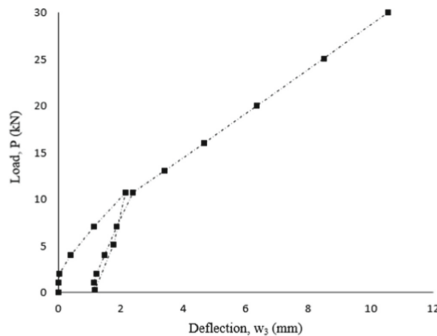


Fig. 10. Exp. Diagram load, P , vs. deflection for orthotropic plate, recorded at the point W_3-A .

5 Conclusions

This paper deals about the analysis of the behaviour of concrete rectangular plates without steel bars reinforcing in tension.

Bending tests were carried out on three concrete plate models: two isotropic and one orthotropic rectangular concrete plate reinforced, respectively, with carbon fibre polymer (CFRP) rods and carbon/steel fibre (C/SF) strips embedded in concrete in the tensile side. From the analysis of the experimental results, the following conclusions can be drawn:

- The use of dry fibres as a net in the tensile concrete zone is a valid method for reinforcing concrete thin plates, in place of steel bars.
- The bond mechanisms have a great influence on the response.
- The bending behaviour of the concrete plate reinforced with steel fibres shows smaller deflections and greater strength than the carbon strips.
- The behaviour of the orthotropic plate model with CFRP rods is adequate to although width of cracks mostly influences the response under loading.

Acknowledgments. The Authors wish to thank all the technicians and students who worked to carry out the experimental tests. The experimental research was developed through funds provided by Polytechnic University of Marche, Italy.

References

1. Capozucca, R., Magagnini, E.: Vibration of RC beams with NSM CFRP with unbonded/notched circular rod damage. *Compos. Struct.* **144**, 108–130 (2016)
2. Bendada, A., Boutchicha, D., Khatir, S., Magagnini, E., Capozucca, R., Abdel, W.M.: Mechanical characterization of an epoxy panel reinforced by date palm petiole particle. *Steel Compos. Struct.* **35**(5), 627–634 (2020)
3. Capozucca, R., Magagnini, E., Vecchiotti, M.V.: Experimental static and dynamic response of RC beams damaged and strengthened with NSM GFRP rod. *Compos. Struct.* **241**, 112100 (2020)
4. Capozucca, R., Magagnini, E.: RC beam models damaged and strengthened with GFRP strips under bending loading and free vibration. *Compos. Struct.* **253**, 112730 (2020)
5. Capozucca, R., Magagnini, E., Bettucci, E.: Delamination buckling of GFRP-strips in strengthened RC beams. *Compos. Struct.* **300**, 116183 (2022)
6. Capozucca, R.: Assessment of CFRP Strengthened RC beams through dynamic tests. *Comp. Part. B: Eng.* **46**, 69–80 (2013)
7. Nabil, F.G., Abdel-Sayed, G., Wahba, J., Sakla, S.: Mathematical solution for carbon fiber-reinforced polymer prestressed concrete skew bridges. *ACI Struct. J.* **96**(6), 981–987 (1999)
8. Michaluk, C.G., Rizkalla, S.H., Tadros, G., Benmokrane, B.: Flexural behavior of one-way concrete slabs reinforced by fiber reinforced plastic reinforcements. *ACI Struct. J.* **95**(3), 353–363 (1998)
9. Zhang, B., Masmoudi, R., Benmokrane, B.: Behaviour of one-way concrete slabs reinforced with CFRP grid reinforcements. *Construct. Build Mater.* **18**(8), 625–635 (2004)
10. Shill, S.K., Garcez, E.O., Al-Ameri, R., Subhani, M.: Performance of two-way concrete slabs reinforced with basalt and carbon FRP rebars. *J. Compos. Sci.* **6**, 74 (2022)
11. Aljazaeri, Z., Alghazali, H.H., Myers, J.J.: Effectiveness of using carbon fiber grid systems in reinforced two-way concrete slab system. *ACI Struct. J.* **117**, 81–89 (2020)

12. El-Gamal, S., El-Salakawy, E., Benmokrane, B.: Behavior of concrete bridge deck slabs reinforced with fiber-reinforced polymer bars under concentrated loads. *ACI Struct. J.* **102**, 727 (2005)
13. Yost, J.R., Goodspeed, C.H., Schmeckpeper, E.R.: Flexural performance of concrete beams reinforced with FRP grids. *J. Compos. Constr.* **5**, 18–25 (2001)
14. Borri, A., Castori, G., Grazini, A., Giannantoni, A.: Composites SRP/SRG: characteristics, testing and applications. *Build. Masonry* **117**, 52–57 (2006)
15. Mahroug, M., Ashour, A., Lam, D.: Tests of continuous concrete slabs reinforced with carbon fibre reinforced polymer bars. *Compos. Part B Eng.* **66**, 348–357 (2014)
16. Bantia, N., Al-Asaly, M., Ma, S.: Behavior of concrete slabs reinforced with fiber-reinforced plastic grid. *J. Mater. Civ. Eng.* **7**, 252–257 (1995)
17. Capozucca, R.: Analysis of the experimental flexural behaviour of a concrete beam grid reinforced with C-FRP bars. *Comp. Struct.* **79**(4), 517–526 (2007)
18. Ouladbrahim, A., Belaidi, I., Khatir, S., Magagnini, E., Capozucca, R., Wahhab, M.A.: Prediction of gurson damage model parameters coupled with hardening law identification of Steel X70 pipeline using neural network. *Met. Mater. Int.* **28**, 370–384 (2022)
19. Khatir, S., Tiachacht, S., Le Thanh, C., Ghandourah, E., Mirjalili, S., Wahab, M.A.: An improved artificial neural network using arithmetic optimization algorithm for damage assessment in FGM composite plates. *Compos. Struct.* **273**, 114287 (2021)
20. Razavi, S.V., Ayazi, M.H., Mohammadi, P.: Artificial neural network for structural behavior prediction of RC one-way slab strengthened by CFRP. *Sci. Res. Essays* **6**(23), 5609–5627 (2011)
21. Capozucca, R., Bossoletti, S., Gabrielloni, M.: Response of concrete plates reinforced with carbon-basalt-steel fibres under loading. In: *Proceedings Fibre Concrete 2013*, 12–13 September, 2013, Prague, Czech Republic (2013)



Structural Health Monitoring for RC Beam Based on RBF Neural Network Using Experimental Modal Analysis

A. Khatir¹(✉), R. Capozucca¹, E. Magagnini¹, S. Khatir², and E. Bettucci¹

¹ Structural Section DICEA, Polytechnic University of Marche, Ancona, Italy
a.khatir@pm.univpm.it

² Soete Laboratory, Faculty of Engineering and Architecture, Ghent University,
Technologiepark Zwijnaarde 903, 9052 Zwijnaarde, Belgium

Abstract. This paper presents an application using Radial basis Function with Neural Network RBF-NN to predict damage identification. Free vibration experiments at various degrees of damage analysis is done to study the complex behavior of RC beams affected by notches. Both intact and damaged states are analyzed based on experimental measurement. Different damages degrees concentrated in the middle area, a beam model with a notch is built. The frequency response function (FRF) envelope acquired by the dynamic experimental tests is established and the changes in normal frequency values are compared with the degree of damage in the models of the RC beams. The action of damaged beams under free vibration is improved by implementing analytical models with equivalent stiffness reduction and identification processes. In order to verify the damage analysis procedure based on vibration testing and the recommended analytical method, a comparison of experimental and analytical results is given as the first stage. In the second stage, the effectiveness of (RBF-NN) is provided for different damage scenarios to predict the notches depth and width of RC beam. The results showed the robustness of RBF-NN to predict the notches depth and width of RC beam with a high accuracy.

Keywords: Structural health monitoring · RBF Neural Network · RC Beam · Vibration analysis · Damage identification

1 Introduction

A very significant topic in structural engineering is the idea of tracking and identifying damaged elements to ensure the safety of users. There are many types of damage measurement, such as acoustic or ultrasonic approaches, obviously, the cost of reconstruction is cheaper than that needed to rebuild the entire building.

The technique of visual inspection has a limited ability to detect damage, especially when damage lies inside the structure and is not noticeable. The vibratory response-based methods of damage detection are licensed and are commonly used on many types

of structures. Applications in industry, for example for aircraft frames Tsyfansky Beresnevich 2000 [1], Dron 2004 [2] ball bearings, or Trendafilova 2008 [3], can be listed here. In specific, in mechanical and civil engineering, vibration techniques are frequently used for research to detect damage to aircraft wings, bridges and beams [4, 5]. In the presence of operational and environmental variations, damage detection using vibration-based damage recognition procedures and machine learning algorithms applied on the basis of the auto-associative neural network, factor analysis, and decomposition of singular value. To detect damage in (SHM) applications [6–10], kernel-based machine learning algorithms have been widely applied. These algorithms have revealed high sensitivity and accuracy in the classification of damage, mostly based on support vector machines (SVMs). Mita and Hagiwara suggested a method to detect local damage in a building structure with a limited number of sensors by using a supervised SVM [11]. In several studies, this process has been extended. For example, a hybrid technique (wavelet SVM) can be considered, where damage-sensitive characteristics are extracted and classified using the SVM through the wavelet energy spectrum [12]. The study of the impact of damage on the rigidity and durability of materials and systems is also of concern to modern composite materials [13–17], which reflect a significant proportion of more recent materials which have also been used in structural engineering in recent years, in particular as repair materials for reinforced concrete and/or steel structures.

A different inverse analysis focused on optimization methods for damage localization and quantification was proposed by Khatir et al. [18–21] in various systems using modal analysis. In order to estimate crack length using an intelligent method, experimental and expanded isogeometric analysis (XIGA) of cracked plates was studied, used to (ANN) methodology by Jaya algorithm [21]. A damage prediction using artificial neural network (ANN) and cuckoo search algorithm in bridge beam-like is suggested by [22]. ANN also combined with butterfly optimization algorithm for steel beam crack location and depth prediction basing on vibration analysis [23]. The improved optimization methodology based on (RBF) Neural Network Combined with Genetic Algorithm for short-term wind power forecasting was presented by Wen-Yeau Chang et al. [24]. The authors explain the experimental behavior of damaged beam models in this paper by complex free vibration experiments, adopting two heterogeneous RC beam models damaged by notches. In the center of the duration, the damage is placed and the vibration tests cause the fall of frequencies to be defined due to the rise in the degree of damage. A comparison between the experimental and theoretical data has allowed us to obtain valuable suggestions on the introduction of non-destructive vibration testing methods in the identification of RC beam damage and on the usefulness of analytical models.

2 Principle of RBF Neural Network

For structures with missing knowledge, the RBF neural network is a valuable technique. It may be used to investigate the connections between a main (reference) sequence and the other comparative sequences in a series [25]. The RBF neural network's theory is explained in this section. The RBF neural network is a forward networks model that has decent accuracy and global approximation while being free of local minima issues. It is a multi-input, multioutput system consisting of an input layer, a hidden layer, and an

output layer The hidden layer performs nonlinear transformations for feature extraction during data processing, and the output layer produces a linear combination of output weights [26]. Figure 1 shows the RBF neural network's composition.

From the input space R^d to the output space R^m , the network performs a nonlinear projection. RBF neural networks' mapping relationship between input and output vector is based on the following function:

$$\text{RBF Neural Network: } \begin{cases} R^d \rightarrow R^m \\ \bar{x} \rightarrow \bar{y} \end{cases} \tag{1}$$

where input vector $\bar{x}_i = \{x_i, \text{for } i = 1, 2, \dots, d\}$,
 output vector $\bar{y}_i = \{y_i, \text{for } i = 1, 2, \dots, m\}$,

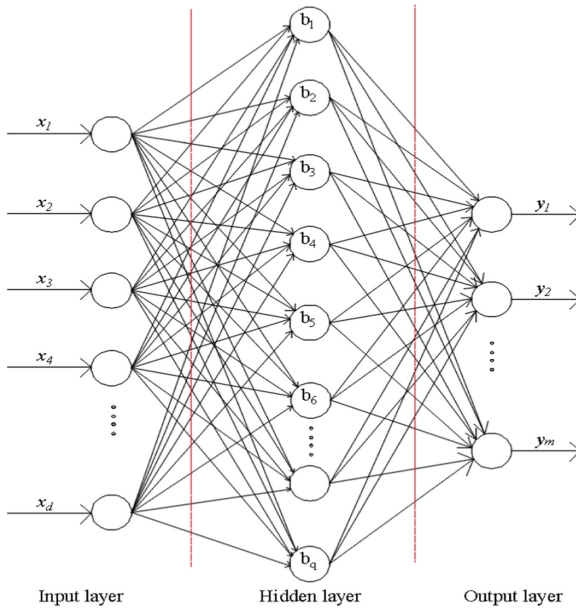


Fig. 1. Architecture of the RBF neural network.

In the following equation, each hidden neuron computes a Gaussian function:

$$b_j(\bar{x}) = \exp \left[\frac{-\|\bar{x}^T - \bar{\mu}_j\|^2}{2\sigma_j^2} \right], \text{for } j = 1, 2, \dots, q \tag{2}$$

where μ_j and σ_j are the center and the width of the Gaussian potential function of the j th neuron in the hidden layer, respectively.

Each output neuron of the RBF neural network computes a linear function in the following form:

$$y_k = \sum_{j=1}^q \omega_{kj} b_j(\bar{x}), \text{for } k = 1, 2, \dots, m, \tag{3}$$

where y_k is output of the k th node in the output layer, ω_{kj} is weight between j th node in the hidden layer and k th node in the output layer, and $b_j(\bar{x})$ is output of the j th node in the hidden layer.

3 Proposed Experimental Work

Experimental dynamic tests were carried out on beam models using a special impact hammer to activate the structural component and accelerometers to calculate device acceleration,. The LAN-XI TYPE 3050 - Brüel & Kjaer data acquisition system was used to conduct the dynamic study of the beam models (Fig. 2(a)). Via the input channels, the piezoelectric accelerometer and the impact hammer (Figs. 2(b), (c)) have been attached, respectively, to the data acquisition system.

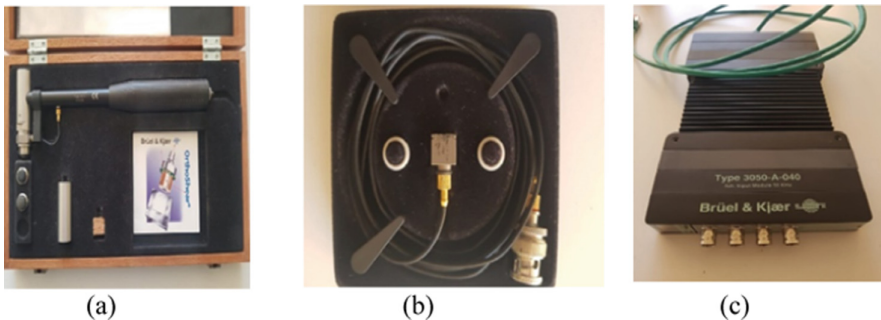


Fig. 2. Instruments adopted for vibration tests: (a) LAN-XI TYPE 3050-Brüel & Kjaer (b) Accelerometer 4508 and (c) Impact hammer 8202-2646 - Brüel & Kjaer.

It was important to calibrate the acquisition data system in relation to the impact hammer to achieve accurate results with reduced errors before proceeding with the experimental investigation. Pulse Labshop - Brüel & Kjaer programme was used to process the frequency domain signals using the Fast Fourier Transform (FFT) technique and obtain the effects of the experimental vibration by calculating the FRFs represented in the frequency domain. A feature known as coherence was considered in order to determine the measurement's reliability. Thus, it was verified for each of the measurements that the value of the coherence was close to one, which permitted control over the results.

3.1 Vibration of RC Beam Without Damage

Experimental free vibration experiments were carried out on RC beam model with free-free ends. The geometrical and mechanical characteristics of the beam are shown in Table 1.

The beam type is reinforced longitudinally and transversely by stirrups placed at an interval of 100 mm as shown in Fig. 3.

For a first approximation, the RC beam model without damage (D0) is assumed as a uniform slender beam that ignores gravity forces, rotary inertia, shear deformation,

Table 1. Geometrical and mechanical characteristics of considered beams.

Width b (mm)	Height h (mm)	Length L (mm)	Young's Modulus E (KN/mm ²)	Density P (N _S ² /mm ⁴ × 10 ⁻⁹)	Moment of Inertia I (mm ⁴ .10 ³)
80	120	1100	28.43	2.360	11520

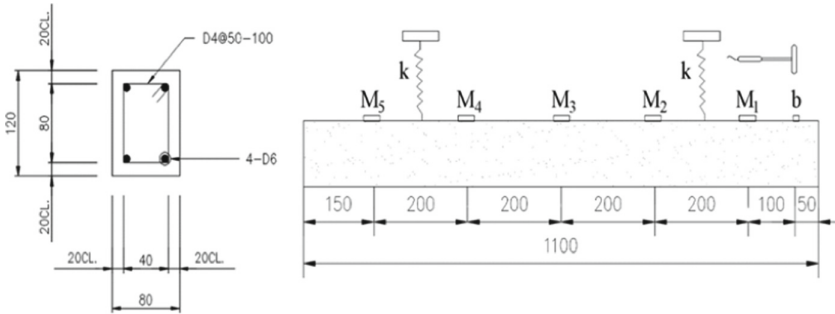


Fig. 3. Considered beam model and section

and damping. Only the element of displacement $v(s,t)$ may be considered for a beam in bending.

In the case of both ends free, the solution of Eq. (1) allows for the expression of circular natural frequency ω_r^f for generic mode r of vibration:

$$\omega_r^f = \left(a_r \cdot \frac{r\pi}{L} \right)^2 \cdot \sqrt{\frac{EI}{\rho A}} \tag{4}$$

where $\lambda_r = r\pi / L$ is the eigenvalue for a simply supported beam.

The eigenvalue for a free end beam at the r mode λ_r^f may be correlated to the value λ_r for a simply supported beam [27]: $\lambda_r^f = \alpha_r \cdot \lambda_r$ with α_r a coefficient that depends on the different r modes of vibration, and equals 1.506, 1.25, 1.167 and 1.125, respectively, for the first four modes.

The first four theoretical frequency values obtained with mechanical parameters given in Table 1 using Eq. (4) for the undamaged beam model are shown in Table 2.

The experimental dynamic experiments were conducted on a beam model using a particular impact hammer and the common technique of calculating the structural element's acceleration with a fixed point of impact (Fig. 3). The dynamic test registered the structure's reaction in nine positions, imparted by impact hammer in one (1) location, with an average of ten (10) beats. The experimental vibration results were obtained using FRFs, which were made up of complex matrices and from which the parameters defining the structure's dynamic behavior were derived. The most popular type of FRFs used in experimental techniques is inertance, which uses the FFT method to return a calculation of amplitude in terms of acceleration beginning from random excitations.

Table 2. Theoretical and experimental frequency values for RC beam model without damage.

Frequency values undamaged RC Beam D0	f_1 [Hz]	$\Delta f_1/f_{1exp}$ [%]	f_2 [Hz]	$\Delta f_2/f_{2exp}$ [%]	f_3 [Hz]	$\Delta f_3/f_{3exp}$ [%]	f_4 [Hz]	$\Delta f_4/f_{4exp}$ [%]
Euler Bernoulli uniform beam	342	-	942	-	1847	-	3052	-
FEM	317	-	817	-	1474	-	2227	-
Experimental average values	323	1.8	835	2.2	1571	6.2	2352	5.3

The experimental program stipulated that the frequency response data file must be re-elaborated in order to determine the quality of the data collected with each measurement. As a result, it was agreed to view the data obtained from the experimentation in the form of the FRFs' dynamic modulus vs. frequency form.

Figure 4 shows the experimental envelope of FRF diagrams with accelerometer vibration measurements for each chosen impact mark point, M_i , for beam model.

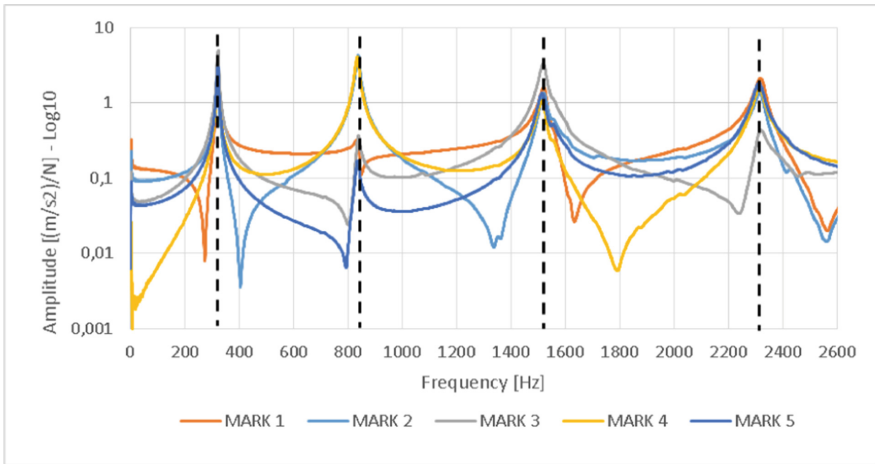


Fig. 4. Experimental envelope of FRF diagrams for undamaged RC beam model for different mark points, M_i $i = 1, \dots, 5$ at damage degree D0.

3.2 Calibration of Experimental Model

The model was calibrated using Finite Element (FE) analysis before extracting the experimental data. The ANSYS code was used for the tridimensional modeling with the aim to analyze the real structure. The mechanical and geometrical properties adopted are

reported in Table 1. The numerical analysis has been developed assuming constraints adopted in the tests. The beam model was hung by four springs having stiffness K_0 , as shown in Fig. 5. The stiffness of springs was selected as updating parameter based on the experimental frequency measurements. Finally, a value of K_0 equal to 1×10^5 N/mm was assumed. The first four values of frequency obtained by FE analysis are presented in Table 2. It is possible to notice that the numerical results are in agreement with experimentation, with variations between 1.8% to 6.2%, in relation to the experimental results.

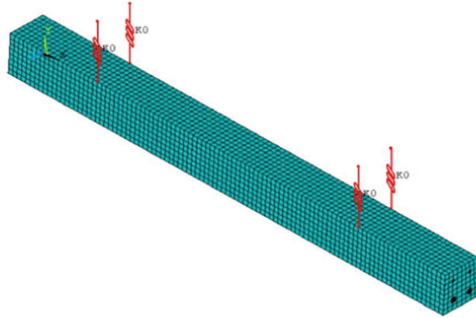


Fig. 5. FE model for intact beam

3.3 Vibration of Damaged RC Beam Models

Notches were drilled into the middle segment of an experimental RC beam, with three damage stage degrees D1, D2, and D3. Damage D1 had a notch width of 5 mm, damage D2 had a notch width of 10 mm, and damage D3 had a notch width of 15 mm.

The experimental FRFs were evaluated at various damage states D_i $i = 1, \dots, 6$ with vibration measurements obtained by accelerometers in various impact points M_i for beam. The average experimental frequency values for undamaged and damaged beams is shown in Table 3 by three different notches on the concrete cover. It is possible to observe the progression of frequency reduction at different steps D_i due to the width of the notch being increased.

Table 3. Experimental average frequency values at damage degree D_i for RC beam model.

Damage degree	f_1 [Hz]	$\Delta f_1/f_{D0}$ [%]	f_2 [Hz]	$\Delta f_2/f_{D0}$ [%]	f_3 [Hz]	$\Delta f_3/f_{D0}$ [%]	f_4 [Hz]	$\Delta f_4/f_{D0}$ [%]
D0	323	-	835	-	1571	-	2352	-
D1	211.72	-34.45	813.08	-2.63	1280.29	-18.50	2241.86	-4.68
D2	187.43	-41.97	797.47	-4.49	1266.66	-19.37	2145.19	-8.79
D3	178.54	-44.72	786.59	-5.80	1261.72	-19.69	2141.76	-8.94

4 Proposed Experimental Work

In this section RBF-NN is provided to estimate the depth and width of notched in RC Beam. After extracting the data, the performance of training is computed as presented in Fig. 6. Four scenarios are considered to test the accuracy of RBF-NN as mentioned in Table 4.

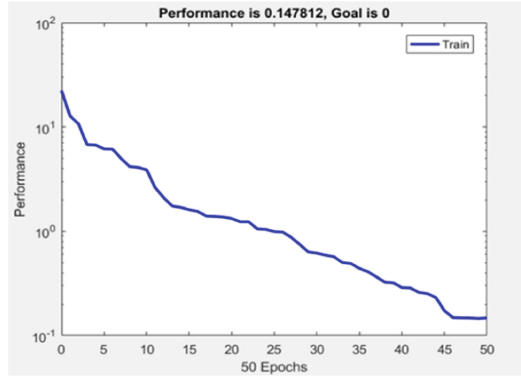


Fig. 6. Training performance using RBF-NN.

Table 4. RBF frequency values at damage degree D_i for RC beam model.

Damage scenario	Depth		Width	
	Exact	Estimated	Exact	Estimated
1	1	0.9975	1	1.0002
2	9	9.0063	7	6.9433
3	3	3.0983	17	16.9382
4	11	11.0055	19	19.1656

Figures 7 and 8 present estimated Depth and width. The provided results showed that RBF-NN can predict both parameters with more accurate.

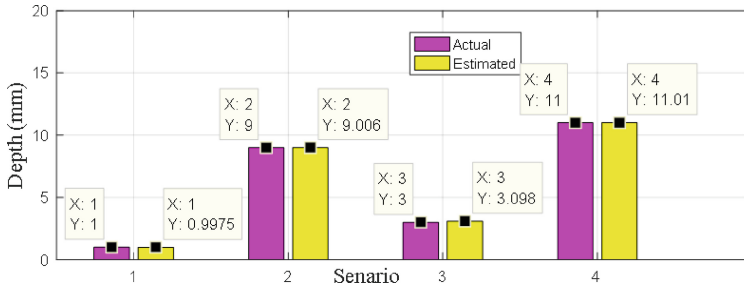


Fig. 7. Estimated notches depth using RBF-NN.

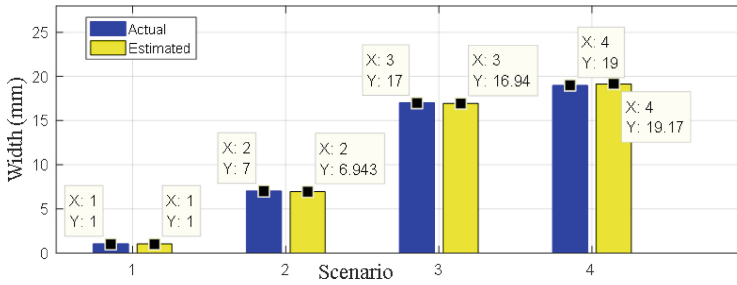


Fig. 8. Estimated notches width using RBF-NN.

5 Conclusion

RBF-NN is used to predict damage identification in RC beam based on the free vibration experiments. Both healthy and damaged cases are performed based on experimental analysis. Different damages degrees concentrated in the middle of the RC beam. The frequency response function (FRF) envelope acquired by the dynamic experimental tests is established, and the changes in normal frequency values are compared with the degree of damage in the models of the RC beams. The action of damaged beams under free vibration is improved by implementing analytical models with equivalent stiffness reduction and identification processes. In order to verify the damage analysis procedure based on vibration testing and the recommended analytical method, a comparison of experimental and analytical results is given as the first stage. In the second stage, the robustness of RBF-NN is provided for different damage scenarios to predict the depth and width of the RC beam. The results showed the RBF-NN can predict the depth and width of RC notches correctly.

References

1. Tsyfansky, S.L., Beresnevich, V.: Non-linear vibration method for detection of fatigue cracks in aircraft wings. *J. Sound Vib.* **236**(1), 49–60 (2000)
2. Dron, J., Bollaers, F.: Improvement of the sensitivity of the scalar indicators (crest factor, kurtosis) using a de-noising method by spectral subtraction: application to the detection of defects in ball bearings. *J. Sound Vib.* **270**(1–2), 61–73 (2004)

3. Trendafilova, I., Cartmell, M.P., Ostachowicz, W.: Vibration-based damage detection in an aircraft wing scaled model using principal component analysis and pattern recognition. *J. Sound Vib.* **313**(3–5), 560–566 (2008)
4. Chance, J., Tomlinson, G.R., Worden, K.: A simplified approach to the numerical and experimental modelling of the dynamics of a cracked beam. In: *Proceedings-SPIE the International Society for Optical Engineering*, p. 778: Citeseer (1994)
5. Polimeno, U., Meo, M.: Detecting barely visible impact damage detection on aircraft composites structures. *Compos. Struct.* **91**(4), 398–402 (2009)
6. Bornn, L., Farrar, C.R., Park, G., Farinholt, K.: Structural health monitoring with autoregressive support vector machines. *J. Vibration Acoustics* **131**(2) (2009)
7. Chong, J.W., Kim, Y., Chon, K.H.: Nonlinear multiclass support vector machine-based health monitoring system for buildings employing magnetorheological dampers. *J. Intell. Mater. Syst. Struct.* **25**(12), 1456–1468 (2014)
8. Khoa, N.L., Zhang, B., Wang, Y., Chen, F., Mustapha, S.: Robust dimensionality reduction and damage detection approaches in structural health monitoring. *Struct. Health Monit.* **13**(4), 406–417 (2014)
9. Kim, Y., Chong, J.W., Chon, K.H., Kim, J.: Wavelet-based AR-SVM for health monitoring of smart structures. *Smart Mater. Struct.* **22**(1), 015003 (2012)
10. Worden, K., Lane, A.: Damage identification using support vector machines. *Smart Mater. Struct.* **10**(3), 540 (2001)
11. Mita, A., Hagiwara, H.: Quantitative damage diagnosis of shear structures using support vector machine. *KSCE J. Civ. Eng.* **7**(6), 683–689 (2003)
12. He, H.X., Yan, W.M.: Structural damage detection with wavelet support vector machine: introduction and applications. *Structural Control and Health Monitoring: The Official Journal of the International Association for Structural Control and Monitoring and of the European Association for the Control of Structures*, vol. 14, no. 1, pp. 162–176 (2007)
13. Arduini, M., Di Tommaso, A., Nanni, A.: Brittle failure in FRP plate and sheet bonded beams. *ACI Struct. J.* **94**(4), 363–370 (1997)
14. Capozucca, R.: Assessment of CFRP strengthened RC beams through dynamic tests. *Compos. B Eng.* **46**, 69–80 (2013)
15. Capozucca, R., Bonci, B.: Notched CFRP laminates under vibration. *Compos. Struct.* **122**, 367–375 (2015)
16. Capozucca, R., Bossoletti, S.: Static and free vibration analysis of RC beams with NSM CFRP rectangular rods. *Compos. B Eng.* **67**, 95–110 (2014)
17. Hassan, N.M., Batra, R.: Modeling damage in polymeric composites. *Compos. B Eng.* **39**(1), 66–82 (2008)
18. Khatir, A., Tehami, M., Khatir, S., Abdel Wahab, M.: Multiple damage detection and localization in beam-like and complex structures using co-ordinate modal assurance criterion combined with firefly and genetic algorithms. *J. Vibroengineering* **18**(8), 5063–5073 (2016)
19. Khatir, S., Belaidi, I., Khatir, T., Hamrani, A., Zhou, Y.-L., Wahab, M.A.: Multiple damage detection in composite beams using Particle Swarm Optimization and Genetic Algorithm. *Mechanics* **23**(4), 514–521 (2017)
20. Khatir, S., Belaidi, I., Serra, R., Wahab, M.A., Khatir, T.: Damage detection and localization in composite beam structures based on vibration analysis. *Mechanics* **21**(6), 472–479 (2015)
21. Khatir, S., Dekemele, K., Loccufer, M., Khatir, T., Wahab, M.A.: Crack identification method in beam-like structures using changes in experimentally measured frequencies and Particle Swarm Optimization. *Comptes Rendus Mécanique* **346**(2), 110–120 (2018)
22. Tran-Ngoc, H., Khatir, S., De Roeck, G., Bui-Tien, T., Wahab, M.A.: An efficient artificial neural network for damage detection in bridges and beam-like structures by improving training parameters using cuckoo search algorithm. *Eng. Struct.* **199**, 109637 (2019)

23. Khatir, A., Capozucca, R., Khatir, S., Magagnini, E.: Vibration-based crack prediction on a beam model using hybrid butterfly optimization algorithm with artificial neural network. *Front. Struct. Civil Eng.* **16**, 1–14 (2022)
24. Chang, W.Y.: Wind energy conversion system power forecasting using radial basis function neural network. In: *Applied Mechanics and Materials*, vol. 284, pp. 1067–1071: Trans Tech Publ (2013)
25. Ya, M.Z., Yu, B.Z., Li, Z.L.: Application of genetic algorithm and RBF neural network in network flow prediction. In: *2010 3rd IEEE International Conference on Computer Science and Information Technology (ICCSIT)*, pp. 298–301 (2010)
26. Yun, Z., Quan, Z., Caixin, S., Shaolan, L., Yuming, L., Yang, S.: RBF neural network and ANFIS-based short-term load forecasting approach in real-time price environment. *IEEE Trans. Power Syst.* **23**(3), 853–858 (2008)
27. Petyt, M.: GB Warburton, *The Dynamical Behaviour of Structures*, Pergamon Press Ltd., Oxford (1976) 008 020 264 7 (H), 0 08 020 363 9 (F), 354+ vi pp.; price£ 12.50, flexicover edition£ 6.25. *J. Sound Vibration* **51**(4), 596–597 (1977)



Experimental Acoustic-Wavelet Method for Damage Detection on Laminated Composite Structures

Morteza Saadatmorad¹, Ramazan-Ali Jafari-Talookolaei¹ (✉),
Mohammad-Hadi Pashaei², and Samir Khatir²

¹ Department of Mechanical Engineering, Babol Noshirvani University of Technology, Babol, Iran

ramazanali@gmail.com

² Soete Laboratory, Ghent University, Ghent, Belgium

Abstract. Since laminated composite structures have many high-speed and lightweight applications, they are subjected to various damages. Thus, damage detection on laminated composite structures is an essential task. In this paper, a novel damage detection method called the Acoustic-wavelet transform (AWT) technique is proposed for damage detection on laminated composite structures. In this way, first, a graphite/epoxy laminated composite plate is constructed using the vacuum infusion processing (VIP) method. Then, several real crack-form and slot-form damage scenarios are considered to evaluate the efficiency of the proposed method for damage detection in real-world applications. One dimensional continuous wavelet transform is applied to detect damages in the measured acoustic signals produced from impacts on laminated composite structures. Findings show that the proposed method is efficient for sound-based crack-form and slot-form damages detection on laminated composite structures. Also, results demonstrate that the proposed AWT technique can detect damaged locations under noisy conditions.

Keywords: Acoustic-wavelet method · Composite structures · Damage detection · Experimental damage detection

1 Introduction

Composite structures, from nano size to macro size, have been vastly employed in many engineering fields such as mechanical engineering, civil engineering, marine engineering, and aerospace engineering because of their unique characteristics like high strength and stiffness, lightweight, and fatigue resistance [1–7]. Laminated composite plates are considered famous composite structures that numerous investigations have been performed about their vibrational responses [8–10].

So far, many studies have been accomplished about damage detection on various structures. In some studies, natural frequencies or frequency responses are used as initial data in damage detection. For example, Zenzen et al. [11] used frequency response and

an optimization technique called particle swarm optimization to detect damages on truss and beam-like structures. One of the most practical frequency-based damage detection methods is the neural network or machine learning algorithms. These algorithms can use the frequencies data of the damaged structures to predict damage location and severity. For example, Tran-Ngoc et al. [12] presented a method of damage detection based on a combination of a hybrid optimization algorithm and artificial neural networks to detect damages on laminated composite structures. The natural frequencies of the first eight modes in the laminated composite plate were selected as the inputs of the neural network, and the location and level of damage were considered as the output of the neural network. Saadatmorad et al. [13] used five natural frequencies as input data of a multilayer perceptron neural network for fixed damages to determine the severity of damages. Saadatmorad et al. [14] used five natural frequencies for feeding an adaptive network-based fuzzy inference system.

Also, many damage detection techniques are based on mode shapes signals. An earlier study on mode shape-based damage detection was conducted by Wahab et al. in 1999 [15]. They used the concept of mode shapes' curvature to detect damages in bridges. Sha et al. [16] studied multiple damage detection of laminated composite beams using data fusion and Teager energy operator-wavelet transform of mode shapes. Gomes et al. [17] developed a two-step damage detection technique based on mode shape's curvature and optimization. Qiao et al. [18] applied mode shape's curvature for damage detection of composite laminated plates.

In addition to the above damage detection techniques, some of them are based on waves and acoustic waves. For instance, Klepka et al. [19] used the impact damage detection method for detecting damages in laminated composites using non-linear Vibro-acoustic wave modulations. Kumar et al. [20] investigated damage detection on composite materials based on the Lamb Wave method. James et al. [21] applied impact-based damage detection on composite plates. In this way, acoustic emission signal signature identification was used for damage detection. Muszkats et al. [22] investigated damage detection of brittle materials based on wavelet transform and entropy evaluation of acoustic emission signals.

In this paper, a novel method called the acoustic-wavelet-based damage detection technique is proposed for detecting defects on laminated composite structures. The effect of types of damages, severity of damages, existence of single or multiple damages, and direction of applying impacts on the efficiency of the proposed technique are evaluated. The rest of this paper is organized as follows. Section 2 deals with the theory of the one-dimensional continuous wavelet transform. In Sect. 3, the proposed technique is introduced. Experimental tests and results are presented in Sect. 4, where five different experimental damage detection scenarios are considered to evaluate our proposed technique's effectiveness and efficiency. Finally, the paper concludes in Sect. 5.

2 One Dimensional Continuous Wavelet Transforms

Wavelet transforms as efficient tools have been used for various structures' damage detection. In terms of dimension, wavelet analyses can be divided into three main classes: one-dimensional, two-dimensional, and three-dimensional wavelet analyses. Based on

the dimension of the processing signal, the dimension of wavelet transform is selected. In the current study, the one-dimensional wavelet analyzes the acoustic signals resulting from impacts. On the other hand, the continuity or discontinuity of wavelet analysis can be divided into two main classes: continuous wavelet analysis and discrete wavelet analysis. This work uses continuous wavelet analysis to analyze the acoustic signals resulting from impacts on laminated composite structures.

Assume the one-dimensional signal $A(t)$ having a subtle discontinuity or damage. In order to identify this discontinuity, it is required to transform its values into another coordinate system using a wavelet function called $\psi(t)$. The following expression indicates a family of wavelets [23]:

$$\psi(t)_{u,s} = \frac{1}{\sqrt{s}} \psi\left(\frac{t-u}{s}\right) \quad (1)$$

where t shows the spatial variable related to the signal $A(t)$, u is shifting factor, and s is scaling factor. Note that the mean value of the wavelet function has to be zero. By using the inner product on the wavelet function $\psi(t)_{u,s}$ by the signal $A(t)$, wavelet coefficients $WCoeff(u, s)$ can be calculated as follows [24]:

$$WCoeff(u, s) = \langle A_{ex}, \psi(t)_{u,s} \rangle = \frac{1}{\sqrt{s}} \int_{-\infty}^{+\infty} A_{ex}(t) \psi\left(\frac{t-u}{s}\right) dt \quad (2)$$

The primary aim of wavelet coefficients is to exaggerate subtle changes in the domain u through scales s . Wavelet coefficients are calculated in the form of convolution product:

$$C(u, s) = \langle A_{ex}, \psi(x)_{u,s} \rangle = \frac{1}{\sqrt{s}} A_{ex} * \psi\left(\frac{-u}{s}\right) \quad (3)$$

Note that the precision of results obtained from the wavelet coefficients is severely related to the vanishing moments. A wavelet function with n vanishing moments satisfies the following relation [25]:

$$\int_{-\infty}^{+\infty} t^k \psi(t) dt = 0, k = 0, 1, 2, \dots, n-1 \quad (4)$$

By re-writing (4) in terms of n th order derivation of the smooth function $\theta_s(t) = \frac{1}{\sqrt{s}} \theta\left(\frac{-t}{s}\right)$ proposed by Mallat [26], the following equation is expressed:

$$\begin{aligned} C(u, s) &= \frac{s^n}{\sqrt{s}} \int_{-\infty}^{+\infty} A_{ex}(t) \frac{d^n}{dt^n} \theta\left(\frac{-(u-t)}{s}\right) dt \\ &= \frac{s^n}{\sqrt{s}} \frac{d^n}{du^n} A_{ex} * \theta\left(\frac{-u}{s}\right) = s^n \frac{d^n}{du^n} (A_{ex} * \theta_s)(u) \end{aligned} \quad (5)$$

Wavelets are expressed by the scaling functions $\varphi(t)$ (i.e., the father wavelets) and the wavelet functions $\psi(t)$ (i.e., the wavelet functions) in the time domain. In this study, Daubechies wavelets developed by Ingrid Daubechies are used to process acoustic signals. The equations for $n = 1$, $n = 2$, $n = 3$, and $n = 10$ are expressed with (6)–(9),

respectively. Also, Figs. 1, 2, 3 and 4 show the scaling functions and the wavelet functions for $n = 1$, $n = 2$, $n = 3$, and $n = 10$, respectively.

$$\int_{-\infty}^{+\infty} t^k \psi(t) dt = 0, k = 0 \tag{6}$$

$$\begin{aligned} (u, s) &= \frac{s^1}{\sqrt{s}} \int_{-\infty}^{+\infty} A_{ex}(t) \frac{d^1}{dt^1} \theta\left(\frac{-(u-t)}{s}\right) dt \\ &= \frac{s^1}{\sqrt{s}} \frac{d^1}{du^1} A_{ex} * \theta\left(\frac{-u}{s}\right) = s^1 \frac{d^1}{du^1} (A_{ex} * \theta_s)(u) \end{aligned}$$

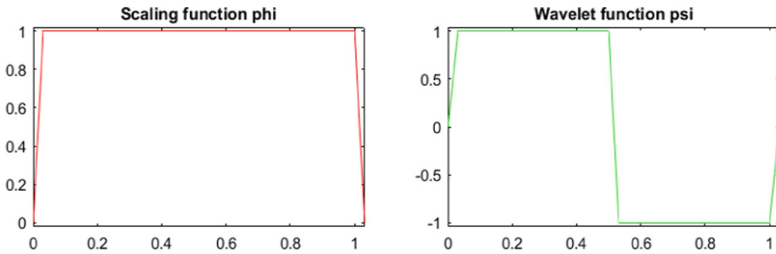


Fig. 1. The scaling function and the wavelet function for $n = 1$ (db1)

$$\begin{aligned} WCoeff(u, s) &= \langle A_{ex}, \psi(t)_{u,s} \rangle = \frac{1}{\sqrt{s}} \int_{-\infty}^{+\infty} A_{ex}(t) \psi\left(\frac{t-u}{s}\right) dt \\ &\int_{-\infty}^{+\infty} t^k \psi(t) dt = 0, k = 0, 1 \\ C(u, s) &= \frac{s^2}{\sqrt{s}} \int_{-\infty}^{+\infty} A_{ex}(t) \frac{d^2}{dt^2} \theta\left(\frac{-(u-t)}{s}\right) dt \\ &= \frac{s^2}{\sqrt{s}} \frac{d^2}{du^2} A_{ex} * \theta\left(\frac{-u}{s}\right) = s^2 \frac{d^2}{du^2} (A_{ex} * \theta_s)(u) \end{aligned} \tag{7}$$

$$\begin{aligned} WCoeff(u, s) &= \langle A_{ex}, \psi(t)_{u,s} \rangle = \frac{1}{\sqrt{s}} \int_{-\infty}^{+\infty} A_{ex}(t) \psi\left(\frac{t-u}{s}\right) dt \\ &\int_{-\infty}^{+\infty} t^k \psi(t) dt = 0, k = 0, 1, 2 \\ C(u, s) &= \frac{s^3}{\sqrt{s}} \int_{-\infty}^{+\infty} A_{ex}(t) \frac{d^3}{dt^3} \theta\left(\frac{-(u-t)}{s}\right) dt \\ &= \frac{s^3}{\sqrt{s}} \frac{d^3}{du^3} A_{ex} * \theta\left(\frac{-u}{s}\right) \\ &= s^3 \frac{d^3}{du^3} (A_{ex} * \theta_s)(u) \end{aligned} \tag{8}$$

$$\begin{aligned}
 WCoeff(u, s) &= \langle A_{ex}, \psi(t)_{u,s} \rangle \\
 &= \frac{1}{\sqrt{s}} \int_{-\infty}^{+\infty} A_{ex}(t) \psi\left(\frac{t-u}{s}\right) dt \\
 \int_{-\infty}^{+\infty} t^k \psi(t) dt &= 0, k = 0, 1, 2, \dots, 9 \\
 C(u, s) &= \frac{s^{10}}{\sqrt{s}} \int_{-\infty}^{+\infty} A_{ex}(t) \frac{d^{10}}{dt^{10}} \theta\left(\frac{-(u-t)}{s}\right) dt \\
 &= \frac{s^{10}}{\sqrt{10}} \frac{d^{10}}{du^{10}} A_{ex} * \theta\left(\frac{-u}{s}\right) \\
 &= s^{10} \frac{d^{10}}{du^{10}} (A_{ex} * \theta_s)(u)
 \end{aligned} \tag{9}$$

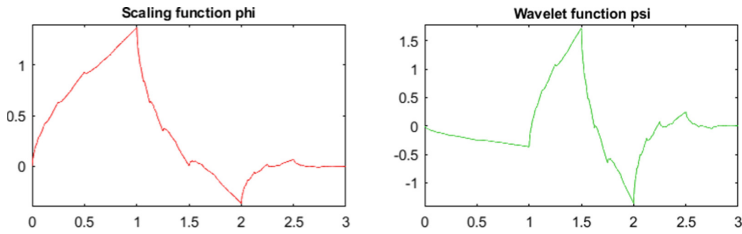


Fig. 2. The scaling function and the wavelet function for $n = 2$ (db2)

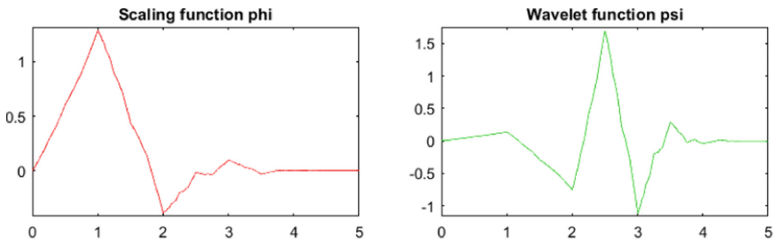


Fig. 3. The scaling function and the wavelet function for $n = 3$ (db3)

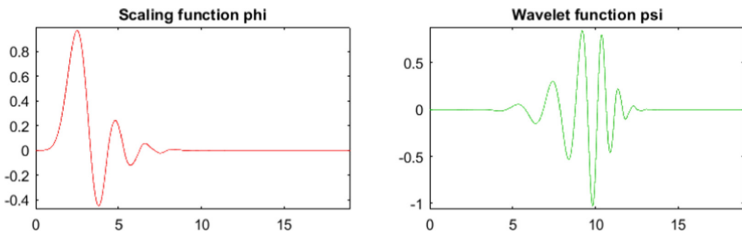


Fig. 4. The scaling function and the wavelet function for $n = 10$ (db10)

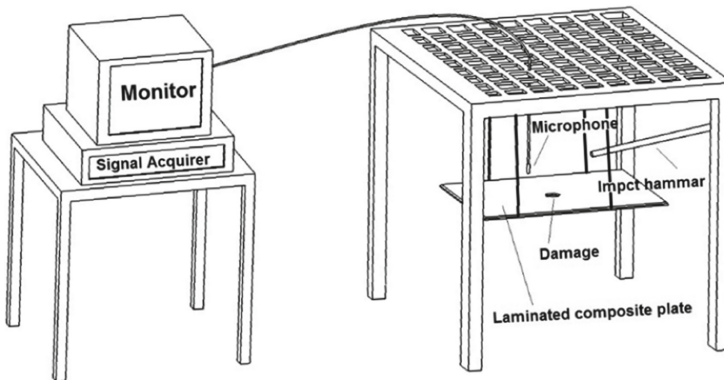
Table 1 shows the general characteristics of the Daubechies wavelet family.

Table 1. General characteristics of the Daubechies wavelet family [27]

Family	Daubechies
Short name	db
Order n	n is a positive integer from 1 to 45
Examples	db1, db3, db10
Bi-orthogonal	Yes
Compact support	Yes
Orthogonal	Yes
DWT	Possible
CWT	Possible
Number of vanishing moments	n
Support width	$2n - 1$
Filters length	$2n$
Symmetry	Far from

3 Proposed Technique

In this research, a new method called the acoustic-wavelet transform (AWT) technique is proposed by combining impact-based acoustic signals and one-dimensional continuous wavelet transform. Figure 5 shows a schematic of the experimental setup in the current study. As seen in Fig. 5, the damaged composite structure is exposed to impact by the impact hammer to produce an acoustic wave. Then, the produced acoustic waves or sounds are converted into electrical signals. Then, electrical signals are processed in Matlab software through the one-dimensional continuous wavelet transform.

**Fig. 5.** Schematic of the experimental setup in the present study

This paper investigates laminated composite plates to evaluate the proposed methodology's effectiveness. The rectangular laminated composite plate creates single and multiple crack-form and slot-form damages. Similar impacts (in terms of their severity) are applied to given structure points. Based on the dimension of the studied structure, in this study, similar impacts are applied on five different locations (five different points) of the structure. A suitable structure health monitoring is performed by having five impact points for the current structure's dimension.

4 Experimental Tests and Results

This section presents experimental tests and results to examine our proposed AWT damage detection method. At the first step, a graphite/epoxy laminated composite plate is constructed using the vacuum infusion processing (VIP) method in the following section.

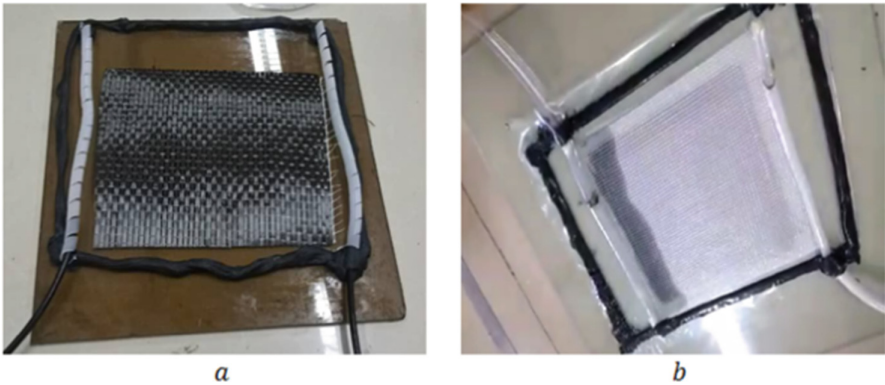


Fig. 6. The rectangular graphite/epoxy composite's construction process using VIP method: a) deploying graphite fibers, b) flowing the mixture of resin and hardener through fibers by vacuuming.

VIP is a method that uses vacuum pressure to insert a resin into the mold. In this way, dry fibers (Fig. 6a) are placed inside the mold with a sealed vacuum bag and the vacuum is applied to the bag. The resin is drawn into the mold through a duct when a complete vacuum is created. This method is used to make large-scale composite parts with high quality and low production volume, and where high strength and low weight are necessary.

After constructing the rectangular graphite/epoxy composite plate, various damage scenarios are considered in the experimental tests and results section. Figure 7 indicates the arrangement of the rectangular laminated composite plate, microphone, impact hammer, and boundary conditions for the current study.



Fig. 7. Deploying the rectangular laminated composite plate, microphone, impact hammer, and boundary conditions.

4.1 Scenario 1

In Scenario 1, single circular-shape damage is applied on the rectangular laminated composite plate. As shown in Fig. 8, five points (i.e., 1, 2, 3, 4, and 5) are specified as impact locations on the rectangular laminated composite plate. Impacts are applied in these points, respectively. The microphone receives the acoustic signals, converts them into electrical signals, and sends them to the computer processing unit.

Figure 5 shows the acoustic signal obtained from the experiment for Scenario 1. There are five predominant peaks in this signal corresponding to five impact points. Also, there is a local peak when the time is equal to 8. It exists because of creating chaos after applying impact. As shown in Fig. 9, it is impossible to identify the obtained damaged peak through observing the acoustic signal. However, using our proposed AWT method, the location of the damaged peak is detected by high accuracy, as seen in Fig. 10.

4.2 Scenario 2

In Scenario 2, single circular-shape damage is applied on the rectangular laminated composite plate. As shown in Fig. 11, seven points (i.e., 1, 2, 3, 4, 5, 6, and 7) are specified as impact locations on the rectangular laminated composite plate. Impacts are applied in these points, respectively. In this scenario, the direction of impact points is diagonal to investigate the effect of the direction of impacts on the accuracy of the results obtained from our proposed AWT method. The microphone receives the acoustic signals, converts them into electrical signals, and sends them to the computer processing unit.



Fig. 8. Five points specified on the rectangular laminated composite plate as impact locations for Scenario 1.

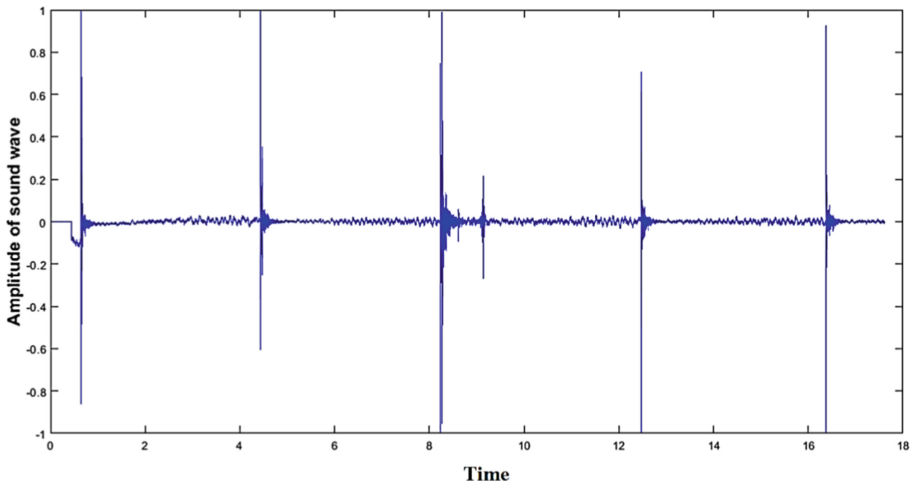


Fig. 9. Acoustic signal obtained from the experiment for Scenario 1

Figure 12 indicates the acoustic signal obtained from the experiment for Scenario 2. As seen in Fig. 13, it is impossible to detect the damaged peak by observing the acquired acoustic signal. Nevertheless, utilizing our proposed AWT technique, the location of the damaged peak is detected by high accuracy, as seen in Fig. 14.

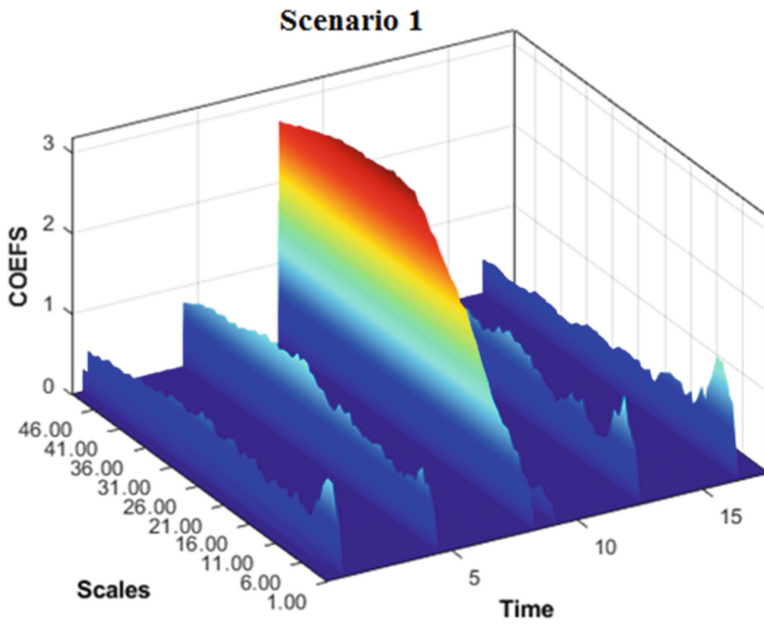


Fig. 10. Result of our AWT proposed method for Scenario 1

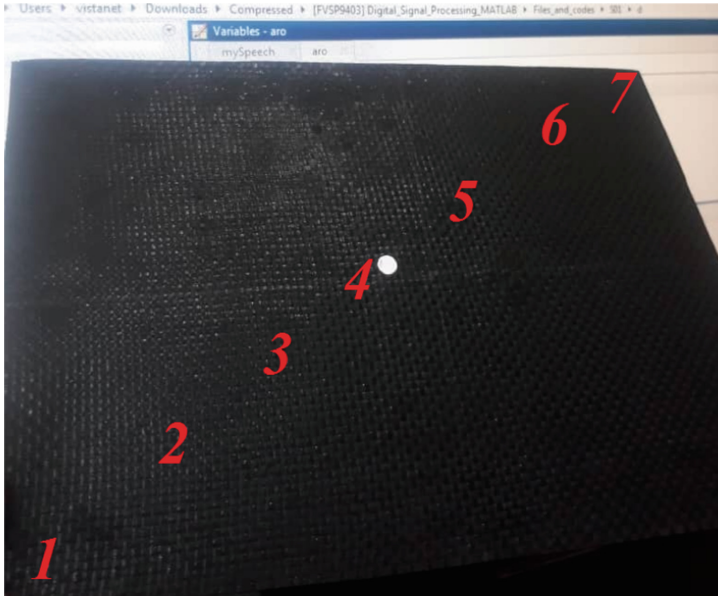


Fig. 11. Seven points specified on the rectangular laminated composite plate as impact locations for Scenario 2.

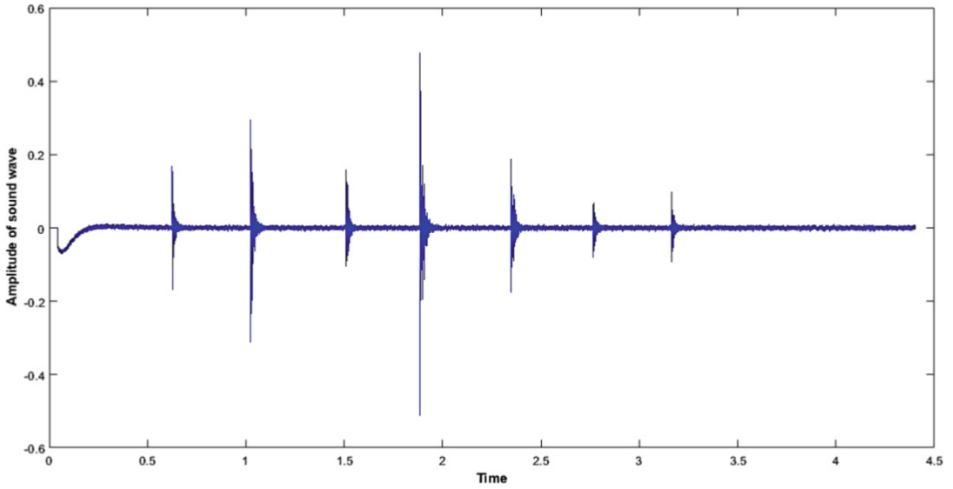


Fig. 12. Acoustic signal obtained from the experiment for Scenario 2

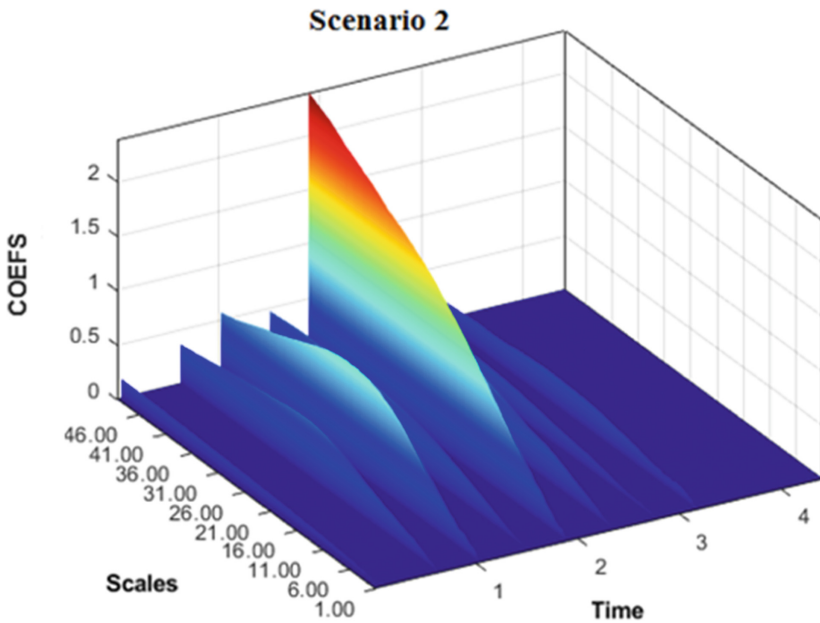


Fig. 13. Result of the AWT proposed method for Scenario 2.

4.3 Scenario 3

Scenario 3 is a multiple damages scenario applied on the rectangular laminated composite plate since our structure has two damages. The first damage is circular damage on the rectangular laminated composite plate, and the second is crack-shape damage, as seen in

Fig. 14. This scenario is tested to evaluate the effect of types of damages on the efficiency of damage detection by our proposed AWT method.

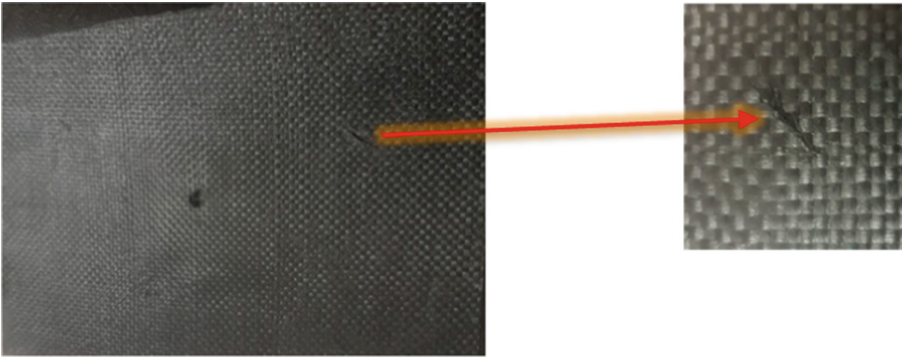


Fig. 14. Multiple damages applied on the rectangular laminated composite plate for scenario 3.

As indicated in Fig. 15, six points (i.e., 1, 2, 3, 4, 5, and 6) are determined as impact locations on the rectangular laminated composite plate. Impacts are imposed in these points, respectively. In this scenario, the direction of impact points is diagonal.

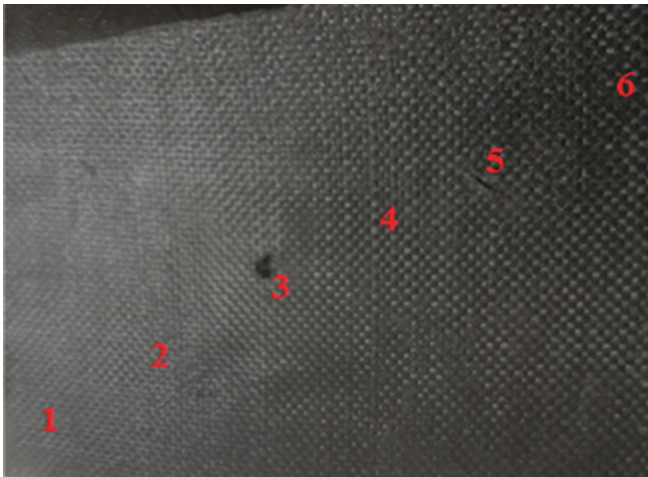


Fig. 15. Six points on the rectangular laminated composite plate as impact locations for Scenario 3.

Figure 16 indicates the acoustic signal obtained from the experiment for Scenario 3. As seen in Fig. 16, it is apparent that it is impossible to detect the damaged peak by observing the acquired acoustic signal. Nevertheless, utilizing our proposed AWT technique, the location of the damaged peak is detected by high accuracy, as seen in Fig. 17. It is seen that the proposed AWT method can detect slight damages with reasonable accuracy.

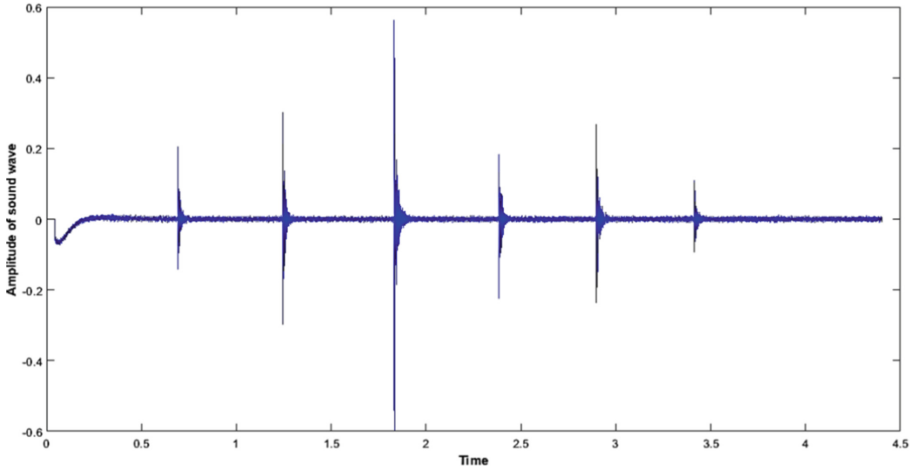


Fig. 16. Acoustic signal obtained from the experiment for Scenario 3

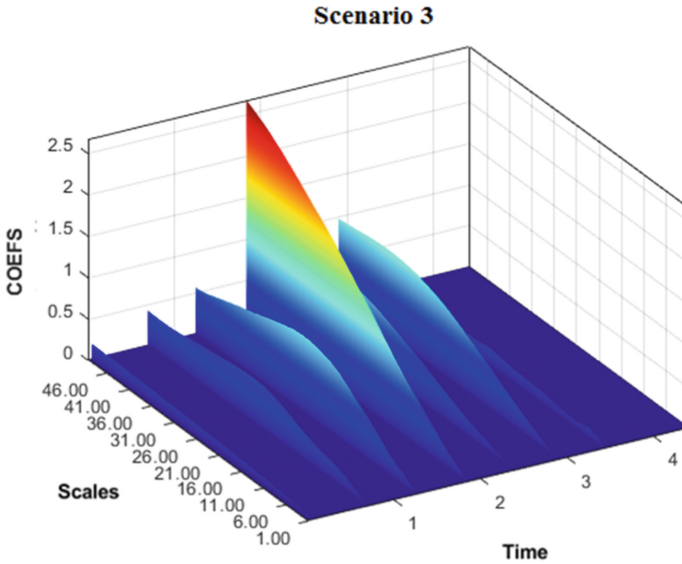


Fig. 17. Result of our AWT proposed method for Scenario 3.

4.4 Scenario 4

Scenario 4 is a multiple damages scenario applied on the rectangular laminated composite plate since our structure has two damages. The first damage is circular damage on the rectangular laminated composite plate, and the second is crack-shape damage, as seen in Fig. 18. However, the size of the crack-shape damage has been increased compared with scenario 3. This scenario is tested to evaluate the effect of the size of damages on the efficiency of damage detection by our proposed AWT method.

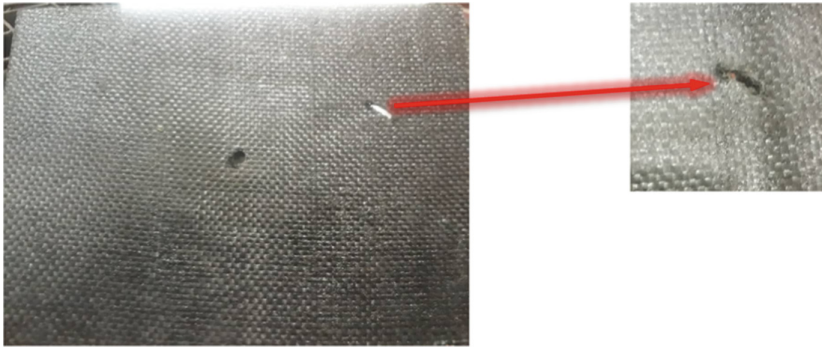


Fig. 18. Multiple damages applied on the rectangular laminated composite plate for scenario 4.

As shown in Fig. 19, five points (i.e., 1, 2, 3, 4, and 5) are specified as impact locations on the rectangular laminated composite plate. Impacts are imposed in these points, respectively. In this scenario, the direction of impact points is diagonal.



Fig. 19. Five points specified on the rectangular laminated composite plate as impact locations for Scenario 4.

Figure 20 shows the acoustic signal obtained from the experiment for Scenario 4.

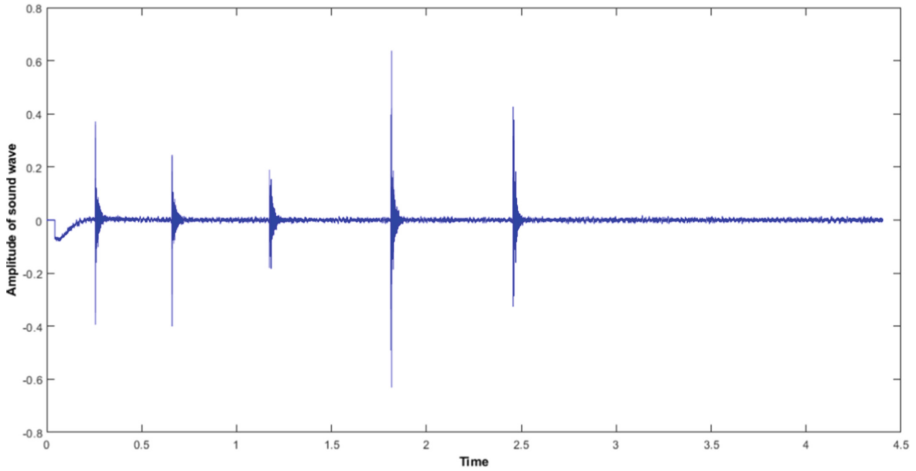


Fig. 20. Acoustic signal obtained from the experiment for Scenario 4.

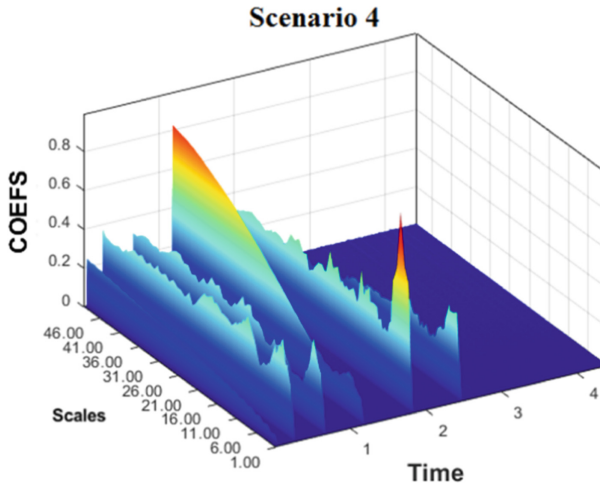


Fig. 21. Result of our AWT proposed method for Scenario 4.

As seen in Fig. 21, two highly-accurate damages are detected using our proposed AWT method. Also, it is seen that as the size of damage increases, the accuracy of damage detection increases. Also, by comparing Figs. 20 and 21 and considering the results of prior scenarios, this scenario shows no relation between the amplitude of sound waves and the location of the damage. The reason is that the wavelet transform is sensitive to local singularities in acoustic signals. The existence of damages creates these local singularities or discontinuities in or sound signals.

In order to assess the performance of the proposed for showing results of wavelet coefficient as two-dimensional, the results of scenario 4 are used as seen in Fig. 22. It is demonstrated that the proposed AWT has very high accuracy as a two-dimensional plot.

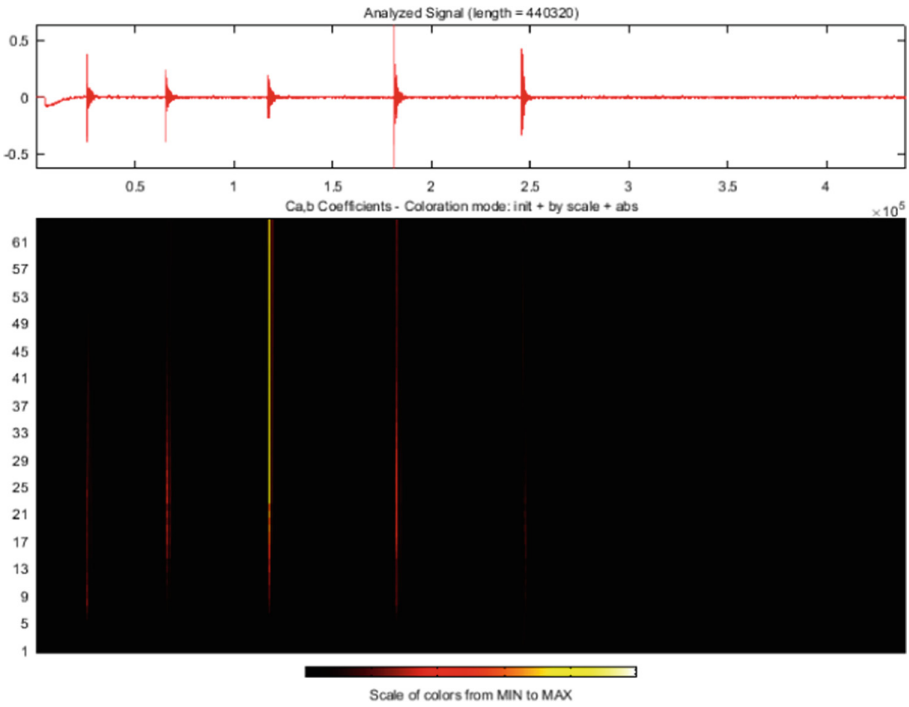


Fig. 22. Results of damage detection by proposed AWT in two dimensions for scenario 4.

4.5 Effect of Noise

In this section, the effect of noises on the performance of the proposed methodology for damage detection is investigated. First of all, the signals obtained from the noisy and noise-free conditions are compared to check the accuracy of the obtained signals using our signal acquisition operation. Figure 23 shows the signal obtained from laboratory's environment under noise-free conditions. As seen in this figure, the maximum variation in amplitude of sound signal is 0.04. Figure 24 shows the laboratory's environment's signal under noisy conditions. This figure shows that the maximum variation in sound signal amplitude is 1, indicating a signal disturbance significantly greater (about 25 times) than the noise-free condition. Therefore, this study applies this condition for damage detection under noisy conditions.

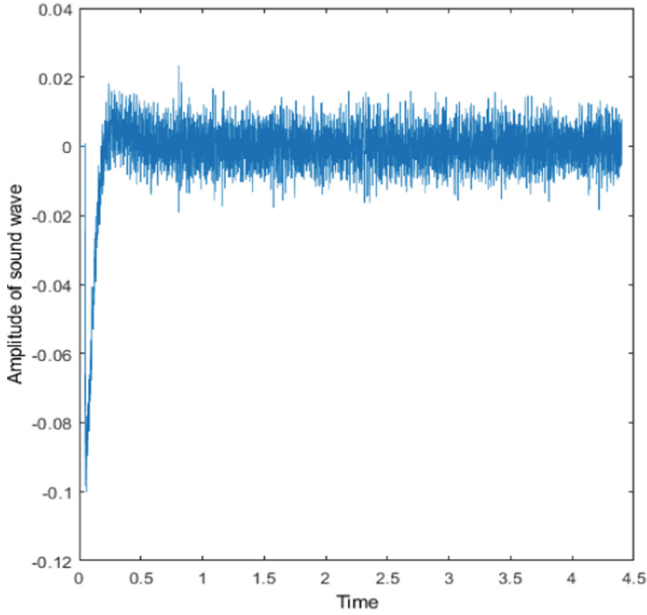


Fig. 23. The signal obtained from laboratory's environment under noise-free conditions.

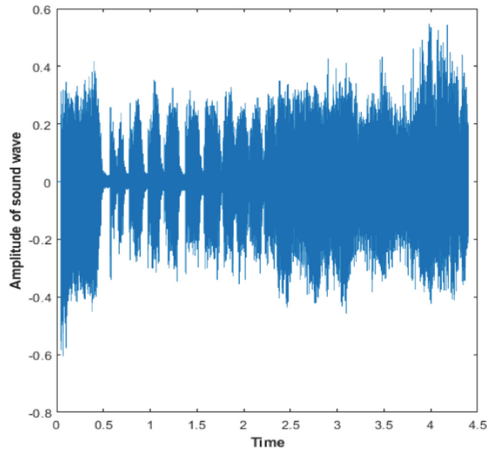


Fig. 24. The signal obtained from laboratory's environment under the noisy conditions.

For testing the performance of the proposed AWT damage detection method under the noisy conditions, six points on the rectangular laminated composite plate as impact locations, as seen in Fig. 25.

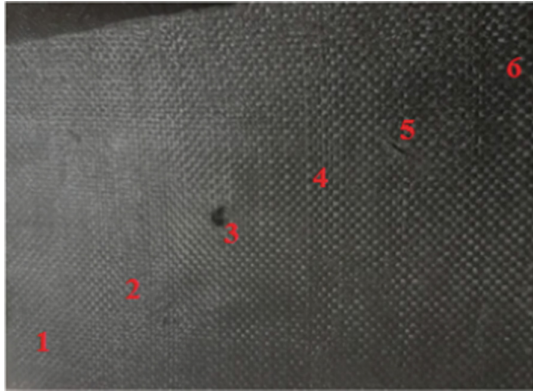


Fig. 25. Six points on the rectangular laminated composite plate as impact locations for the noisy conditions.

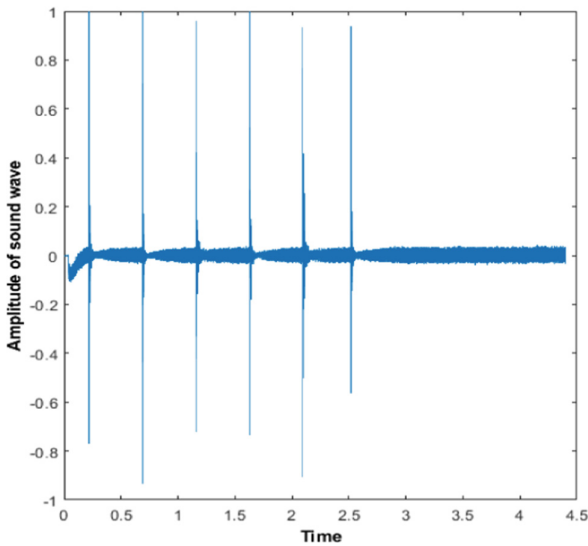


Fig. 26. Acoustic signal obtained from the experiment for the noisy conditions.

As seen in Fig. 26, the acoustic signal obtained from the experiment for the noisy conditions includes many noises compared with the previous four signals. Also, according to Fig. 27, the proposed AWT method can detect damaged locations with high accuracy even under noisy conditions.

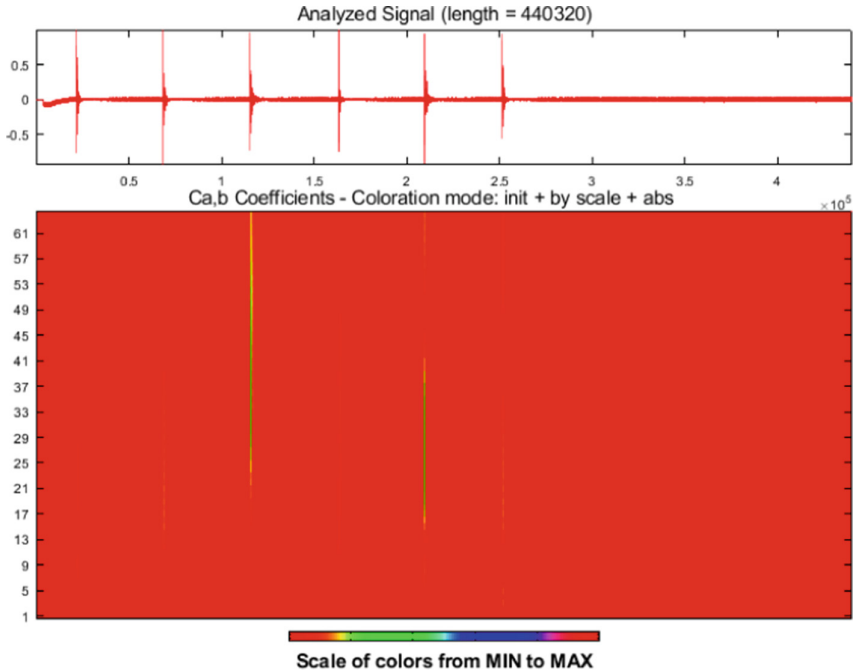


Fig. 27. Result of the proposed AWT method for the noisy conditions.

5 Conclusions

This paper introduces a novel, and efficient damage detection method called the Acoustic-wavelet transform (AWT) for damage detection on structures. The studied structure is a rectangular laminated composite plate of graphite-epoxy and constructed using the vacuum infusion processing (VIP) method. Concluding remarks of the present study are summarized as follows:

- The proposed Acoustic-wavelet transform (AWT) is a high-accuracy damage detection method.
- The AWT has high performance in all the considered damage scenarios.
- It is impossible to detect the damages from observing the peaks of the acquired acoustic signal.
- Nevertheless, utilizing the proposed AWT technique, the location of the damaged peak is detected with high accuracy.
- There is no relation between the amplitude of sound waves and the location of the damage.
- The AWT is sensitive to local singularities in acoustic signals; as a result, it detects damages with high precision.
- As the size of damage increases, the accuracy of damage detection increases.
- The proposed AWT has very high accuracy as the two-dimensional wavelet coefficient views.

Acknowledgement. The first three authors acknowledge the funding support of Babol Noshirvani University of Technology through Grant program No. BNUT/965919012/99.

References

1. Wang, W.Z., Wang, D.Z., Mottershead, J.E., Lampeas, G.: Identification of composite delamination using the krawtchouk moment descriptor. In: *Key Engineering Materials*, vol. 569, pp. 33–40. Trans Tech Publications Ltd. (2013)
2. Mofidian, R., Barati, A., Jahanshahi, M., Shahavi, M.H.: Fabrication of novel agarose–nickel bilayer composite for purification of protein nanoparticles in expanded bed adsorption column. *Chem. Eng. Res. Des.* **159**, 291–299 (2020)
3. Shahavi, M.H., Selakjani, P.P., Abatari, M.N., Antov, P., Savov, V.: Novel biodegradable poly (lactic acid)/wood leachate composites: investigation of antibacterial, mechanical, morphological, and thermal properties. *Polymers* **14**(6), 1227 (2022)
4. Khalili, M., Razmjou, A., Shafiei, R., Shahavi, M.H., Li, M.C., Orooji, Y.: High durability of food due to the flow cytometry proved antibacterial and antifouling properties of TiO₂ decorated nanocomposite films. *Food Chem. Toxicol.* **168**, 113291 (2022)
5. Dorieh, A., Selakjani, P.P., Shahavi, M.H., Pizzi, A., Movahed, S.G., Pour, M.F., Aghaei, R.: Recent developments in the performance of micro/nanoparticle-modified urea-formaldehyde resins used as wood-based composite binders: a review. *Int. J. Adhesion Adhesives* **114**, 103106 (2022)
6. Kargarnovin, M.H., Ahmadian, M.T., Jafari-Talookolaei, R.A., Abedi, M.: Semi-analytical solution for the free vibration analysis of generally laminated composite Timoshenko beams with single delamination. *Compos. Part B Eng.* **45**(1), 587–600 (2013)
7. Pour, M.F., Edalat, H., Dorieh, A., Kiamahalleh, M.V., Shahavi, M.H.: Durability-related performance of reinforced bondline by phenol formaldehyde/nano SiO₂ composite in Laminated Veneer Lumber (LVL). *Journal of Building Engineering*, 105191 (2022)
8. Zenzen, R., Khatir, S., Belaidi, I., Le Thanh, C., Wahab, M.A.: A modified transmissibility indicator and Artificial Neural Network for damage identification and quantification in laminated composite structures. *Compos. Struct.* **248**, 112497 (2020)
9. Thai, C.H., Ferreira, A.J.M., Wahab, M.A., Nguyen-Xuan, H.: A generalized layerwise higher-order shear deformation theory for laminated composite and sandwich plates based on isogeometric analysis. *Acta Mechanica* **227**(5), 1225–1250 (2016)
10. Saenz-Castillo, D., Martín, M. I., Calvo, S., Güemes, A.: Real-time monitoring of thermal history of thermoplastic automatic lamination with FBG sensors and process modelling validation. *Smart Mater. Struct.* **29**(11), 115004 (2020)
11. Zenzen, R., Khatir, S., Belaidi, I., Wahab, M.A.: Structural health monitoring of beam-like and truss structures using frequency response and particle swarm optimization. In: *Numerical Modelling in Engineering*, pp. 390–399. Springer, Singapore, August 2018
12. Tran-Ngoc, H., Khatir, S., Ho-Khac, H., De Roeck, G., Bui-Tien, T., Wahab, M.A.: Efficient Artificial neural networks based on a hybrid metaheuristic optimization algorithm for damage detection in laminated composite structures. *Compos. Struct.* **262**, 113339 (2021)
13. Saadatmorad, M., Jafari-Talookolaei, R.A., Pashaei, M.H., Khatir, S., Abdel Wahab, M.: Application of multilayer perceptron neural network for damage detection in rectangular laminated composite plates based on vibrational analysis. In: *Proceedings of the 2nd International Conference on Structural Damage Modelling and Assessment*, pp. 163–178. Springer, Singapore (2022)

14. Saadatmorad, M., Jafari-Talookolaei, R.A., Pashaei, M.H., Khatir, S., Abdel Wahab, M.: Adaptive network-based fuzzy inference for damage detection in rectangular laminated composite plates using vibrational data. In: Proceedings of the 2nd International Conference on Structural Damage Modelling and Assessment, pp. 179–196. Springer, Singapore (2022)
15. Wahab, M.A., De Roeck, G.: Damage detection in bridges using modal curvatures: application to a real damage scenario. *J. Sound Vib.* **226**(2), 217–235 (1999)
16. Sha, G., Radzienski, M., Soman, R., Cao, M., Ostachowicz, W., Xu, W.: Multiple damage detection in laminated composite beams by data fusion of Teager energy operator-wavelet transform mode shapes. *Compos. Struct.* **235**, 111798 (2020)
17. Gomes, G.F., Giovani, R.S.: An efficient two-step damage identification method using sunflower optimization algorithm and mode shape curvature (MSDBI-SFO). *Eng. Comput.* **38**(2), 1711–1730 (2020). <https://doi.org/10.1007/s00366-020-01128-2>
18. Qiao, P., Lu, K., Lestari, W., Wang, J.: Curvature mode shape-based damage detection in composite laminated plates. *Compos. Struct.* **80**(3), 409–428 (2007)
19. Klepka, A., Pieczonka, L., Staszewski, W.J., Aymerich, F.: Impact damage detection in laminated composites by non-linear vibro-acoustic wave modulations. *Compos. B Eng.* **65**, 99–108 (2014)
20. Kumar, S.N., Srikanth, K., Subbaratnam, B., Jena, S.P.: Damage detection in composite materials using lamb wave method. In: IOP Conference Series: Materials Science and Engineering, vol. 998, No. 1, p. 012066. IOP Publishing, December 2020
21. James, R., Joseph, R., Giurgiutiu, V.: Impact damage detection in composite plates using acoustic emission signal signature identification. In: Active and Passive Smart Structures and Integrated Systems XIV, vol. 11376, p. 113760K. International Society for Optics and Photonics, May 2020
22. Muszkats, J.P., Zitto, M.E., Sassano, M., Piotrkowski, R.: Application of wavelet transform to damage detection in brittle materials via energy and entropy evaluation of acoustic emission signals. In: Muszkats, J.P., Seminara, S.A., Troparevsky, M.I. (eds.) Applications of Wavelet Multiresolution Analysis. SSSS, vol. 4, pp. 75–88. Springer, Cham (2021). https://doi.org/10.1007/978-3-030-61713-4_5
23. Yunhui, S., Qiuqi, R.: Continuous wavelet transforms. In: Proceedings 7th International Conference on Signal Processing, 2004. Proceedings. ICSP 2004, vol. 1, pp. 207–210. IEEE, August 2004
24. Rucka, M., Wilde, K.: Application of continuous wavelet transform in vibration based damage detection method for beams and plates. *J. Sound Vib.* **297**(3–5), 536–550 (2006)
25. Saadatmorad, M., Jafari-Talookolaei, R.A., Pashaei, M.H., Khatir, S.: Damage detection on rectangular laminated composite plates using wavelet based convolutional neural network technique. *Compos. Struct.* **278**, 114656 (2021)
26. Mallat, S., Hwang, W.L.: Singularity detection and processing with wavelets. *IEEE Trans. Inf. Theory* **38**(2), 617–643 (1992)
27. Daubechies, I.: Ten lectures on wavelets. Society for industrial and applied mathematics (1992)



Damage Identification in Thin Steel Beams Containing a Horizontal Crack Using the Artificial Neural Networks

Amirhossein Heshmati¹, Morteza Saadatmorad¹, Ramazan-Ali Jafari Talookolaei¹(✉), Paolo S. Valvo², and Samir Khatir³

¹ School of Mechanical Engineering, Babol Noshirvani University of Technology, Babol, Mazandaran, Iran

ramazanali@gmail.com, ra.jafari@nit.ac.ir

² Department of Civil and Industrial Engineering, University of Pisa, Pisa, Italy

³ Ho Chi Minh City Open University, Ho Chi Minh City, Vietnam

Abstract. This investigation presents damage identification in thin steel beams containing a horizontal crack using artificial neural networks. In this way, finite element modeling of the cracked beam is developed to generate natural frequencies corresponding to various horizontal cracks scenarios. Then, the artificial neural network is used to create a predictor model for localizing horizontal cracks in steel beams. Results of the current paper show that The proposed technique is an effective method for detecting horizontal crack damage in steel beams. The regression index obtained in this study is equal to 0.979.

Keywords: Structural health monitoring · Damage identification · Artificial neural networks · Steel beams · Horizontal cracks

1 Introduction

Structural analysis and structural health monitoring are two essential issues in structural engineering from nano size to macro size [1–10]. The objective of structural health monitoring is to prevent the failure of structures [11–14]. As a result, structural health monitoring prevents additional costs for repairing and reconstruction of damaged structures [15–17]. In this regard, vibration-based analysis of damaged structures plays an essential role in structural health monitoring [18–22]. Generally, there are two main types of analysis of damaged structures: Forward analysis and inverse analysis [23–28].

The forward analysis deals with modeling damages to provide modal characteristics of structures such as mode shapes and their corresponding natural frequencies [29–32]. Also, the forward analysis may use to obtain dynamic responses of the damaged structures [33–36]. In this field, much research has been conducted.

In reverse analysis, on the other hand, the goal is to obtain the position or extent of the damage by having the vibrational properties of the system. So far, much research has been done in this area. Some of these approaches are based on optimization, a part of them are based on the mode shapes, the others are based on machine learning

algorithms. In this research, one of the machine learning algorithms called the artificial neural network algorithm is used to detect horizontal cracks in steel beams, including a vertical crack. In this way, first, the modeling of finite components of horizontal cracks in steel beams is described in the next section. Then the artificial neural network is introduced, the technique proposed in this paper, and then numerical examples and results are presented, and finally, conclusions are presented.

2 Basic Mathematical Formulations

2.1 Geometry

In order to investigate the damage identification problem, a thin isotropic beam of length L with a rectangular cross-sectional area A , width b , and thickness h is modeled in the same procedure as [37]. As shown in Fig. 1-b, the damaged beam is modeled by the combination of four intact sub-beams, which is separated by a through-the-width horizontal crack of length L_2 which is located at the midplane and a distance L_1 from the left end of the beam. In this manner, each sub-beam has a length and thickness of $L_i \times h_i (i = 1 - 4)$ where i represents the number of sub-beams, $h_1 = h_4 = h$, $L_2 = L_3$, and $L_4 = L - L_1 - L_2$.

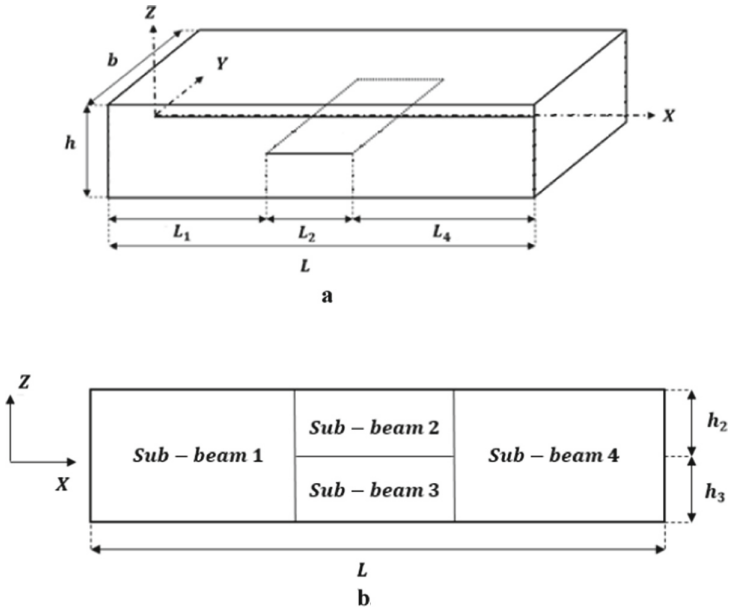


Fig. 1. a. The geometry of isotropic beam, b. Representation of beam into four sub-beams.

2.2 Finite Element Modeling

To study the vibration analysis of the presented beam, in this paper, the Euler-Bernoulli beam theory is adopted to establish vibration equations. Therefore, a higher-order beam

element as demonstrated in Fig. 2 with three nodes and six degrees of freedom, including vertical displacement w and slope w' is introduced.

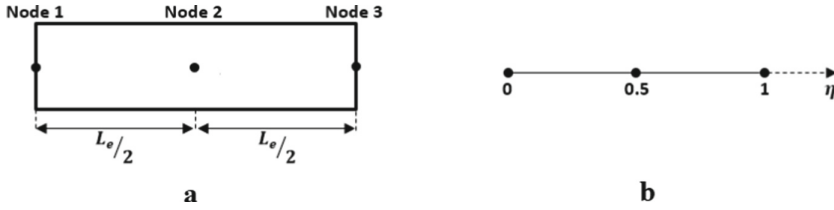


Fig. 2. (a) Higher-order beam element. (b) intrinsic coordinate of the element

The displacement field equation for the higher-order beam element can be interpolated via the Hermite interpolation function and in terms of the intrinsic coordinate as:

$$w = \sum_{i=1}^3 \left[w_{2i-1}(\eta) w_i + \Lambda_{2i}(\eta) w'_i \right] = [\Lambda] \{d\} \quad (1)$$

where η is the intrinsic coordinate, i.e. $\eta = \frac{x}{L_e}$ and L_e is the length of the respective element. As well, $\{d\}$ indicates the vector of DOFs and $\Lambda_i(\eta)$ are the shape functions associated with i th degrees of freedom which are given as:

$$\Lambda_1(\eta) = 1 - 23\eta^2 + 66\eta^3 - 68\eta^4 + 24\eta^5$$

$$\Lambda_2(\eta) = L_e(\eta - 6\eta^2 + 13\eta^3 - 12\eta^4 + 4\eta^5)$$

$$\Lambda_3(\eta) = 16\eta^2 - 32\eta^3 + 16\eta^4$$

$$\Lambda_4(\eta) = L_e(-8\eta^2 + 32\eta^3 - 40\eta^4 + 16\eta^5)$$

$$\Lambda_5(\eta) = 7\eta^2 - 34\eta^3 + 52\eta^4 - 24\eta^5$$

$$\Lambda_6(\eta) = L_e(-\eta^2 + 5\eta^3 - 8\eta^4 + 4\eta^5) \quad (2)$$

$$\{d\} = \{w_1 \ w'_1 \ w_2 \ w'_2 \ w_3 \ w'_3\} \quad (3)$$

The energy approach is utilized to obtain the element stiffness and mass matrices, which is not described in detail here [38, 39]. Hence, the potential and kinetic energy of an element can be stated in terms of displacement vector as follows [40]:

$$U_e = \frac{1}{2} \{d\}^T [K_e] \{d\} \quad (4)$$

$$T_e = \frac{1}{2} \{\dot{d}\}^T [M_e] \{\dot{d}\} \tag{5}$$

Thus, the element stiffness matrix can be obtained as:

$$[K_e] = \int_0^1 (EI)_e [\Lambda_{,xx}]^T [\Lambda_{,xx}] L_e d\eta \tag{6}$$

Likewise, the element mass matrix can be expressed as follows:

$$[M_e] = \int_0^1 m_e [\Lambda]^T [\Lambda] L_e d\eta \tag{7}$$

In which, m_e and $(EI)_e$ are the density and flexural stiffness of the typical element, respectively.

Equations (6) and (7) give the element stiffness and mass matrices of each sub-beams. To obtain the total corresponding matrices $[K]$ and $[M]$, the stiffness and mass matrices are assembled. To do this, the displacement continuity conditions have been established at the junction of sub-beams (1-2-3) and (2-3-4). Regarding Fig. 3, the deflection and slope of the connecting nodes at the tips of the crack are equal. Therefore, the corresponding entries of the stiffness and mass matrices of connected sub-beams are superposed to constitute the whole beam's total stiffness and mass matrices.

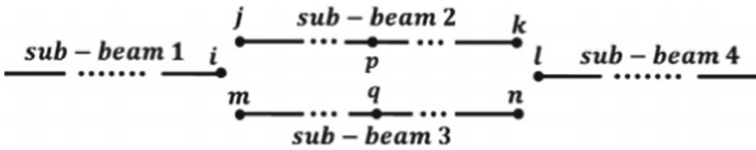


Fig. 3. Delamination boundaries

2.3 Solution Method

The free vibrations equation of motion for the entire structure is acquired as follows:

$$[M] \{\ddot{\Delta}\} + [K] \{\Delta\} = \{0\} \tag{8}$$

where $[\Delta]$ Indicates the nodal DOFs of the whole model. Considering a general solution of $\{\Delta\} = \{\Delta_0\} e^{\hat{i}\omega t}$ for Eq. (8), and assuming $\lambda = \omega^2$ yields eigenvalue problem as:

$$([K] - \lambda[M]) \{\Delta_0\} = \{0\} \tag{9}$$

Which gives natural frequency ω and corresponding mode shapes of the system $\{\Delta\}$.

2.4 Artificial Neural Network

This study uses a feed-forward ANN to localize damage levels in beams with horizontal cracks. Figure 4 indicates that our MLP contains the input, hidden, and output layers. Nodes in hidden and output layers utilize a non-linear function.

The weighted sum of input data is calculated as following [41]:

$$input_k = \sum_{i,k=1}^{n,m} b_k + w_{ik} * x_i; k = (1 : m); i = (1 : n) \quad (10)$$

where w_{ik} show weight between the i^{th} neurons and the k^{th} neurons, b_k indicates the bias ratio of hidden layers and inputs; x_i show the output in i^{th} neurons in the input layer; m and n are the number of the neurons in hidden layer and input layer, respectively. Furthermore, $input_k$ are the input of k^{th} neurons in the hidden layer.

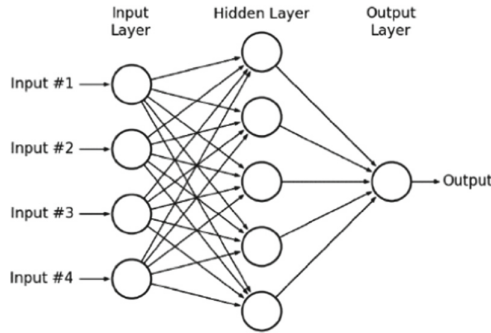


Fig. 4. Architecture of an MLP [41]

In this article, after calculating the $input_k$ of a neuron on a layer, the nonlinear function is applied through the following relation to compute the output for the j^{th} neuron [41]:

$$output_j = \left(\frac{2}{1 + e^{-2input_j}} \right) - 1 \quad (11)$$

The function is called the Tan-Sigmoid transfer function. The diagram of such a function is shown in Fig. 5.

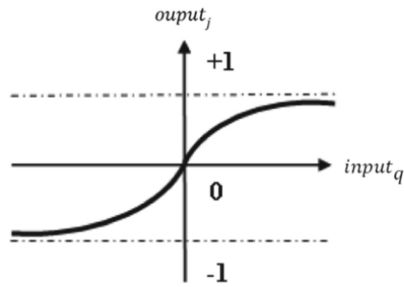


Fig. 5. Tan-Sigmoid activation function [41]

Note that, in Eq. (11), $input_q$ is input of q^{th} neuron in the output layer, and $output_j$ denotes j^{th} neuron related to the output layer.

3 Proposed Approach

The current study uses a machine learning-based approach to damage detection in steel beam structures with a horizontal crack. Figure 6 shows the flowchart of the proposed technique used in the present study. As seen, the finite element method performs problem modeling using the equivalence technique of a damaged beam with a horizontal crack approximated with four intact beams. A database is then created to perform the interpolation by the Artificial Neural Network.

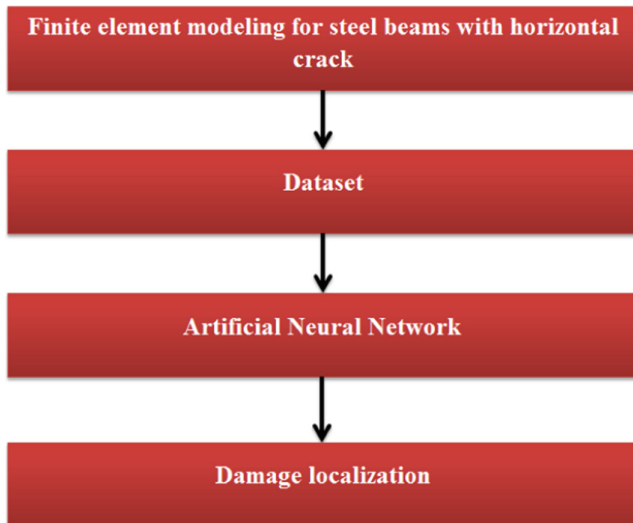


Fig. 6. Flowchart of the proposed technique used in the present study

In this way, the artificial neural network inputs are the first five natural frequencies. The artificial neural network output is the location of the horizontal crack of the desired size in the considered steel beam. In the next section, results are presented.

4 Results and Discussion

The results of this study is presented in this section. The characteristics of the considered beam are presented in Table 1. Three hundred samples of the first five natural frequencies and their corresponding crack positions are used as databases to evaluate the method's performance presented in this paper.

Table 1. The characteristics of the considered beam

Characteristics	Values
Length	100 (cm)
Thickness	1 (cm)
Width	1 (cm)
Young modulus	200 (Gpa)
Density	7800 (Kg/m ³)
Crack length	0.3 (cm)
Number of element	500

The distribution of the Artificial Neural Network outputs (horizontal crack positions) is shown in Fig. 7. As can be seen, the distribution of artificial neural network outputs used in this research is uniform. Also, the horizontal crack length of the beam in this research is 0.3 cm, which is small enough to detect damage.

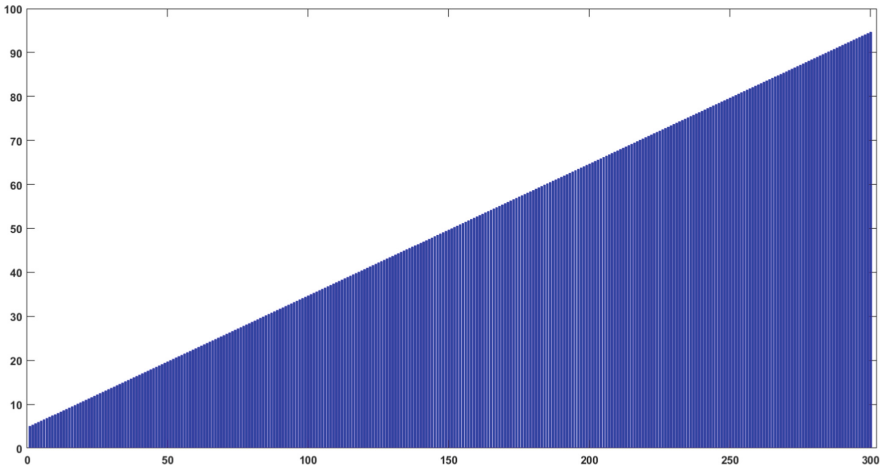


Fig. 7. The distribution of artificial neural network outputs

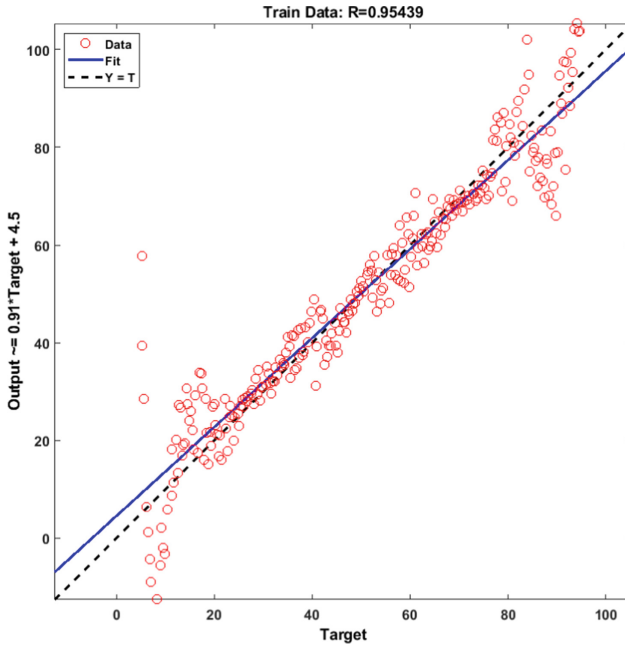


Fig. 8. Result of training process of ANN

Result of training process is shown in Fig. 8. Also, Result of test process is shown in Fig. 9.

Figures 8 and 9 show that the regression indices for training and testing processes are 0.954 and 0.979, respectively, demonstrating our predicting model’s good approximation and efficiencies. Figure 10 shows the accuracy of the model created in this research.

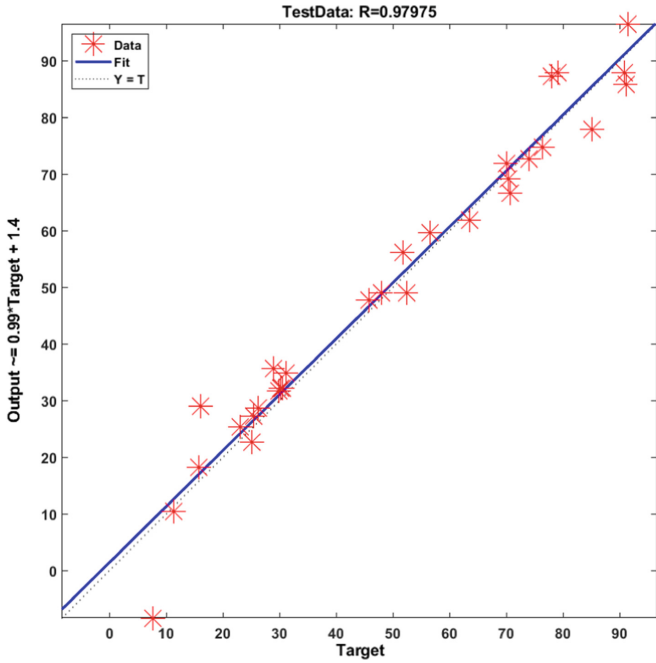


Fig. 9. Result of training process of ANN

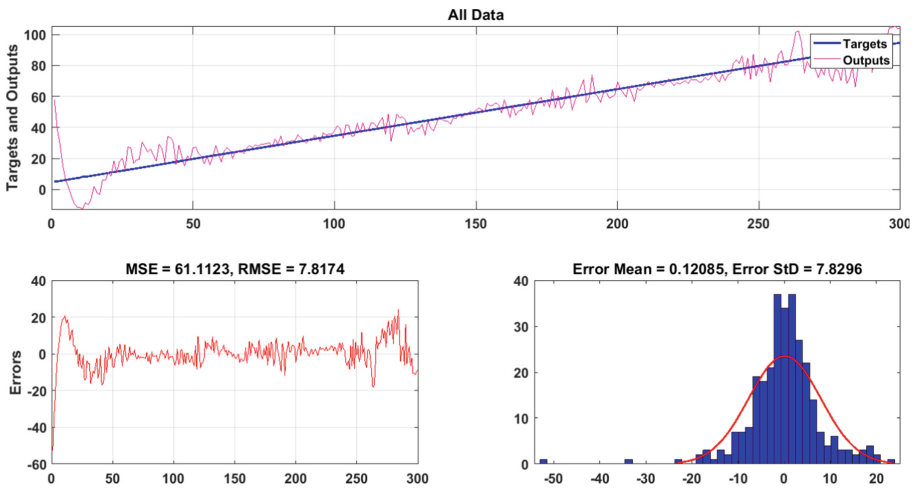


Fig. 10. The accuracy of the model created in this research

Figure 11 presents the accuracy of the predictive ANN model for seventeen damage scenarios. As can be seen, ANN identifies the approximate location of the damages with sufficient certainty for the considered damages.

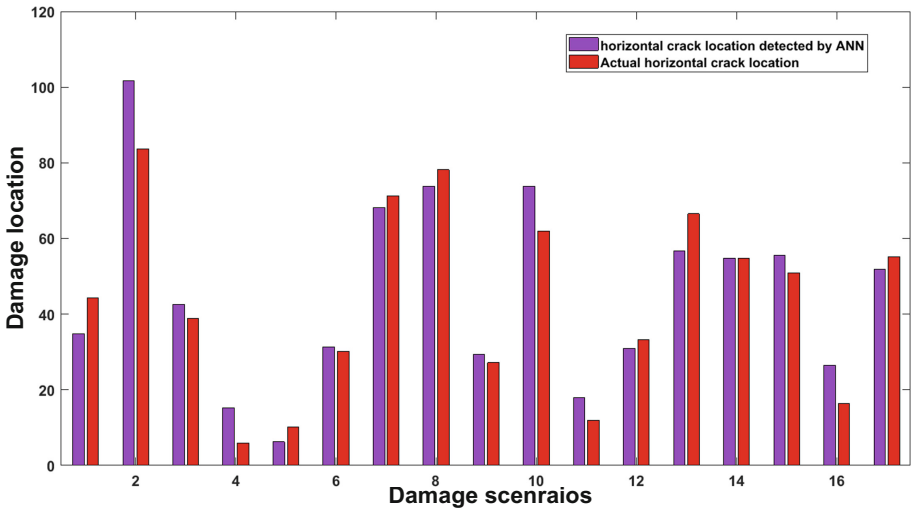


Fig. 11. Seventeen damage scenarios for evaluating the accuracy of the predictive ANN model

Also, to imagine the quantified numerical differences between the actual location of the crack and the location of crack detected by ANN, Table 2 is presented.

Table 2. The quantified numerical differences between the actual location of the crack and the location of crack detected by ANN

No.	Actual location of crack (cm)	Location of crack detected by ANN (cm)
1	34.8745477050543	44.3000000000000
2	54.8354852050543	54.8000000000000
3	42.5893914550543	38.9000000000000
4	68.1792352050543	71.3000000000000
5	6.21048520505428	10.1000000000000
6	31.3589227050543	30.2000000000000
7	68.1792352050543	71.3000000000000
8	73.7651727050543	78.2000000000000

As listed in Table 2, the location of cracks detected by ANN is well compatible with the actual location of cracks.

5 Conclusions

Structural health monitoring is one of the most critical efforts to prevent the failure of the structures before it occurs. Various methods have been proposed to monitor the

structure's health, many of which are considered non-destructive tests. One of the most popular non-destructive tests is vibration-based non-destructive tests. These tests are also known as vibration-based damage detection techniques. In this research, the detection of damage to steel beams with a horizontal crack is investigated using artificial neural networks. In this way, first, a beam is equated with a horizontal crack with four intact beams. In this way, the finite element method is used. After modeling, they are using the finite element method, databases consisting of the first five natural frequencies and the position of the horizontal crack in the steel beam are created and fed to the artificial neural network. The results of this study show that the neural network created in this paper can predict the crack position with acceptable accuracy by having the first five natural frequencies.

References

1. Khatir, S., Belaidi, I., Khatir, T., Hamrani, A., Zhou, Y.L., Wahab, M.A.: Multiple damage detection in composite beams using Particle Swarm Optimization and Genetic Algorithm. *Mechanics* **23**(4), 514–521 (2017), 4, 487–509, 2011
2. Mashhadzadeh, A.H., Fathalian, M., Ahangari, M.G., Shahavi, M.H.: DFT study of Ni, Cu, Cd and Ag heavy metal atom adsorption onto the surface of the zinc-oxide nanotube and zinc-oxide graphene-like structure. *Mater. Chem. Phys.* **220**, 366–373 (2018)
3. Hassanpour, M., et al.: Ionic liquid-mediated synthesis of metal nanostructures: Potential application in cancer diagnosis and therapy. *J. Ionic Liquids* **2**, 100033 (2022)
4. Mofidian, R., Barati, A., Jahanshahi, M., Shahavi, M.H.: Optimization on thermal treatment synthesis of lactoferrin nanoparticles via Taguchi design method. *SN Appl. Sci.* **1**(11), 1–9 (2019). <https://doi.org/10.1007/s42452-019-1353-z>
5. Kazemeini, H., Azizian, A., Shahavi, M.H.: Effect of chitosan nano-gel/emulsion containing buniun persicum essential oil and nisin as an edible biodegradable coating on escherichia coli o157: H7 in rainbow trout fillet. *J. Water Environ. Nanotechnol.* **4**(4), 343–349 (2019)
6. Jafari, B., Khatamnejad, H., Shahavi, M.H., Domeyri Ganji, D.: Simulation of dual fuel combustion of direct injection engine with variable natural gas premixed ratio. *Int. J. Eng.* **32**(9), 1327–1336 (2019)
7. Sun, Z., Nagayama, T., Nishio, M., Fujino, Y.: Investigation on a curvature-based damage detection method using displacement under moving vehicle. *Struct. Control. Health Monit.* **25**(1), e2044 (2018)
8. Fathi, A., Limongelli, M.P.: Statistical vibration-based damage localization for the S101 bridge. Flyover Reibersdorf, Austria. *Struct. Infrastructure Eng.* **17**(6), 857–871 (2021). Guo, J., Hu, C. J., Zhu, M. J., & Ni, Y. Q. (2021)
9. Guo, J., Hu, C.-J., Zhu, M.-J., Ni, Y.-Q.: Monitoring-based evaluation of dynamic characteristics of a long span suspension bridge under typhoons. *J. Civ. Struct. Heal. Monit.* **11**(2), 397–410 (2021). <https://doi.org/10.1007/s13349-020-00458-5>
10. Khatir, S., Tiachacht, S., Benaissa, B., Le Thanh, C., Capozucca, R., Abdel Wahab, M.: Damage Identification in Frame Structure Based on Inverse Analysis. In: Wahab, M.A. (ED.) *SDMA 2021*, pp. 197–211. Springer, Singapore (2022). DOI: https://doi.org/10.1007/978-981-16-7216-3_15
11. Saadatmorad, M., Jafari-Talookolaei, R.A., Pashaei, M.H., Khatir, S.: Damage detection on rectangular laminated composite plates using wavelet based convolutional neural network technique. *Compos. Struct.* **278**, 114656 (2021)
12. Limongelli, M.P., et al.: Vibration Response-Based Damage Detection. *Structural Health Monitoring Damage Detection Systems for Aerospace*, 133 (2021)

13. Saadatmorad, M., Jafari-Talookolaei, R.A., Pashaei, M.H., Khatir, S., Abdel Wahab, M.: Adaptive network-based fuzzy inference for damage detection in rectangular laminated composite plates using vibrational data. In: Abdel Wahab, M. (ed.) Proceedings of the 2nd International Conference on Structural Damage Modelling and Assessment, pp. 179–196. Springer, Singapore (2022). Doi: https://doi.org/10.1007/978-981-16-7216-3_14
14. Saadatmorad, M., Jafari-Talookolaei, R.A., Pashaei, M.H., Khatir, S., Abdel Wahab, M.: Application of multilayer perceptron neural network for damage detection in rectangular laminated composite plates based on vibrational analysis. In: Abdel Wahab, M. (ed.) Proceedings of the 2nd International Conference on Structural Damage Modelling and Assessment, pp. 163–178. Springer, Singapore (2022). Doi: https://doi.org/10.1007/978-981-16-7216-3_13
15. Pisani, M.A., Limongelli, M.P., Giordano, P.F., Palermo, M.: On the effectiveness of vibration-based monitoring for integrity management of prestressed structures. *Infrastructures* **6**(12), 171 (2021)
16. Khatir, S., Dekemele, K., Loccufer, M., Khatir, T., Wahab, M.A.: Crack identification method in beam-like structures using changes in experimentally measured frequencies and Particle Swarm Optimization. *Comptes Rendus Mécanique* **346**(2), 110–120 (2018)
17. Behtani, A., Tiachacht, S., Khatir, T., Khatir, S., Wahab, M.A., Benaissa, B.: Residual Force Method for damage identification in a laminated composite plate with different boundary conditions. *Frattura ed Integrità Strutturale* **16**(59), 35–48 (2022)
18. Tiachacht, S., Bouazzouni, A., Khatir, S., Wahab, M.A., Behtani, A., Capozucca, R.: Damage assessment in structures using combination of a modified Cornwell indicator and genetic algorithm. *Eng. Struct.* **177**, 421–430 (2018)
19. Saadatmorad, M., Siavashi, M., Jafari-Talookolaei, R.A., Pashaei, M.H., Khatir, S., Thanh, C.L.: Multilayer perceptron neural network for damage identification based on dynamic analysis. In: Bui, T.Q., Cuong, L.T., Khat, S. (ed.) *Structural Health Monitoring and Engineering Structures*, pp. 29–48. Springer, Singapore (2021). Doi: https://doi.org/10.1007/978-981-16-0945-9_3
20. Khatir, S., Tiachacht, S., Le Thanh, C., Ghandourah, E., Mirjalili, S., Wahab, M.A.: An improved artificial neural network using arithmetic optimization algorithm for damage assessment in FGM composite plates. *Compos. Struct.* **273**, 114287 (2021)
21. Benaissa, B., Hocine, N.A., Khatir, S., Riahi, M.K., Mirjalili, S.: YUKI Algorithm and POD-RBF for Elastostatic and dynamic crack identification. *J. Comput. Sci.* **55**, 101451 (2021)
22. Saadatmorad, M., Siavashi, M., Jafari-Talookolaei, R.A., Pashaei, M.H., Khatir, S., Thanh, C.L.: Genetic and particle swarm optimization algorithms for damage detection of beam-like structures using residual force method. In: *Structural Health Monitoring and Engineering Structures*, pp. 143–157. Springer, Singapore (2021)
23. Yang, Y., Liu, H., Mosalam, K.M., Huang, S.: An improved direct stiffness calculation method for damage detection of beam structures. *Struct. Control. Health Monit.* **20**(5), 835–851 (2013)
24. Park, H.S., Oh, B.K.: Damage detection of building structures under ambient excitation through the analysis of the relationship between the modal participation ratio and story stiffness. *J. Sound Vib.* **418**, 122–143 (2018)
25. Wahab, M.A., De Roeck, G.: Damage detection in bridges using modal curvatures: application to a real damage scenario. *J. Sound Vibration*, **226**(2), 217–235 (1999)
26. Yazdanpanah, O., Seyedpoor, S.M.: A new damage detection indicator for beams based on mode shape data. *Struct. Eng. Mech.* **53**(4), 725–744 (2015)
27. Dahak, M., Touat, N., Kharoubi, M.: Damage detection in beam through change in measured frequency and undamaged curvature mode shape. *Inverse Probl. Sci. Eng.* **27**(1), 89–114 (2019)
28. Ratcliffe, C.P.: Damage detection using a modified Laplacian operator on mode shape data. *J. Sound Vib.* **204**(3), 505–517 (1997)

29. Jafari-Talookolaei, R.A., Abedi, M., Hajianmaleki, M.: Vibration characteristics of generally laminated composite curved beams with single through-the-width delamination. *Composite Struct.* **138**, 172–183 (2016)
30. Jafari-Talookolaei, R. A., & Abedi, M. (2014). Analytical solution for the free vibration analysis of delaminated Timoshenko beams. *The Scientific World Journal* (2014)
31. OmidDezyani, S., Jafari-Talookolaei, R. A., Abedi, M., Afrasiab, H.: Vibration analysis of a microplate in contact with a fluid based on the modified couple stress theory. *Modares Mech. Eng.* **17**(2), 47–57 (2017)
32. Jafari-Talookolaei, R.A., Kargarnovin, M.H., Ahmadian, M.T., Abedi, M.: An investigation on the nonlinear free vibration analysis of beams with simply supported boundary conditions using four engineering theories. *J. Appl. Math.* **2011**, 1–17 (2011)
33. Ramian, A., Jafari-Talookolaei, R.A., Valvo, P.S., Abedi, M.: Free vibration analysis of sandwich plates with compressible core in contact with fluid. *Thin-Walled Struct.* **157**, 107088 (2020)
34. Jafari-Talookolaei, R.A., Abedi, M., Kargarnovin, M.H., Ahmadian, M.T.: Dynamic analysis of generally laminated composite beam with a delamination based on a higher-order shear deformable theory. *J. Compos. Mater.* **49**(2), 141–162 (2015)
35. Jafari-Talookolaei, R.A., Abedi, M., Kargarnovin, M.H., Ahmadian, M.T.: Dynamics of a generally layered composite beam with single delamination based on the shear deformation theory. *Sci. Eng. Compos. Mater.* **22**(1), 57–70 (2015)
36. Jafari-Talookolaei, R.A., Kargarnovin, M. H., Ahmadian, M. T., & Abedi, M. (2011). Analytical expressions for frequency and buckling of large amplitude vibration of multilayered composite beams. *Advances in Acoustics and Vibration*, 2011
37. Jafari-Talookolaei, R.A., Kargarnovin, M.H., Ahmadian, M.T.: Dynamic response of a delaminated composite beam with general lay-ups based on the first-order shear deformation theory. *Compos. Part B: Eng.* **55**, 65–78 (2013)
38. Jafari-Talookolaei, R.A., Abedi, M., Attar, M.: In-plane and out-of-plane vibration modes of laminated composite beams with arbitrary lay-ups. *Aeros. Sci. Technol.* **66**, 366–379 (2017)
39. Kargarnovin, M.H., Ahmadian, M.T., Jafari-Talookolaei, R.A., Abedi, M.: Semi-analytical solution for the free vibration analysis of generally laminated composite Timoshenko beams with single delamination. *Compos. Part B: Eng.* **45**(1), 587–600 (2013)
40. Jafari-Talookolaei, R.A., Kargarnovin, M.H., Ahmadian, M.T.: Free vibration analysis of cross-ply layered composite beams with finite length on elastic foundation. *Int. J. Comput. Methods* **5**(01), 21–36 (2008)
41. Zainal-Mokhtar, K., Mohamad-Saleh, J.: An oil fraction neural sensor developed using electrical capacitance tomography sensor data. *Sensors* **13**(9), 11385–11406 (2013)



Polycarbonate Degradation Under Heat and Irradiation

Sonya Redjala¹ (✉), Said Azem¹, and Nourredine Aït Hocine²

¹ Department of Mechanical Engineering, Mouloud Mammeri University of Tizi-Ouzou, Tizi Ouzou, Algeria

radjalasonya@gmail.com

² LaMé, INSA Centre Val de Loire, 3 rue de la Chocolaterie, BP 3410, 41034 Blois, France

Abstract. The aim of this work is to study the effect of the exposure of a polycarbonate (PC) to the simultaneous effects of heat and ultraviolet radiation. PC is an amorphous polymer widespread in commerce. Transparency, impact resistance, and low density are just a few of the many intriguing properties of this material, this is why it is used like a material of greenhouses, windows of headlights, body parts, anti-shock windows, anti-vandal panes. However, long exposure to the heat and radiation makes it fragile and translucent. In this study, we have submitted the PC to the simultaneous action of ultraviolet (UV) with wavelength of 253nm combined to temperature of 120 °C for 72, 144 and 2016 h. The effects were highlighted by the physico-chemical analyzes and mechanical tests. Thus, the modification of chemical bonds was revealed by spectrometry by spectroscopy FTIR and changes of the mechanical properties was revealed by the compression and traction tests.

Keywords: Polycarbonate · Thermal aging · Irradiation · FTIR · Mechanical properties

1 Introduction

Recently, very expensive conventional inorganic materials for optical components like glasses and semiconductors have been gradually replaced by polymeric materials which are cost effective with ease of processing [1]. Polymers are also used in food, cosmetics, cement, and even further in one of the challenges outlined by the human being which is the involvement of these materials in the human body. Indeed, in biomedical applications polymers seem interesting because of their properties such as chemical inertia, low molecular weight, ease of processing, etc. [2].

The PC is appreciated for its transparency, impact resistance and ease of implementation. It is used in several applications such as building materials, displays, and vehicle components, as well as agriculture. However, exposure to inclement weather causes physical and chemical [3, 4] aging. As a result, these mechanisms provoke changes in the structural within time, consequently, the properties of the material [5, 7].

In this article, we have studied mixed aging, which consists of exposure of polycarbonate samples to a combined action of UV and temperature. For this, aging under UV-C

($\lambda = 253$ nm) combined with isothermal treatments 120 °C for 72, 144 and 216 h, were carried out on the polycarbonate of bisphenol A. Then, a physico-chemical analyzes such as FTIR and mechanical tests were carried out in order to demonstrate the effects of aging on the various properties.

2 Experimental Techniques

2.1 Aging

Polycarbonate samples were aged in a specific heating chamber and under ultraviolet radiation. This is equipped with two Philips type UV lamps producing radiation with a wavelength of 253 nm and energy of 4.3 eV. They are mounted and ventilated under the vault to prevent degradation under the effect of heat. Inside the enclosure, an electrical resistance is used to heat the samples to a controlled temperature. A sheet is installed above the resistance to properly distribute the heat in the enclosure. The samples are placed on a metal grid allowing rapid homogenization of the temperature. A sensor records the temperature in the vicinity of the specimens and transmits the information to a Eurotherm type regulator which allows the heating rate and the set temperature to be controlled by means of a power dimmer. Thermal insulation is provided by a layer of alumina wool placed on the walls and the floor of the enclosure. Note that only one side of the samples is exposed directly to UV radiation.

2.2 Different Analyzes and Tests Used

Fourier Transform Infrared Spectroscopy (FTIR). The analysis mode used is transmission with a resolution of 2cm^{-1} , scanning intervals ranging from 650 to 4000cm^{-1} , and a number of scans set at 25. The samples are obtained by superficial scraping from the face directly exposed to UV radiation (EF). The transmission mode was adopted since polycarbonate is a transparent material.

The FTIR of bland PC reveals the molecular chains of this material, such as double bonds $\text{C} = \text{C}$ and $\text{C} = \text{O}$ as well as mono-bonds $\text{C}-\text{C}$ and $\text{C}-\text{H}$.

Tensile Test. Tensile tests were carried out on dumbbell-shaped specimens until fracture, using an MTS Criterion Model 43 type tensile machine. These tests were driven by the strain rate of the sample recorded by a 0.55 m Tacron type CCD camera, from four spots carried on the useful part of the specimens, two in the longitudinal direction and two in the transverse direction. The initial distances between these spots are respectively 6 and 3 mm. Thus, the instantaneous deformations are deduced from the modification of these distances, during the test. The strain rate is fixed at 0.0012/min. The objective of these tests is to determine the mechanical properties of the material in the virgin state and after aging.

The nominal stresses σ_n and ϵ_n strains are calculated by the relations (1) and (2):

$$\sigma_n = F / S_0 \tag{1}$$

$$\epsilon_n = \Delta l / l_0 \tag{2}$$

where F is the applied force and S_0 , Δl and l_0 are, respectively, the initial section, the elongation and the initial length of the useful area of the test specimen.

The tensile specimens were cut according to the ASTM D638 standard. The dimensions are shown in Table 1.

Table 1. Standard dimensions of tensile specimens.

Test	Norm	Dimensions						
Traction (M-I)	ASTM D638	L3	L1	b1	b2	h	L0	L
		> 150	60 ± 0,5	10 ± 0,5	20 ± 0,5	< 10	50 ± 0,25	115 ± 5

To avoid any stress concentration at the specimen shoulders, we optimized the shape of the working area using finite element simulation, using Solid Works. The final shape of the sample, obtained by milling, is shown in Fig. 1.

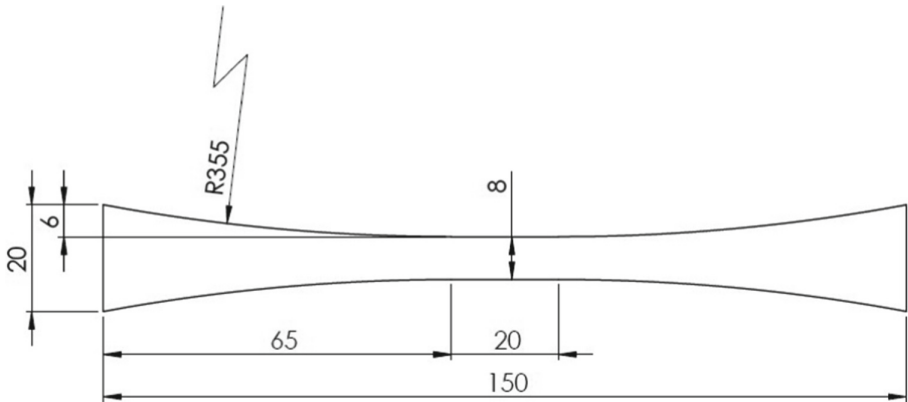


Fig. 1. Optimized shape of tensile specimens.

Compression Test. The samples are compressed by applying a gradual and continuous force until they break. The sample is placed on the profile face so as to orient the aged surface in the direction of the application of the force. The dimensions of the specimen are 10 × 10 × 4.5 mm. The recording of the deformations in the axial and transverse directions is provided by a CCD camera type Tamron 0.55 m oriented on one of the faces with four spots. Two spots are arranged in the direction of application of the force and

separated by 8mm while two others, arranged in the transverse directions, are separated by 2 mm. The results of the compression tests are analyzed in large deformations.

The true stress and the true strain are calculated using the following relations:

$$\sigma_{\text{True}} = \sigma_n (1 - \varepsilon_n) \tag{3}$$

$$\varepsilon_{\text{True}} = \ln (1 - \varepsilon_n) \tag{4}$$

With negative nominal strain: $\varepsilon_n = \Delta l/l_0 < 0$.

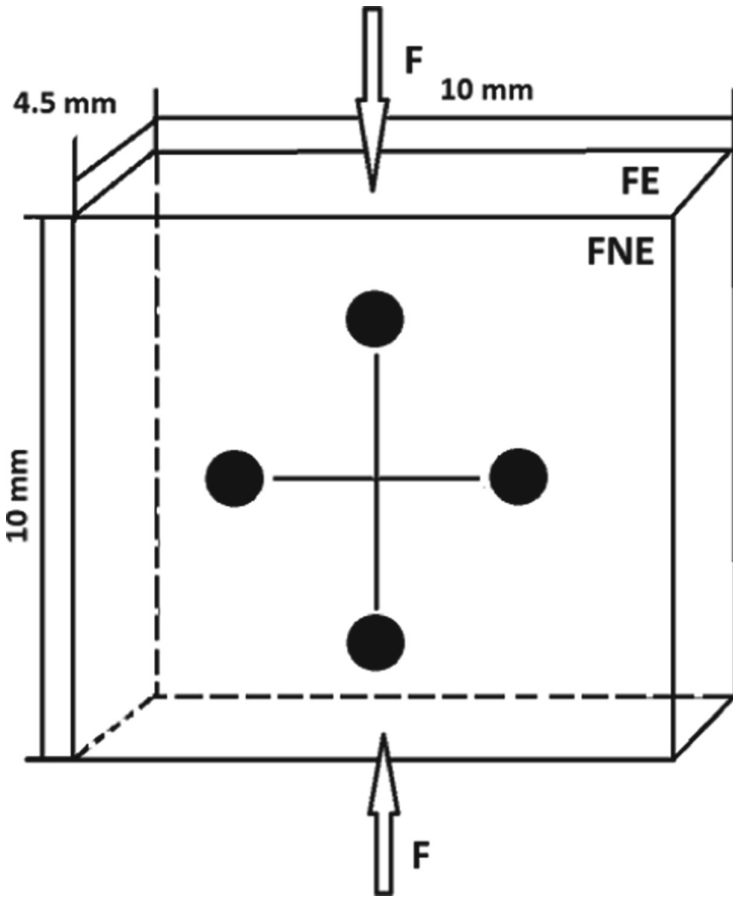


Fig. 2. Direction of loading of the sample in monotonic compression.

The camera loses visibility of the spots from the first minutes of compression as the material has a barrel effect. This is why we programmed the machine to switch from video control to crosshead control, beyond 10% deformation. We have not reached the total rupture of the virgin and temperature aged material because the maximum load necessary for their rupture exceeds the maximum capacity of the machine, which is 10 kN.

3 Results and Discussions

3.1 Fourier-Transform Infrared Spectroscopy (FTIR)

Figure 3 shows the spectra of virgin PC and aged under UV combined to a temperature of 120 °C, for 72, 144 and 216 h.

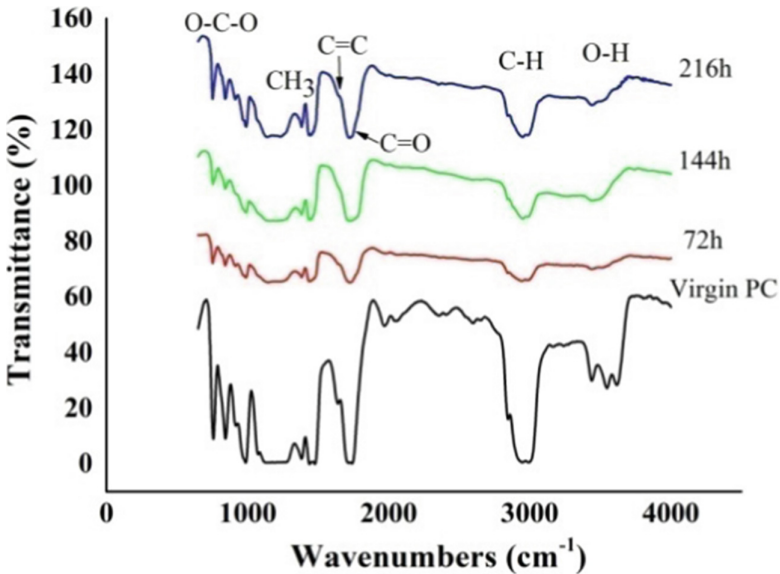


Fig. 3. Transmission IRTF spectra of PC aged under UV combined to 120 °C for 72, 144 and 216h.

This figure shows a gradual attenuation of the IRTF peaks as the aging time increases.

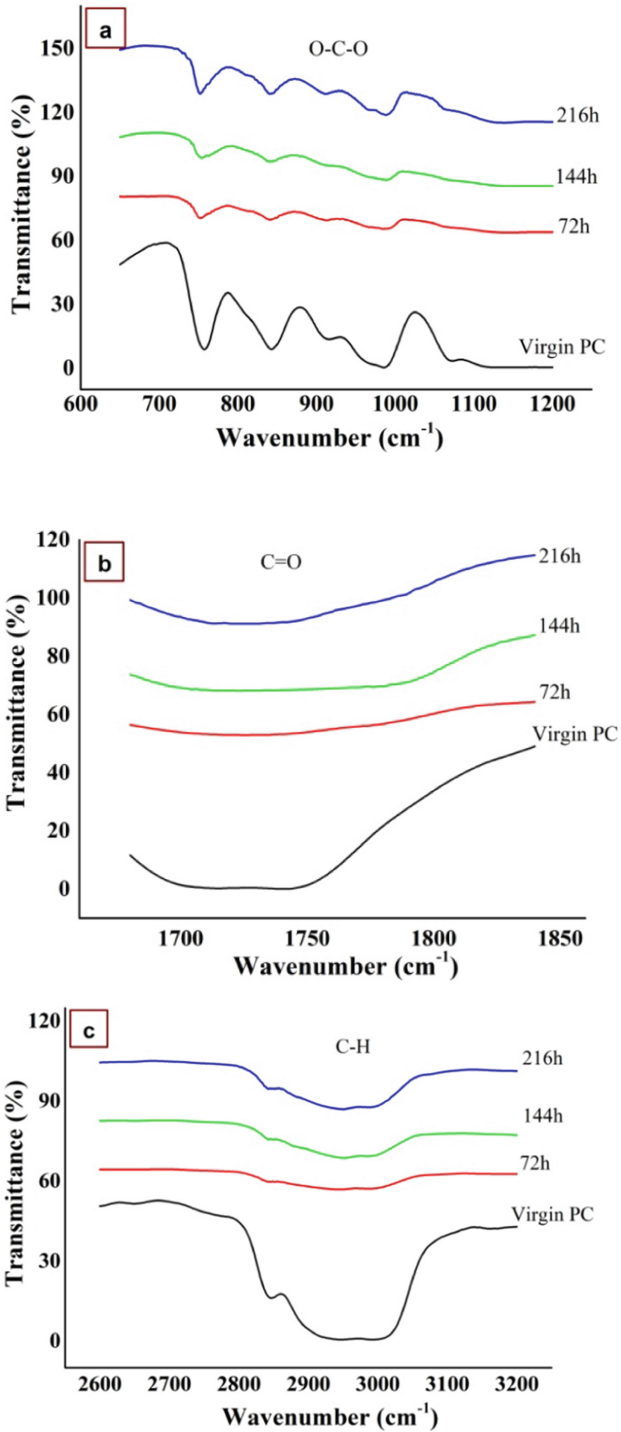


Fig. 4. Zoom of IRTF spectra, a) O-C-O band, b) C = O band, c) C-H band, d) O-H band.

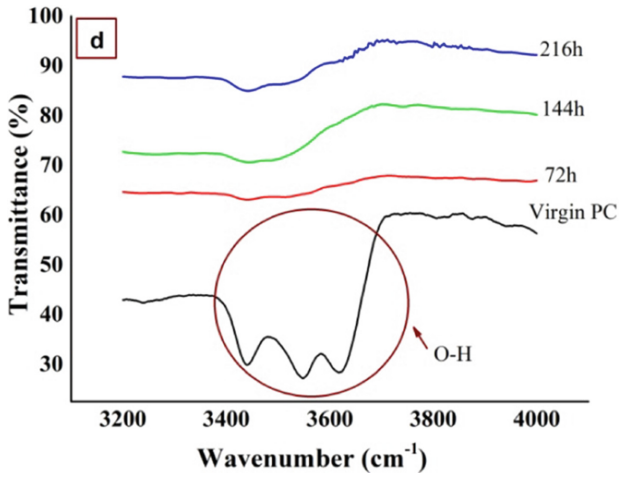


Fig. 4. (continued)

The IRTF peaks (relating to the CH, C = O, OCO and OH bonds) of the PC aged under UV, at 120 °C, decrease for 72 and 144 h then increase again for 216 h of exposure as shown in Fig. 2. This corresponds to an increase in transmittance which testifies to a rupture of a number of these bonds for durations of 72 and 144h. On the other hand, for 216 h of exposure, a growth of the peaks (Fig. 4) justifies the formation of new bonds by the phenomenon of recombination and by oxidation. [8].

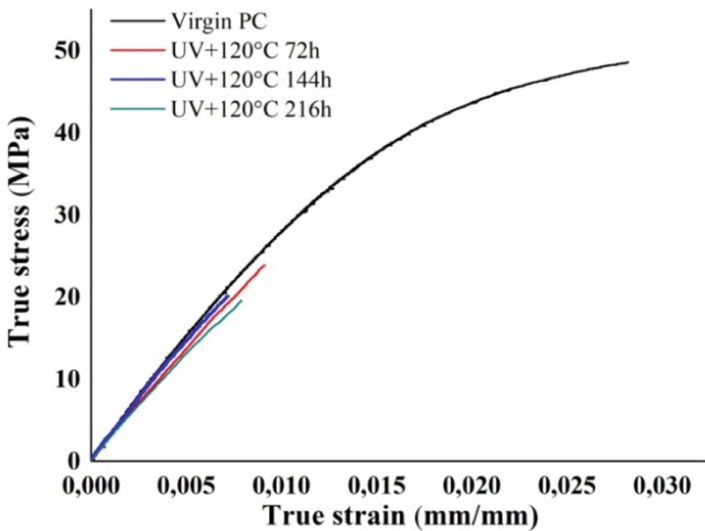


Fig. 5. Traction curves of virgin and aged PC under UV combined to 120 °C, for 72, 144 and 216h.

3.2 Tensile Test

Figure 5 represents the curves of monotonic traction of the virgin and aged PC under UV combined to 120 °C.

Table 2 groups the values of the Young’s modulus (E), true stress at break and the true strain at break as a function of aging time.

Table 2. Mechanical properties virgin and aged PC under UV + 120 °C in monotonic traction.

Mechanical properties	Young’s modulus E (Mpa)	Rupture Stress (Mpa)	Rupture Strain
Virgin PC	2969	48.6	0.028
Aging over 72 h	2689	23	0.009
Aging over 144 h	2912	20	0.007
Aging over 216 h	2546	19	0.007

Young’s modulus decrease for 72 h of aging time then increases gradually for 144 and 216 h. Also, the stress and strain at rupture values of have a sudden decrease from virgin value to aged material at 72 h. Then, they decrease slowly for 144 h and 216 h (Table 2).

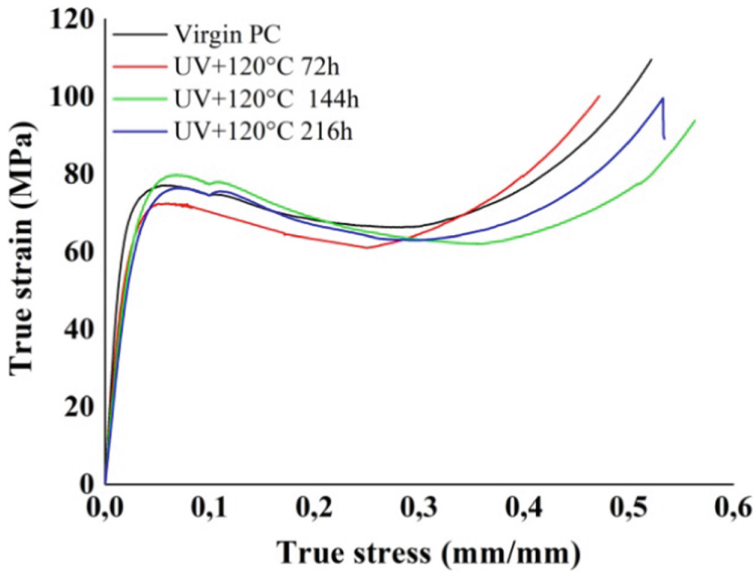


Fig. 6. Compression curves of virgin and aged PC under UV combined to 120 °C, for 72, 144 and 216h.

3.3 Compression Test

The curves monotonic compression of the virgin and aged PC under UV combined to 120 °C are presented in Fig. 6.

Table 3 groups the values of the mechanical properties of virgin and aged PC under UV combined to 120 °C compression test. We note a decrease in Young's modulus and an increase in flow threshold constraint as a function of aging time.

Table 3. Mechanical properties virgin and aged PC under UV + 120 °C in monotonic compression.

Mechanical properties	Young's modulus E (Mpa)	Flow threshold constraint S_e (Mpa)
Virgin PC	4232	76,6
Aging over 72 h	3449	73
Aging over 144 h	2872	80
Aging over 216 h	2482	77

Figure 7 shows the change in Young's modulus of aged PC in tension and compression as a function of aging time. We notice that Young's modulus gradually decreases in traction and a fluctuation in compression where it decreases at 72 h, increases at 144 h and decreases again at 216 h.

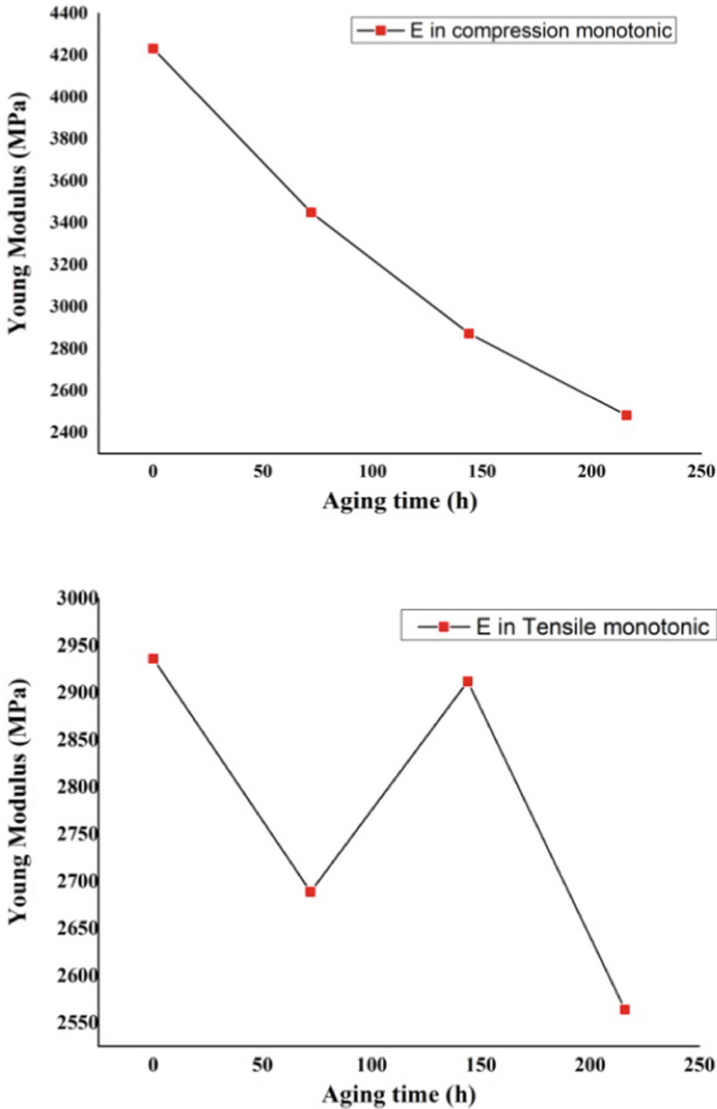


Fig. 7. Evolution of Young's modulus of the aged PC in compression and in tension test.

4 Conclusion

PC subjected to the combined action of UV and temperature undergoes a significant deterioration of its properties. The modification of these properties is a consequence of the splitting of molecular chains induced by the action of UV energy and temperature. After aging, we noted:

- Splitting in chemical chains revealed by IRTF.

- An increase in the yield point.
- A decrease in the Young modulus of the material.

Thus, this study shows a degradation of the properties of polycarbonate following aging under UV combined to 120 °C for 72, 144 and 216 h.

References

1. Eve, S., Mohr, J.: Study of the surface modification of the PMMA by UV-radiation, *Procedia Engineering*. Study *Procedia Eng.*, 237–240 (2009)
2. Jagielski, J., Turos, A., Bielinski, D., Abdul-Kader, M., Piatkowska, A., Nucl, A.: Ion-beam modified polymers for biomedical applications. *Instruments Methods Phys. Res. Sect. B: Beam Interact. with Mater. Atoms* **261**, 690–693 (2007)
3. Ho, C.H., Vu-Khanh, T.: Effects of time and temperature on physical aging of polycarbonate. *Theor. Appl. Fracture Mech.* **2**(39), 107–116 (2003)
4. Schnell, H.: *Chemistry and physics of polycarbonate*. Inter-science, New York (1964)
5. Boubakri, A., Haddar, N., Elleuch, K., Bienvenu, Y.: *C. R. Mecanique* (339), 666–673 (2011)
6. El-Ghazaly, M., ShAydarous, A., Al-Thomali, T.A.: Ultraviolet radiation of short wavelength (UVC) induced-modifications in optical properties of PADC. *Life Sci. J.* **4**(10), 2446–2450 (2013)
7. Golden, J.H., Hammant, B.L., Hazell, E.A.: *J. Appl. Polym. Sci.* **11**, 1571–1579 (1967)
8. Redjala, S., Azem, S., Ait Hocine, N.: Thermoplastique degradation under heat and irradiation. *Key Engineering Mater.* **904**, 196–201 (2022)



Influence of Decarburization on the Erosion and Corrosion Resistance of a High Chromium Cast Iron

ElJersifi Adnane^{1,2}(✉), Chbihi Abdelouahed¹, Semlal Nawal³, Bouaouine Hassan², and Naamane Sanae¹

¹ Moroccan Foundation for Advanced Science Innovation and Research (MAScIR), Mohammed ElJazouli, Rabat Design Center, Rabat, Morocco

a.eljersifi@mascir.ma

² Mohammedia School of Engineers (EMI), Mohammed V University, Avenue Ibn Sina B.P. 765 Agdal, Rabat, Morocco

³ OCP Group S.A., 2-4, Rue Al Abtal-Hay Erraha, 20200 Casablanca, Morocco

Abstract. In this paper, we present a case study that illustrates the detrimental effects decarburization has on the resistance of high chromium cast iron to erosion and corrosion. Two samples are analysed: the first was extracted from a heat-treated impeller used for phosphoric acid slurry pumping. This resulted in decarburization and a gradual change in microstructure from the surface to the core of the material where zones closer to the surface not only had a smaller CVF (Carbide Volume Fraction) but formed a continuous carbide network which facilitated cracking propagation. This led to a significant drop in surface hardness. The second sample was extracted from an unused, non-treated pump made using a similar chemical composition to the failed impeller. This sample had a microstructure that is uniform across its regions. Samples were subjected to corrosion testing in a phosphoric acid solution at 80 °C, and then cleaned and eroded using a sand jet impingement erosion tester, and corrosion-tested again in the same conditions. A comparison is made each time between the mass losses and polarization curves of the samples as well as a microstructural analysis of their cross-sections to evaluate the erosion and corrosion resistance of the high chromium cast irons at their two different states.

Keywords: Erosion · Corrosion · Decarburization · Chromium carbides · High chromium cast iron · Microstructure

1 Introduction

The wet process of phosphoric acid production starts with the reaction of sulfuric acid and crushed phosphate rocks slurry at 80 °C [1, 2]. This generates a phosphoric acid slurry at a concentration around 29% which is then sent to the filtering stage using slurry pumps. Although pure phosphoric acid is only mildly corrosive, the slurry contains impurities such as chlorides and sulfides which aggravates corrosion conditions [3, 4].

The impellers are also affected by erosion wear from the constant flow of phosphogypsum and unreacted rock particles as well as cavitation erosion. The synergy that exists between erosion and corrosion leads to accelerated damage [5–8] and further reduces the service life of impellers and multiplies lengthy maintenance shutdowns. A careful choice of the alloys used for such application and their fabrication processes is, therefore, essential. High-chromium cast irons are an example of such materials, as they have high resistance to both wear and corrosion [9]. There exist several variants of those alloys depending on the microstructure and alloying elements, but they all share a composite microstructure made of a network of hard chromium carbides in a softer matrix. These carbides are what confers to the material its high wear resistance and it is why some researchers chose to focus their optimization efforts on the increase of the carbide volume fraction (cvf) [10] or the precipitation of additional secondary carbides in the matrix through destabilization heat treatments [11]. These heat treatments have the additional advantage of leading to a partially or fully martensitic matrix which is harder and more wear resistant [9, 12]. They can however cause decarburization, which may lead to higher wear rates and loss of fatigue resistance [13]. Decarburization is a phenomena that occurs at high temperatures and leads to the oxidation of carbon. This, in turn, leads to the carbide dissolution and carbon diffusion through the matrix [14]. If no environment control is done during heat treatment and decarburization is observed, machining is often the tool used to remove the surface layer affected by it [13].

The alloy studied in this paper is a high chromium cast iron of the ferritic variant. These variants are generally more corrosion resistant due to the higher cr/c ratio [15]. However, there are still vulnerable to the same micro-galvanic form of corrosion that affects multi-phases characterised by high corrosion potential differences between their phases [16, 17]. There isn't enough literature about the effect of heat treatments on this particular variant of high chromium cast irons, as they don't experience any phase transformations [15]. Carbon restoration is another convenient tool. It consists of coating the component in a carbon-rich layer and exposing it to the same heat treatment conditions as before [18].

The Impeller, Studied in This Paper, Operates in the Same Phosphoric Acid Slurry Environment at 80 °C Described Above Which Additionally Contains Phosphogypsum Particles [19, 20]. in a Previous Study, the Authors Have Examined the Failure of the Impellers Used in This Environment [21], and Have Identified Decarburization as One of the Mechanisms Leading to Its Early Failure. In This Paper, This is Analysed Further, and the Effects of Decarburization on the Loss of Resistance to Erosion and Corrosion is Investigated as Well as Resistance to the Corrosive Effect of Chlorides.

2 Methodology

To study the effect decarburization had on the erosion and corrosion resistance of the impeller, two sets of samples were extracted: the first from a standard non-decarburized ferritic high chromium cast iron, henceforth called “Sample A”, and the second from the failed impeller itself, called “Sample B”, which was cast using a similar alloy.

From each set, one sample was taken for the determination of the alloys' chemical compositions using spark emission optic spectrometry using an SEOS 2.

Another set of samples was used for surface and cross-sectional examination using SEM microscopy coupled with EDX analysis, as well as determining surface hardness and Vickers microhardness values along their cross-sections. To that extent they were polished using multiple SiC emery papers up to a 1200-grit as well as solutions containing diamond particles with sizes of up to 1 μm . Etching was done using a 10% Nital solution. The SEM-EDX analysis was done using FEI Tecnai G2 120kV SEM equipped with an EDX analyser and operated at an accelerating voltage of 20.0 kV, at a high vacuum, for a working distance of 10 mm, and a spot size of 3. The hardness tests were done using an AFRI WIKI 90JS hardness tester equipped with a Vickers indenter according to the ISO6506 standard.

The third set of samples was used for successive erosion and corrosion tests. For that purpose, copper cables were then used to provide an electrical connection to the potentiostat and were fixed to the samples using silver conductive paste. Cold-setting resin was then poured and the samples were polished using 1200-grit emery paper. **Error! Reference source not found.** shows the assembly of the samples mounted in cold-setting resin with the sample holder Figs. 1, 2, 3, 4, 5, 6, 7, 8, 9 and 10.

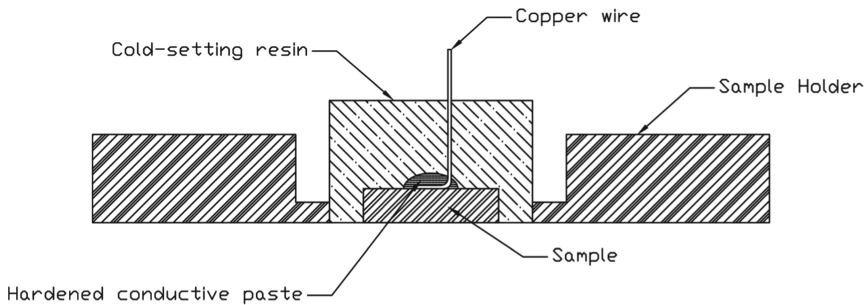


Fig. 1. Schematic of the sample-sample holder assembly.

These samples were then used for corrosion testing in a 29% phosphoric acid solution at 80 °C that is extracted from the impeller's working environment which was located after the reaction of sulfuric acid and crushed phosphate rocks slurry. The same samples were then cleaned first in demineralized water, then in 99% ethanol. They were then air dried, weighed, eroded using a jet-impingement sand erosion tester, cleaned, weighed once more, and then used for corrosion testing in the same conditions.

The jet-impingement erosion tester [22] used for this study was designed for the simulation of sand reflectors' erosion and operates by ejecting sand particles at a fixed speed using compressed air. For this study, a 3D printed sample holder was made to hold the samples that were smaller compared to the ones the sand erosion tester was designed for.

Error! Reference source not found. Shows the erosion test bench used in this study (left), a 3D model of the sample holder (top right corner) and the sample holder set up inside the test bench (bottom right corner).

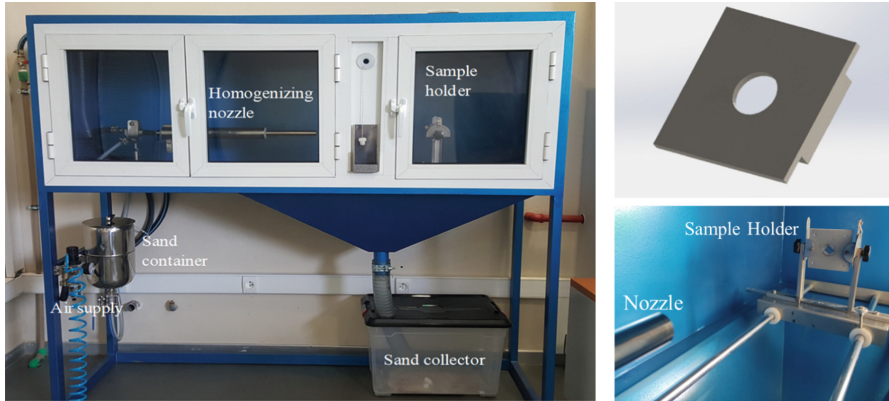


Fig. 2. Left – experimental erosion test bench, Top right corner – 3D model of the sample holder, Bottom right corner - the sample holder set up inside the test bench.

The erosion testing was done by ejecting 2 g of silicon carbide particles five times against the sample at a 90° angle and a velocity of $15 \text{ m}\cdot\text{s}^{-1}$. The particles' size ranged between 500 and $710 \mu\text{m}$.

As for the corrosion testing, the samples were kept in a phosphoric acid solution, extracted from the impeller's working environment, for 60 min, or until the potential-versus-time curve stabilized. This was followed by potentiodynamic measurements which were performed at 20 mv/min. The solution was kept at 80°C during the entire testing time. These tests were performed and monitored using a BioLogic SP-50 potentiostat.

As mentioned in the previous section, chlorides are present in the phosphoric solution and as it represents a risk factor for the impellers, further testing was done to characterize their effect on the alloys, in both states. This was done by embedding samples in resin on all but one surface and submerged in a 3.5% NaCl solution for 24 h. Samples were then cleaned using 99% ethanol, air dried, and examined using SEM-EDX.

3 Results and Discussion

The compositions of both samples are given in Table 1 below:

Table 1. Chemical composition of samples A and B in terms of mass percentage.

	C	Si	P	S	Mn	Cr	Mo	Ni	Fe
Sample A	1.1	0.67	0.027	0.028	0.17	26.37	2.31	2.56	<i>Balance</i>
Sample B	0.86	1.15	0.025	0.019	0.38	29.65	1.94	0.2	<i>Balance</i>

Both alloys are variants of the high chromium cast irons family of stainless steel. They present a dual microstructure where a matrix contains a network of hard chromium

Table 2. Electrical parameters determined after corrosion testing.

		i_{corr} ($\mu\text{A}/\text{cm}^2$)	E_{corr} (mV)	i_{p} ($\mu\text{A}/\text{cm}^2$)	β_{A} (mV)	β_{C} (mV)
Sample A (decarburized)	Before erosion	284.838	127.324	1013.45	52.7	87
	After erosion	348.947	99.411	1158.95	63.6	86.6
Sample B	Before erosion	1.024	341.316	21.685	47.7	20.7
	After erosion	1.592	347.172	29.715	67.1	31.2

carbides. In the case of sample B (**Error! Reference source not found.** – a), the non-decarburized sample, the matrix is ferritic in nature and no change occurs from the surface of the sample to its interior. In sample A, however, changes are observed (**Error! Reference source not found.** – b). On the surface, almost no carbides are detected, but as we move deeper into the core, a network of long and thin chromium carbides enveloping the grains is observed with noticeable decohesion with the matrix (**Error! Reference**

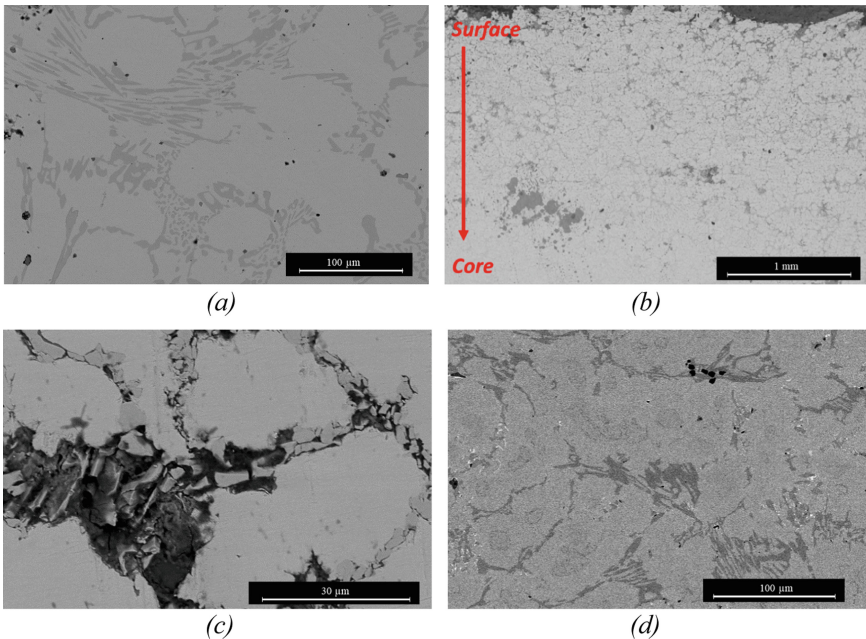


Fig. 3. Circular BackScatter SEM micrographs of high chromium cast iron samples: (a) – Non-decarburized samples (Magnification = 500x), (b) – Decarburized sample from the surface to the core (Magnification = 60x), (c) – Decarburized sample near the surface (Magnification = 2400x), (d) – Decarburized sample at its core (Magnification = 600x).

source not found. – c). At the core, colonies of smaller carbides form the characteristic microstructure of a high chromium cast iron (**Error! Reference source not found.** – d). This sample's microstructure as well as the decarburization effect on it is described in more detail elsewhere [21].

After being exposed to the sand particles impingement, visible erosion pits can be seen on the samples' surfaces as seen in **Error! Reference source not found.**. Mass losses of 1.48% and 0.6% were registered for the decarburized and non-decarburized samples respectively.

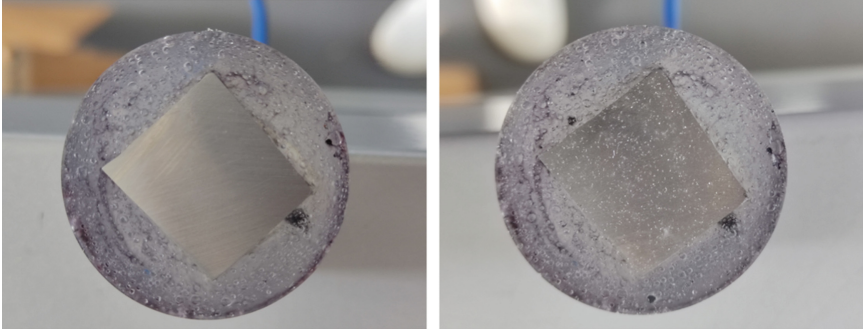


Fig. 4. Image of a non-decarburized sample before erosion (left) and after erosion (right)

The results of the corrosion testing provided the alloys' electrical parameters, given in **Error! Reference source not found.**, as well as the potentiodynamic curves shown in **Error! Reference source not found.**.

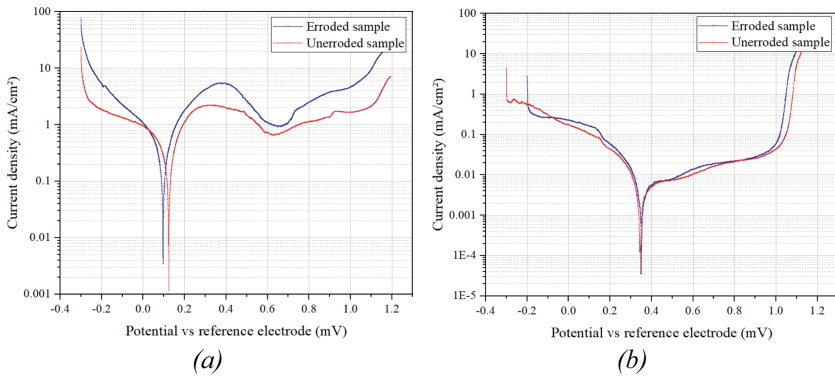


Fig. 5. Image of a non-decarburized sample before erosion (left) and after erosion (right)

Pitting was more severe in the case of the decarburized sample as shown by the SEM observations on the surface of both samples (**Error! Reference source not found.** – a).

EDX analysis also show that the decarburized sample retained high content in chlorides even after cleaning (**Error! Reference source not found.**).

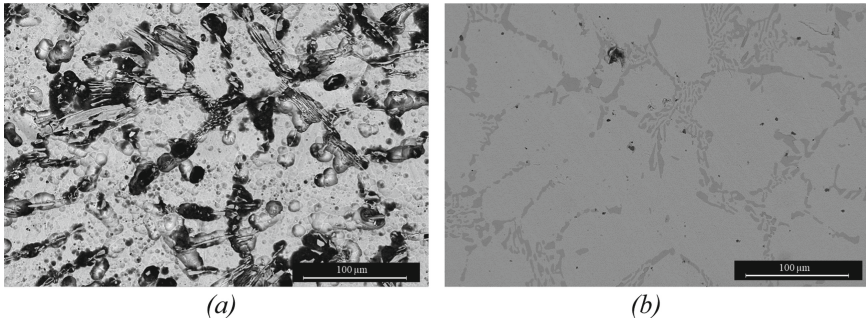


Fig. 6. Circular BackScatter SEM micrographs of the surfaces of both samples after submersion in a 3.5% NaCl solution (Magnification = 500x): (a) – Sample A (decarburized sample), (b) – Sample B (Non-decarburized sample)

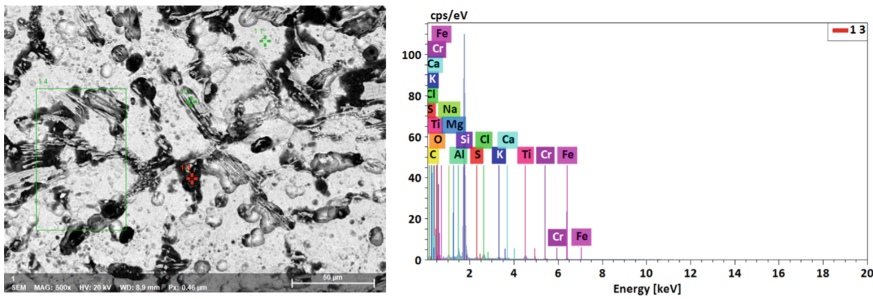


Fig. 7. SEM micrograph and corresponding EDX diffractogram of an elemental analysis at one of the corrosion pits

Surface hardness, as determined in the previous study, reached a value of around 20 HBW. In this study, microhardness curves were done for each sample's cross-section starting 0.3 mm from its surface and moving into the core material. The results (**Error! Reference source not found.**) show that, unlike the decarburized sample where a sharp loss of hardness occurs between the surface and the core material, sample A is unaffected and presents a nearly constant hardness value.

Microstructurally, it can be seen that unlike sample B, sample A was exposed to a heat treatment which lead to its decarburization. The decarburized layer itself reach depths of only up to 1.2 mm, but the effects of heat treatment are noticeable until the 2 mm mark. In this intermediary layer, heat treatment led to the formation of a continuous network of thin carbides that facilitate cracking propagation [21], [23]. An outer layer can also be observed around the carbides where carbon content lowers by 49% due to the decarburization effect (**Error! Reference source not found.**).

Resistance to corrosion was also affected. Sample B, the non-decarburized sample, exhibited similar electrochemical behavior before and after erosion as both curves were almost superposed one on top of the other. The curves were characterized by a short-lived oxide layer following the corrosion potential that was almost identical in both cases. This is followed by a pseudo-passive state where the current density increase is small

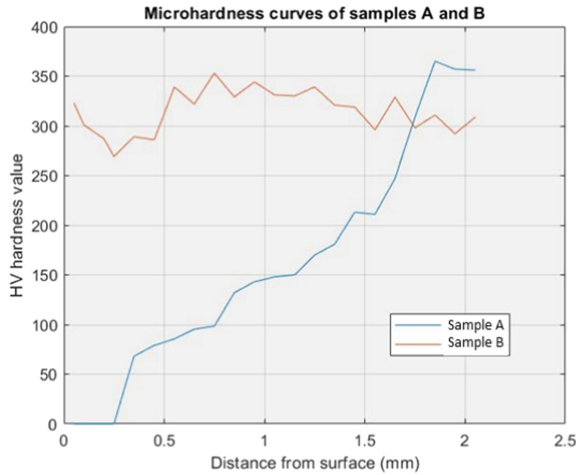


Fig. 8. Microhardness curve measured on the cross-section of decarburized sample

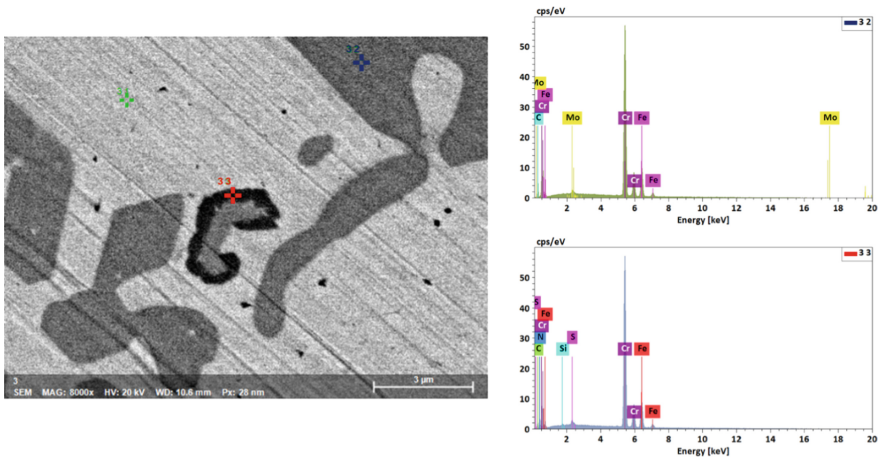


Fig. 9. SEM micrograph and corresponding EDX diffractograms of the elemental analysis done at the carbide (blue) and at its outer layer (red)

starting from a minimum value of $21.685 \mu\text{A}/\text{cm}^2$ in the case of the non-eroded sample and $29.715 \mu\text{A}/\text{cm}^2$ in the case of the eroded sample. Beyond 1 V, the passive layer is destroyed in both cases. In the zones where some difference was noticeable, such as the zone between 500 mV and 700 mV, current densities were lower in the uneroded case. As for sample A, although the overall shapes of both curves are also similar, differences in the electrochemical parameters were more pronounced. The overall resistance to the environment is lower as well. A significant increase in the corrosion current density, I_{CORR} , was detected after erosion testing as well as an increase of the passive current density, i_p , to a value of $1.15 \text{ mA}/\text{cm}^2$. An active-passive transition peak can be seen after the Tafel region, followed by a less protective pseudo-passive layer. In that region, current

densities were two orders of magnitudes higher than they were in the non-decarburized case. The layer's stability only lasted in the vicinity of the 600 mV mark. Current densities increased at a larger rate than they were for sample B reaching values above 5 mA/cm^2 just before reaching the water oxidation potential at around 1.1 V.

This difference, before and after erosion, is due to the well-known erosion-enhanced corrosion mechanism where the local acidification that happens in the generated erosion pits causes accelerated corrosion rates and makes passive layer formation harder to establish in Ref [7]. Next, The removal of work hardened surfaces (caused by continuous particle impingement) by corrosion is another synergy mechanism that is worth noting as it exposed unhardened surfaces to more erosion.

Finally, the detachment of grains and the intensive cracking at the carbide-matrix interface provided paths for the corrosive agents to penetrate deeper into the material which accelerated corrosion. This can be seen from a cross-sectional SEM examination of sample A shown in **Error! Reference source not found.** below. It shows that, even after polishing was done carefully, carbides were absent and left a porous layer that acts similarly to erosion pits and further accelerates corrosion rates.

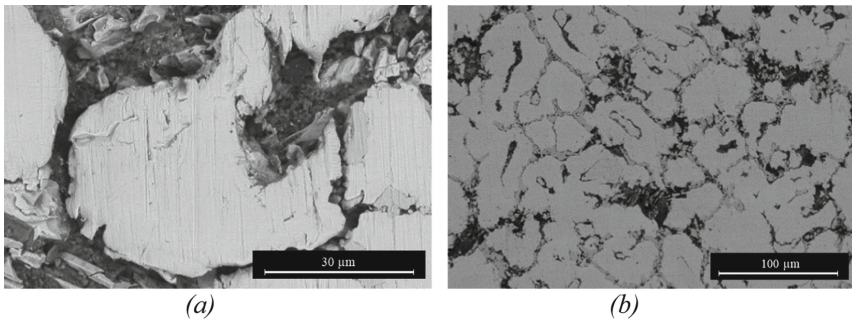


Fig. 10. SEM micrographs of a decarburized high chromium cast iron sample at a magnification of: (a) – $\times 2400$, (b) – $\times 600$

Furthermore, surface hardness values affect those synergy mechanisms as well as the lower surface hardness value in the case of the decarburized sample, which was caused by the reduced carbide volume fraction, which means that its surface is more vulnerable to sand impingement which could result in deeper erosion pits. This will in turn accelerate corrosion rates and make passivation harder to establish in this case as was observed in the polarization curves.

4 Conclusion

The effect of decarburization on the erosion-corrosion resistance of a high chromium cast iron has been investigated in this study. It has been found that several erosion impingements on the surface of the studied alloys reduced its corrosion resistance properties through increased corrosion and passive current densities and a reduced passive domain.

It has also been found that decarburization in these alloys further reduces those parameters, as well as causing a higher susceptibility to pit and that the effect of erosion on those samples is more pronounced than their non-decarburized counterparts. Further study of the erosion-corrosion resistance of these alloys can be of use to slurry pump manufacturers and their clients, and the use of an experimental test bench that is designed with the various currents inside a slurry pump in mind will be the subject of future studies.

Acknowledgments. The authors would like to thank OCP Group S.A. for providing the data and samples used for this study.

Statements and Declarations.

Funding: This work was financially supported by the OCP foundation; Grant no: MAT-NAA-01–2017, 2018.

Financial Interests: The authors declare that they have no known competing financial interests or personal relationships that could have appeared to influence the work reported in this paper.

References

1. Dorozhkin, S.V.: Fundamentals of the wet-process phosphoric acid production 2 kinetics and mechanism of $\text{CaSO}_4 \cdot 0.5\text{H}_2\text{O}$ surface crystallization and coating formation. *Ind. Eng. Chem. Res.* **36**(2), 467–473 (1997)
2. Aiming, F., Jinming, L., Ziyun, T.: Failure analysis of the impeller of a slurry pump subjected to corrosive wear. *Wear* **183**, 876–882 (1995)
3. Hajji, M.A., Guenbour, A., Jallouli, E.M., Ben Bachir, A., BELCADI, S.: Influence des chlorures et des sulfures sur la corrosion des alliages inoxydables en milieu phosphorique. *Ann. Chim. Sci. des Matériaux* **27**(4), 27–38 (2002)
4. Alves, H., Agarwal, D., Stenner, F., Hoxha, A.: Alloys suitable for phosphoric acid applications. In: NACE - International Corrosion Conference Series, p. NACE-06221 (2006)
5. Harvey, T.J., Wharton, J.A., Wood, R.J.K.: Development of synergy model for erosion – corrosion of carbon steel in a slurry pot. *Tribol. – Mater. Surf. Interfaces* **1**(1), 33–47 (2007)
6. Islam, A., Farhat, Z.N., Ahmed, E.M., Alfantazi, A.M.: Erosion enhanced corrosion and corrosion enhanced erosion of API X-70 pipeline steel. *Wear* **302**, 1–10 (2013)
7. Wood, R.J.: Erosion-corrosion synergism for multi-phase flowline materials. *La Houille Blanche* **7**(8), 3–8 (1992)
8. Wood, R.J.K., Hutton, S.P.: The synergistic effect of erosion and corrosion: trends in published results. *Wear* **140**(2), 387–394 (1990)
9. Tabrett, P., Sare, I.R., Ghomashchi, M.R.: Microstructure-property relationships in high chromium white iron alloys. *Int. Mater. Rev.* **41**(2), 59–82 (1996)
10. Powell, G.L.F., Brown, I.H., Nelson, G.D.: Tough hypereutectic high chromium white iron – a double in situ fibrous composite. *Adv. Mater. Res.* **32**, 111–114 (2008)
11. Guitar, M.A., et al.: High chromium cast irons: destabilized-subcritical secondary carbide precipitation and its effect on hardness and wear properties. *J. Mater. Eng. Perform.* **27**(8), 3877–3885 (2018)
12. Karantzalis, A.E., Lekatou, A., Diavati, E.: Effect of destabilization heat treatments on the microstructure of high-chromium cast iron: a microscopy examination approach. *J. Mater. Eng. Perform.* **18**(8), 1078–1085 (2009)

13. Cioffi, R.D.: A comparison study on depth of decarburization and the role of stable carbide forming elements in 1075 plain carbon steel and 440A stainless steel (2012)
14. Efremenko, V.G., Chabak, Yu.G., Lekatou, A., Karantzalis, A.E., Efremenko, A.V.: High-temperature oxidation and decarburization of 14.55 wt pct Cr-Cast Iron in Dry Air Atmosphere. *Metall. and Mater. Trans. A.* **47**(4), 1529–1543 (2016). <https://doi.org/10.1007/s11661-016-3336-7>
15. Cramer, S.D., Covino, B.S. (eds.): *Corrosion: Materials*. ASM International (2005). <https://doi.org/10.31399/asm.hb.v13b.9781627081832>
16. Sydberger, T., Nordin, S.: Corrosivity of wet process phosphoric acid. *Corrosion* **34**(1), 16–22 (1978)
17. ElJersifi, A., Chbihi, A., Semlal, N., Bouaouine, H., Naamane, S.: “Failure analysis of a high chromium carbon steel impeller operating in phosphoric acid slurry. *Wear* **476**(15), 203660 (2021)
18. Matal, A., Karim, M., Naamane, S.: Development and calibration of an experimental test bench simulating solar reflectors erosion. *Sol. Energy* **201**(2019), 724–731 (2020)
19. Vardavoulias, M., Papadimitriou, G., Pantelis, D.: Effect of $M7C3 \rightarrow M23C6$ transformation on fracture behaviour of cast ferritic stainless steels. *Mater. Sci. Technol.* **9**(8), 711–717 (1993)



Experimental Research on New Sustainable Geopolymer Mortars Reinforced and Not Reinforced with Natural Fibers

Alberto Viskovic¹(✉), Michał Lach², Łukasz Hojdys³, Piotr Krajewski³, and Arkadiusz Kwiecien³

¹ University “G. d’Annunzio” of Chieti-Pescara, Chieti, Italy
a.viskovic@unich.it

² Faculty of Materials Science and Physics, Cracow University of Technology, Kraków, Poland

³ Faculty of Civil Engineering, Cracow University of Technology, Kraków, Poland

Abstract. The paper describes experimental research voted to verify the mechanical characteristics of very sustainable geopolymer mortars and to try to improve their mechanical characteristic using natural fibers.

Particularly, there were used and tested geopolymer mortars using a geopolymer matrix obtained from very cheap and sustainable fly ashes (as they come from the waste recycling). About the natural fibers, they were used hemp short fibers as they are very durable and sustainable.

It was designed and performed a bending test program for twelve reference samples of geopolymer mortar beams (without fibers) divided into two group of six samples with different proportions between fly ashes and sand. Then, it was designed and performed the bending test program for the geopolymer mortars with the addition of hemp short fibers: twelve samples with a lower percentage of fiber and twelve samples with a higher percentage of fibers. Each group of twelve samples was divided into two group of six samples with different proportions between fly ashes and sand.

Then it was designed and performed a compression test program: there were used the same beams, after their cracking in the bending tests, to obtain cubic samples (after a regularization of the faces). Thus, there were twenty-four reference cubic samples without fibers and forty-eight cubic samples with fibers for the compression tests.

Keyword: Sustainable mortars · Geopolymer mortars · Fly ashes · Natural fibers · Hemp fibers · Experimental laboratory tests · Mortars mechanical characteristics

1 Introduction

1.1 The Research Background Philosophy

To improve human sustainability on our planet, the buildings construction and the buildings use sectors are also involved.

In the last decades the attention was mainly oriented to the reduction of energy demand during the use of the buildings and to the reduction of a building footprint considering all its life, from the construction up to the demolition. But for the building footprint the attention was initially focused only on the non-structural materials and elements. It is time to consider that the structural materials are a big part of the total material used in a building.

In all the buildings' structural typologies, today in use, there is a large use of steel and Portland cement mortars and concretes. Both steel and Portland cement, have a large footprint in terms of CO₂ emissions during their production processes. Thus, improving of sustainability is directly related to a reduction of the use of steel and Portland cement. The Portland cement may be substitute with natural hydraulic cements (like the pozzolanic cement) or geopolymers. Geopolymers may be obtained starting from pozzolanic or tufa rock powder or by fly ashes produced in waste incinerators.

1.2 The Research Specific Target

The specific target of the research was to verify the mechanical characteristics of a geopolymer mortar and to try to improve their mechanical characteristic. For this last aim it was interesting to use a dispersion of short natural fibers.

Particularly they were used and tested geopolymer mortars using a geopolymer matrix obtained from very cheap and sustainable fly ashes (as they come from the waste recycling).

2 Background Knowledge

2.1 Materials Defined "Geopolymers"

The term "geopolymer" identifies a vast class of inorganic materials with a polymeric structure, (both synthetic and natural). In the broadest sense of the term, they are inorganic materials whose structure resembles that of classic organic polymers. However, the same term can also refer to ceramic materials formed by chemical reaction at relatively low temperatures (below 350 °C), whose mechanical resistance is comparable to that of many traditional high temperature consolidated ceramics [1].

Geopolymers are therefore synthetic materials which, obtained by chemical reaction between an activating solution and a reactive powder, are consolidated at low temperatures from the environment to a maximum of about 120 °C, obtaining a material with excellent chemical and physical properties and with a wide range of potential applications [2]. Depending on the raw materials, extremely different geopolymer products are obtained.

2.2 Historical Notes About Geopolymers

In the 40s of the last centuries, it was discovered that alkaline activation was an efficient method to accelerate the latent pozzolanic activity of aluminosilicate minerals rich in calcium such as blast furnace slag. In these systems the water-mineral interactions are

accelerated by the presence of alkali in the solution, with a consequent rapid hardening [3–5]. These “alkali-activated slag cements” or Trief, were used on a large scale in building materials until the early 1950s.

Between 1960 and 1970, Victor Glukhovsky, a scientist of Ukrainian origin active at the Kiev Institute of Civil Engineering (KICE, USSR), made the greatest contribution in the identification of hydrated calcium silicates and calcium and sodium aluminosilicates hydrates as phases which formed during the above process [6]. In his studies, he also noticed how the clays reacted during the alkaline treatment to give sodium aluminosilicates hydrates. Glukhovsky called the cements produced with this technology “silicate concrete soil” (1959) and the binders “cement soil” (1967).

Flint et al. [7], in 1946, at the National Bureau of Standards, developed an alumina extraction process starting from a bauxite with a high silica content, in which one of the intermediate stages involved the precipitation of a compound simil-hydrosodalite. Only three years later, Borchert and Keidel prepared hydrosodalite by reacting kaolinite with a concentrated solution of NaOH at 100 °C. In 1963, Howell achieved the synthesis of zeolite “A” using calcined kaolin instead of kaolinite. In 1969, Bessons, Caillér and Hénin [8], at the French museum of natural history in Paris, developed the synthesis of hydrosodalite starting from various phyllosilicates (kaolinite, montmorillonite and halloysite) at 100 °C in concentrated caustic soda.

The geopolymers properly named were developed only in 1976 by Joseph Davidovits. The great interest on these materials developed as a result of numerous catastrophic fires that occurred in France between 1970 and 1972; events amplified by the extensive use of common organic plastics. The development of non-combustible and non-flammable plastic materials thus became the main target of Davidovits’ career, who developed aluminosilicate materials with amorphous to semi-crystalline networks, which he called “geopolymers” [9, 10].

These new materials saw their first application as fire resistant construction products, between 1973 and 1976, for example, as chipboard panels coated on both sides with geopolymer nanocomposite material produced in a single stage [11]. However, the real turning point came between 1978 and 1980, when the Davidovits’ company developed a geopolymeric liquid binder by reacting a meta-kaolin with an alkaline silicate solution. The patent for this discovery was filed in 1979 and was called “Geopolymite” [12]. From the first Davidovits patent to today, interest in these materials has grown enormously, especially since the early 21st century, with a relative increase in scientific publications and congresses on the subject.

3 Experimental Research

3.1 Experimental Tests Program

It was designed a bending test program for twelve reference samples of geopolymer mortar beams (without fibers) divided into two group of six samples with different proportions between fly ashes (Fig. 1a) and sand. Then, it was designed the bending test program for the geopolymer mortars with the addition of hemp short fibers (Figs. 1b, 1c): twelve samples with a lower percentage of fiber and twelve samples with a higher

percentage of fibers. Each group of twelve samples was divided into two group of six samples with different proportions between fly ashes and sand.



Fig. 1. Fly ashes (a), different type of natural (not treated) hemp fibers (b) and (c).

Thus, it was also designed to use the same beams, after their cracking in the bending tests, to obtain cubic samples (after a regularization of the faces) for compression tests. The program was to have up to a maximum of twenty-four reference cubic samples without fibers and forty-eight cubic samples with fibers for the compression tests.

3.2 Sample Preparation

Two variants of geopolymer mortar samples with the addition of natural mixed fibers (dry) and reference samples without the addition of fibers were made. The samples were made in the form of $4 \times 4 \times 16$ cm, 6 pieces of each batch:

- 1) samples based on fly ash (70%), general construction sand (30%);
- 2) samples based on fly ash (50%), general construction sand (50%);
- 3) samples based on fly ash (70%), general construction sand (30%) and natural fibers in the amount of 1% by weight;
- 4) samples based on fly ash (70%), general construction sand (30%) and natural fibers in the amount of 3% by weight;
- 5) samples based on fly ash (50%), general construction sand (50%) and natural fibers in the amount of 1% by weight;
- 6) samples based on fly ash (50%), general construction sand (50%) and natural fibers in the amount of 3% by weight.

All the samples solidification was activated with 10M r-r NaOH and sodium glass in a ratio of 2.5 by weight at a temperature of 75 °C for at least 16 h. Then the samples were disassembled and left in the same conditions (ambient temperature 20 °C and 50% air humidity) for 28 days of seasoning. In the case of samples with fibers, the fibers were added just after a first mixing with the activator solution.

3.3 Experimental Tests

There were carried out two typologies of test:

- a) four-point bending test on beams 40x40x160mm³, based on the standard EN 12390–5,
- b) compression test on cubic samples (halves beam, 40x40x40mm³) obtained cutting the cracked sample after the bending test.

There were calculated the mean and the characteristic values of strengths. The characteristic values were determined according to EC0 Annex D (values of kn factor are taken from Table D1).

Bending Tests. In Table 1 are reported the bending test results, for the reference samples based on fly ash (70%) and general construction sand (30%). Data are provided in terms of tensile strength by bending ($f_{t,fl}$) and the evaluations of the mean value ($f_{t,fl,mean}$), the standard deviation (SD) and the characteristic value ($f_{t,fl,k}$).

Table 1. Bending tests (1) reference samples. Fly ash (70%), sand (30%): tensile strength by bending ($f_{t,fl}$), mean value ($f_{t,fl,mean}$), standard deviation (SD) and characteristic value ($f_{t,fl,k}$)

Sample	F _{max}	$f_{t,fl}$	$f_{t,fl,mean}$	SD	CV	kn EC0	$f_{t,fl,k}$
	N	N/mm ²	N/mm ²	N/mm ²			N/mm ²
7030_0p1	2014.375	4.72119					
7030_0p2	2530.448	5.93074					
7030_0p3	3530.756	8.27521					
7030_0p4	2565.255	6.01232					
7030_0p5	2390.918	5.60371					
7030_0p6	3415.918	8.00606	6.42	1.41	0.22	2.18	3.36

In Table 2 are reported the same bending test results for the reference samples based on fly ash (50%) and general construction sand (50%). In Fig. 2a and b are reported, respectively, the fracture surfaces in reference samples based on fly ash (70%) and general construction sand (30%) (a) and based on fly ash (50%) and general construction sand (50%) (b).

Table 2. Bending tests (2) reference samples. Fly ash (50%), sand (50%).

Sample	Fmax	f _{t.fl}	f _{t.fl.mean}	SD	CV	kn _{EC0}	f _{t.fl.k}
	N	N/mm ²	N/mm ²	N/mm ²			N/mm ²
5050_0p1	4006.95	9.39129					
5050_0p2	3196.602	7.49204					
5050_0p3	3440.173	8.06291					
5050_0p4	3540.54	8.29814					
5050_0p5	3760.65	8.81402					
5050_0p6	3843.399	9.00797	8.51	0.69	0.08	2.18	7.00

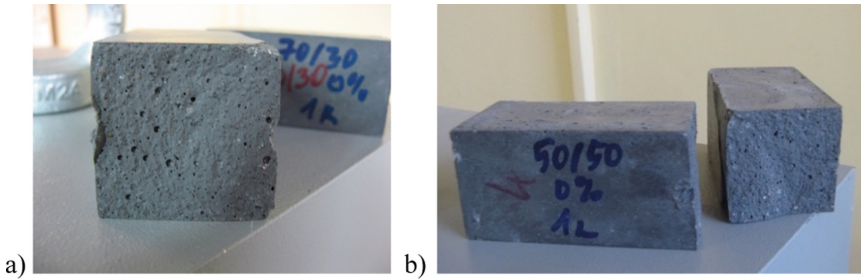


Fig. 2. Fracture surface in a reference sample based on: fly ash (70%) and general construction sand (30%) (a); fly ash (50%) and general construction sand (50%) (b).

In Table 3 is reported the summary of the bending test results, in terms of tensile strength by bending mean value, standard deviation and characteristic value, for each different sample typology: “7030_0p” fly ash (70%), general construction sand (30%) and fibers (0%); “5050_0p” fly ash (50%), general construction sand (50%) and fibers (0%); “7030_1p” fly ash (70%), general construction sand (30%) and fibers (1%); “5050_1p” fly ash (50%) and general construction sand (50%) and fibers (1%); “7030_3p” fly ash (70%), general construction sand (30%) and fibers (3%); “5050_3p” fly ash (50%) and general construction sand (50%) and fibers (3%).

Table 3. Summary of the bending tests results.

Type of sample	f _{t.fl.mean}	SD	f _{t.fl.k} (EC0)
	N/mm ²	N/mm ²	N/mm ²
7030_0p	6.42	1.41	3.36
5050_0p	8.51	0.69	7.00

(continued)

Table 3. (continued)

Type of sample	$f_{t.fl.mean}$	SD	$f_{t.fl.k. (EC0)}$
7030_1p	7.30	0.87	5.40
5050_1p	8.31	0.41	7.43
7030_3p	6.70	0.35	5.92
5050_3p	7.76	0.99	5.59

In Fig. 3a, b, c and d are reported, respectively, the fracture surfaces in samples based on: fly ash (70%), general construction sand (30%) and fibers (1%) (a); fly ash (50%), general construction sand (50%) and fibers (1%) (b); fly ash (70%), general construction sand (30%) and fibers (3%) (c); fly ash (50%) and general construction sand (50%) and fibers (3%) (d).

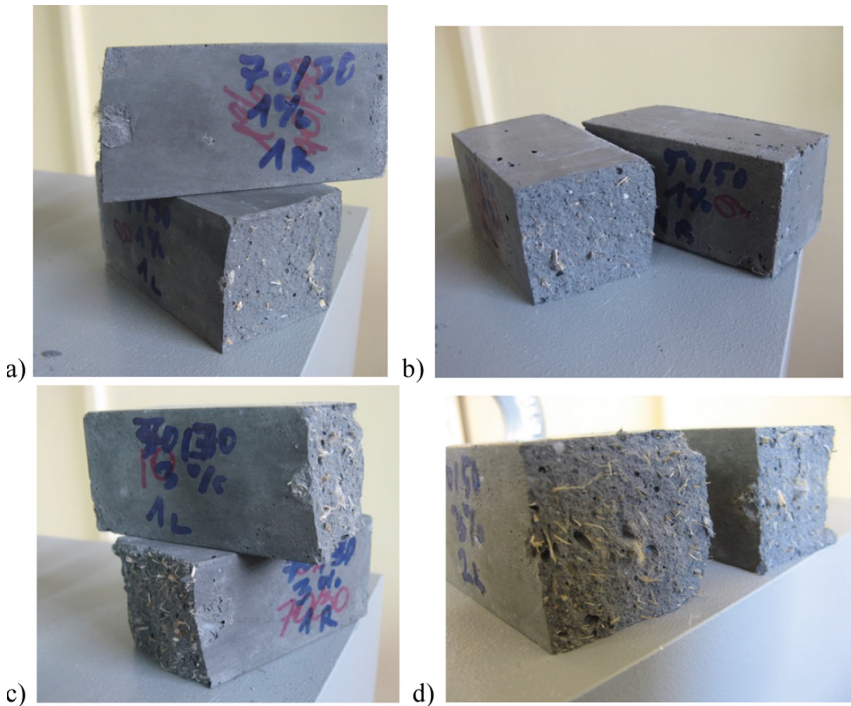


Fig. 3. Fracture surface in a sample based on: fly ash (70%), general construction sand (30%) and fibers (1%) (a); fly ash (50%), general construction sand (50%) and fibers (1%) (b); fly ash (70%), general construction sand (30%) and fibers (3%) (c); fly ash (50%), general construction sand (50%) and fibers (3%) (d).

Compression Tests. In Table 4 are reported the compression test results, for the reference samples based on: fly ash (70%) and general construction sand (30%). Data are provided in terms of compression strength (f_c) and the evaluations of the mean value ($f_{c,mean}$), the standard deviation (SD) and the characteristic value (f_{ck}).

The final letter L and R in the sample name simply indicate that they are obtained two sample, “half Right” and “half Left”, from the same sample used in the previous bending test. The mean value, the standard deviation and the characteristic value are calculated on all the samples, L and R together.

Table 4. Compression tests (1) reference samples. Fly ash (70%), sand (30%): compression strength (f_c), mean value ($f_{c,mean}$), standard deviation (SD) and characteristic value (f_{ck}).

Sample	Fmax	f_c	$f_{c,mean}$	SD	CV	kn _{EC0}	$f_{ck,EC0}$
	kN	N/mm ²	N/mm ²	N/mm ²			N/mm ²
7030_0p1L	89.27	55.79					
7030_0p1R	88.05	55.03					
7030_0p2L	100.02	62.51					
7030_0p2R	98.25	61.41					
7030_0p3L	93.65	58.53					
7030_0p3R	91.16	56.98					
7030_0p4L	99.18	61.99					
7030_0p4R	98.02	61.26					
7030_0p5L	97.71	61.07					
7030_0p5R	96.32	60.20					
7030_0p6L	90.87	56.79					
7030_0p6R	100.85	63.03	59.5	2.79	0.05	1.87	54.3

In Table 5 are reported the same compression test results for the reference samples based on fly ash (50%) and general construction sand (50%).

Table 5. Compression tests (2) reference samples. Fly ash (50%), sand (50%).

Sample	Fmax	f_c	$f_{c,mean}$	SD	CV	kn _{EC0}	$f_{ck,EC0}$
	kN	N/mm ²	N/mm ²	N/mm ²			N/mm ²
5050_0p1L	99.52	62.20					
5050_0p1R	102.34	63.96					

(continued)

Table 5. (continued)

Sample	Fmax	f _c	f _{c.mean}	SD	CV	kn _{EC0}	f _{ck EC0}
5050_0p2L	96.81	60.51					
5050_0p2R	103.59	64.74					
5050_0p3L	105.04	65.65					
5050_0p3R	97.92	61.20					
5050_0p4L	107.61	67.26					
5050_0p4R	103.42	64.64					
5050_0p5L	109.86	68.66					
5050_0p5R	108.14	67.59					
5050_0p6L	108.89	68.06					
5050_0p6R	102.96	64.35	64.9	2.68	0.04	1.87	59.9

In Fig. 4a and b are reported, respectively, the photo of the compression test on a reference sample based on fly ash (70%) and general construction sand (30%) (a) and based on fly ash (50%) and general construction sand (50%) (b).

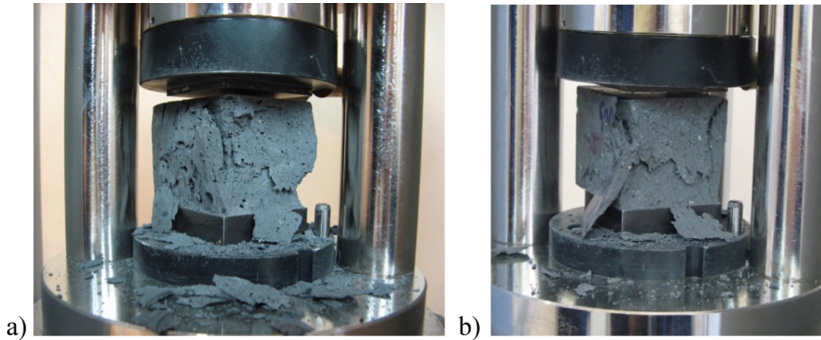


Fig. 4. Compression collapse in a reference sample based on: fly ash (70%) and general construction sand (30%) (a); fly ash (50%) and general construction sand (50%) (b).

In Table 6 is reported the summary of the compression test results for each type of sample typology, in terms of compression strength mean value, standard deviation and characteristic value.

Table 6. Summary of the compression tests results.

Type of sample	$f_{c..mean}$	SD	$f_{ck. (EC0)}$
	N/mm^2	N/mm^2	N/mm^2
7030_0p	59.5	2.79	54.3
5050_0p	64.9	2.68	59.9
7030_1p	54.7	4.49	46.3
5050_1p	53.8	3.84	46.6
7030_3p	41.7	3.36	35.4
5050_3p	43.9	2.73	38.8

In Fig. 5a and b are reported, respectively, the compression collapses in samples based on fly ash (70%), general construction sand (30%) and fibers (1%) (a); based on fly ash (50%), general construction sand (50%) and fibers (1%) (b).

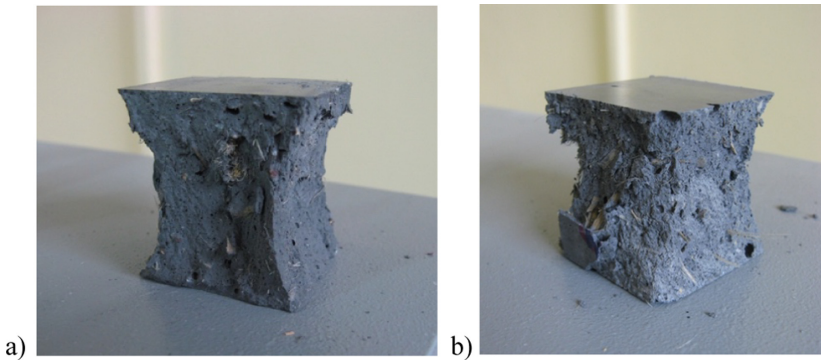


Fig. 5. Compression collapse in a sample based on: fly ash (70%), general construction sand (30%) and fibers (1%) (a); fly ash (50%), general construction sand (50%) and fibers (1%) (b).

In Fig. 6a and b are reported, respectively, the compression collapses in samples based on fly ash (70%), general construction sand (30%) and fibers (3%) (a); based on fly ash (50%) and general construction sand (50%) and fibers (3%) (b).

4 Observations on the Geopolymer Mortars Tests Results

The results show a general better performance in the case of 50% - 50% proportions between fly ashes and sand. Moreover, in the case of that 50%-50% proportions, the reference samples show a higher tensile resistance which is only 1/8,5 of the respective compression strength, against a ratio 1/16 (between tensile and compression strength) in the case of 70%-30% proportions between fly ashes and sand. But what is more noticeable, it is a very high compression strength in both cases: $f_{ck} = 54,3N/mm^2$ (for

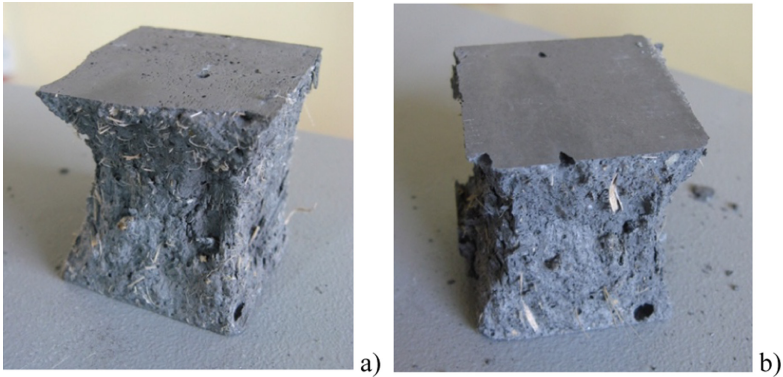


Fig. 6. Compression collapse in a sample based on: fly ash (70%), general construction sand (30%) and fibers (3%) (a); fly ash (50%), general construction sand (50%) and fibers (3%) (b).

70%-30% proportions) and $f_{ck} = 59,9\text{N/mm}^2$ (for 50%-50% proportions), the double of the better traditional mortars. These geopolymer mortars may be considered very “super mortars” and named “M50” in comparison to the normal ones.

Adding a 1% of fibers by weight, there is an increment in tensile resistance in both cases of proportions between fly ashes and sand. On the contrary, adding a 3% of fibers there is an increment in tensile resistance in case of 70%-30% proportions, while there is a decrement in case of 50%-50% proportions. On the contrary to that was expected, adding hemp fibers, the compression strength decreases in any case: $f_{ck} = 46,3\text{N/mm}^2$ and $f_{ck} = 46,6\text{N/mm}^2$, respectively in case 70%-30% and 50%-50% proportions and 1% of fibers, while they are $f_{ck} = 35,4\text{N/mm}^2$ and $f_{ck} = 38,8\text{N/mm}^2$, respectively in case 70%-30% and 50%-50% proportions and 3% of fibers. This means that the increment in tensile strength don't give a confinement effect to the mortar (with a consequent supposed increment in compression strength) as it generally happens with normal mortars. These results may be explained with a different mechanical behavior of the geopolymer mortars respect to the traditional ones and it may be related to the higher performances of the binder basic geopolymer material.

In any case the geopolymer mortars with fibers have very high compression strengths in comparison to the traditional ones and may be considered “M40” in case of 1% of fibers and “M30” in case of 3% of fibers by weight. Moreover, there is a better ratio (respect to the normal mortars) between the tensile and compression strength: they are 1/8,5 and 1/6,3 respectively with 70%-30% and 50%-50% proportions between fly ashes and sand, with 1% of fibers; while they are 1/6 and 1/7 respectively with 70%-30% and 50%-50% proportions, with 3% of fibers.

5 Conclusions and Future Research

The results show as the geopolymer binder material has a very different behavior respect the Portland binder or the pozzolanic or others natural hydraulic mortar binders. The future research may follow some different paths and purposes:

- a) to research of higher mechanical performances for the geopolymer mortars, without adding fibers,
- b) to use geopolymer mortars as matrix for FRCM like reinforcements for historical masonries (to bond natural fiber fabric to masonry surfaces),
- c) to search a better use of the short fibers, that may be useful to obtain lighter structural geopolymer materials.

In the (a) case, the research has to be oriented to find the better mix design in terms of proportions between fly ashes and sand and in terms of the better calibration of diameters of the sand granules or in terms of a good mix of different sand diameters; moreover, the research has also to find the better proportions among the activator, the fly ashes and the sand, in relation of the different porosity of different sands.

In the (b) case, using an improved geopolymer mortar (from case (a)), it may be interesting to study the debonding strength of FRCM like reinforcements.

In the (c) case, it may be useful to explore the field of prefabricated structural and non-structural elements.

References

1. Roy, D.M.: New Strong Cement Materials: Chemically Bonded Ceramics. *Science* **235**(4789), 651–658 (1987). <https://doi.org/10.1126/science.235.4789.651>
2. Duxson P.: The structure and thermal evolution of metakaolin geopolymers: PhD Thesis, University of Melbourne, Australia (2006)
3. Khale, D., Chaudhary, R.: Mechanism of geopolymerization and factors influencing its development: a review. *J. Mater. Sci.* **42**(3), 729–746 (2007). <https://doi.org/10.1007/s10853-006-0401-4>
4. Duxson, P., Fernández-Jiménez, A., Provis, J.L., Lukey, G.C., Palomo, A., van Deventer, J.S.J.: Geopolymer Technology: The Current State of the Art. *J. Mater. Sci.* **42**, 2917–2933 (2007). <https://doi.org/10.1007/s10853-006-0637-z>
5. Lee, W.K.: Solid-Gel Interactions in Geopolymers: Ph.D. Thesis, University of Melbourne, Australia (2002)
6. Glukhovskiy, V.D. Soil silicates, their properties, technology and manufacturing and fields application, Doct Tech Sc. Degree Thesis, Civil Engineering Institute, Kiev, Ukraine (1965)
7. Flint, E.P., Clarke, W.F., Newman, E.S., Shartsis, L., Bishop, D.L., Wells, L.S.: Extraction of Alumina from Clays and High-Silica Bauxites. *J. Res. Nat. Bur. Stand.* **36**, 63 (1946)
8. Besson, H., Caillere, S., Henin, S.: Conditions for preparation of hydrosodalite at low temperature (in French). *C. Rend. Acad. Sci.* **D269**, 1367 (1969)
9. Davidovits, J.: (2008 1st edition – 2020 5th edition) *Geopolymer Chemistry & Applications - Chapt. 1*, Institut Géopolymère (Geopolymer Institute), Saint-Quentin, France, ISBN 9782954453118
10. Davidovits, J.: 30 years of successes and failures in geopolymer applications. Market trends and potential breakthrough. Geopolymer 2002 conference. October 28–29 2002 Melbourne, Australia (2002)
11. US Patent 3,950,47;4,028,454
12. FR Patent 2.424.227 04/09/1979



Mechanical Performance of Reinforced Pultruded Columns for Curtain Walls

Rosa Agliata^(✉), Michele Serpilli, and Placido Munafò

Università Politecnica delle Marche, DICEA, Ancona, Italy
r.agliata@staff.univpm.it

Abstract. The present work is aimed at evaluating the mechanical performance of pultruded beams subjected to bending stresses through experimental tests. Such beams are intended to be used in a curtain wall construction system as a variant to a patent application (n.102020000025636) which includes wood columns. This variant wants to meet the need of smaller dimensions of the columns and keep guaranteeing the mechanical performance. The columns are made of pultruded I-beams, reinforced with glued metal plates and two prestressed threaded bars placed in the central axis of symmetry of the section. First, the materials (pultruded, steel plates, threaded bars and structural glue) are mechanically characterized; then, three types of columns are tested by means of a 3-point bending test and 3 loading/unloading cycles: (i) n. 1 beam with no reinforcement plates or pretension bars, (ii) no. 2 beams with reinforcement plates and no pretension bars, (iii) no. 2 beams with reinforcement plates and pretension bars. The maximum deformation in the elastic range for all reinforced beams (11.48 mm) is measured by applying a load of approximately 10 kN, corresponding to a wind pressure of more than double the requirement for windows (2000 Pa). The contribution of the threaded bars to the maximum applicable load is negligible, which can be ascribed to their placement in the middle of the section. This first solution is chosen because of the small dimensions of the GFRP profile section.

Keywords: Pultruded columns · Mechanical performance · Curtain wall

Nomenclature

E_t	Young's modulus in tension
ε_t	Tensile strain
ε_y	Yielding strain
ε_{\max}	Tensile strain at failure
σ_t	Tensile strength
σ_y	Yielding stress
σ_{ys}	Tensile yield strength
σ_{\max}	Tensile strength at failure
τ	Shear strength
k	Stiffness
W_t	Working temperature

A_t	Application temperature
T_g	Glass transition temperature
S_t	Service temperature

1 Introduction

Within the curtain wall market segment, the current demand is increasingly oriented towards large glazed surfaces and transparent casing supported by lean frames (typically stainless steel or aluminum), to which the load of the glass panels is transferred [1, 2]. This trend leads to the need, also confirmed by the latest regulatory developments, of ever-growing high-performance (mechanical, energetic and environmental) materials and components.

Glass Fiber Reinforced Polymer (GFRP) pultruded profiles are a good solution to satisfy these requirements, thanks to their light, strong and durable features. GFRP matrix also has low thermal and electrical conductivity. All these characteristics made GFRP profiles started being used in many branches of civil engineering by the end of last century. Significant applications have been made in the field of windows frames [3, 4] but also bridges and building structures [5]. Thanks to their increase in structural applications, GFRP pultruded profiles have been widely investigated in their mechanical properties. A number of studies have been carried out on samples [6–9], also under critical conditions [10, 11], as well as on full-scale elements such as joints [12, 13], profiles [14] or panels [15]. Some studies also focused on GFRP behaviour when coupled with other materials [16–19].

In this work the mechanical performance of pultruded GFRP beams subjected to bending stresses is evaluated through laboratory tests. These beams are included in the patent n. 102015000087569 “Sistema per la realizzazione di facciate per edifici”, concerning smaller-section columns for curtain wall systems, reinforced with pretended bars or strands. They are intended to be used in a curtain wall construction system as a variant to a patent application (n.102020000025636) which involves wood columns (Fig. 1). Such curtain wall system has been designed to be structurally simpler, more flexible and rapid to assemble compared to the solutions available on the market, allowing effective and robust support even in the case of very large glazed panels (i.e., 3.00 x 3.00 m). Supplementary features are: low environmental impact thanks to the lower number of components compared to analogous solutions available on the market, good thermal insulation, possibility of both industrial and handcrafted production. In addition to the mentioned characteristics, the variant with the pultruded columns tested in this piece of research wants to meet the need of smaller dimensions of the columns, guaranteeing a comparable mechanical performance.



Fig. 1. Curtain wall system prototype.

2 Materials and Methods

The tested columns are made of pultruded GFRP I-beams (section 15.5 x 7.5 cm), reinforced with 2 mm thick metal plates (covering the entire upper surface of the wing) and two prestressed threaded M16 bars (Fig. 2). The steel plates, bonded to the beams at the upper surface of the wings with structural epoxy glue in the transversal direction, have the dual purpose of limiting the deformation of the GFRP and facilitating the use of bolted joints to fix the glazed panels. This avoids the insertion of bolts directly in pultruded profiles, which interrupts the fibres of the material and reduces its mechanical performance.

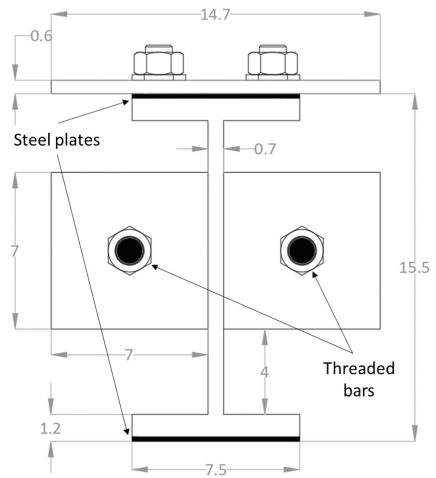
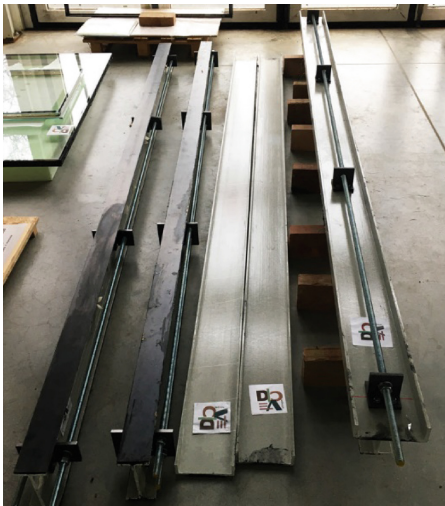


Fig. 2. Tested GFRP I-beams: picture (left) and sketch of the cross section (right)

The bars, bonded to the beam with two L-shaped steel profiles, have the purpose of increasing the GFRP bearing capacity and limit its deformations in order to contain the dimensions and better respond to the market demand requiring almost seamless surfaces. Because of the small dimensions of the profile section, and to make the curtain wall structure resistant to both wind pressure and depression, as a first solution the bars have been placed in the central axis of symmetry of the section. This solution is easy-to-make, though placing the rods closer to the profile wings would improve the mechanical response.

2.1 Material Characterization

This section describes the mechanical characteristics of the materials used in the experimental campaign, i.e., GFRP beams, steel plates, threaded bars and structural glue. GFRP pultruded profiles are manufactured by Fibrolux (Germany), S275JR steel plates are manufactured by Termoforgia (Italy), the structural adhesive is a two-component epoxy (2K) EPX (3M™ Scotch-Weld™ Epoxy Adhesive 7260). The properties of the materials, as reported by the manufacturers in their technical sheets, are reported in Tables 1 and 2.

Table 1. Technical and mechanical parameters of the GFRP profiles and steel plates as reported by manufacturers.

GFRP profiles*			Steel plates**			
E_t (GPa)	σ_t (MPa)	ε_t (%)	E_t (GPa)	σ_{ys} (MPa)	σ_t (MPa)	ε_t (%)
26	400	1.5	210	326.7	385.5	29.1

* according to EN 755–2

**according to EN 10025–2:2004.

Table 2. Technical and mechanical parameters of the adhesive as reported by manufacturer.

Adhesive	EPX
Chemical base	Two-part epoxy
Viscosity	Thixotropic
W_t (min)	16
A_t (°C)	15 ÷ 25
T_g (°C)	66.87
S_t (°C)	-40 ÷ 80
τ^* (MPa)	29.40*
E_t (MPa)	1500

(continued)

Table 2. (continued)

Adhesive	EPX
ε_t ** (%)	-
Use	Semi-Structural

* On aluminium-steel adherends

** At failure.

The mechanical properties of the threaded rods (M16, CL 8.8) have been previously experimentally characterized [18, 20] using tensile tests according to UNI EN 10002-1. The tensile tests were performed with a Zwick-Roell ZMART.PRO universal tensile machine with a loading speed rate of 1.27 mm/min. Table 3 shows the mechanical parameters measured by the tensile tests.

Table 3. Mechanical characteristics for M8 rods (experimental) [20].

Material	E_t (GPa)	σ_{max} (MPa)	ε_{max} (%)	σ_y (MPa)	ε_y (%)
M16 rods	214 ± 14.24	663.17 ± 7.45	0.65 ± 0.00	600 ± 9.01	0.28 ± 0.02

2.2 Test Settings

A 3-point bending test simulating the wind load to which the structural parts of a facade or windows can be subject, is carried out according to UNI EN ISO 14125 [21] on three types of columns: (i) n. 1 beam with no reinforcement plates or pretension bars (N), (ii) no. 2 beams with reinforcement plates and no pretension bars (R1, R2), (iii) no. 2 beams with reinforcement plates and pretension bars (RB1, RB2). The vertical force is applied by means of a hydraulic jack (maximum load 500 kN). A settling load of about 4 kN is first applied on the middle axis and then, removed. Next the transversal displacements are measured with 3 LVDT devices (whose position is shown in Fig. 3 and detailed in Table 4) by applying a load until a maximum deflection of $L/250$ is reached for each column, where L is the span of the beam. The beam is then unloaded. The loading/unloading cycle is repeated 3 times for each tested column. Figure 3 shows a sketch of the test setup and Table 4 reports the specifications of the tested columns.

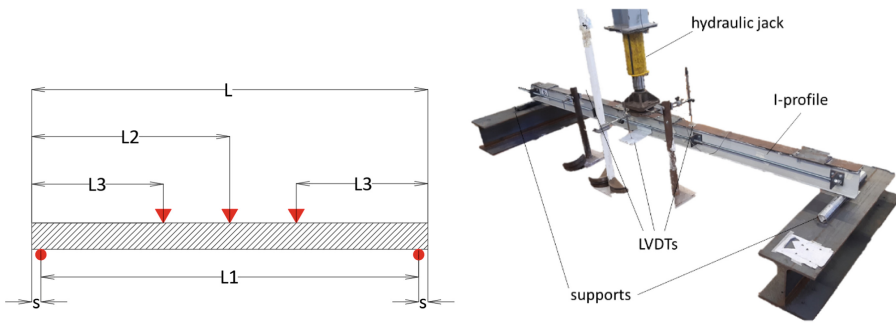


Fig. 3. Test setup: sketch (left) and picture (right). In the sketch, red triangles indicate the position of the LVDTs, red circles stand for the supports.

Table 4. Characteristics of the tested columns.

Column type	L (cm)	S (cm)	L1 = L-2s (cm)	L2 (cm)	L3 (cm)	$\delta_{lim_L/2} = L1/250$ (mm)
GFRP with no reinf. plates or pretens. bars (N)	305	7	291	152.5	100	11.64
GFRP with reinf. plates with and without pretens. bars (R and RB)	301	7	287	150.5	100	11.48

3 Results

Figure 4 shows the results of the 3-point bending test on all tested GFRP pultruded columns. The blue lines indicate data acquired by the LVDT placed at L/3-left side, green lines are for L/3-right side, orange lines indicate LVDT in the central axis (L/2). Red bar stands for the limit deformation of L1/250 for each column. Results are also summarized in Table 5. For N type column, only the L/3-right side curve is displayed since, for a technical issue, the L/3-left side measurement is not acquired.

The curves show a global linear trend for both loading/unloading phases. A nonlinear behavior is locally registered after the load changes its direction. The maximum applied load is comparable for all reinforced configurations (R_i and RB_i), with a maximum difference of 0.53 kN (5.3%) recorded between the two configurations reinforced with steel rods (RB1 and RB2). The stiffness, calculated as the average on the three load cycles for each column, is comparable for all configuration (except the N type, for which the shape of the load/displacement diagram made useless its calculation). These observations seem to show that in this case the contribution in strength of the threaded bars is negligible, which can be ascribed to the positioning of the rods in the central axis of the column. To improve the contribution of the bars, it is sufficient to move them

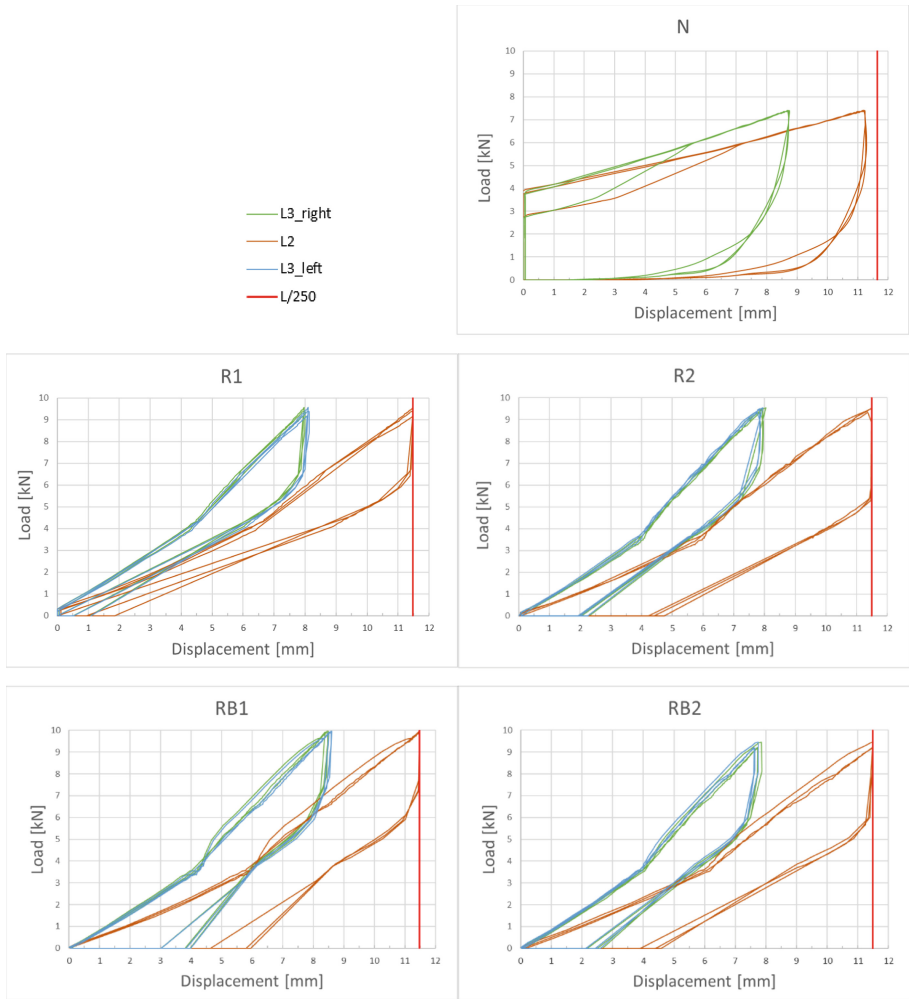


Fig. 4. Results of the 3-point bending test.

towards the section fibres under tension. This solution responds to the higher possibility that the structure is subject to pressure stress rather than depression; on the other hand, a double bar solution would satisfy both stress conditions, but requires larger dimensions of the profile.

In any case, no residual deformation is recorded, which confirms that all measurements are performed in the elastic range. Within the latter, the maximum deformation for all reinforced beams (11.48 mm) is measured by applying a load that settles around 10 kN, corresponding to a wind pressure of more than double the requirement for windows (2000 Pa).

Table 5. Main results of the 3-point bending test.

Column type	δ_{\max} L/2	Max load	k
	(mm)	(kN)	(kN/mm)
N	11.24	7.40	-
R1	11.48	9.57	0.82 ± 0.017
R2		9.54	0.82 ± 0.009
Mean Values		9.56	0.82
RB1		9.97	0.86 ± 0.004
RB2		9.44	0.81 ± 0.013
Mean Values		9.71	0.83

4 Conclusions

In this study, an experimental campaign to analyze the mechanical performance of reinforced pultruded columns intended for curtain walls is carried out.

Three types of GFRP columns are subject to a 3-point bending test with 3 load/unload cycles.

GFRP columns are a valid alternative to obtain slender frames and may be an effective variant to wooden column used in the patent application n.102020000025636.

Results show that adding threaded bars to GFRP columns reinforced with steel plates placing them in the central axis of the beam has no influence on the maximum applicable load, being equal the ultimate deformation.

Possible future developments will focus on similar loading tests carried out on columns with the threaded bars placed in the area of the tensile fibres of the I-section. This will require the design of an appropriate technical-constructive solution in order to keep small the dimensions of the section and, at the same time, increase the contribution of pre-tensioned bars, (i.e., the configuration reported in Fig. 5). In addition, a variant having double pretension bars (in order to respond to both pressure and depression stress) and slightly greater dimension of the section is currently under development for a future experimental test campaign.

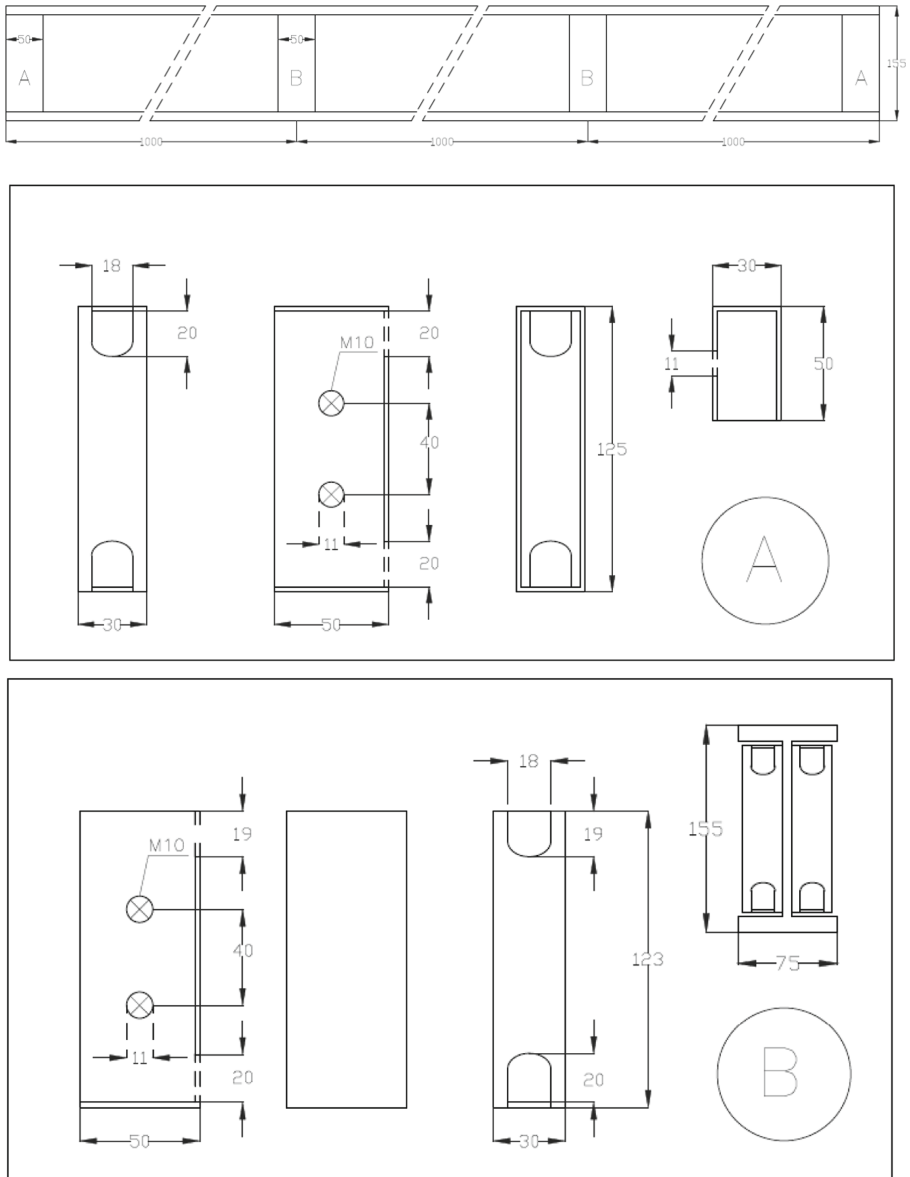


Fig. 5. Hypothesis for a double bar profile section

References

1. Górka, M.: Use of aluminium and glass facades in urban architecture, *Bud. i Archit.* 18 029–040 (2020). <https://doi.org/10.35784/bud-arch.586>

2. Marchione, F., Munafò, P.: Applicazione della tecnologia adesiva a componenti edilizi innovativi: dalla verifica tecnico-costruttiva alla realizzazione. In: Sicignano, E., (Ed.) *Colloqui.AT.e* 2021, EdicomEdizioni, Salerno, pp. 1359–1373 (2021)
3. Appelfeld, D., Hansen, C.S., Svendsen, S.: Development of a slim window frame made of glass fibre reinforced polyester. *Energy Build* 2010; 42:1918e25
4. Dispenza, C., Pisano, A.A., Fuschi P.: Numerical simulations of the mechanical characteristics of glass fibre reinforced C-profiles. *Compos Sci Technol* 2006; 66:2980e9
5. Keller, T.: Recent all-composites and hybrid fibre-reinforced polymer bridges and buildings. *Prog Struct Eng Mater* 2001; 3:132e40
6. Chacon, Y.G., Paciornic, S., d'Almeida J.R.M.: Microstructural evaluation and flexural mechanical behavior of pultruded glass fiber composites. *Mater Sci Eng A* 2010; 528:172e9
7. Sa, M.F., Gomes, A.M., Correia, J.R., Silvestre, N.: Creep behavior of pultruded GFRP elements e Part 1: literature review and experimental study. *Compos Struct* 2011; 93:2450e9
8. Turvey, G.J.: Torsion test on pultruded GRP sheet. *Compos Sci Technol* 1988;58: 1343e51
9. Keller, T., Tirelli, T., Zhou, A.: Tensile fatigue performance of pultruded glass fiber reinforced polymer profiles. *Compos Struct* 2005; 68:235e45
10. Stazi, F., Giampaoli, M., Nisi, L., Rossi, M., Munafò, P.: Mechanical performance reduction of GFRP specimens with polyester matrix exposed to continuous condensation. *Compos. B Eng.* **99**, 330–339 (2016)
11. Bai, Y., Vallée, T., Keller, T.: Delamination of pultruded glass fiber-reinforced polymer composites subjected to axial compression. *Compos Struct* 2009; 91:66e73
12. Stazi, F., Giampaoli, M., Rossi, M., Munafò, P.: Environmental ageing on GFRP pultruded joints: comparison between different adhesives. *Compos. Struct.* **133**, 404–414 (2015)
13. Carrion, J.E., LaFave, J.M., Hjelmstad, K.D.: Experimental behavior of monolithic composite cuff connections for fiber reinforced plastic box sections. *Compos Struct* 2005; 67:333e45
14. Feo, L., Mosallam, A.S., Penna, R.: Mechanical behavior of web-flange junctions of thin-walled pultruded I-profiles: an experimental and numerical evaluation. *Compos part B* 2013; 48:18e39
15. Bank, L.C., Oliva, M.G., Bae, H.-U., Bindrich, B.V.: Hybrid concrete and pultruded plank slabs for highway and pedestrian bridges. *Constr Build Mater* 2010; 24:552e8
16. Ascione, F., Berardi, V.P., Feo, L., Giordano, A.: An experimental study on the longterm behavior of CFRP pultruded laminates suitable to concrete structures rehabilitation. *Compos Part B* 2008; 39:1147e50
17. Alderucci, T., Rossi, M., Chiappini, G., Munafò, P.: Effect of different aging conditions on the shear performance of joints made between GFRP and glass with a UV absorbance coating. *Int. J. Adhes. Adhes.* **94**, 76–83 (2019)
18. Giampaoli, M., Terlizzi, V., Rossi, M., Chiappini, G., Munafò, P.: Mechanical performances of GFRP-steel specimens bonded with different epoxy adhesives, before and after the aging treatments. *Compos. Struct.* **171**, 145–157 (2017)
19. Munafò, P., Marchione, F., Chiappini, G., Marchini, M.: Effect of nylon fabric reinforcement on the mechanical performance of adhesive joints made between glass and GFRP. *Frattura e Integrità Strutturale*, (59) (2022)
20. Marchione, F., Chiappini, G., Rossi, M., Scoccia, C., Munafò, P.: Experimental assessment of the static mechanical behaviour of the steel-glass adhesive joint on a 1: 2 scale tensegrity floor prototype. *J. Build. Eng.* **53**, 104572 (2022)
21. Norm, D.I.N.: EN ISO 14125 (2011)



Vibration-Based Damage Assessment in Truss Structures Using Local Frequency Change Ratio Indicator Combined with Metaheuristic Optimization Algorithms

Amar Kahouadji¹, Samir Tiachacht¹ (✉) , Mohand Slimani¹ , Amar Behtani¹, Samir Khatir², and Brahim Benaissa³

¹ Laboratory of Mechanics, Structure, and Energetics (LMSE), Mouloud Mammeri University of Tizi-Ouzou, B.P. N°17 RP, 15000 Tizi Ouzou, Algeria

samir.tiachacht@ummto.dz

² Soete Laboratory, Faculty of Engineering and Architecture, Ghent University, Technologiepark Zwijnaarde 903, B-9052 Zwijnaarde, Belgium

³ Design Engineering Laboratory, Toyota Technological Institute, Nagoya, Japan

Abstract. Structural damage assessment is of a crucial importance issue in civil, mechanical and aerospace engineering. In this study, an approach based on Local Frequency Change Ratio (LFCR) as a damage indicator and optimization techniques as a tool of damage identification is proposed. Firstly, simple and multiple damage locations are detected using the concept of LFCR. Secondly, to determine the extent of the damage accurately, an optimization problem is investigated using an objective function based on the LFCR indicator. Five recent optimization algorithms are presented, namely, Prairie Dogs Optimization (PDO), Tasmanian Devil Optimization (TDO), Artificial Ecosystem-based Optimization (AEO), Student Psychology Based Optimization (SPBO) and Flow Direction Algorithm (FDA). To test the performance of the proposed approach, two structures are studied, including a 20-Bar 2D Truss and a 28-Bar 3D Truss with different scenarios of damage. The numerical results show that the LFCR can detect and locate the damage precisely and the presented optimization techniques can define its severity accurately. Moreover, the convergence and the CPU time analysis are discussed, where a comparison between the algorithms reveals the supremacy of the SPBO over the other optimization techniques. In terms of convergence, the PDO algorithm provides less competitive outcomes.

Keywords: Damage identification · Local frequency change ratio · Optimization · SPBO · TDO · AEO

1 Introduction

The need to enhance the safety and reliability of structures during their functional time and the advances in computing systems and algorithms have led to the increase and development of new methods and strategies in Structural Health Monitoring (SHM).

The vibration-based damage assessment approaches have been proven to be effective. It is based on the change in modal parameters of the structure such as frequencies and mode shapes [1]. This approach has been widely studied [1, 2]. As stated by Rytter [3], damage detection methods include four categories: detection, localization, assessment and prognosis of the remaining life of the structure. Many methods have been introduced for level 1, level 2, and level 3 in vibration-based SHM during the two last decades. Level 4 is generally related to the fields of fatigue, fracture mechanics and structural design assessment [1]. Several approaches of damage inverse identification have been suggested using metaheuristic approaches [4–9]. Gomes et al. [10] reviewed the vibration-based damage detection and identification methods with inverse problems, using algorithm optimization and artificial neural networks. Zenzen et al. [11] used a damage identification technique based on FRF and a new optimization technique namely, Bat Algorithm (BA) in beam-like and truss structures. Benaissa et al. [6, 12, 13] suggested a method based on Radial Basis Functions for quick structural response calculation and different optimization methods for identifying crack size and position, based on boundary displacement. Zhou and Abdel Waheb [14] suggested two new damage indicators through the mathematical interrelationship between the modal assurance criterion (MAC) and cosine similarity measure, called the cosine-based indicator (CI) and the extended transmissibility damage indicator ETDI. Lately, Khatir et al. [8, 15] presented a two steps approach based on an improved Frequency Response Function (FRF) method and optimization algorithms including GTO, DOA, AVOA and GBO to identify the damage in complex truss structures. The obtained results revealed that the enhanced indicator can detect the damage even with the noise of 2% and the four optimization techniques can assess the damage extent precisely. Tiachacht et al. [16] proposed a modified Cornwell indicator combined with a Genetic Algorithm (GA) to detect, localize and quantify damage in 2D truss and 3D frame structures. The numerical results showed that the proposed method affords more accurate results than similar past research. The LFCR indicator was used by Khatir et al. [17, 18] to locate the damage in three-layer laminated composite plates. They conclude that LFCR can predict the damage accurately with a noise of 2%.

So far, many methods have been introduced to detect, localize and assess the extent of damage in structures. This paper investigates the use of LFCR indicators in 2D and 3D truss structures. Following that, an objective function is used based on the same indicator to quantify the damage in five recent optimization algorithms after excluding healthy elements to speed up the process of damage identification. The results reveal that the LFCR can detect and localise single and multiple damages in truss structures and the optimization algorithms discussed perform well in identification in terms of accuracy.

2 Local Frequency Change Ratio Indicator

The local frequency change ratio (LFCR), first suggested by Shi et al. [19] to detect and locate the damage in structures. Mathematically, structural damage reveals itself in the stiffness and mass matrices, and physically by changes in the modal properties of structures [20]. Using mode shapes for a damaged and an undamaged structure, the local

frequency of the j^{th} element to the i^{th} mode shape can be calculated as:

$$LF_{ij}^u = \frac{\varnothing_{ui}^T K_j \varnothing_{ui}}{\varnothing_{ui}^T M_j \varnothing_{ui}} \quad (1)$$

$$LF_{ij}^d = \frac{\varnothing_{di}^T K_j \varnothing_{di}}{\varnothing_{di}^T M_j \varnothing_{di}} \quad (2)$$

The basic idea is that the damage in the j^{th} element reduces the stiffness in this element only and that the mode shape \varnothing_i is considered not to be sensitive to a small change in the local stiffness. The Local Frequency of the j^{th} element indicates a large change in the presence of a damage, while other elements will only change a bit [17]. Thus, if the damage occurs in element j of the structure its LFCR value becomes larger than the other elements. LFCR is defined as:

$$LFCR_{ij} = \frac{|LF_{ij}^d - LF_{ij}^u|}{|LF_{ij}^u|} \quad (3)$$

3 Metaheuristic Algorithms

In this study, five metaheuristic algorithms are used for quantifying the damage in 2D and 3D truss structures.

3.1 Artificial Ecosystem-Based Optimization (AEO)

Zhao et al. [21] introduced Artificial Ecosystem-based Optimization which is a new nature-inspired metaheuristic optimization algorithm. It is a population-based optimizer based on the flow of energy in an ecosystem on the earth; Artificial Ecosystem-based Optimization mimics three unique behaviours of living organisms, namely production, the consumption, and the decomposition.

3.2 Tasmanian Devil Optimization (TDO)

The Tasmanian Devil Optimization is a novel bio-inspired metaheuristic algorithm developed by Dehghani et al. [22] to mimic the behaviour of the Tasmanian Devil in nature. TDO is inspired by the Tasmanian devil feeding mechanism in two strategies of live prey hunting and then the carnivore eating.

3.3 Prairie Dogs Optimization (PDO)

The Prairie Dog Optimization Algorithm is a new natural-inspired population-based metaheuristic algorithm developed by Ezugwu et al. [23], this algorithm mimics the behaviour of Prairie dogs. After the initial random distribution of the PDO algorithm repetitively the same search processes to explore near-optimal solutions. And updated the best solutions found in each iteration [23].

3.4 Flow Direction Algorithm (FDA)

The Flow Direction Algorithm is a new search approach designed by Karami et al. [24]. FDA is inspired by the flow direction in lower altitudes and attempting to reach the lowest height in a drainage basin. The main FDA assumptions are listed as follows:

1. Each flow has a position defined by a height.
2. There exist β positions around each flow, each of which is defined its height.
3. The flow velocity is directly related to the slope.
4. The flow direction is toward the lowest altitude.
5. The outlet point is the position corresponding to the optimal objective function.

3.5 Student Psychology Based Optimization (SPBO)

Das et al. [25] created a novel population-based optimization algorithm named, student psychology-based optimization (SPBO) for solving optimization problems. The SPBO is inspired by the psychology of the students who are giving more effort to obtain the highest grade and become the best student in the class. The authors studied the psychology of different students in schools and universities in India over four years. Based on this investigation, the students of a class may be categorized into four categories, best students, good students, average students and students who try to improve randomly.

It assumes that the top student will always try to remain at the top of the class rank. Thus maintaining higher marks in the class. This algorithm performs this by having the top student give more effort in each of the subjects than any other student. The following equation implements the improvement of the best student. X_{best} are the marks of the best student, and X_j is a randomly selected student j in a particular subject. $rand$ is a randomly generated number between 0 and 1. k is another randomly selected parameter but it's either 1 or 2.

$$X_{bestnew} = X_{best} + (-1)^k \times rand \times (X_{best} - X_j) \quad (4)$$

There exist another type of student, that is focused on one particular subject, their improved effort is expressed by the following equation.

$$X_{new i} = X_{best} + rand \times (X_{best} - X_i) \quad (5)$$

The above-average type of student tries to spend more effort compared to the average students in the class as well as tries to follow the effort given by the best student. Their behaviour is simulated by the following expression, where X_i are the marks obtained by the i th, and X_{mean} is the average performance of the class in that particular subject.

$$X_{new i} = X_i + [rand \times (X_{best} - X_i)] + [rand \times (X_i - X_{mean})] \quad (6)$$

Each student is assigned an interesting value in each subject. Their spent effort is proportional to their interest. The student is assumed to give an effort equivalent to the average class effort if the student has a low interest. But there exists a type of student that will try to balance by giving higher effort to other subjects in order for the overall

marks to improve. Called the subject-wise average student. These different student types or psychologies, are selected randomly and expressed as follows, where X_i are the marks obtained by student i and $mean$ is the average marks obtained by the class in that particular subject.

$$X_{new i} = X_i + [rand \times (X_{mean} - X_i)] \tag{7}$$

Except for these three mentioned types of psychologies, there exists the last type of student that try to improve their performance by themselves. They do that by spending effort on a random subject. Their performance is guided through the following equation where, X_{min} and X_{max} are respectively the minimum and the maximum limit of marks of the subject.

$$X_{new i} = X_{min} + [rand \times (X_{max} - X_{min})] \tag{8}$$

4 Numerical Examples

In this section, two structures were chosen namely, a 20-Bar 2D truss and a 28-Bar 3D truss to verify the robustness of the proposed approach. The 20-Bar planar truss as shown in Fig. 1 was used in various works; it was used in topology optimization by Tejani et al. [26] and Kaveh and Zolghadr [27] and in damage detection by Khatir et al. [15]. The material properties of this structure are presented in Table 1. Two scenarios of damage are applied to this structure by reduction of stiffness as clarified in Table 2. And the natural frequencies of the damaged and undamaged cases are presented in Table 3.

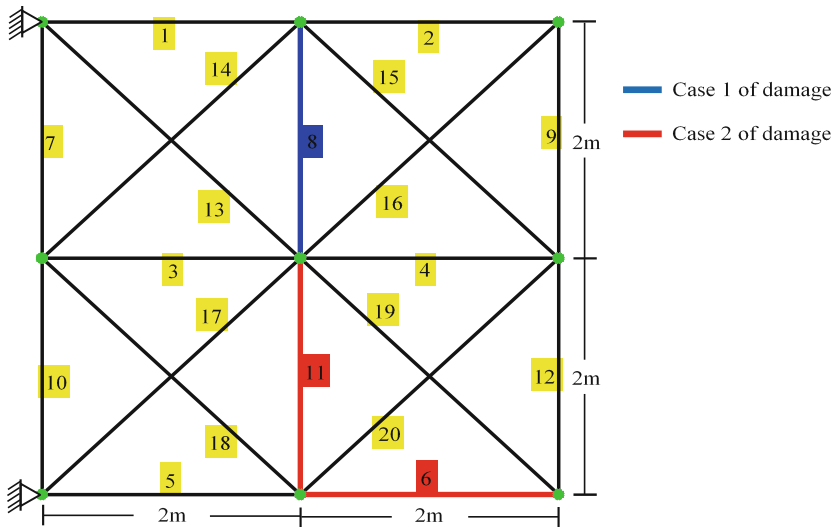


Fig. 1. 20-Bar planar truss with two scenarios of damage.

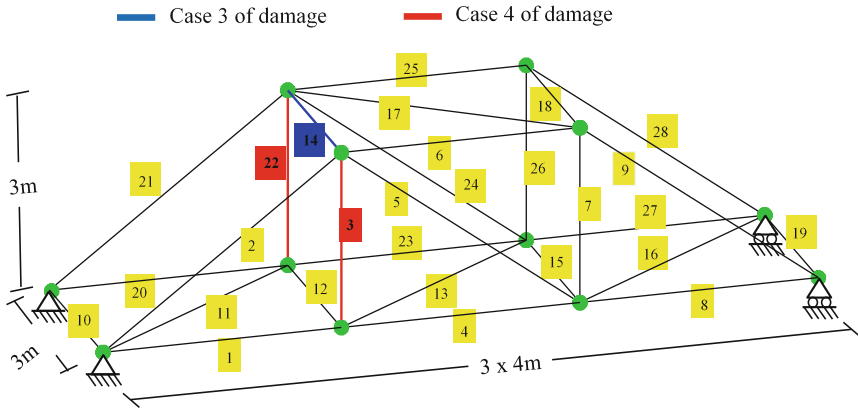


Fig. 2. 28-Bar space truss with two scenarios of damage.

The 28-Bar space truss indicated in Fig. 2 was used in the damage identification field by Mohan et al. [28] and Khatir et al. [15].

The material properties are shown in Table 4. Details about damage scenarios related to this structure are illustrated in Table 5. And the healthy and damaged natural frequencies are presented in Table 6.

Table 1. Material properties of the 20-bar planar truss.

Material property	Value
Modulus of elasticity (Gpa)	69
Material density (kg/m ³)	2740
Number of DOFs	14

Table 2. Damage scenarios for the 20-Bar planar truss.

Case	Element no	Reduction in stiffness
Case 1	8	15%
Case 2	6	20%
	11	25%

Table 3. Healthy and damaged natural frequencies of the 20-Bar planar truss.

Mode	Healthy (Hz) [26]	[27]	[15]	Actual FEM	Damaged (Hz)	
					Case 1	Case 2
1 st	120.0	119.1877	120,0965	120,0965	120,0225	119,8230
2 nd	192.1	191.3607	200,2618	200,2618	200,2618	199,8201

Table 4. Material properties of the 28-bar space truss.

Material property	Value
Modulus of elasticity (kN/m ²)	2.1
Material density (kg/m ³)	2740
Cross sectional area (m ²)	0.01

Table 5. Damage scenarios for the 28-Bar space truss.

Case	Element no	Reduction in stiffness
Case 3	14	20%
Case 4	3	15%
	22	25%

Table 6. Healthy and damaged natural frequencies of the 28-Bar space truss.

Mode	Healthy (Hz) [28]	[15]	Actual FEM	Damaged (Hz)	
				Case 3	Case 4
1 st	24.5266	24.5266	24.5266	24.5265	24.5265
2 nd	51.7618	51.7618	51.7618	51.7618	51.7544
3 rd	65.2664	65.2664	65.2664	65.2616	65.2493
4 th	100.0528	100.0528	100.0528	100.0143	100.0069
5 th	114.2814	114.2814	114.2814	114.2197	114.2564

4.1 Damage Localization Based on LFCR

In this section, the LFCR indicator is implemented in order to detect and localize the damaged elements in 2D and 3D truss structures with single and multiple damage scenarios. As mentioned above, if damage occurs in an element, its LFCR value becomes larger than the other ones. In Fig. 3 and 4 before truncation, we can distinguish between healthy and damaged elements clearly. Therefore, the results show that the LFCR can be used to localize the damaged elements accurately. Next, we eliminate the healthy elements as shown in Fig. 3 and 4 after truncation to use only damaged ones in optimization algorithms to assess their rate of damage.

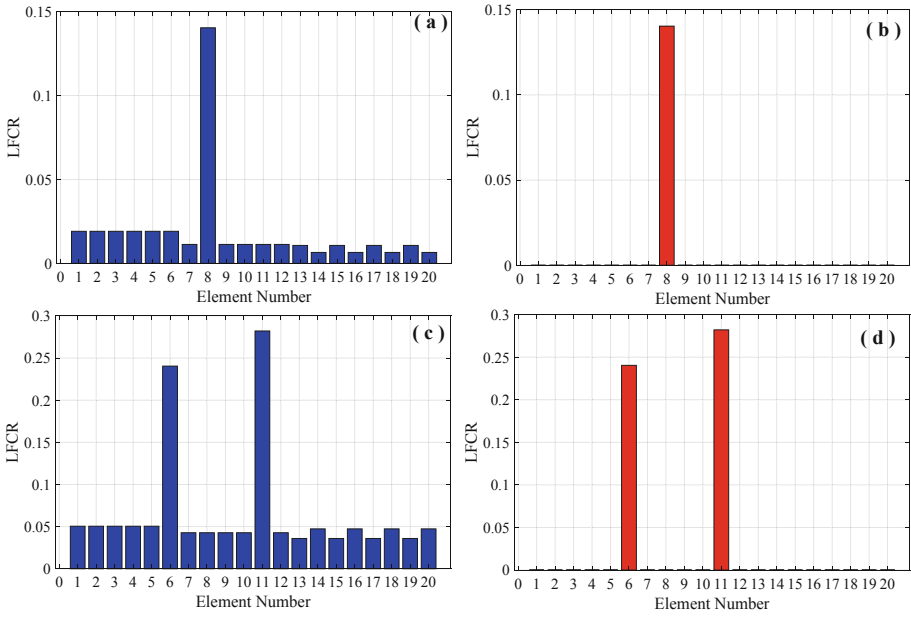


Fig. 3. Damage localization in 20-Bar planar truss: (a) and (c) case 1 and case 2 without truncation. (b) and (d) case 1 and case 2 with truncation.

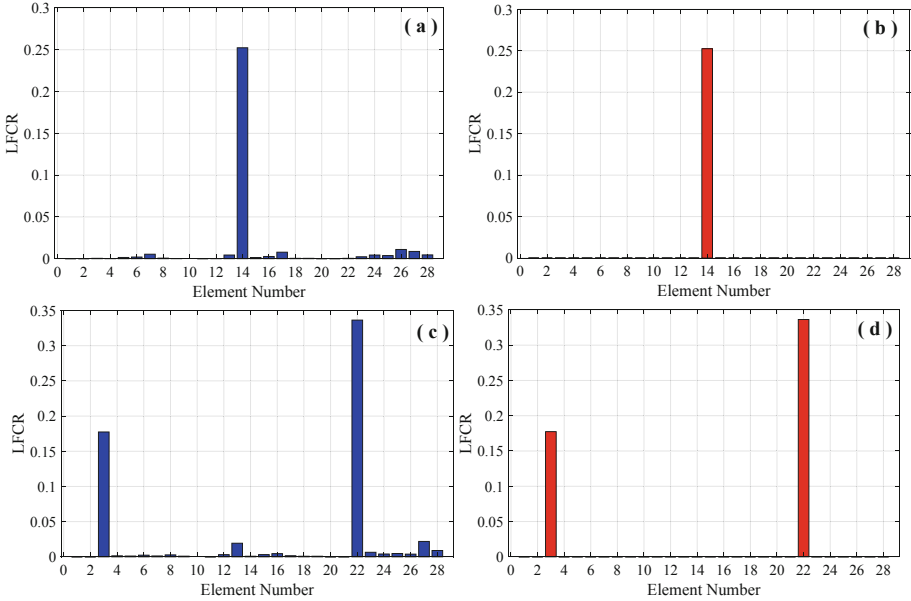


Fig. 4. Damage localization in 28-Bar space truss: (a) and (c) case 3 and case 4 without truncation. (b) and (d) case 3 and case 4 with truncation.

4.2 Damage Quantification Using Optimization Algorithms

AEO, TDO, PDO, SPBO and FDA are used to quantify the damage in the located elements by LFCR using an objective function based on the indicator defined in Eq. (3). The number of iterations is set to 200 for all cases in view of convergence. The population size is set to 50 for all algorithms and cases investigated in this paper; this size provided very high precision results in optimizing engineering problems by the five techniques [21–25]. The obtained results are illustrated in Fig. 5, 6, 7, 8 and 9.

According to Fig. 5, in the case of single damage in the 20-Bar planar truss, it can be seen that the damage is quantified with high precision by the five optimization algorithms; AEO, TDO, PDO, SPBO and FDA. The convergence is achieved by the five techniques. However, SPBO converged after 77 iterations, while TDO, AEO and FDA converged after 80, 111 and 136 iterations respectively.

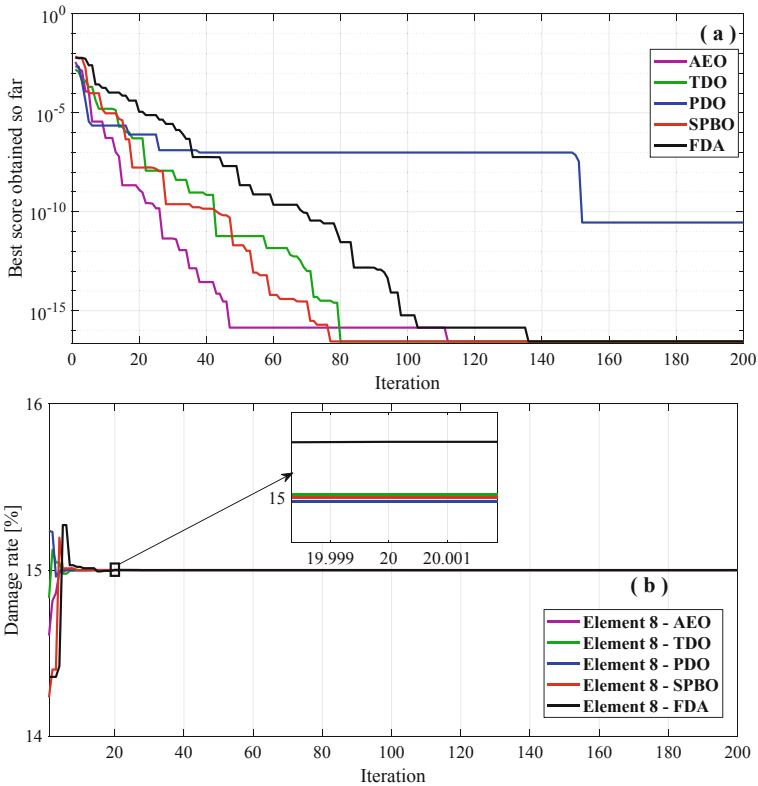


Fig. 5. Case 1 of the 20-Bar planar truss: (a) Fitness, (b) Damage quantification.

For the case 2 shown in Fig. 6, the level of damage is evaluated correctly by all algorithms, SPBO excels in convergence over the other algorithms indicating its robustness.

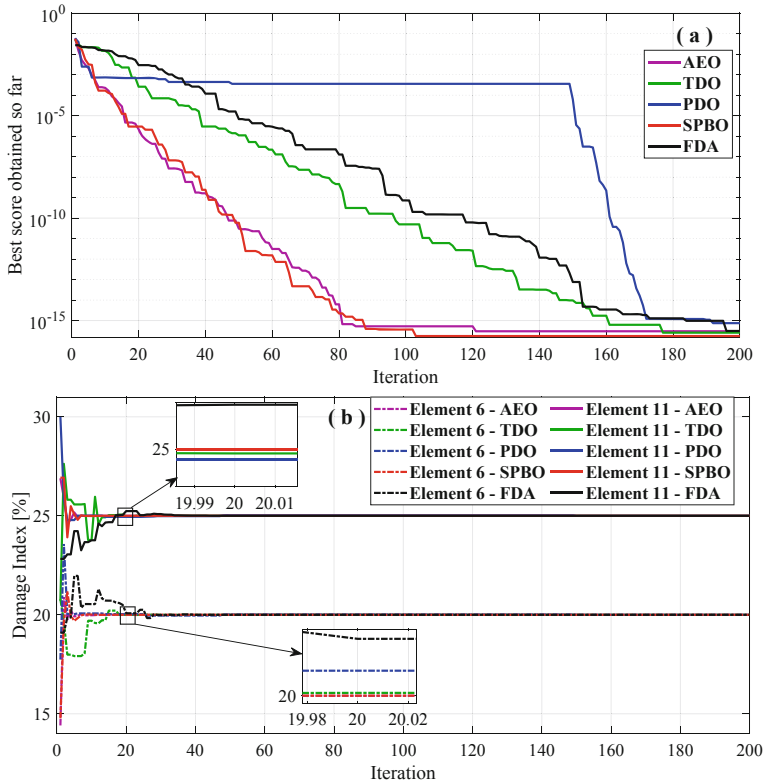


Fig. 6. Case 2 of the 20-Bar planar truss: (a) Fitness, (b) Damage quantification.

In case 3, the 28-Bar space truss is subjected to single damage scenario. According to the results illustrated in Fig. 7, we can see that AEO, TDO, PDO, SPBO and FDA can assess the severity of damage with high accuracy. As well, SPBO converged first after 105 iterations.

In the last case, the multiple damage in the 28-Bar space truss is identified precisely. SPBO showed its reliability in convergence over the other optimization approaches as illustrated in Fig. 8.

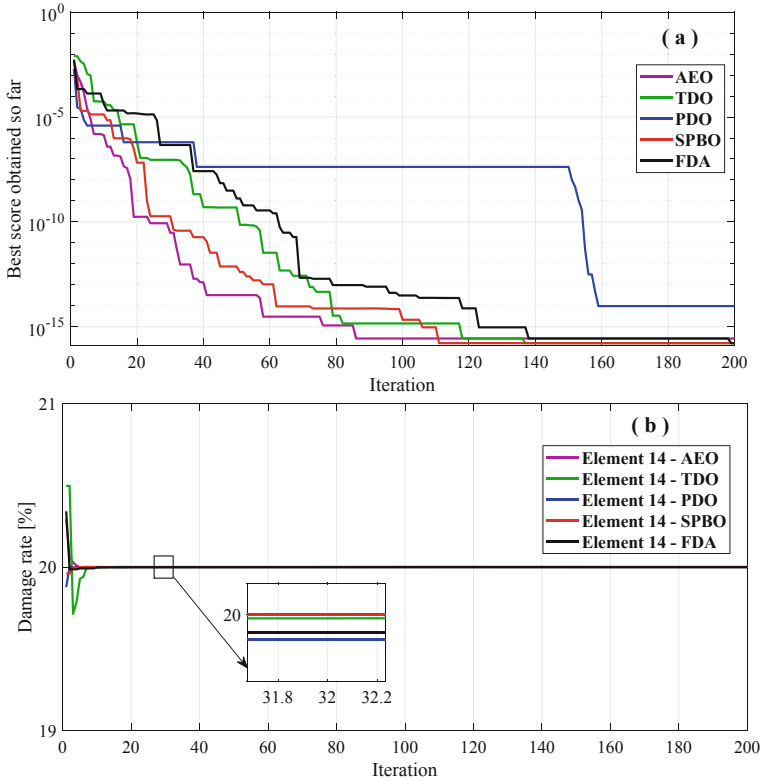


Fig. 7. Case 3 of the 28-Bar space truss: (a) Fitness, (b) Damage quantification.

In Table 7, the damage severity in all cases identified by the five algorithms for different values of iteration is summarized. The results show that the SPBO is more accurate than the other techniques.

SPBO displays its outperformance in term of CPU time as show in Table 8. Its superiority can be observed in case 1 and case 3. Despite.

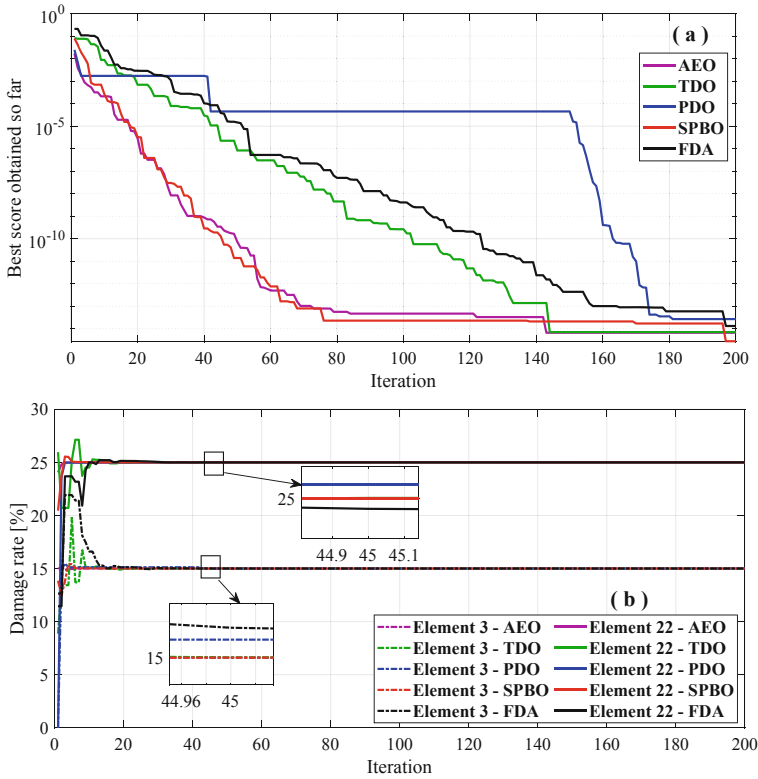


Fig. 8. Case 4 of the 28-Bar space truss:: (a) Fitness, (b) Damage quantification.

Table 7. Damage index comparison for all cases

Case	Element	Iteration	1	30	100	150	200
1	8	AEO	14.6056935	15.0000000	15.0000000	15.0000000	15.0000000
		TDO	14.8312891	14.9999987	15.0000000	15.0000000	15.0000000
		PDO	15.2365219	15.0000138	15.0000105	14.9999921	15.0000000
		SPBO	14.2346841	15.0000000	15.0000000	15.0000000	15.0000000
		FDA	14.3576191	14.9997062	15.0000000	15.0000000	15.0000000
2	6	AEO	14.41192907	19.99999864	20.00000000	20.00000000	20.00000000
		TDO	20.78743141	20.00307263	20.00000000	20.00000000	20.00000000
		PDO	17.73976832	19.96251951	20.01645984	20.00523821	20.00000000
		SPBO	14.77186278	19.99999793	20.00000000	20.00000000	20.00000000
		FDA	19.09834600	19.98797797	19.99999995	20.00000000	20.00000000

(continued)

Table 7. (continued)

Case	Element	Iteration	1	30	100	150	200
	11	AEO	26.89408112	24.99999815	25.00000000	25.00000000	25.00000000
		TDO	20.71184128	24.99506170	25.00000000	25.00000000	25.00000000
		PDO	29.99992195	24.98402785	25.02612214	24.99690938	25.00000000
		SPBO	26.92671286	25.00000556	25.00000000	25.00000000	25.00000000
		FDA	22.82396041	25.08878203	25.00000005	25.00000000	25.00000000
3	14	AEO	20.29352758	20.00000000	20.00000000	20.00000000	20.00000000
		TDO	20.49707259	19.99999425	20.00000000	20.00000000	20.00000000
		PDO	19.87691356	19.99996026	20.00000265	20.00000265	20.00000000
		SPBO	19.95977937	19.99999999	20.00000000	20.00000000	20.00000000
		FDA	20.34148939	19.99997059	20.00000000	20.00000000	20.00000000
4	3	AEO	14.97647462	15.00000009	15.00000000	15.00000000	15.00000000
		TDO	8.86629671	14.99950483	15.00000002	15.00000000	15.00000000
		PDO	14.84021149	15.11786472	15.00106890	15.00106890	15.00000000
		SPBO	13.85055623	14.99999910	15.00000000	15.00000000	15.00000000
		FDA	12.63813044	15.07306547	14.99999973	15.00000000	15.00000000
	22	AEO	24.04963444	24.99999954	25.00000000	25.00000000	25.00000000
		TDO	25.96052115	25.00433509	25.00000001	25.00000000	25.00000000
		PDO	23.62037944	24.97602713	25.00235710	25.00235710	25.00000000
		SPBO	20.44753904	24.99999849	25.00000000	25.00000000	25.00000000
		FDA	11.44786372	25.02290960	25.00000008	25.00000000	25.00000000

The SPBO has been shown to outweigh the other algorithms in CPU time in case 1 and 3 as show in Table 8. Despite its outperformance in convergence in all cases, the SPBO comes third in case 2 and 3 in terms of CPU time.

Table 8. CPU time for all cases.

-	Case 1	Case 2	Case 3	Case 4
SPBO	101.6621	208.9543	200.2409	403.5311
TDO	151.7568	157.4523	300.6136	304.1386
AEO	203.5734	209.4044	399.6174	404.4210
FDA	202.8542	209.3159	399.4498	404.0336
PDO	101.9066	105.2952	200.5830	202.7063

5 Conclusion

In this paper, we proposed the use of LFCR combined with five recent metaheuristic optimization algorithms for single and multiple damage identification in 2D and 3D truss structures. FEM models were built in MATLAB for 20-Bar planar truss and 28-Bar space truss to obtain modal parameters. LFCR was shown to localize the damage with precision in the studied structures. As well, the damaged elements localized by LFCR to eliminate the healthy elements were investigated in an optimization problem using AEO, TDO, PDO, SPBO and FDA algorithms with an objective function based on LFCR. The results showed that the optimization techniques used can quantify the damage accurately. Moreover, the convergence and the CPU time analysis are discussed, where a comparison between the five algorithms revealed the outperformance of the SPBO over the other optimization approaches.

References

1. Doebbling, S.W., Farrar, C.R., Prime, M.B., Shevitz, D.W.: Damage identification and health monitoring of structural and mechanical systems from changes in their vibration characteristics: a literature review (1996)
2. Das, S., Saha, P., Patro, S.K.: Vibration-based damage detection techniques used for health monitoring of structures: a review. *J. Civ. Struct. Heal. Monit.* **6**(3), 477–507 (2016)
3. Rytter, A.: Vibrational based inspection of civil engineering structures (1993)
4. Al Thobiani, F., Khatir, S., Benaissa, B., Ghandourah, E., Mirjalili, S., Wahab, M.A.: A hybrid PSO and Grey Wolf Optimization algorithm for static and dynamic crack identification, *Theor. Appl. Fract. Mech.* **118**, 103213 (2022)
5. Behtani, A., Tiachacht, S., Khatir, T., Khatir, S., Wahab, M.A., Benaissa, B.: Residual force method for damage identification in a laminated composite plate with different boundary conditions. *Frattura ed Integrità Strutturale* **16**(59), 35–48 (2022)
6. Benaissa, B., Aït Hocine, N., Belaidi, I., Hamrani, A., Pettarin, V.: Crack identification using model reduction based on proper orthogonal decomposition coupled with radial basis functions. *Struct. Multidiscip. Optim.* **54**(2), 265–274 (2016)
7. Khatir, S., Wahab, M.A., Benaissa, B., Köppen, M.: Crack identification using eXtended IsoGeometric analysis and particle swarm optimization,” in *Fracture, fatigue and wear*, 2018, pp. 210–222: Springer
8. Khatir, S., et al.: Damage identification in steel plate using FRF and inverse analysis. *Frattura ed Integrità Strutturale* **15**(58), 416–433 (2021)
9. Samir, K., Brahim, B., Capozucca, R., Wahab, M.A.: Damage detection in CFRP composite beams based on vibration analysis using proper orthogonal decomposition method with radial basis functions and cuckoo search algorithm. *Compos. Struct.* **187**, 344–353 (2018)
10. Gomes, G.F., Mendez, Y.A.D., Da Silva Alexandrino, P., da Cunha, S.S., Ancelotti, A.C.: A review of vibration based inverse methods for damage detection and identification in mechanical structures using optimization algorithms and ANN *Arch. Comput. Methods Eng.* **64**(4), 883–897 (2019)
11. Zenzen, R., Belaidi, I., Khatir, S., Wahab, M.A.: A damage identification technique for beam-like and truss structures based on FRF and Bat Algorithm. *Comptes Rendus Mécanique* **346**(12), 1253–1266 (2018)
12. Benaissa, B., Belaidi, I., Hamrani, A.: Identifying defect size in two dimensional plates based on boundary measurements using reduced model and genetic algorithm. *J. Sci. Technol.* **2**(1) (2017)

13. Benaissa, B., Köppen, M., Wahab, M.A., Khatir, S.: Application of proper orthogonal decomposition and radial basis functions for crack size estimation using particle swarm optimization. *J. Phys. Conf. Ser.* **842**(1), 012014. IOP Publishing (2017)
14. Zhou, Y.-L., Wahab, M.A.: Cosine based and extended transmissibility damage indicators for structural damage detection. *Eng. Struct.* **141**, 175–183 (2017)
15. Khatir, S., Tiachacht, S., Thanh, C.-L., Tran-Ngoc, H., Mirjalili, S., Wahab, M.A.: A robust FRF Damage Indicator combined with optimization techniques for damage assessment in Complex Truss Structures Case Stud. *Constr. Mater.* e01197 (2022)
16. Tiachacht, S., Bouazzouni, A., Khatir, S., Wahab, M.A., Behtani, A., Capozucca, R.: Damage assessment in structures using combination of a modified Cornwell indicator and genetic algorithm. *Eng. Struct.* **177**, 421–430 (2018)
17. Khatir, S., Tiachacht, S., Le Thanh, C., Khatir, T., Capozucca, R., Abdel Wahab, M.: Damage detection in laminated composite plates based on local frequency change ratio indicator. In: Wahab, M.A. (ed.) *Proceedings of the 13th International Conference on Damage Assessment of Structures. LNME*, pp. 887–898. Springer, Singapore (2020). https://doi.org/10.1007/978-981-13-8331-1_71
18. Slimani, M., Khatir, T., Tiachacht, S., Boutchicha, D., Benaissa, B.: Experimental sensitivity analysis of sensor placement based on virtual springs and damage quantification in CFRP composite. *J. Mater. Eng. Struct. JMES* **9**(2), 207–220 (2022)
19. Shi, Z., Law, S., Zhang, L.: Two stages damage detection in structure based on modal data. In: *Proceedings of the 15th International Modal Analysis Conference*, vol. 3089, p. 665 (1997)
20. Ge, M., Lui, E.M.: Structural damage identification using system dynamic properties. *Comput. Struct.* **83**(27), 2185–2196 (2005)
21. Zhao, W., Wang, L., Zhang, Z.: Artificial ecosystem-based optimization: a novel nature-inspired meta-heuristic algorithm. *Neural Comput. Appl.* **32**(13), 9383–9425 (2019)
22. Dehghani, M., Hubálovský, Š., Trojovský, P.: Tasmanian devil optimization: a new bio-inspired optimization algorithm for solving optimization algorithm. *IEEE Access* **10**, 19599–19620 (2022)
23. Ezugwu, A.E., Agushaka, J.O., Abualigah, L., Mirjalili, S., Gandomi, A.H.: Prairie dog optimization algorithm. *Neural Comput. Appl.* **34**(22), 1–49 (2022)
24. Karami, H., Anaraki, M.V., Farzin, S., Mirjalili, S.: Flow Direction Algorithm (FDA): a novel optimization approach for solving optimization problems. *Comput. Ind. Eng.* **156**, 107224 (2021)
25. Das, B., Mukherjee, V., Das, D.: Student psychology based optimization algorithm: a new population based optimization algorithm for solving optimization problems. *Adv. Eng. Softw.* **146**, 102804 (2020)
26. Tejani, G.G., Savsani, V.J., Bureerat, S., Patel, V.K., Savsani, P.: Topology optimization of truss subjected to static and dynamic constraints by integrating simulated annealing into passing vehicle search algorithms. *Eng. Comput.* **35**(2), 499–517 (2018)
27. Kaveh, A., Zolghadr, A.: Topology optimization of trusses considering static and dynamic constraints using the CSS. *Appl. Soft Comput.* **13**(5), 2727–2734 (2013)
28. Mohan, S.C., Yadav, A., Maiti, D.K., Maiti, D.: A comparative study on crack identification of structures from the changes in natural frequencies using GA and PSO. *Eng. Comput.* **31**(7), 1514–1531 (2014)



Improved ANN for Damage Identification in Laminated Composite Plate

Mohand Slimani¹, Samir Tiachacht¹ (✉), Amar Behtani¹, Tawfiq Khatir²,
Samir Khatir³, Brahim Benaissa⁴, and Mohamed Kamel Riahi^{5,6}

¹ Laboratory of Mechanics, Structure, and Energetics (LMSE), Mouloud Mammeri University of Tizi-Ouzou, B.P. N°17 RP, 15000 Tizi-Ouzou, Algeria

samir.tiachacht@ummto.dz

² University Centre Salhi Ahmed, Naama, Algeria

³ Ho Chi Minh City Open University, Ho Chi Minh City, Viet Nam

⁴ Design Engineering Laboratory, Toyota Technological Institute, Nagoya, Japan

⁵ Department of Mathematics, Khalifa University of Science and Technology, Po. Box 27788, Abu Dhabi, UAE

⁶ Emirates Nuclear Technology Center (ENTC), Khalifa University of Science and Technology, Po. Box 127788, Abu Dhabi, UAE

Abstract. This paper presents an improved Artificial Neural Network (ANN) for structural health monitoring of composite materials. Simply supported three-ply $[0^\circ 90^\circ 0^\circ]$ square laminated plate modeled with a 9×9 grid is provided and validated based on the literature review. Modal strain energy change ratio (MSE_{Cr}) is used to localize the damaged elements and eliminate the healthy elements. Next, improved ANN using the Arithmetic optimization algorithm (AOA) used for structural quantification. AOA aims to optimize the parameters of ANN for better training. Several scenarios are considered to test the accuracy of the presented approach. The results showed that the approach can localize and quantify the damage correctly.

Keywords: Artificial intelligence · Inverse problem · Damage detection · Structural quantification · Metaheuristic optimization

1 Introduction

All mechanical structures under vibrations are subject to local damage. This is one of the major factors that influence the laws related to maintenance, as it is determinant of the lifetime of a mechanical piece and is indicator for pursuing piece change in a regular fashion. These rules allow us to take a passive role in avoiding danger and to avoid financial risks. Moreover, structural health monitoring (SHM) is the discipline of actively watching the integrity of mechanical structures through sensors at the first place, then modeling and damage detection on the second place. This maintenance approach can be costly and is mainly used for expensive structures. But the rapid development of such methods attracted more adoption in recent years [1–3].

Based on research literature, there exist three levels of damage identification. The first is to recognize the presence of damages [4]. The second level is to identify its position and the last is to estimate its severity [5–7]. To achieve all three levels, researchers use inverse analysis to compare the actual vibrational response of the structure to several other responses issued from simulation through an optimization algorithm [8–12]. Researchers study various structural responses and build multiple damage indicators based on them [4, 13–17]. On the other hand, the challenge of the ill-posed inverse problem appears in many indicators when one structural response may correspond to complete damage parameters. Metaheuristic optimization algorithms are well placed to solve this problem. They can explore the search space and overcome the local minimums traps, thus finding the correct damage parameters in these cases [5, 6, 8, 9, 18–20].

The inverse analysis can be very demanding computationally, as it requires the simulation of the problem several times in each iteration [4]. Several times here means a value equal to the population size in modern metaheuristic algorithms. So, using a suitable optimization algorithm is critical in terms of computational cost. Moreover, the performance of metaheuristic algorithms is guided by their tuning parameters, like the mutation chance and crossover rate in the genetic algorithm, for example. Each problem requires specific tuning of these parameters to take full advantage of the algorithm potential. But as opposed to most metaheuristic algorithms, the Jaya algorithm does not contain such parameters, which makes it flexible in solving various engineering problems [11].

Significant studies were presented in the field of the structural response of damaged structures, such as truss structures with the use of a flexibility-based approach [21]. The modal analysis of laminated composite with different boundary conditions [9, 14, 22, 23]. The power spectrum and time-frequency analysis are used to identify vibration modes damages in beam-like structures using [7, 24]. And the swept-sine acoustic excitation are used for estimation of natural frequencies in Ref [25]. Rao et al. [26] studied the high-frequency wave characteristic in steel anchor-concrete composite, for damage detection. Non-mechanical crack detection techniques are also investigated in research studies [27, 28]. Hakim and Razak [29] indicated that the methods based on natural frequency can detect global changes, but the method that are based on mode shape data are more accurate for detecting local changes. Researchers created several damage indicators throughout the last two decades. Petrone et al. [30] presented and analyzed various damage identification techniques in different damage scenarios. One of the earliest is the Flexibility Strain Energy-Based Index (FSEBI), Guo [19] proposed a two-stage method based on the Genetic Algorithm (GA) to detect the damage region and the severity.

An improved method for damage identification has been introduced based on assessing the nonlinearity of cracked structures [31]. Another indicator was suggested in [32], called the Response Vector Assurance Criterion (RVAC). Ref [1] investigated the use of the transmissibility technique function instead of FRF in the RVAC. This technique was extended in [33] where it was employed for damage detection in metro tunnel structures. The Residual Force Vector was also found useful for damage identification in truss structure in [34].

Arefi et al. [35] suggested a modified Modal Strain Energy Damage Index (MSEDI) and studied its performance in different structures. And in Ref [36] an indicator based on mode shapes reconstruction was proposed, using an improved reduction system (IRS).

A generalized flexibility matrix change was proposed by for damage identification. And [37] presented the approach of wavelet transform (WT) and Teager Energy Operator (TEO), considering multiple damage identification cases in a composite structure. Ref [38] presented the method of damage detection using sparse sensors installation by System-Equivalent Reduction and Expansion Process (SEREP). Damage identification in beam-like structures using deflections obtained by modal flexibility matrices was presented by [13].

2 AOA-ANN

The Arithmetic algorithm is a population-based metaheuristic search algorithm. It uses Four basic search behaviors, each of which is based on the basic arithmetic operators (division, multiplication addition, and subtraction). The exploitation phase is characterized using the two operators of subtraction and addition, according to the following equations:

$$X_{i,j}(C + 1) = \begin{cases} best(X_j) - MOP \times [(UB_j - LB_j) \times \mu + LB_j] & \text{if } rand < 0.5 \\ best(X_j) + MOP \times [(UB_j - LB_j) \times \mu + LB_j] & \text{if } rand > 0.5 \end{cases} \quad (1)$$

where $X_{i,j}(C)$ is the i th solution at the j^{th} position, and $best(X_j)$ is the historical best position found by the j^{th} solution. LB_j and UB_j are the lower boundary and the upper boundary of solution j . μ is a tuning parameter for this algorithm, it is set by the user, 0.5 is a commonly used value for multimodal problems. Rand is a random value between 0 and 1 generated at the instance of checking the logical statement. Lastly, MOP is the Math Optimizer Probability, calculated at each iteration according to the following expression:

$$MOP = 1 - \frac{C^{1/\alpha}}{M^{1/\alpha}} \quad (2)$$

where C is the current iteration, M represents the maximum number of iterations, and α is the second tuning parameter for this algorithm, called the sensitive parameter and it tracks the search' exploitation accuracy, it is commonly fixed at a value of 5.

The exploration phase of the AOA algorithm is characterized using the two operators of multiplication and division, this behavior is expressed by the following equations, where ϵ is an integer of a small value.

$$X_{i,j}(C + 1) = \begin{cases} best(X_j) \div (MOP + \epsilon) \times [(UB_j - LB_j) \times \mu + LB_j] & \text{if } rand < 0.5 \\ best(X_j) \times MOP \times [(UB_j - LB_j) \times \mu + LB_j] & \text{if } rand > 0.5 \end{cases} \quad (3)$$

Figure 1. Denotes the structure of the AOA algorithm. Where MOA is a term called Math Optimizer Accelerated calculated at each iteration using the following expression, where min and max are respectively, the minimum and maximum values of the accelerated function.

$$MOA(C) = \min + C \times \left(\frac{\max - \min}{M} \right) \quad (4)$$

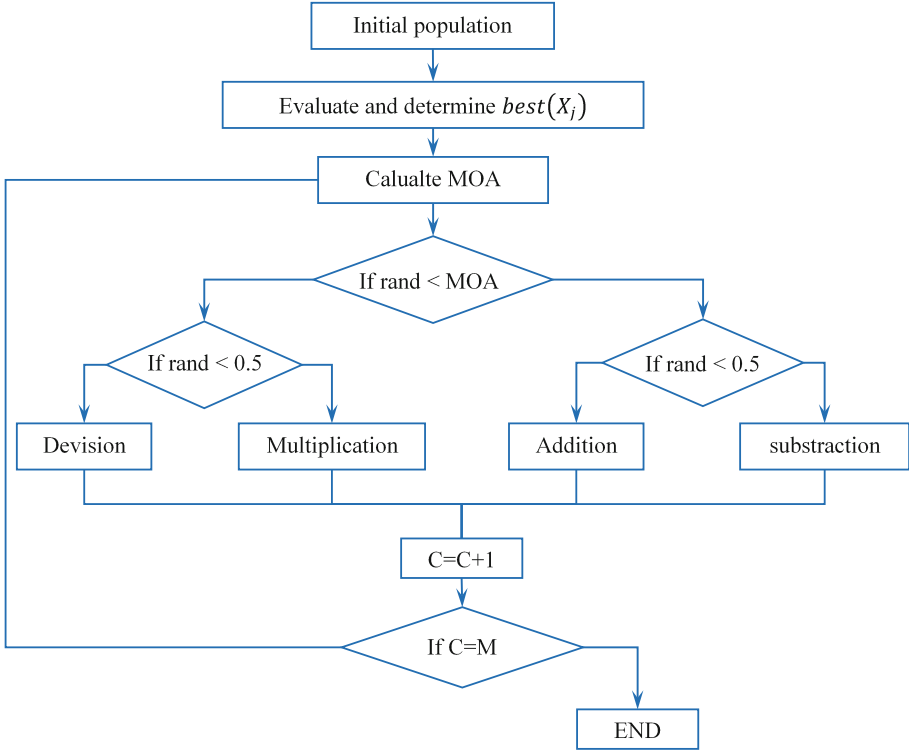


Fig. 1. AOA algorithm structure.

3 Theoretical Background

In this section, we describe the preliminaries and essential definitions.

3.1 Modal Strain Energy Change Ratio

Nel is the number of elements with reduced stiffness. The damage parameter $\delta_i (i = 1, 2, \dots, nel)$ is presented in the following equation:

$$K_d = \sum_{i=1}^{nel} (1 - \delta_i) k_i^e \tag{4}$$

The matrix K_d represents the damaged stiffness, where k_i^e is the stiffness of the i^{th} element and δ_i is a damage parameter with a value between 0 and 1; i.e., 0 for intact and 1 is fully damaged structures.

The modal strain energy (MSE) for undamaged and damaged structures are presented in the following formulation:

$$MSE_{ij}^h = \frac{1}{2} (\phi_i^h)^T K_j \phi_i^h ; MSE_{ij}^d = \frac{1}{2} (\phi_i^d)^T K_j \phi_i^d \tag{5}$$

i^{th} is the mode number and j^{th} is the index number of element. K_j presents the stiffness matrix. h and d represents the healthy and damaged systems, respectively, and ϕ_i is mode shape, T is the vector transpose. ($MSEcr$) is the modal strain energy change ratio, it is proposed in this paper to predict the exact location of the damage. It can be expressed by the total energy in the structure, as the sum of MSE 's of all elements:

$$MSEcr_j = \frac{1}{m} \sum_{j=1}^m \frac{MSEcr_{ij}}{MSEcr_{ij}^{max}} \tag{6}$$

where

$$MSEcr_{ij} = \frac{|MSE_{ij}^d - MSE_{ij}^h|}{MSE_{ij}^h}; MSEcr_{ij}^{max} = \max_k \{MSEcr_{ik}\} \tag{7}$$

The damage identification experiment is performed on a three-ply $[0^\circ \ 90^\circ \ 0^\circ]$ composite plate, with square dimensions, and under the simply supported boundary conditions. We assume that all layers of the laminate are made of the same linearly elastic composite material, have the same thickness, and the same density. With the following characteristics: $E_1/E_2 = 40$, $G_{12} = G_{13} = 0.6E_2$; $G_{23} = 0.5E_2$; $\nu_{12} = 0.25$, where the index 1 and 2 are for the directions parallel and perpendicular to the fibre orientation. The plate is modeled in two methods. First, in the Finite Element Method, with three discretization levels for each square side, 9 elements. 15 elements and 20 elements. Figure 1 shows the considered composite and the 9×9 meshing. And in the Isogeometric Analysis method, with the discretization of 9 and 14 for each square side. The choice of the number of elements is made based on the related research by Ritz [39] and Reddy [40], to be able to compare our simulation results for the same conditions. We compare the vibrational modes in the undamaged structure in Table 1.

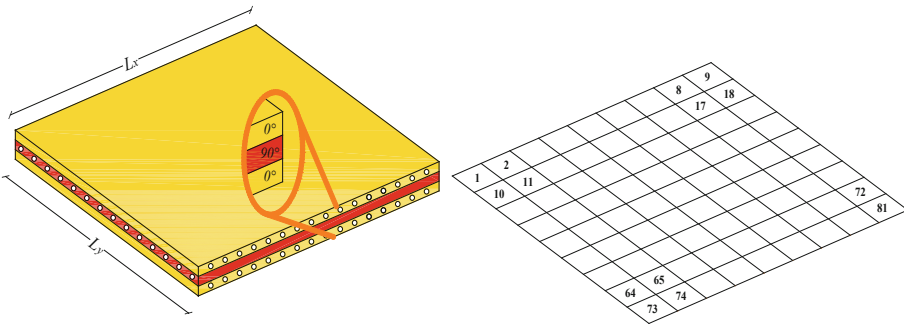


Fig. 2. Simply supported three-ply $[0^\circ \ 90^\circ \ 0^\circ]$ square laminated plate modeled with a grid of 9×9 .

The simulation results show that IGA simulation is more close to reference results than the Finite Element Method (FEM), in terms of precision, the vibrational modes error is within the uncertainty margin and within the difference between the Ritz results in [39] and Reddy results in [40]. In terms of discretization levels, the vibrational modes

Table 1. Natural frequencies of the undamaged plate structure.

		Grid	Mode 1							
			1	2	3	4	5	6	7	8
Intact	FEM	9 × 9	10.16	27.23	32.62	41.55	69.58	69.58	74.28	78.85
		14 × 14	7.44	17.28	24.98	29.85	44.76	44.76	55.40	58.09
		20 × 20	6.62	14.00	22.85	26.41	37.25	37.25	50.38	51.31
	IGA	9 × 9	6.60	9.42	16.23	24.78	27.25	27.25	30.00	37.90
		14 × 14	6.60	9.42	16.15	24.77	26.55	26.55	29.96	37.40
	Liew (p-Ritz) [39]	9 × 9	6.63	9.45	16.21	25.11	26.69	26.69	30.32	37.81
		14 × 14	6.63	9.45	16.21	25.11	26.66	26.66	31.31	37.79
Reddy [40]	9 × 9	6.62	9.44	16.20	25.11	26.65	26.65	30.31	37.78	
Damaged	Case 1	9 × 9	6.60	9.41	16.19	24.76	27.16	27.16	29.84	37.57
	Case 2	9 × 9	6.54	9.30	16.17	24.27	27.16	27.16	29.84	37.71
	Case 3	9 × 9	6.40	9.42	15.87	24.72	27.14	27.14	29.94	37.83
	Case 4	9 × 9	6.59	9.41	16.22	24.72	27.23	27.23	29.84	37.75
	Case 5	9 × 9	6.60	9.41	16.22	24.74	27.23	27.23	29.88	37.78

are found equivalent, with the same number of elements, i.e. 9 and 14. However, the FEM errors are very high in the same discretization level and could reach equivalent vibrational modes 1 and 4 with the discretization of 20×20 elements. The rest modes cannot be considered correct, as they are very far from the references. The FEM requires a higher number of elements, however, in the study of damage identification by damage indicators, the number of elements is very important, as the damage is simulated as the change in the rigidity of selected elements.

Table 1. Also, show the vibrational modes of the plate in the presence of five different damage scenarios using IGA. These damage scenarios vary in terms of positioning from corner edge like in scenario 1 (element 8) to center in scenario 3 (element 41) to side edge like scenario 4 (element 64). They also vary in severity, between 10% reduction of rigidity to 30%. As shown in Table 2. These choices are made to create to test the ability of the suggested method in identifying variable damage cases in terms of their position and also in terms of their similarity of vibrational mode responses, like cases 4 and 5, which have very close modes, and case 1 and 5, that have close first four modes. And cases 1 and 2 have the same 6th and 7th modes.

Table 2. Damage scenarios for laminated composite plate structure.

	Case 1	Case 2	Case 3	Case 4	Case 5
Damaged element	8	21	41	64	72
% Reduction in stiffness	30%	20%	10%	15%	25%

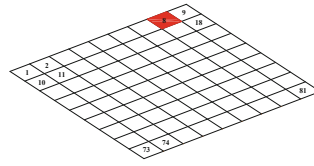
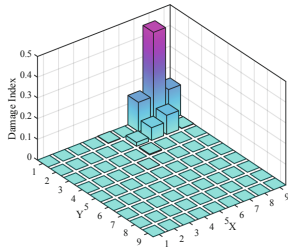
The damage identification results by strain energy change ratio are shown in Fig. 2, along with 9×9 meshing of the composite plate, where the actual damaged elements are marked in red. The result shows that the indicator successfully predicts the region of the damage. However, the neighboring elements are assigned a damage value in all cases, even though they are not damaged. And we notice that the central element is the least affected by this error (3 false damages). And the most affected in case 2. Where the damage is near the edge of the plate, with 15 false damages, the other edge cases have a relatively similar number of false damaged elements (4 to 5). On the other hand, the predicted damage severity error of this method is very high.

3.2 Damage quantification using AOA-ANN

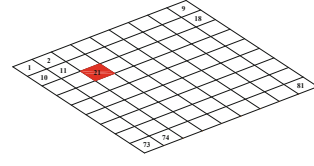
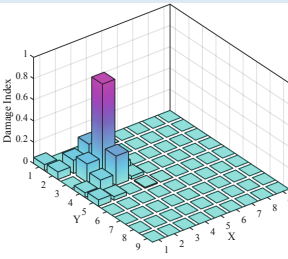
ANN in this paper is used to model the vibrational characteristics of the undamaged composite plate and the presence of damages in various positions. It can learn such characteristics from a learning dataset by optimizing the weights and biases of the network nodes. Because the vibration output can be very close for different damages, it is critical to distinguish the right damages corresponding to each response. We investigated the network training using the AOA algorithm. For its higher ability to reach the global optimum than classical training algorithms. The objective is to minimize the Root-Mean-Square Error of the network, which is expressed by Eq. 5. With l_i l_i denotes actual output as considered in the target set. O_i O_i is the output corresponding to i^{th} i^{th} data point in the training set, and d is the number of data points considered in the training dataset.

$$Error = \sqrt{\frac{\sum_{i=1}^n (O_i - l_i)^2}{d}} \quad (8)$$

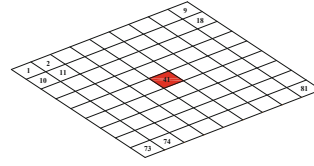
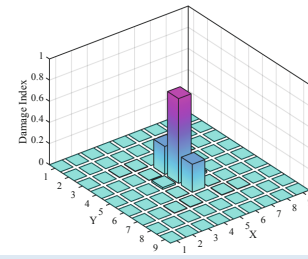
Figure 3. Shows the regression results, comparing the real and estimated responses in the five testing cases of damaged plates, indicating that the suggested technique can reproduce the vibrational response in an accurate manner. With lowest R-value equal to 0.998 in the first testing case. Notice that the estimated responses in close response are accurately distinguishable. Like cases 4 and 5. And cases 1 and 2.



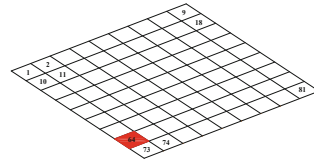
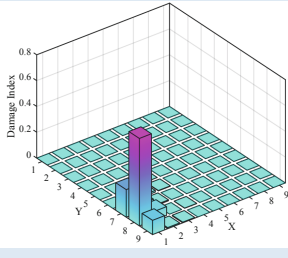
Case 1



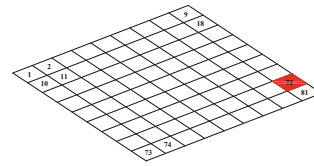
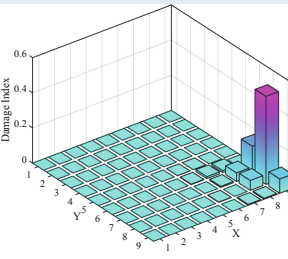
Case 2



Case 3

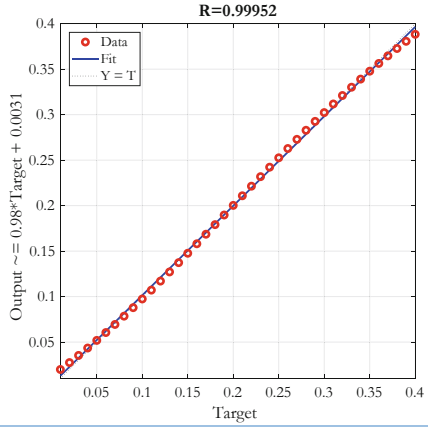
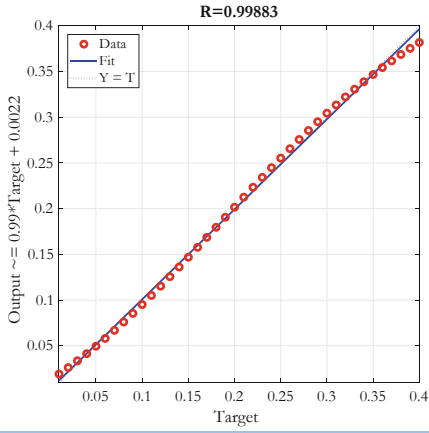


Case 4



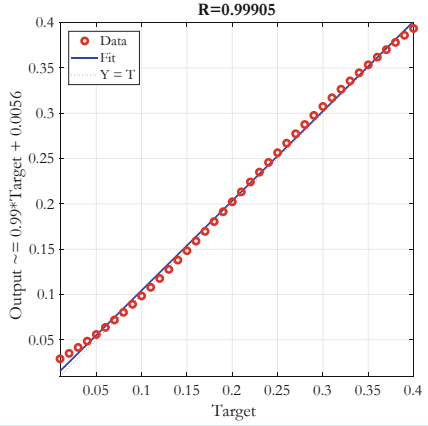
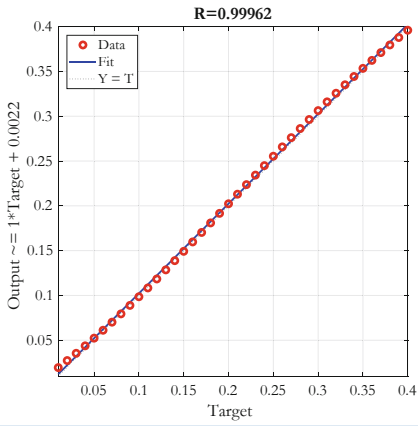
Case 5

Fig. 3. Identification of damage for different damage scenarios using IGA-MSEcr.



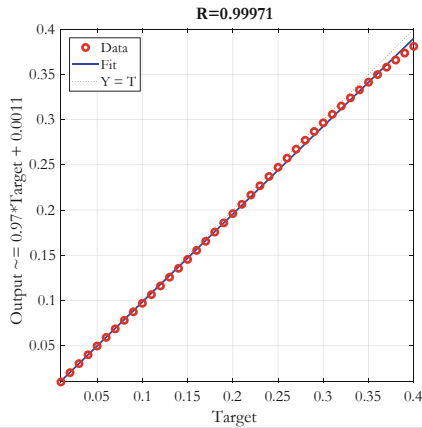
Case 1

Case 2



Case 3

Case 4



Case 5

Fig. 4. The regression plot for each damage case.

Table 3. Damage scenarios.

	The best solution fitness		CPU Time [s]
	At iteration 50	At iteration 100	
Case 1	0.00005496800	0.00003356700	68.94327
Case 2	0.00005604700	0.00001602000	69.52839
Case 3	0.00005124800	0.00001628000	69.81313
Case 4	0.00003781200	0.00003781200	68.41801
Case 5	0.00003981600	0.00003981600	69.1692

After establishing the improved ANN model, we use it to identify the damage properties in the testing cases. And the fitness convergence results are shown in Table 3. Indicating the estimated damages fitness value reached a low error value, with most of the progress being made within 50 iterations. CPU time indicates equivalent results in all cases. Figure 4. Compares the damage characteristics corresponding to these error values, summarizing the five test cases in one graph. All the damages are identified accurately, With the first case corresponding with the highest error between real damage severity and estimated damage severity equal to 4.4%. Indicating that the accuracy in this problem in terms of fitness value should be very high, as a fitness value of 0.00003 can be equivalent to a 5% error in damage estimation. Table 4. Provides the details of the estimated damages.

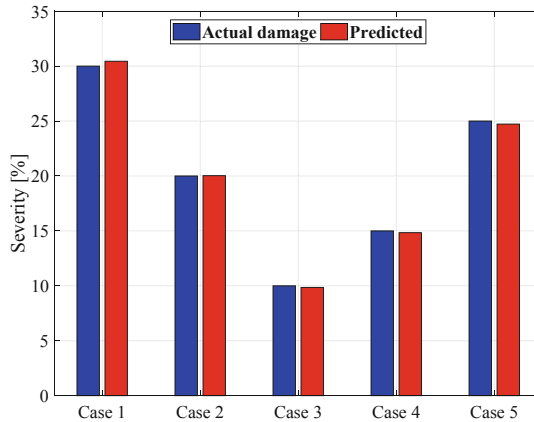
**Fig. 5.** Actual and predicted damage for all cases.

Table 4. Damage scenarios.

	Case 1	Case 2	Case 3	Case 4	Case 5
Actual Damage	30%	20%	10%	15%	25%
Predicted	30.444%	20.027%	9.855%	14.837%	24.723%

4 Conclusion

This paper investigates damage identification in the laminated composite plate using an improved Artificial Neural Network with the AOA algorithm. The composite plate is simulated using the FEM method and validated against other methods from literature. In the first section, we examined the performance of the Modal Strain Energy Change Ratio indicator, where we found its good performance in estimating the area in which the damage can be located, but it has limitations in terms of precise damage severity estimation. In the next stage, we suggested using the ANN to improve the damage identification results. The network is trained using the AOA algorithm, and its results showed a significant improvement in estimation quality. The suggested method can distinguish between close vibrational responses corresponding to various damages. The results showed that our method overcomes the challenge by predicting the exact damaged element with maximum error of about 4.4% of the actual damage.

References

- Heylen, W., Lammens, S., Sas, P.: Modal Analysis Theory and Testing. Katholieke Universiteit Leuven, Faculty of Engineering, Department of Mechanical Engineering, Division of Production Engineering. Machine Design and Automation (1998)
- Hakim, S.J.S., Razak, H.A.: Structural damage detection of steel bridge girder using artificial neural networks and finite element models. *Steel Compos. Struct.* **14**(4), 367–377 (2013)
- Gordan, M., et al.: Recent developments in damage identification of structures using data mining. *Latin Am. J. Solids Struct.* **14**(13), 2373–2401 (2017)
- Khatir, S., Tiachacht, S., Benaissa, B., Le Thanh, C., Capozucca, R., Abdel Wahab, M.: Damage identification in frame structure based on inverse analysis. In: Abdel Wahab, M. (ed.) Proceedings of the 2nd International Conference on Structural Damage Modelling and Assessment. LNCE, vol. 204, pp. 197–211. Springer, Singapore (2022). https://doi.org/10.1007/978-981-16-7216-3_15
- Benaissa, B., et al.: YUKI algorithm and POD-RBF for elastostatic and dynamic crack identification. *J. Comput. Sci.* **55**, 101451 (2021)
- Khatir, S., Wahab, M.A., Benaissa, B., Köppen, M.: Crack identification using eXtended IsoGeometric analysis and particle swarm optimization. In: Abdel Wahab, M. (ed.) FFW 2018. LNME, pp. 210–222. Springer, Singapore (2019). https://doi.org/10.1007/978-981-13-0411-8_21
- Samir, K., et al.: Damage detection in CFRP composite beams based on vibration analysis using proper orthogonal decomposition method with radial basis functions and cuckoo search algorithm. *Compos. Struct.* **187**, 344–353 (2018)
- Al Thobiani, F., et al.: A hybrid PSO and grey wolf optimization algorithm for static and dynamic crack identification. *Theoret. Appl. Fract. Mech.* **118**, 103213 (2022)

9. Benaissa, B., Aït Hocine, N., Belaidi, I., Hamrani, A., Pettarin, V.: Crack identification using model reduction based on proper orthogonal decomposition coupled with radial basis functions. *Struct. Multidiscip. Optim.* **54**(2), 265–274 (2016). <https://doi.org/10.1007/s00158-016-1400-y>
10. Benaissa, B., Belaidi, I., Hamrani, A.: Identifying defect size in two dimensional plates based on boundary measurements using reduced model and genetic algorithm. *J. Sci. Technol.* **2**(1), 115–120 (2017)
11. Syafruddin, W.A., Köppen, M., Benaissa, B.: Does the jaya algorithm really need no parameters? In: *IJCCI* (2018)
12. Slimani, M., et al.: Experimental sensitivity analysis of sensor placement based on virtual springs and damage quantification in CFRP composite. *J. Mater. Eng. Struct.* «JMES» **9**(2), p. 207–220 (2022)
13. Koo, K.Y., et al.: Damage detection in beam-like structures using deflections obtained by modal flexibility matrices. *Smart Struct. Syst.* **4**(5), 605–628 (2008)
14. Samir, K., et al.: Genetic algorithm based objective functions comparative study for damage detection and localization in beam structures. In: *Journal of Physics: Conference Series* (2015). IOP Publishing
15. Behtani, A., et al.: Residual Force Method for damage identification in a laminated composite plate with different boundary conditions. *Frattura ed Integrità Strutturale* **16**(59), 35–48 (2022)
16. Khatir, S., et al.: Damage identification in steel plate using FRF and inverse analysis. *Frattura ed integrità strutturale-fracture and structural integrity* **58**, 416–433 (2021)
17. Khatir, S., et al.: Damage identification in steel plate using FRF and inverse analysis. *Frattura ed Integrità Strutturale* **15**(58), 416–433 (2021)
18. Dinh-Cong, D., Dang-Trung, H., Nguyen-Thoi, T.: An efficient approach for optimal sensor placement and damage identification in laminated composite structures. *Adv. Eng. Softw.* **119**, 48–59 (2018)
19. Guo, H.Y.: A two-stage method to identify structural damage sites and extents by using evidence theory and micro-search genetic algorithm (vol 23, pg 769, 2009). *Mech. Syst. Signal Process.* **25**(7), 2796–2797 (2011)
20. Althobiani, F., et al.: A hybrid PSO and Grey wolf optimization algorithm for static and dynamic crack identification. *Theor. Appl. Fracture Mech.* **118**, 103213 (2021)
21. Miguel, L.F.F., et al.: Damage detection in truss structures using a flexibility based approach with noise influence consideration. *Struct. Eng. Mech.* **27**(5), 625–638 (2007)
22. Ferreira, A., Castro, L.M., Bertoluzza, S.: A high order collocation method for the static and vibration analysis of composite plates using a first-order theory. *Compos. Struct.* **89**(3), 424–432 (2009)
23. Benaissa, B., et al.: Application of proper orthogonal decomposition and radial basis functions for crack size estimation using particle swarm optimization. In: *Journal of Physics: Conference Series* (2017). IOP Publishing
24. Gillich, G.R., Praisach, Z.I.: Modal identification and damage detection in beam-like structures using the power spectrum and time-frequency analysis. *Signal Process.* **96**, 29–44 (2014)
25. Mituletu, I.C., Gillich, G.R., Maia, N.M.M.: A method for an accurate estimation of natural frequencies using swept-sine acoustic excitation. *Mech. Syst. Signal Process.* **116**, 693–709 (2019)
26. Rao, R., Sasmal, S.: Detection of flaw in steel anchor-concrete composite using high-frequency wave characteristics. *Steel Compos. Struct.* **31**(4), 341–359 (2019)
27. Haddar, H., Riahi, M.K.: Near-field linear sampling method for axisymmetric eddy current tomography. *Inverse Prob.* **37**(10), 105002 (2021)

28. Haddar, H., Jiang, Z., Riahi, M.K.: A Robust Inversion Method for Quantitative 3D Shape Reconstruction from Coaxial Eddy Current Measurements. *J. Sci. Comput.* **70**(1), 29–59 (2017)
29. Hakim, S.J.S., Razak, H.A.: Modal parameters based structural damage detection using artificial neural networks - a review. *Smart Struct. Syst.* **14**(2), 159–189 (2014)
30. Petrone, G., et al.: Damage detection through structural intensity and vibration based techniques. *Adv. Aircr. Spacecraft Sci.* **4**(6), 613–637 (2017)
31. Lee, H.P., Lim, S.P., Khun, M.S.: Diversion of energy flow near crack tips of a vibrating plate using the structural intensity technique. *J. Sound Vib.* **296**(3), 602–622 (2006)
32. Mao, Z., Todd, M.: A model for quantifying uncertainty in the estimation of noise-contaminated measurements of transmissibility. *Mech. Syst. Signal Process.* **28**, 470–481 (2012)
33. Feng, L., et al.: Damage detection of metro tunnel structure through transmissibility function and cross correlation analysis using local excitation and measurement. *Mech. Syst. Signal Process.* **60**, 59–74 (2015)
34. Nobahari, M., Ghasemi, M.R., Shabakhty, N.: Truss structure damage identification using residual force vector and genetic algorithm. *Steel Compos. Struct.* **25**(4), 485–496 (2017)
35. Arefi, S.L., Gholizad, A., Seyedpoor, S.M.: A modified index for damage detection of structures using improved reduction system method. *Smart Struct. Syst.* **25**(1), 1 (2020)
36. Li, J., et al.: A generalized flexibility matrix based approach for structural damage detection. *J. Sound Vib.* **329**(22), 4583–4587 (2010)
37. Sha, G., et al.: Multiple damage detection in laminated composite beams by data fusion of Teager energy operator-wavelet transform mode shapes. *Compos. Struct.* **235**, 111798 (2020)
38. Ghannadi, P., Kourehli, S.S.: Data-driven method of damage detection using sparse sensors installation by SEREPa. *J. Civ. Struct. Heal. Monit.* **9**(4), 459–475 (2019). <https://doi.org/10.1007/s13349-019-00345-8>
39. Liew, K.M.: Solving the vibration of thick symmetric laminates by reissner/mindlin plate theory and thep-ritz method. *J. Sound Vib.* **198**(3), 343–360 (1996)
40. Reddy, J.N.: *Mechanics of Laminated Composite Plates- Theory and Analysis*. CRC Press, Boca Raton, FL (1997)



An Analytical Approach for Describing the Bond Mechanism Between FRP and Curved Masonry Substrate

Yu Yuan and Gabriele Milani^(✉)

Department of Architecture, Built Environment and Construction Engineering (ABC),
Politecnico di Milano, Piazza Leonardo da Vinci 32, 20133 Milan, Italy
gabriele.milani@polimi.it

Abstract. Nowadays, the application of externally bonded FRP (Fiber Reinforced Polymer) material to reinforcement projects for existing buildings has become quite usual. In the applications of masonry structures, the curved masonry members, including arches, vaults, domes, etc., as common bearing components in masonry structures, have also received attention. The curvature of the substrate will introduce additional normal stress to the FRP-masonry interface, leading to different bond behaviors according to experimental observations. This paper attempts to reproduce the behavior of FRP strengthened curved masonry prism under shear, under the assumption of a classical model including three parts of an elastic FRP strip, a zero-thickness interface, and a rigid substrate. By simplifying the interface stress-slip law into a three-stage linear relationship, i.e., the initial elastic stage, the softening stage, and the residual strength stage, the analytical solutions of the stress and strain along the full length of the FRP can be obtained. The effect of the normal stress appearing along the interface is manifested by the change in the interface relationship. The effectiveness of the analytical model is verified by comparison with existing experimental data and numerical model. Due to the fast and stable calculation procedure, this model can explore the influence of various parameters on the model behavior at a small computational cost, and give some insight into the bonding mechanism of FRP reinforced curved structures.

Keywords: FRP strengthening · Masonry · Closed-form solution · Bond-slip model

1 Introduction

In recent years, the strengthening approach of externally applying FRP (Fiber Reinforced Polymer) onto structure surface has been proved to be efficient and holds several advantages such as fast and flexibility, small space occupation, and little effect on structure self-weight. This composite material has also been widely applied in masonry structures when the issues regarding material compatibility are not serious, and the reversibility controversy regarding architectural heritages doesn't exist. There have been many practical engineering cases and related research [1, 2]. One topic received less attention yet

quite common is that, the reinforcement of curved structures such as arches, vaults, and domes, which are important and common load-bearing members. When adopting an externally bonded approach for such structures, the curvature of the substrate will bring additional normal stress along the FRP-masonry interface, and it can be predicted that the effect of bonding will be affected to a certain extent.

At present, an experimental approach to test the bond behavior of FRP strengthened curved masonry structures on the basis of the classic shear test was developed [3, 4], meanwhile loading tests directly on reinforced arches or vaults were carried out as well [5–7]. Furthermore, some predictive models were developed, either based on the analysis model [8, 9] or using numerical modeling methods [10–12]. The single-lap shear tests conducted by Rotunno et al. [3] can be unutilized as a starting point for modeling assumptions, and an approach to verify the current research. In this experimental campaign, a modified experimental set-up (see Fig. 1) was developed to test the bond behavior of five sets of carbon-FRP reinforced curved masonry prisms. Both internal and external strengthening approaches were considered, and each approach was tested with one higher and one lower substrate curvature, as well as flat prisms, were tested for comparison. Cohesive failure (CF), interface failure (IF), prismatic failure (PF), and fiber failure (FF) were observed during the testing. For most intrados cases, the combination of CF (near the loading edge) and IF (near the free edge) modes occurred, it can be explained that, the peeling effect brought by the substrate curvature became prominent after part of the FRP strip was detached. While for extrados cases, the most common failure mode is CF.

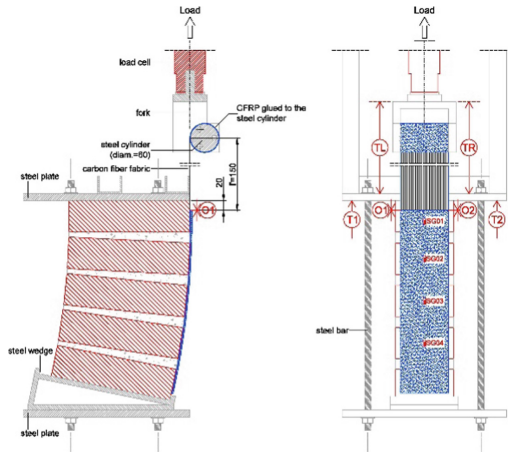


Fig. 1. The shear test set-ups for strengthened curved masonry prisms [3]

These experimental facts give us the opportunity to consider an FRP strip with elastic behavior, a rigid substrate in our model, and an interface that lumped all the non-linearities being the only position where the failure can occur. Furthermore, the experimental results also reveal that the load-bearing capacity is promoted for the extrados strengthening case, while deduced for the intrados case compared to the flat one.

And the load-bearing capacity for extrados (intrados) cases increases (decreases) with the curvature, indicating that the curvature of the substrate plays an important role in the curved cases. After we lumped all the non-linearities along the interface, the influence of curvature can be taken into account in the interfacial relationship by the effect of normal stress on friction.

In this article, an analytical model to reproduce the bond behavior under the first experimental approach will be introduced. Compared to some existing modeling approaches, this approach only asks for a few simple and clearly-defined parameters while can quickly and steadily produce results of both global and local bond behavior, which allows for exploration of the theoretical bond mechanism with little computational effort. The article is structured as below: the second section will illustrate the mathematical model and analytical solutions; the third section will present the validation against existing experimental data and numerical models; the fourth section will perform a series of sensitive analyses regarding interface and substrate parameters.; the last section will summarize main conclusions draw in this article.

2 The Analytical Model and Solutions

2.1 The Analytical Model

A simplified mathematical model is presented in this section as sketched in Fig. 2a. It is assumed that the external force F is applied at the end of the unbonded reinforcement strip in a direction tangential to the strip axis. Materials and external forces are assumed to be uniform across the width of the reinforcement. As discussed previously, the model consists of three components: (i) a linear elastic FRP strip; (ii) a rigid and fixed masonry substrate; (iii) a zero-thickness interface that obeys a piecewise linear tangential stress-slip relationship dependent on the local normal stress (Fig. 2b), including three stages: the first linear elastic stage, the second linear descending softening stage, and the third constant residual tangential strength. It can be easily obtained by force analysis that, for the extrados case, the interface normal stress will be compressive thus a positive factor for friction, while the opposite for the intrados case. The mathematical expressions for the interface law are:

$$\begin{cases} \tau_1(s) = Ks & (0 < s \leq s_e) \\ \tau_2(s) = K_1s + \tau_{max}^* (1 - \frac{K_1}{K}) & (s_e < s \leq s_r) \\ \tau_3(s) = \tau_r & (s_r < s) \end{cases} \quad (1)$$

in which $\tau(s)$ is the tangential stress at the interface, a dependent variable of the slip of the FRP strip, s . Parameters K and K_1 indicate the slope of the elastic and softening stages, s_e is the maximum slip value of the elastic phase, s_u is the ultimate slip value for the flat case, s_e and s_r are the maximum slip value for the elastic and softening stages, respectively.

The maximum bond strength τ_{max}^* and the interface residual strength τ_r depends on the interface normal stress σ_n :

$$\tau_{max}^* = \tau_{max} + \sigma_n \tan\phi \quad (2)$$

$$\tau_r = \sigma_n \tan \phi_r \tag{3}$$

in which ϕ is the friction angle, and ϕ_r is the residual friction angle of the interface, τ_{max} is the maximum bond strength for the flat case. The values of these parameters usually can be inferred and presumed from experimental data.

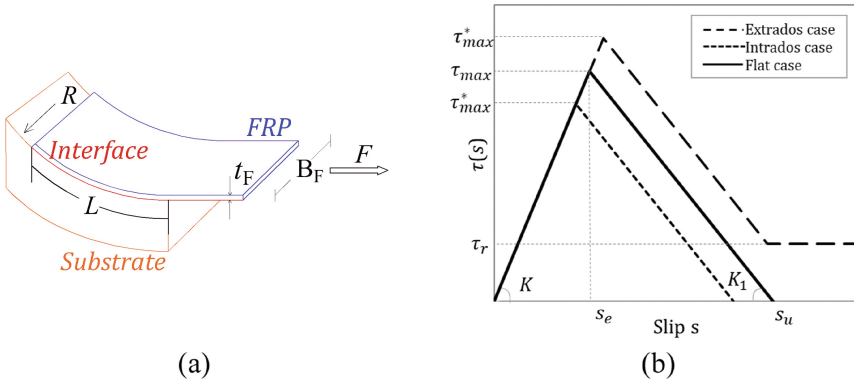


Fig. 2. The simplified mathematical model (a), and the interface law adopted (b).

2.2 Derivation of the ODE

For both extrados and intrados cases, an infinitesimal portion of the FRP strip is considered to gain the governing ODE. The longitudinal direction of the FRP strip is assumed to be x_I . The independent variable x ($0 \leq x \leq L$) defines the position of any point along the glued length L , and the abscissa $x = 0$ identifies the position of the free edge. The equilibrium of the infinitesimal portion of the reinforcement along the tangential direction x_I can be written as follows for both the extrados and intrados cases:

$$t_F \frac{d\sigma_F}{dx} = \tau(s) \tag{4}$$

where σ_F is the tensile stress of the FRP strip along its longitudinal direction. The constitutive law for the elastic FRP material is:

$$\sigma_F = E_F \varepsilon_F \tag{5}$$

in which E_F is the elastic modulus, and ε_F is the normal strain of the FRP strip. With the assumption of the rigid substrate and subjected to no displacement, the interface slip value is equal to the elastic displacement of the FRP, i.e.:

$$\varepsilon_F = \frac{ds}{dx} \tag{6}$$

The governing ODE can be derived by substituting Eqs. (5) and (6) into Eqs. (4):

$$\frac{d^2s}{dx^2} = \frac{\tau(s, \sigma_n)}{E_F t_F} \tag{7}$$

To calculate the interface normal stress σ_n , write the equilibrium along the normal direction x_2 :

$$\frac{d^2s}{dx^2} = \frac{\tau(s, \sigma_n)}{E_F t_F} \tag{8}$$

With the substitution of σ_n into the interface stress-slip law, Eq. (7) is a second-order non-linear differential equation with s and the dependent variable x . The following calculations will be given based on the extrados strengthening case, for the intrados case, it would be easy to replace the sign of the normal stress to gain the corresponding solutions.

2.3 The Closed-Form Solutions

To derive a closed-form solution for the previous ODE, it is necessary to assign a gradually increasing slip value s_0 at the free edge, so the following Initial Condition (Cauchy) problem can be written with the boundary conditions:

$$\begin{cases} \frac{d^2s}{dx^2} = \frac{\tau(s, \sigma_n)}{E_F t_F} \\ \left. \frac{ds}{dx} \right|_{x=0} = 0 \\ s(0) = s_0 \end{cases} \tag{9}$$

The slip value $s(x)$ will monotonically increase with x along the interface, considering three stages of the interface law, five possible situations will arise regarding the whole interface state: (i) only stage 1; (ii) stages 1 and 2; (iii) stages 1, 2 and 3; (iv) stages 2 and 3; (v) only stage 3. The following contents will present the closed-form solutions under the three different interface law stages, as well as the transformation points among different states that can be determined via the principle of continuity. The given slip value as the free end to trigger different situations can be reversibly determined by the known slip conditions for different interface states. Finally, the analytical procedure can be implemented into MATLAB to realize automatic calculation via any given material and geometric parameters. The calculation procedure will be terminated if a negative value appeared for the slope of the s - x relationship.

The First Stage. Let us assume that the first stage is active from the free edge up to x_e . A point with abscissa x_l belonging to the elastic interface stage and its slip $s_l(x_l)$ can be obtained by solving the Cauchy problem Eq. (7) with $\tau(s, \sigma_n) = K_s$:

$$s_1(x_1) = \frac{s_0}{2} (e^{\gamma x_1} + e^{-\gamma x_1}) \quad (0 \leq x_1 \leq x_e) \tag{10}$$

where, $\gamma = \sqrt{K/(E_F t_F)}$. If $x_e \leq L$, the value of x_e can be determined assuming that at x_e the tangential stress is equal to the maximum bond strength:

$$x_e = \frac{1}{\gamma} \operatorname{arcosh}(X_a) = \frac{1}{\gamma} \operatorname{arcosh}\left(\frac{\tau_{\max}}{\alpha_1 - \alpha_2}\right) \tag{11}$$

in which:

$$\begin{cases} x_a = \frac{\alpha_1}{\alpha_1 - \alpha_2} \\ \alpha_1 = E_F t_F s_0 \gamma^2 \\ \alpha_2 = E_F t_F s_0 \gamma \frac{\tan \phi}{R} \end{cases} \tag{12}$$

The Second Stage. The solutions at this stage can be obtained similarly:

$$s_2(x_2) = e^{\beta x_2} (C_1 \sin \sqrt{\alpha} x_2 + C_2 \cos \sqrt{\alpha} x_2) - \frac{1 - K_1/K}{K_1} \tau_{\max} (0 \leq x_2 \leq x_r) \tag{13}$$

in which:

$$\begin{cases} \alpha = -\left(\frac{K_1}{K} - 1\right)^2 \frac{\tan^2 \phi}{4R^2} - \frac{K_1}{E_F t_F} \\ \beta = \frac{1}{2} \left(1 - \frac{K_1}{K}\right) \frac{\tan \phi}{R} \\ C_1 = \frac{1}{\sqrt{\alpha}} \left[\frac{s_0}{2} (e^{\gamma x_e} - e^{-\gamma x_e}) - C_2 \beta \right] \\ C_2 = \frac{1 - K_1/K}{K_1} \tau_{\max} + \frac{s_0}{2} (e^{\gamma x_e} + e^{-\gamma x_e}) \end{cases} \tag{14}$$

The constants C_1 and C_2 can be determined via the continuous conditions at x_e :

$$\begin{cases} s_2(0) = s_1(x_e) \\ \frac{ds_2}{dx_2} |_{x_2=0} = \frac{ds_1}{dx_1} |_{x_1=x_e} \end{cases} \tag{15}$$

The Third Stage. To solve the Cauchy problem for the third stage, the following ODE with initial conditions is considered, where $x_2 = x_r$:

$$\begin{cases} \frac{d^2 s_3}{dx^2} = \frac{\tau_r}{E_F t_F} \\ s_3(0) = s_2(x_r) \\ \frac{ds_3}{dx_3} |_{x_3=0} = \frac{ds_2}{dx_2} |_{x_2=x_r} \end{cases} \tag{16}$$

3 Validations

3.1 Approaches for Validation

The experimental campaign conducted by Rotunno et al. [3] and the numerical model proposed by Milani et al. [12] were utilized for validation of the present model. The numerical model is based on the same experimental facts and adopts a similar mathematical model as in this present model. Only for a stable and robust calculation procedure, the numerical model assumes a smooth exponential function for the interface law. The

interface law also allows the incorporation of the interface normal stress, exhibiting an infinite ductility and an asymptotic residual strength in terms of the interface behavior.

The parameters needed in the present model are selected as the same in the numerical model proposed by Milani et al. As discussed in the literature [12], two approaches were developed to calibrate the parameters: the first one is a manual procedure adjusted by trial and error; the second more rigorous one is based on a least-square optimization. The comparisons of the gained values of parameters indicate that the two procedures provided similar results, leading to small differences from an engineering point of view. Thus, the first manual procedure was adopted out of convenience here.

The parameters involved are listed in Table 1. For the flat case, when assuming a large enough value for the substrate radius, the present model can be utilized as well. As an important parameter that controls the behavior of the residual strength stage, there is not enough experimental data to calibrate the parameter ϕ_r . In this study, it is assumed to be equal to the friction angle ϕ , due to the hypothesis that the friction angle defining the residual strength cannot be larger than that of the undamaged interface.

Table 1. Parameters adopted to validate the present model.

Label	R [mm]	E_F [MPa]	t_F [mm]	B_F [mm]	L [mm]	τ_{max} [N/mm ²]	s_e [mm]	s_u [mm]	ϕ [°]	ϕ_r [°]
CAE	1500	250000	0.165	100	382	1.37	0.093	0.324	35	35
CBE	3000	250000	0.165	100	354					
CAI	1500	250000	0.165	100	330					
CBI	3000	250000	0.165	100	330					
Flat	10^8	250000	0.165	100	330				-	-

3.2 Results of the Analysis

Global Responses. As presented in Fig. 3, the results gained by the present analytical model (the black lines) are compared with the numerical results (the red line) and experimental data (the blue envelope). Thanks to the clear definition needed in the analytical solutions, the different stages situation of the interface can be indicated in the global curved via different line types. An increase after Stage 3 appeared on the interface is clearly expressed for the extrados strengthened cases (cases CAE and CBE), due to the non-zero residual friction strength. And this increase is more obvious under the higher substrate radius (Case CAE), due to a higher interface normal stress.

Compared with the numerical model, the results are quite similar in terms of the ultimate strength and slip values. The present model always exhibits slightly smaller strength values, due to the smaller shear stress values adopted in the assumed interface laws. And a major difference lies in the post-peak behavior, in our model, a snap-back phenomenon can be observed. The snap-back phenomenon indicates the unloading of the fiber strip due to the softening of the interface, which normally appears under a sufficiently long bond length. This phenomenon requires specific experimental set-ups to avoid the brittle sudden failure of the specimen after peak load is reached, the detail

and typical experimental results can be found in the literature [13]. The numerical model doesn't exhibit such behavior since, in that model, the ODE system is solved as a BVP (Boundary Value Problem), rather than an IVP (Initial Value Problem) in this analytical model. One boundary condition is the increasing known load applied at the loading edge of the FRP strip, naturally, the decrease of load and the snap-back phenomenon won't appear.

Compared with the experimental data, it can be concluded that the modeling curved is satisfactory in terms of the trend and ultimate load, however always yield an obviously smaller ultimate slip. This problem is identified in the numerical model. This can be attributed to the simplifications existing in the model which ignore the ductility of the strengthened system, for example, the possible internal slippage and damage of the FRP strip, the damage propagation inside the substrate, the interlocking effect due to the uneven surface around the mortar joints.

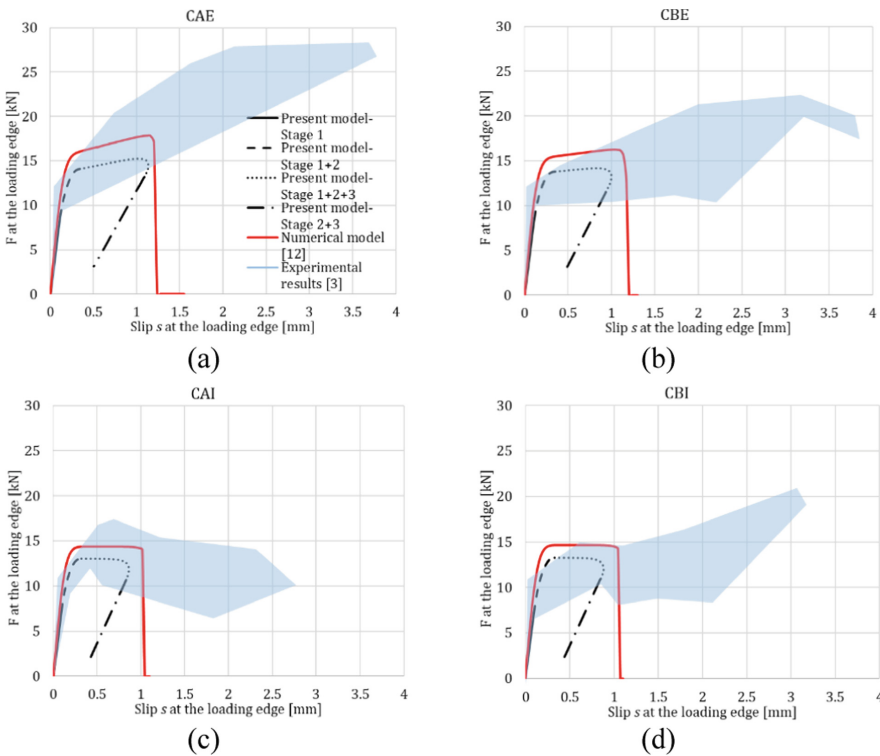


Fig. 3. Load-slip curves gained via the present model, numerical model [12], and shear tests [3] for case CAE (a), CBE (b), CAI (c), CBI (d).

Local Responses The current analytical procedure also allows determining the stress and displacement distributions along the interface. Take the case CAE as an example,

the results are presented in Fig. 4. The appearances of different interface stages are also available by the different colors and types of lines. The distinct divisions of the color (the interface stages) in the slip distribution (Fig. 4a) give a perfect verification of the correctness of the calculation. As can be normally observed in shear tests, the peak of the shear stress will gradually transfer from the loading edge to the free edge (Fig. 4b), and the stress level gradually declines towards the end of the loading procedure (Fig. 4c).

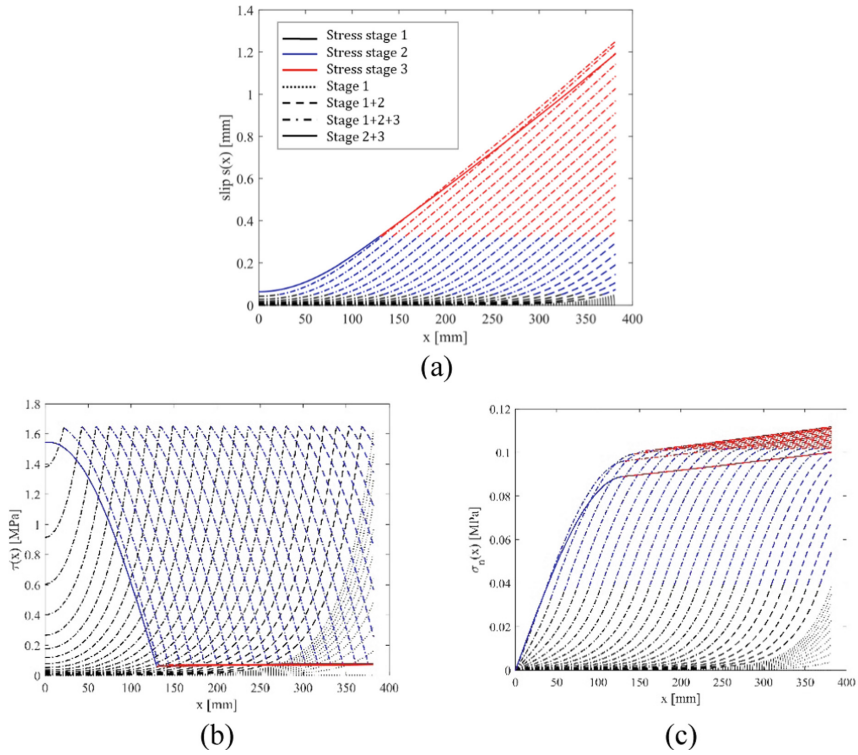


Fig. 4. Distributions of interface slip (a), shear stress (b), and normal stress (c) for case CAE.

4 Sensitive Analysis

For this present model dedicated to the curved substrate, it would be interesting to investigate the effect of substrate curvature on the relative parameter sensitivity. In the present model, the substrate curvature will affect the interface normal stress, and further influence the shear stress via the friction angles ϕ and ϕ_r by Mohr-Coulomb law. From common sense, when the curvature of the substrate is larger (closer to the flat case), the normal stress along the interface is smaller, which is consistent with the trend of the calculation results displayed in Fig. 5. And as the curvature of the substrate increases, the

bond strength will increase; the effect of friction angles on the intrados strengthening is smaller than that of the extrados strengthening, due to the smaller normal stress appearing intrados case.

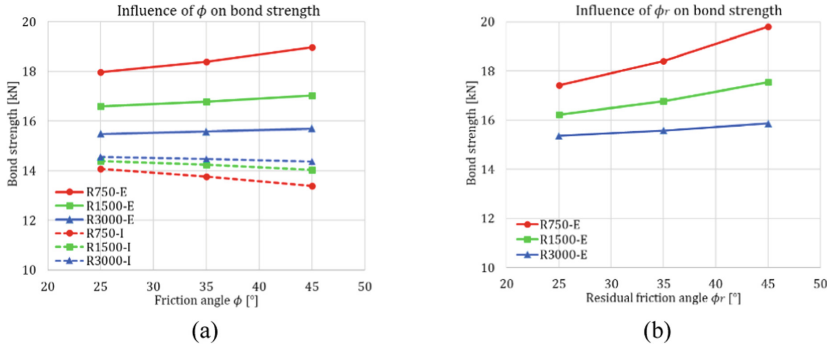


Fig. 5. Influences of ϕ (a) and ϕ_r (b) on bond strength for different substrate curvature radii.

5 Conclusions

In this article, a fast and stable analytical model was proposed to describe the bond behavior of FRP applied on curved substrates. The mathematical model was developed based on the shear test set-ups for FRP strengthened curved masonry prism. The nonlinearities were all lumped at the interface, and a three-section line was adopted for the interface stress-slip law which will vary according to the interface normal stress. After comparing with the experimental load-slip curves, it can be considered that this present model can ideally reproduce the trend and ultimate strength. And the investigations on the influences of the parameters showed consistency with experimental observations as well. Moreover, compared to the numerical model solved as BVP, this model can reproduce the snap-back phenomenon.

However, both the present model and the numerical model exhibit a smaller ultimate strength due to the simplifications that ignored the ductility of the strengthened system. Further studies may take into account the deformation and damage of the substrate, or change the mathematical formula for describing the post-peak interface behavior, to improve the ductility of the model.

Acknowledgments. Yu Yuan would like to acknowledge the financial support provided by the Chinese Scholarship Council (CSC) for performing her Ph.D. program at the Technical University of Milan, Italy.

References

1. Valluzzi, M.R., Modena, C., de Felice, G.: Current practice and open issues in strengthening historical buildings with composites. *Mater. Struct.* **47**(12), 1971–1985 (2014). <https://doi.org/10.1617/s11527-014-0359-7>
2. Vaculik, J., Visintin, P., Burton, N.G., Griffith, M.C., Seracino, R.: State-of-the-art review and future research directions for FRP-to-masonry bond research: Test methods and techniques for extraction of bond-slip behaviour. *Constr. Build. Mater.* **183**, 325–345 (2018). <https://doi.org/10.1016/j.conbuildmat.2018.06.103>
3. Rotunno, T., Fagone, M., Bertolesi, E., Grande, E., Milani, G.: Single lap shear tests of masonry curved pillars externally strengthened by CFRP strips. *Compos. Struct.* **200**, 434–448 (2018). <https://doi.org/10.1016/j.compstruct.2018.05.097>
4. Rotunno, T., Fagone, M., Bertolesi, E., Grande, E., Milani, G.: Curved masonry pillars reinforced with anchored CFRP sheets: an experimental analysis. *Compos. B Eng.* **174**, 107008 (2019). <https://doi.org/10.1016/j.compositesb.2019.107008>
5. Valluzzi, M.R., Valdemarca, M., Modena, C.: Behavior of brick masonry vaults strengthened by FRP laminates. *J. Compos. Constr.* **5**(3), 163–169 (2001). [https://doi.org/10.1061/\(ASCE\)1090-0268\(2001\)5:3\(163\)](https://doi.org/10.1061/(ASCE)1090-0268(2001)5:3(163))
6. Oliveira, D.V., Basilio, I., Lourenço, P.B.: Experimental behavior of FRP strengthened masonry arches. (2010). [https://doi.org/10.1061/\(ASCE\)CC.1943-5614.0000086](https://doi.org/10.1061/(ASCE)CC.1943-5614.0000086)
7. Carozzi, F.G., Poggi, C., Bertolesi, E., Milani, G.: Ancient masonry arches and vaults strengthened with TRM, SRG and FRP composites: experimental evaluation. *Compos. Struct.* **187**, 466–480 (2018). <https://doi.org/10.1016/j.compstruct.2017.12.075>
8. Carloni, C., Focacci, F.: FRP-masonry interfacial debonding: an energy balance approach to determine the influence of the mortar joints. *Eur. J. Mech. A. Solids* **55**, 122–133 (2016). <https://doi.org/10.1016/j.euromechsol.2015.08.003>
9. Caggiano, A., Martinelli, E., Faella, C.: A fully-analytical approach for modelling the response of FRP plates bonded to a brittle substrate. *Int. J. Solids Struct.* **49**(17), 2291–2300 (2012). <https://doi.org/10.1016/j.ijsolstr.2012.04.029>
10. Grande, E., Milani, G.: Modeling of FRP-strengthened curved masonry specimens and proposal of a simple design formula. *Compos. Struct.* **158**, 281–290 (2016). <https://doi.org/10.1016/j.compstruct.2016.09.017>
11. Fedele, R., Milani, G.: A numerical insight into the response of masonry reinforced by FRP strips. the case of perfect adhesion. *Compos. Struct.* **92**(10), 2345–2357 (2010). <https://doi.org/10.1016/j.compstruct.2010.03.014>
12. Milani, G., Fagone, M., Rotunno, T., Grande, E., Bertolesi, E.: Development of an interface numerical model for C-FRPs applied on flat and curved masonry pillars. *Compos. Struct.* **241**(7), 112074 (2020b). <https://doi.org/10.1016/j.compstruct.2020.112074>
13. Carrara, P., Ferretti, D., Freddi, F.: Debonding behavior of ancient masonry elements strengthened with CFRP sheets. *Compos. B Eng.* **45**(1), 800–810 (2013). <https://doi.org/10.1016/j.compositesb.2012.04.029>



Collapse Analysis of Reinforced Masonry Arches: A Comparison of Associated and Non-associated Sliding

Yiwei Hua^(✉) and Gabriele Milani

Department of Architecture, Built Environment and Construction Engineering,
Politecnico di Milano, Piazza Leonardo da Vinci 32, 20133 Milan, Italy
yiwei.hua@polimi.it

Abstract. In this paper, the standard formulation for rigid block limit analysis is extended to simulate the effect of innovative strengthening (FRP/FRCM), with a suitable modification of the constitutive constraint that governs the behavior of contact joints. The proposed modeling is applied to both associated and non-associated sliding. The change of the failure surface of a representative contact joint after the reinforcement is first derived. Casting it into a standard matrix form, the constitutive constraint in the lower bound theory is then modified to account for the strengthening effect. After that, the proposed technique is also extended to solve a non-associated problem. Utilizing this technique, the collapse of a 9-block 2D arch with FRP reinforcement is analyzed to compare predictions from associated and non-associated formulations. Detailed parametric studies are carried out to understand the influence of the critical parameters on the difference in the results from these two formulations. The results show that when analyzing the arch with reinforcement, the associated limit analysis may predict an incorrect collapse mechanism as well as an overestimated collapse load. Such overestimation could reach 70.5% in some cases. Employment of non-associated formulation is very necessary for more precise collapse analysis of reinforced masonry arches.

Keywords: Rigid block limit analysis · Reinforcement · Masonry arch · Associated sliding · Non-associated sliding

1 Introduction

Historical masonry building is a widespread type of architectural heritage in the eastern and western world. To preserve these valuable constructions, their structural behavior should be primarily investigated. Recent boom of computational Operational Research give rise to the popularity of rigid block limit analysis. This approach is becoming a standard tool to quickly understand the collapse performance of block structures, precisely taking into account the real arrangement of the bricks in the structure at the same time [1–5]. Based on some pioneering works [6–9], such analysis now has been applied to complex and large-scale collapse problems [10–15].

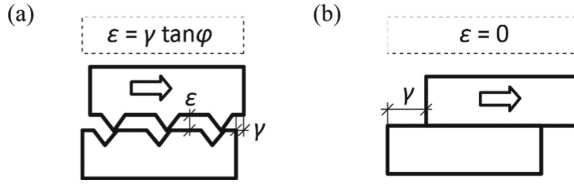


Fig. 1. Typical sliding model for rigid block limit analysis: (a) associative (“sawtooth”) sliding; (b) Coulomb friction, non-associated sliding.

On the other hand, thanks to the development of composite materials, innovative strengthening techniques have been widely adopted to retrofit these historical masonry buildings (e.g. external FRP strips or FRCM grids). Many numerical scientists attempted to simulate such a strengthening effect through the aforementioned rigid block limit analysis. In these contributions, most of them did not accurately consider the sliding behavior among the bricks, where an associated sliding model was employed [16, 17]. Such a model will be correct if the collapse only involves flexural hinges while once sliding among the bricks is triggered, an obvious separation (dilation) at the contact joint will appear due to the associativity. As mentioned by Drucker [18], such a dilation fit the reality only when friction is sawtooth (Fig. 1a). For a classical Colom friction (Fig. 1b), the associated sliding model may lead to an incorrect prediction of the collapse mechanism.

This work will develop a simple modeling approach to consider the reinforcement, as an extension of standard rigid block limit analysis. Such modeling will not only apply to associated limit analysis but is also convenient to be used in Sequential Linear Programming (SLP) procedure which is a promising iterative scheme to solve non-associated problems [12]. We first analytically investigate the change of the limit surface after the reinforcement of a reprehensive contact joint. The constitutive law in the standard associated limit analysis (Lower Bound theory), is then updated to implicitly model the reinforcement layer. Finally, we illustrate how to apply this modeling strategy to solve non-associated sliding collapse, utilizing the SLP procedure.

The collapse of a 2D FRP-reinforced arch with both associated and non-associated sliding is analyzed to compare the collapse mechanism and the ultimate load predicted by these two sliding models. Then, a detailed parametric study is carried out to observe the influence of critical parameters on those differences. Based on these results, the accuracy and applicability of the associated formulation are discussed.

2 Methods

Before the derivation of the limit surface for the interface after the reinforcement, we would first recall the formulation of classic associated rigid block limit analysis. Such a formulation can be deduced from both static and kinematic points of view, namely Lower Bound (LB) and Upper Bound (UB) theories (Eq. (1) and Eq. (2)), respectively [11]. These two formulations are a pair of dual Linear Programming (LP) problems,

which always give a consistent optimal solution.

$$\begin{aligned}
 & \text{maximize } \alpha \\
 & \text{subject to } \mathbf{Ax} = \alpha \mathbf{f}_L + \mathbf{f}_D \\
 & \quad \quad \quad \mathbf{Nx} - \mathbf{c}_0 = \mathbf{z} \\
 & \quad \quad \quad \mathbf{z} \leq 0
 \end{aligned} \tag{1}$$

$$\begin{aligned}
 & \text{minimize } -\mathbf{f}_D^T \mathbf{u} + \mathbf{c}_0^T \mathbf{p} \\
 & \text{subject to } \mathbf{f}_L^T \mathbf{u} = 1 \\
 & \quad \quad \quad \mathbf{A}^T \mathbf{u} = \mathbf{q} \\
 & \quad \quad \quad \mathbf{N}^T \mathbf{p} = \mathbf{q}, \quad \mathbf{p} \geq 0
 \end{aligned} \tag{2}$$

Among all the constraints in the above two LP problems, the second constraint in Eq. (1) defines a limit surface for the resultant forces at contact joints (Fig. 2). All the possible interfacial resultants should remain within the limit surface and any force state that reaches the edges will imply discontinuous velocities at the joint.

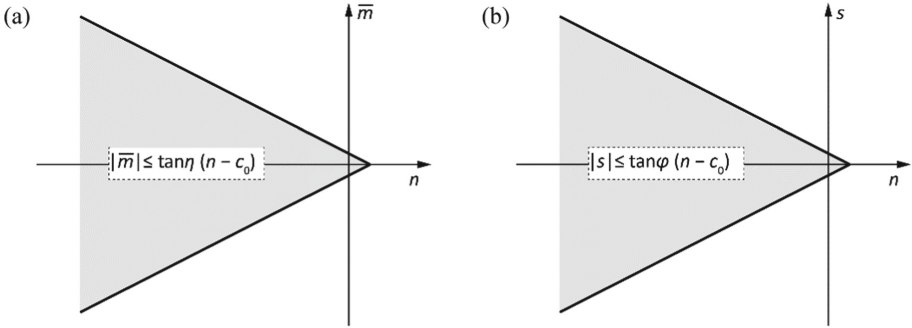


Fig. 2. Limit surfaces for the interface resultant forces (no reinforcement but with a small normal cohesion c_0): (a) m - n limit surfaces; (b) s - n limit surfaces.

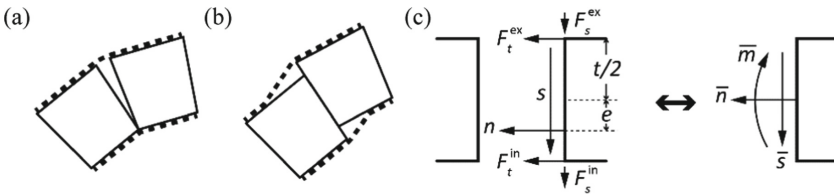


Fig. 3. (a) flexural hinge failure; (b) sliding failure (c) interface resultant forces after strengthening and equivalent description

$$\begin{aligned}
 |e| &= \left| \frac{\bar{m} - F_t^{\text{in}} \tan \eta + F_t^{\text{ex}} \tan \eta}{\bar{n} - F_t^{\text{in}} - F_t^{\text{ex}} - c_0} \right| \leq \tan \eta \\
 (\bar{n} - F_t^{\text{in}} - F_t^{\text{ex}} - c_0) \tan \varphi + |\bar{s}| - F_s^{\text{in}} - F_s^{\text{ex}} &\leq 0 \\
 0 \leq F_t^{\text{in}} \leq F_{t,\text{max}}^{\text{in}}, \quad 0 \leq F_t^{\text{ex}} \leq F_{t,\text{max}}^{\text{ex}} \\
 0 \leq F_s^{\text{in}} \leq F_{s,\text{max}}^{\text{in}}, \quad 0 \leq F_s^{\text{ex}} \leq F_{s,\text{max}}^{\text{ex}}
 \end{aligned} \tag{3}$$

Intuitively, the above limit surface will definitely change once accounting for the reinforcement. If a flexural hinge is triggered (Fig. 3a), the reinforcement strip will produce extra tensile forces (F_t^{ex} and F_t^{in}) at the separation (Fig. 3c), because of the its debonding failure against the substrate. Two sliding cohesions F_s^{ex} and F_s^{in} will also be involved when sliding happens due to the peeling failure (Fig. 3b). Therefore, the formulation of the updated limit surface then becomes Eq. (3).

Plotting the updated failure surfaces defined in Eq. (3), we can observe a significant expansion of the original failure surfaces due to the strengthening. Specifically, both $\bar{m}-\bar{n}$ and $\bar{s}-\bar{n}$ surfaces are translated along the positive direction of \bar{n} axis, resulting in a larger area for tensile normal forces (Fig. 4a); $\bar{s}-\bar{n}$ surface is also moved along the \bar{s} axis (Fig. 4b).

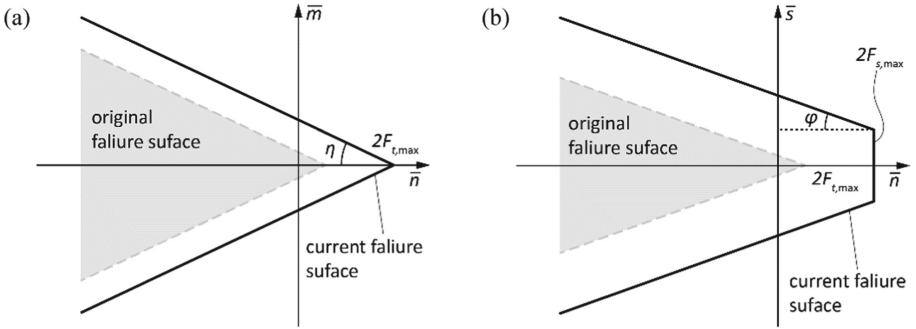


Fig. 4. Change of the failure surfaces due to the reinforcement: (a) $\bar{m}-\bar{n}$ limit surfaces; (b) $\bar{s}-\bar{n}$ limit surfaces.

Equation (3) can be transferred into a standard matrix form Eq. (4). Compared with the formulation in classical limit analysis (Eq. (1)), we merely need to add a spurious cohesion term \mathbf{c}_m , implicitly modeling the reinforcement layer. Specifically, the components of \mathbf{c}_m at a specific interface j are majorly dependent on four extra ultimate cohesion forces brought by strengthening (Eq. (5)). Those cohesion forces can be simply computed based on the properties of the reinforced material.

$$\mathbf{N}\mathbf{x} - \mathbf{c}_0 - \mathbf{c}_m = \mathbf{z}, \quad \mathbf{z} \leq 0 \quad (4)$$

$$\mathbf{c}_{m,j} = \begin{bmatrix} c_{m,j}^{r+} \\ c_{m,j}^{r-} \\ c_{m,j}^{s+} \\ c_{m,j}^{s-} \end{bmatrix} = \begin{bmatrix} (F_{t,\max}^{\text{in}} + F_{t,\max}^{\text{ex}}) \sin \varphi_j + (F_{s,\max}^{\text{in}} + F_{s,\max}^{\text{ex}}) \cos \varphi_j \\ (F_{t,\max}^{\text{in}} + F_{t,\max}^{\text{ex}}) \sin \varphi_j + (F_{s,\max}^{\text{in}} + F_{s,\max}^{\text{ex}}) \cos \varphi_j \\ 2F_{t,\max}^{\text{in}} \sin \eta_j \\ 2F_{t,\max}^{\text{ex}} \sin \eta_j \end{bmatrix} \quad (5)$$

As a consequence, the updated LB/UB associated formulations to take into account the strengthening effect are given as Eqs. (6) and (7), respectively.

$$\begin{aligned} & \text{maximize } \alpha \\ & \text{subject to } \mathbf{A}\mathbf{x} = \alpha \mathbf{f}_L + \mathbf{f}_D \\ & \quad \mathbf{N}\mathbf{x} - \mathbf{c}_0 - \mathbf{c}_m = \mathbf{z} \\ & \quad \mathbf{z} \leq 0 \end{aligned} \quad (6)$$

$$\begin{aligned}
 &\text{minimize } -\mathbf{f}_D^T \mathbf{u} + \mathbf{c}_0^T \mathbf{p} + \mathbf{c}_m^T \mathbf{p} \\
 &\text{subject to } \mathbf{f}_L^T \mathbf{u} = 1 \\
 &\quad \mathbf{A}^T \mathbf{u} = \mathbf{q} \\
 &\quad \mathbf{N}^T \mathbf{p} = \mathbf{q}, \mathbf{p} \geq 0
 \end{aligned} \tag{7}$$

We proceed to extend such a technique to solve a non-associated sliding problem. The SLP procedure is commonly employed to tackle this difficult problem [12]. This procedure breaks a non-associated problem into a series of associated limit analyses which can be managed through a robust LP solver. Iteratively solving these LP problems, the dilation angles for the discontinuous velocity will be gradually reduced while the constraints for the interfacial resultants remain (Fig. 5). The solution for these associated problems will eventually converge to a non-associated one. The proposed modeling technique for the strengthening effect is quite convenient to be applied to the SLP procedure. Similarly, a spurious cohesion term \mathbf{c}_m computed according to the properties of reinforced material is supplemented in the associated analysis of each iterative step.

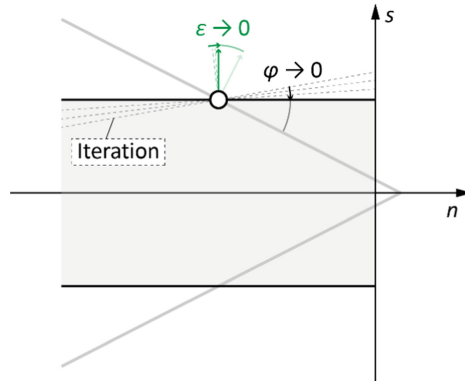


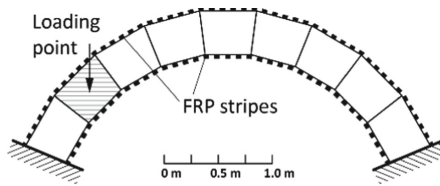
Fig. 5. Change of the limit surfaces and reduction of the dilation during the iterations.

3 Results

In this section, we take a 9-block 2D arch with both-side FRP reinforcement as an example for further collapse analysis based on the proposed modeling approach (Fig. 6). Table 1 lists the properties of the FRP and the bricks. Two ultimate cohesion forces $F_{t,max}$ and $F_{s,max}$ are computed based on the code CNR-DT200 [19] and the peel strength testing [20], respectively.

Table 1. Several parameters for the FRP and the bricks.

FRP	Thickness t_f [mm]	0.16
	Young's Module E_f [GPa]	230
	$F_{t, \max}$ [kN]	29.7
	$F_{s, \max}$ [kN]	9.86
Brick	Width/Height/Depth [mm]	500/400/400
	Compressive strength f_{bc} [MPa]	8
	Tensile strength f_{bt} [MPa]	0.8
	Frictional angle φ [°]	30

**Fig. 6.** Case study: a 9-block 2D arch with both-side FRP strengthening.

The differences in the collapse results from associated and non-associated formulations are mainly concerned in this section. Therefore, detailed parametric studies are carried out to observe the influence of critical parameters, including frictional angle φ and two cohesion forces $F_{t, \max}$ and $F_{s, \max}$, on those differences. Associated and non-associated collapses are predicted through LP and SLP procedures, respectively.

Figure 7 illustrates the variation of the ultimate load as well as the collapse mechanism along with the change of the friction angle φ (ranging from 20° to 40°). Generally, the ultimate load for the collapse will grow if φ increases, for both associated and non-associated collapse. When the φ increases, we observe three collapse mechanisms: local-sliding, hinge-sliding-mixing, and 4-hinge mechanism. In the observed range of φ , the associated formulation tends to produce a collapse purely with flexural hinges, indicating that the associated sliding model may overly restrict the sliding at contact joints. The non-associated formulation always predicts a smaller load multiplier. This means that associated limit analysis may overestimate the collapse load. Such an overestimation significantly rises with a decrease of φ . The maximum can reach 48.6%.

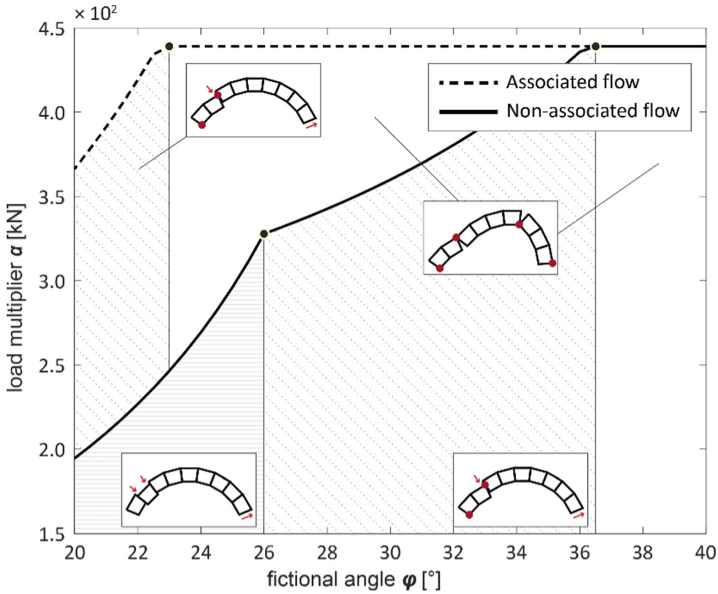


Fig. 7. Load multiplier α vs. frictional angle ϕ : comparison of associated and non-associated sliding.

The impact of the tensile cohesion force $F_{t,max}$ is then investigated on the collapse performance of the arch (Fig. 8). The growth of the $F_{t,max}$ will give rise to the increase of load multiplier. Note that only standard 4-hinge collapse is produced by associated formulation while the sliding appears in the mechanisms predicted by the non-associated limit analysis. In the condition of large tensile cohesion, sliding is more likely to take place because flexural failure is almost forbidden by the reinforcement layer. As a result, when $F_{t,max}$ is large, the collapse turns into a local-sliding one. In this case, the load multiplier predicted by non-associated analysis is much smaller than the associated prediction (with a maximum difference of 60.7%), ascribed to their different failure mode.

Finally, we conduct a parametric study regarding the sliding cohesion force $F_{s,max}$ (Fig. 9). The collapse of the arch with an associated sliding does not change when the ultimate cohesion force varies. When $F_{s,max}$ is low, the non-associated limit analysis gives a local-sliding collapse with a very small ultimate load. In this case, the overestimation of the associated limit analysis thus becomes critical, with a maximum of 70.5%. The ultimate load from the non-associated formulation grows with the increase of the sliding cohesion force because the sliding among the bricks is gradually prevented by the FRP strips. If $F_{s,max}$ is large enough, the collapse predicted by the non-associated limit analysis turns to a pure-hinge failure, in line with the results from the associated formulation.

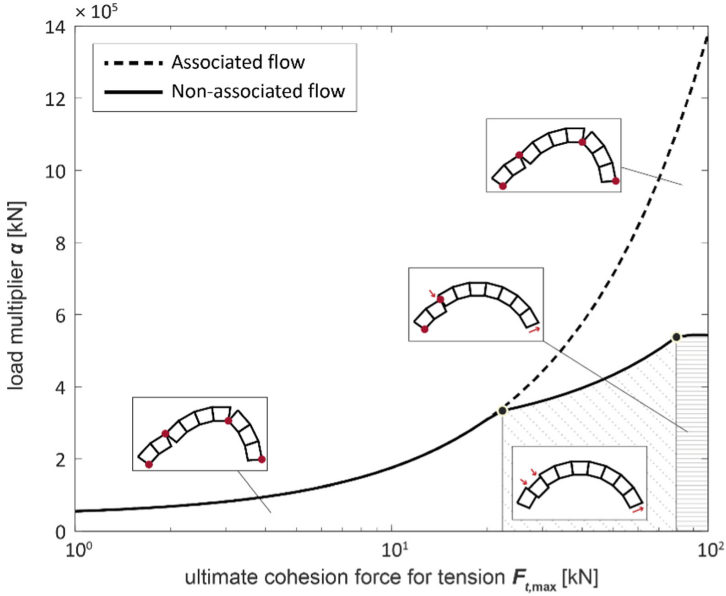


Fig. 8. Load multiplier α vs. ultimate cohesion force for tension $F_{t,max}$: comparison of associated and non-associated sliding.

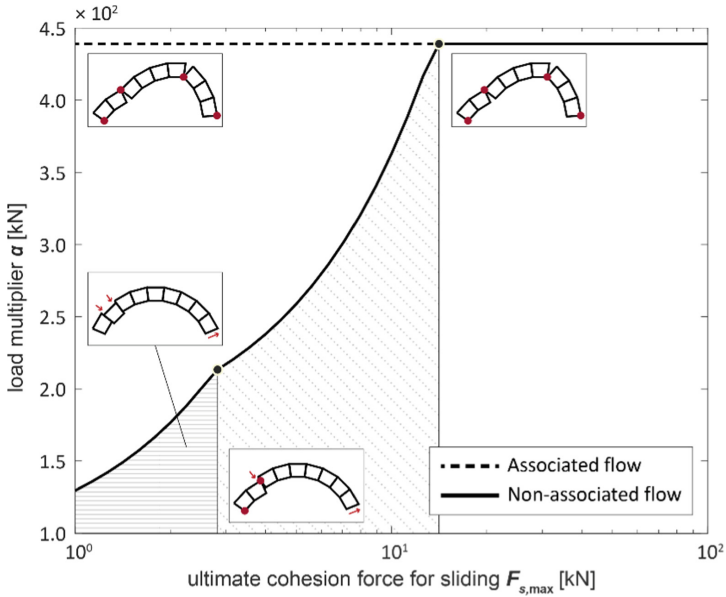


Fig. 9. Load multiplier α vs. ultimate cohesion force for sliding $F_{s,max}$: comparison of associated and non-associated sliding.

4 Conclusions

This paper extends the classical rigid block limit analysis to consider the innovative strengthening effect, applied to both associated and non-associated sliding problems. The constitutive constraint defining the failure surface in the standard formulation is updated to consider such a strengthening effect, with the addition of a spurious cohesion term. A 2D arch with both-side FRP reinforcement is taken as an example to compare the collapse results with associated and non-associated sliding. Detailed parametric studies are conducted to observe the influence of the critical parameters on the difference between associated and non-associated predictions. The main conclusion can be drawn as follows:

- The associated sliding model may give rise to an incorrect collapse mechanism of the arch once the reinforcement is taken into account. According to the parametric studies, associated limit analysis tends to give a standard 4-hinge collapse, indicating the sliding among the bricks is overly restricted due to the associativity.
- The associated formulation may also overestimate the collapse load. According to the parametric studies, such an overestimation increases with the growth of tensile cohesion and drop of the friction angle and sliding cohesion. The maximum could reach 70.5% for the associated prediction.
- The associated and non-associated formulations give a consistent prediction only if the collapse is a standard 4-hinge mechanism.
- Therefore, we suggest to employ a non-associated limit analysis for general collapse prediction. Associated formulation can only remain to be used if there is no sliding involved in the collapse, to save computational cost.

References

1. Makris, N., Alexakis, H.: The effect of stereotomy on the shape of the thrust-line and the minimum thickness of semicircular masonry arches. *Arch. Appl. Mech.* **83**(10), 1511–1533 (2013). <https://doi.org/10.1007/s00419-013-0763-4>
2. Chiozzi, A., Grillanda, N., Milani, G., Tralli, A.: UB-ALMANAC: an adaptive limit analysis NURBS-based program for the automatic assessment of partial failure mechanisms in masonry churches. *Eng Fail Anal* **85**, 201–220 (2018). <https://doi.org/10.1016/j.engfailanal.2017.11.013>
3. Chiozzi, A., Malagù, M., Tralli, A., Cazzani, A.: ArchNURBS: NURBS-based tool for the structural safety assessment of masonry arches in MATLAB. *J Comput Civ Eng* **30**, 4015010 (2016). [https://doi.org/10.1061/\(asce\)cp.1943-5487.0000481](https://doi.org/10.1061/(asce)cp.1943-5487.0000481)
4. Grillanda, N., Valente, M., Milani, G.: ANUB-Aggregates: a fully automatic NURBS-based software for advanced local failure analyses of historical masonry aggregates. *Bull. Earthq. Eng.* **18**(8), 3935–3961 (2020). <https://doi.org/10.1007/s10518-020-00848-6>
5. Portioli, F.P.A.: Rigid block modelling of historic masonry structures using mathematical programming: a unified formulation for non-linear time history, static pushover and limit equilibrium analysis. *Bull. Earthq. Eng.* **18**(1), 211–239 (2019). <https://doi.org/10.1007/s10518-019-00722-0>

6. Livesley, R.K.: Limit analysis of structures formed from rigid blocks. *Int J Numer Methods Eng* **12**, 1853–1871 (1978)
7. Livesley, R.K.: A computational model for the limit analysis of three-dimensional masonry structures. *Meccanica* **27**, 161–172 (1992). <https://doi.org/10.1007/BF00430042>
8. Heyman, J.: The stone skeleton. *Int. J. Solids Struct.* **2**, 249–256, IN1–IN4, 257–264, IN5–IN12, 265–279 (1966). [https://doi.org/10.1016/0020-7683\(66\)90018-7](https://doi.org/10.1016/0020-7683(66)90018-7)
9. Kooharian, A.: Limit analysis of voussoir (Segmental) and concrete arches. *ACI J. Proc.* **49**, 317–328 (1952). <https://doi.org/10.14359/11822>
10. Portioli, F., Casapulla, C., Gilbert, M., Cascini, L.: Limit analysis of 3D masonry block structures with non-associative frictional joints using cone programming. *Comput Struct* **143**, 108–121 (2014). <https://doi.org/10.1016/j.compstruc.2014.07.010>
11. Ferris, M.C., Tin-Loi, F.: Limit analysis of frictional block assemblies as a mathematical program with complementarity constraints. *Int J Mech Sci* **43**, 209–224 (2001). [https://doi.org/10.1016/S0020-7403\(99\)00111-3](https://doi.org/10.1016/S0020-7403(99)00111-3)
12. Gilbert, M., Casapulla, C., Ahmed, H.M.: Limit analysis of masonry block structures with non-associative frictional joints using linear programming. *Comput Struct* **84**, 873–887 (2006). <https://doi.org/10.1016/j.compstruc.2006.02.005>
13. Orduña, A., Lourenço, P.B.: Three-dimensional limit analysis of rigid blocks assemblages. Part II: Load-path following solution procedure and validation. *Int J Solids Struct* **42**, 5161–5180 (2005). <https://doi.org/10.1016/j.ijsolstr.2005.02.011>
14. Milani, G., Lourenço, P.B., Tralli, A.: Homogenised limit analysis of masonry walls, Part II: Structural examples. *Comput Struct* **84**, 181–195 (2006). <https://doi.org/10.1016/j.compstruc.2005.09.004>
15. Chiozzi, A., Milani, G., Tralli, A.: A Genetic Algorithm NURBS-based new approach for fast kinematic limit analysis of masonry vaults. *Comput Struct* **182**, 187–204 (2017). <https://doi.org/10.1016/j.compstruc.2016.11.003>
16. Caporale, A., Feo, L., Hui, D., Luciano, R.: Debonding of FRP in multi-span masonry arch structures via limit analysis. *Compos Struct* **108**, 856–865 (2014). <https://doi.org/10.1016/j.compstruct.2013.10.006>
17. Caporale, A., Feo, L., Luciano, R., Penna, R.: Numerical collapse load of multi-span masonry arch structures with FRP reinforcement. *Compos Part B Eng* **54**, 71–84 (2013). <https://doi.org/10.1016/j.compositesb.2013.04.042>
18. Drucker, D.C.: Coulomb Friction, Plasticity, and Limit Loads. *J Appl Mech* **21**, 71–74 (1954). <https://doi.org/10.1115/1.4010821>
19. CNR-DT200 Guide for the design and construction of externally bonded FRP systems for strengthening existing structures. C.N.R., National Research Council, Italy (2013)
20. Panizza, M., Garbin, E., Valluzzi, M.R.: Peel strength testing of FRP applied to clay bricks. In: *Proceedings of the 8th International Conference on Fracture Mechanics of Concrete and Concrete Structures, FraMCoS 2013*, pp 562–570 (2013)



Deep Neural Network and YUKI Algorithm for Inner Damage Characterization Based on Elastic Boundary Displacement

Nasreddine Amoura¹, Brahim Benaissa²(✉), Musaddiq Al Ali³, and Samir Khahir⁴

¹ LMP2M Laboratory, Yahia Fares University of Medea, New Urban Pole, 26000 Médéa, Algeria

amoura.nasreddine@univ-medea.dz

² Design Engineering Lab, Department of Mechanical Systems Engineering, Toyota Technological Institute, 2-12-1, HisakataNagoya, Aichi 468-8511, Tenpaku-Ku, Japan
Benaissa@toyota-ti.ac.jp

³ Department of Advanced Science and Technology, Toyota Technological Institute, 2-12-1, HisakataNagoya, Aichi 468-8511, Tenpaku-Ku, Japan

⁴ Ho Chi Minh City Open University, Ho Chi Minh, Viet Nam

Abstract. The efficiency of deep neural networks has been proven in several research fields. In this study, we suggest using this method of inverse crack identification based on the structural response of boundary displacement. This structural response is particularly challenging for surrogate modelling due to the overall similarity in the effect of different cracks. From the inverse problem perspective, this corresponds to a problem of many local minima. To solve this problem we use the newly suggested search technique of the dynamic search space reduction by the YUKI algorithm, build to solve this type of problem. We compare the performance of the suggested approach of the RBF modelling technique in terms of direct problem prediction and inverse problem identification accuracy. Deep Neural Networks are found to have better performance in both problems, although the computation time is significantly higher than RBF.

Keywords: YUKI algorithm · Crack identification · Deep ANN · Inverse problem

1 Introduction

In the framework of inverse crack identification the goal is to predict the unknown crack, defined by its parameters P [1, 2], based only on accessible structural response measurements $u(P_0)$. The most commonly used are the vibrational response and the mechanical responses. However, they face the challenge of the ill-Posedness [3–8], as the measured structural response may be insensitive to different cracks, and very different values of P can correspond to close measurements. Additionally, from the optimization problem perspective, this is a non-differentiable problem.

The crack identity P is dictated by the considered inverse problem. Thus, the correct numerical simulation of the problem is very important. The second difficulty is related

© The Author(s), under exclusive license to Springer Nature Switzerland AG 2023

R. Capozucca et al. (Eds.): ICSCES 2022, LNCE 317, pp. 220–233, 2023.

https://doi.org/10.1007/978-3-031-24041-6_18

to structural response characteristic in relation to variation to the crack parameters [9]. The existence of local minima is inevitable in these type of problems. Where local optimization algorithms cannot guarantee to attain the global minimum. Plus they require the problem to be differentiable. For these reasons, global optimization algorithms are needed [3, 10, 11].

An efficient algorithm is capable of finding the global minimum, regardless of the starting point in the search field. Global methods simulate a sample of parameters by exploiting only the information provided by the calculation of $f(P)$. To get the global minimum of a function using global methods, it would be necessary to go through all the space of the independent variables, which is generally impossible for classical optimization methods, given the size of the space and the number of variables.

In the inverse problem stage, the optimization algorithm is applied. Its goal is to find the closest response to one consequence of the crack to be identified [6]. The structural response is measured at the reference specimen. The optimization algorithm will then search for the crack parameters that correspond to the measured response. By calculating the structural response $u(P)$ corresponding to a possible crack P . The fitness function value is the error between this vector and the reference structural response $u(P_0)$ caused by the real crack parameters. [12]. Figure 1 depicts the inverse crack identification approach. Where the optimal crack identity is the one that provides a fitness function value less or equal to a limit. This limit varies from one case to another and also on the nature of the crack parameters. It is decided after knowing the fitness function equivalent to the wanted precision. The stopping criterion is considered based on the number of iterations. The number of iterations depends on the optimization algorithm, so the optimal crack identity can be reached if the optimization algorithm is fast enough.

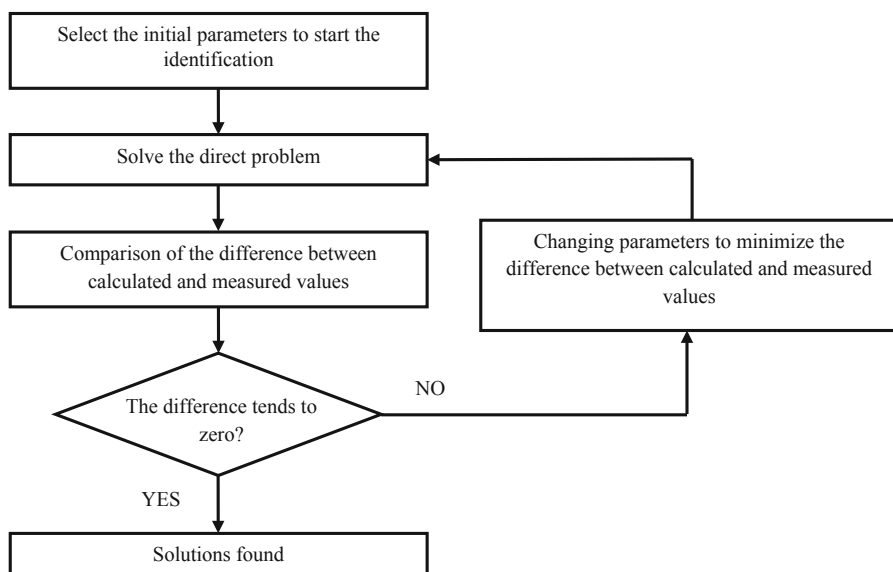


Fig. 1. Inverse crack identification approach

The structural response researchers have suggested several approaches based on ANN [13], Weinstein et al. suggested. One of the early deep learning works in this field of vibration analysis is made by Barai et al. [14] in damage identification Zang et al. [15] suggested an approach based on frequency response functions as input to ANN. Abdeljaber et al. [16] designed a real-time damage identification strategy based on one-dimensional convolutional neural networks. In the studies based on the mechanical response, Stavroulakiset al [17, 18] created a crack identification method based on backpropagation neural networks for structural response generation, using the boundary element method to create the training data. Khaleghi et al. [19] suggested an inner fracture characteristics approach based on artificial neural networks under noisy measurement.

2 Numerical Simulation

In elastostatics, the sum of all forces on the structure is equal to zero, and the displacements are not a function of time [20–22]. The equilibrium equations are stated as:

$$\sigma_{ij,j} + b_i = 0, \quad i, j = 1, 2, 3 \tag{1}$$

σ_{ij} is the Cauchy stress tensor. b_i represents the body-force components. And the strains ε_{ij} are defined by:

$$\varepsilon_{ij} = \frac{1}{2}(u_{i,j} + u_{j,i}), \quad i, j = 1, 2, 3 \tag{2}$$

$u_{i,j}$ are the displacement component. Considering that the material is elastic, homogenous and isotropic, Eqs. (1) and (2) are related by Lamé’s equation:

$$\sigma_{ij} = \lambda \varepsilon_{kk} \delta_{ij} + 2\mu \delta_{ij}, \quad i, j, k = 1, 2, 3 \tag{3}$$

The Kronecker-delta function δ_{ij} is written as follows:

$$\delta_{ij} = \{1 \quad i = j, \quad 0 \quad i \neq j\} \tag{4}$$

$$\lambda = \frac{2\nu\mu}{(1 - 2\nu)} \tag{5}$$

$$\mu = \frac{E}{2(1 + \nu)} \tag{6}$$

where λ Lamé constant, and μ is the shear modulus. The strains have to satisfy the following compatibility equations:

$$\frac{\partial \varepsilon_{ij}}{\partial x_i \partial x_k} - \frac{\partial}{\partial x_i} \left(-\frac{\partial \varepsilon_{jk}}{\partial x_i} + \frac{\partial \varepsilon_{ik}}{\partial x_j} + \frac{\partial \varepsilon_{ij}}{\partial x_k} \right) = 0, \quad i, j, k = 1, 2, 3 \text{ and } i \neq j \neq k \tag{7}$$

The problem is defined as follows. Let Ω denote an open set with boundary Γ subject to the boundary conditions:

$$u = \underline{u}_i \text{ on } \Gamma_u, \tag{8}$$

$$t = \underline{t}_i \text{ on } \Gamma_t \tag{9}$$

Where

$$\Gamma = \Gamma_u \cup \Gamma_t, \Gamma_u \cap \Gamma_t = \emptyset \tag{10}$$

And

$$\underline{\Omega} = \Omega \cup \Gamma \tag{11}$$

The problem is: given u_i , t_i and b_i ; find $u_i(y)$, $y \in \underline{\Omega}$. Furthermore, the plane strain is assumed and therefore:

$$\varepsilon_{zz} = \varepsilon_{xz} = \varepsilon_{yz} = 0 \tag{12}$$

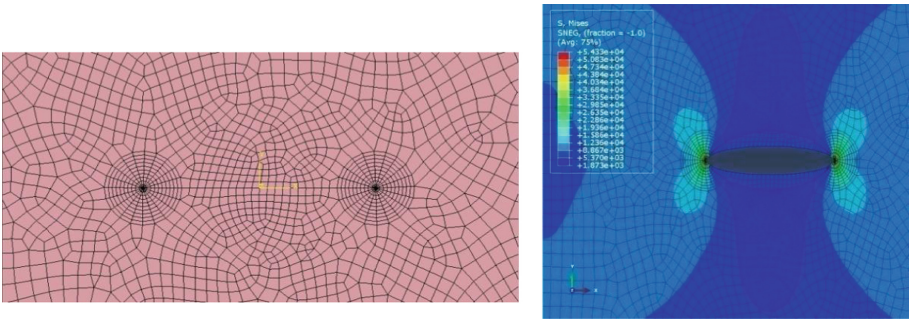


Fig. 2. Display of meshing around the crack tips and Von Mises constraint

The simulations in this paper are made using Abaqus. It is a powerful finite element simulation tool used in many fields of mechanical studies. It has special features dedicated to fracture mechanics, which makes this tool very advantageous, such that the crack segment model, the calculation of J integral, and different crack propagation laws.

In this section, we present a simulation of a cracked plate of a rectangular shape with 1 mm thickness, having dimensions of 30 mm height and 10 mm width, it is subjected to traction force from the upper and the lower sides. The Young modulus and Poisson coefficient of the material were respectively $E = 210 \text{ GPa}$ and $\nu = 0.3$. The vertical sides have meshed with 80 quadrilaterals and the horizontal side with 30 elements. The meshing of the crack has been divided into two main areas; the area of the crack tip, covering both crack endings, and the area of the middle of the crack. The sweep function is used to mesh the crack tips, with radius of the circle is 0.5 mm. 20 elements along the contour of the circle, and 10 elements along the radius of the circle, resulting in a total of 200 elements at each crack tip as shown in Fig. 2. Along with the the Von Mises constrain.

The majority of crack identification studies are based on boundary data because boundaries are considered the only accessible part of the structure. In the case studied

in this paper, the horizontal boundaries (upper and lower boundaries) are subjected to boundary conditions, in real cases; it means interaction with other structures of solicitations, which makes them inaccessible for measurements, leaving the vertical boundaries to be the only source of information.

3 Radial Basis Functions Modelling

Radial Basis Functions (RBF) are very efficient for interpolation between existing data [23, 24]. To approximate a function $f(x)$, where x is an M -dimensional vector, RBF requires the information in a form of a set of N nodes x_i , for which the values of the function are known. For any new value of x the interpolation is performed involving just a few nearby nodes. The approach of RBF performs it one continuous function, defined over the whole domain. The approximation is written as the combination of g_i functions:

$$f(x) \approx \sum_{i=1}^N \alpha_i g_i(x) \quad (13)$$

This equation is defined once the basis functions g_i are selected and the coefficients α_i are known. Where α_i are the combination coefficients. For the radial basis functions, the Euclidian distance is considered in this paper.

$$g_i(x) = g_i(\|x - x_i\|), i = 1, 2, \dots, N \quad (14)$$

To determine the coefficients α_i , the interpolation needs to be exact in all N nodes, therefore, the system of N equations defined by:

$$f(x_j) = y_j = \sum_{i=1}^N \alpha_i g_i(x_j), j = 1, \dots, N \quad (15)$$

where y_j are known values of the function in the nodes. Introducing the following matrix notation

$$G = \begin{bmatrix} g_1(x_1) & \dots & g_N(x_1) \\ \vdots & \ddots & \vdots \\ g_1(x_N) & \dots & g_N(x_N) \end{bmatrix}; \alpha = [\alpha_1, \alpha_2, \dots, \alpha_N]^T; Y = [y_1, y_2, \dots, y_N]^T \quad (16)$$

The system can be written as:

$$\alpha \cdot G = Y \quad (17)$$

Matrix Eq. (15) is solved for the interpolation coefficients α_i . The interpolation coefficients are computed once and for all, and involve the known values at the nodes. Once this is achieved, we can approximate the function at any given point [23]. Considering that the results of Eq. (13) are exact in the nodes, and gives interpolated results for any new value of x . The RBF represents one approximation valid for the whole domain in which the original data were situated.

The results is a model that is able of reproducing the original data field, plus interpolated values for any new set of parameters within the initial variables domain. The results of extrapolation outside this domain may be of poor accuracy [23]. We use the RBF model to retrieve the values of the unknown geometric crack parameters in this study. And employed to provide the structural response, representing the direct model.

4 Deep Artificial Neural Network

Deep ANN has been used widely in a wide range of engineering problems [25, 26]. Theoretically, it has the power to connect the problem’s input and target features in nonlinear and complex spaces, given enough neurons in the hidden layers. With the wide availability of ANN tools and open source codes, engineers only have to solve the issue of the number of layers, and the number of neurons in each layer [27].

The information is stored in the node’s weights. Thus for the network to approximate the system’s output, these weights are optimized in a process called training. Figure 3. Illustrates the Deep ANN network. Training of collected data is used to model the characteristics of the system. During the training, the process uses a smaller set of data called the validation dataset is used test the quality of the network predictions, and change the parameters to achieve high precision [28].

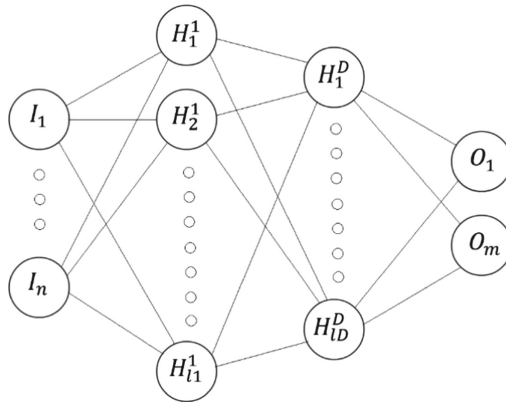


Fig. 3. Von Mises constraint ANN structure to determine damage level

The Deep ANN is characterized by multiple hidden layers, besides the input layer and the output layer. The number of hidden layers is denoted in the figure by D , the number of input and output neurons are denoted by n and m respectively, and the number of neurons in each hidden layer is denoted by l . Each neuron is connected to all the neurons in the next layer, and the strength of the connection is weighted though w_{ij}^k . Each neuron is assigned a bias value β . In the training phases, the optimization algorithm will find the optimal weights and biases combinations that correspond to the lowest prediction error, according to the testing data set.

5 YUKI Algorithm

YUKI algorithm is a newly suggested method [20], with an innovative search space reduction technique. It uses simple steps to focus on interesting search areas, and dynamically changes the size and position of the search focus. The first idea of YUKI algorithm is to create a local search area smaller than the search domain, it is positioned around

the absolute best solution at the current iteration X_{best} , and its size is calculated as the distance between this point and the $X_{MeanBest}$. Where MeanBest is the centre of the point cloud representing the historical best founts found by each solution. LT and LB are the top and bottom boundaries of the local search area respectively. They are calculated as follows:

$$D = |X_{best} - X_{MeanBest}| \tag{1}$$

$$LT = X_{best} + D \tag{2}$$

$$LB = X_{best} - D \tag{3}$$

The second idea of this algorithm is to dedicate two parts of the population to exploration and exploitation simultaneously, by splitting the population. One part is assigned to exploration outside the local search area, and the other is assigned to focus on searching inside the local search area. The size of the population dedicated to each part is determined by the EXP parameter, which should be between 0 and 1. 0.6 for example, means 60% of the population will be dedicated to exploring outside the focus area, and 40% will focus the search inside the local search area.

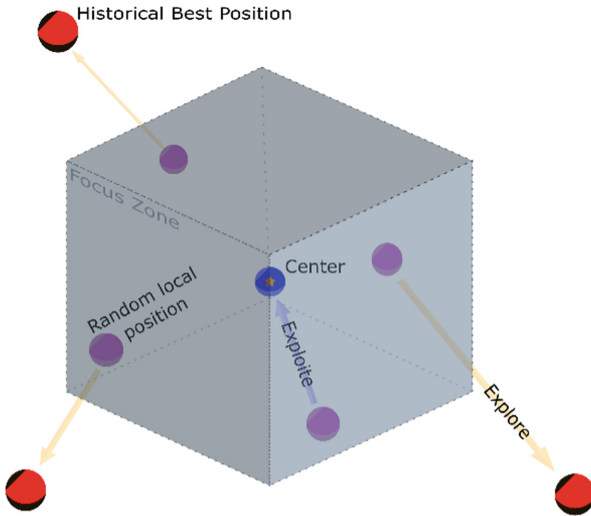


Fig. 4. Illustration of the focus zone exploration strategy

This is done by first, generating a random distribution of points inside the local search area, then assigning the dedicated search populations selected for exploration outside the local search area. Exploration spread is directed to look toward the historical best points as follows:

$$E = X_{loc} - X_{best} \tag{5}$$

where X_{loc} denotes a position of the selected point to be directed toward exploration, and X_{best} is the historical best point found by this individual particle. The next position will then be calculated as follows:

$$X_{new} = X_{loc} + E \tag{6}$$

For the solutions dedicated to the exploitation inside the local search zone, we first calculate the distance from the centre Eq. (7), then calculate the next position as in Eq. (8). Where $rand$ here is the random value between 0 and 1. And for each solution. Figure 4 illustrates the YUKI algorithm ideas.

$$F = X_{loc} - X_{best} \tag{7}$$

$$X_{new} = X_{loc} - rand \times F \tag{8}$$

These simple steps lead to the complex behaviour of the local search area, as it can dynamically reduce its size if new solutions are found inside, or increase the size significantly if better solutions are found outside. The location of this focus area also changes automatically throughout the search. With the progress of iterations, the local search area tends to reduce in size leading to focusing on the optimal position at the end of the search.

6 ANN and RBF for Direct Problem Representation

The boundary displacement responses are collected from 67 simulations. The boundary conditions are constant but crack sizes and positions vary. The size of the crack varies between 0 and 5 mm, and its position is located between -10 and 10 on the Y-axis and -2 and 2 on the X-axis (Fig. 5). Each node in the vertical boundaries is considered a sensor point, thus the total number of 162 data points, 81 from the left side and 81 from the right vertical side boundary.

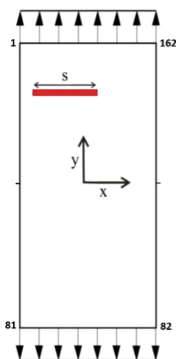


Fig. 5. Illustration of the simulated problem with crack parameters.

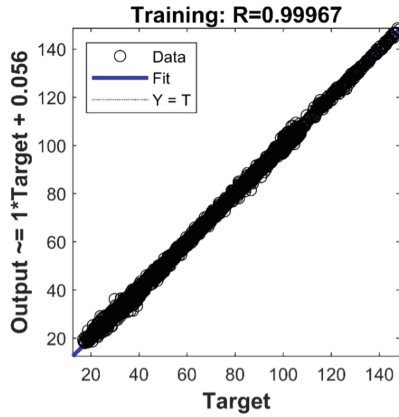


Fig. 6. Displays the training results for the deep ANN network.

These results are used to build surrogate models using RBF and ANN networks. Several ANN designs have been investigated. After statistical analysis, the backpropagation architecture with these layers (60:150:250:200:180) has been selected for further study. Figure 6 displays the training results for this deep ANN network, using conjugate gradient backpropagation with Fletcher-Reeves updates.

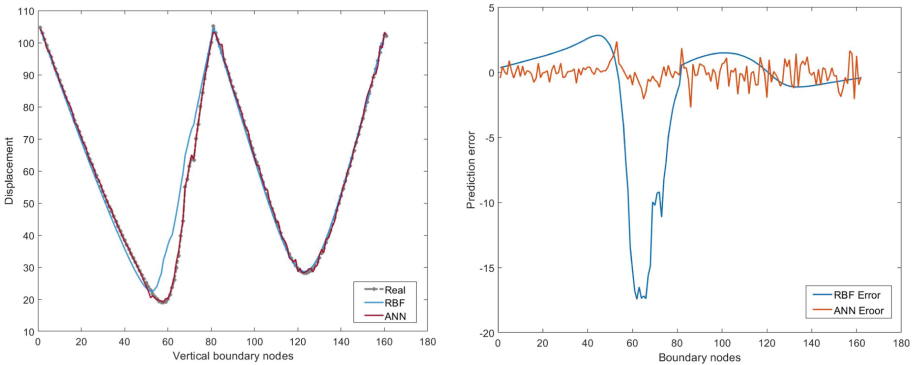


Fig. 7. Boundary displacement prediction error, using deep ANN and RBF networks.

Figure 7 Shows the boundary displacement prediction error using deep ANN and RBF. Where the considered example is a crack at the lower left side with center coordinates $(-1.75, -9.5)$ and a size of 3.2 mm. The left side graph compares the predictions to of the real displacement field. And on the right side graph the prediction errors of deep ANN and RBF. These figures show an advantage for Deep ANN in terms of overall accuracy, it also indicates that although RBF has a smoother displacement field, more appropriate in this case than the results found by deep ANN, RBF faces a challenge in predicting the displacement at that boundary node in the proximity of the crack. These results are found in other examples and are indicative of the overall predictions.

7 Crack Identification Results

The crack identification is formulated as an optimization problem, as suggested in Fig. 1, the goal is to find the crack corresponding to the boundary displacement response most close to the measurement, the closeness is calculated as described in Eq. (9). We considered 4 segments of the displacement field, representing the four quarters of the vertical boundaries.

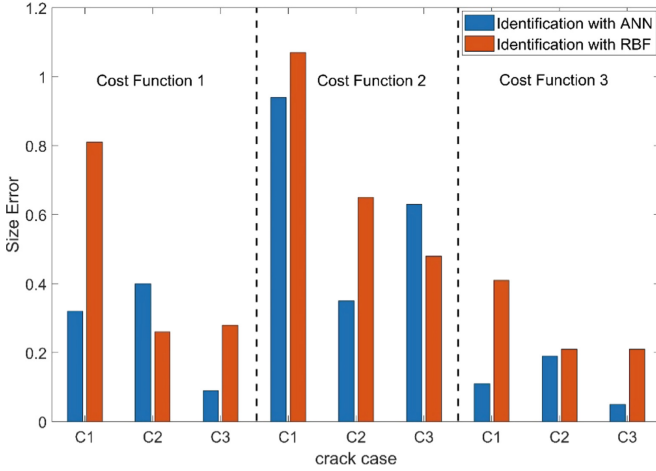


Fig. 8. Crack size prediction based on boundary displacement using Deep ANN and RBF.

Due to the unsymmetric nature of the problem, we assume that this approach help identify the region in which the crack exists more efficiently than if we consider the boundary displacement field as a whole. Three cost functions were considered, expressed in Eqs. (10), (11) and (12).

$$f^i(P) = \frac{\|u^i(p_0) - u^i(p)\|^2}{\|u^i(p_0)\|^2} \text{ with } i = 1, 2, 3, 4. \tag{9}$$

$$F_1(P_{opt}) = \min(f^1(P), f^2(P), f^3(P), f^4(P)) \tag{10}$$

$$F_2(P_{opt}) = \text{Mean}(f^1(P), f^2(P), f^3(P), f^4(P)) \tag{11}$$

$$F_2(P_{opt}) = F_1 + F_2 \tag{12}$$

The first function takes into consideration only the boundary quarter corresponding to the minimum fitness value. This is designed to isolate the noisy effect created by the rest of the data points. The second function is similar to the case where we consider the whole boundary displacements, it has the advantage of having better knowledge of the effect of each particular crack on the boundary displacement field.

The last function takes into consideration the advantages of both functions, and it is assumed in this case, that the fitness of wrong crack identities will be amplified due to having the error considered twice. Tables 1, 2 and 3 show the identification errors in terms of crack size and position, the error is calculated as the Euclidian distance between the real crack centre and the centre of the predicted crack. The first crack is C1 with centre coordinates (-1.7, -9.5) and a size of 3.2 mm, the C2 centre is at (1.6, 3.8) and a size of 3.1 mm. C3 is positioned at (-0.15, 0.15) and has a size of 4.6 mm.

Table 1. Identification results based on the first fitness function (Eq. 10).

Fitness Function F_1	ANN Error (mm)		RBF Error (mm)	
	Size	Position	Size	position
C1	0.32	0.877268	0.81	1.203703
C2	0.4	0.297321	0.26	0.766877
C3	0.09	0.632456	0.28	0.764003

Table 2. Identification results based on the second fitness function (Eq. 11).

Fitness Function F_2	ANN Error (mm)		RBF Error (mm)	
	Size	Position	Size	position
C1	0.94	1.216306	1.07	1.66331
C2	0.95	1.097315	0.25	1.02
C3	0.63	0.45607	0.48	1.17047

Table 3. Identification results based on the third fitness function (Eq. 12).

Fitness Function F_3	ANN Error (mm)		RBF Error (mm)	
	Size	Position	Size	position
C1	0.11	0.494975	0.78	1.203703
C2	0.19	0.221359	0.21	0.408534
C3	0.05	0.284253	0.21	0.550818

The crack identification error varies between 0.22 mm and 1.6 mm in terms of position, and between 0.05 and 1.07 mm in terms of crack size. The results suggest that, overall, the third fitness function corresponds to the highest identification accuracy for both crack size and location. Figure 8 Shows this advantage in crack size prediction. It also shows that Deep ANN is favourable in most cases compared to RBF modelling. This is due to the higher boundary displacement accuracy. However, the fitness evaluation using Deep ANN is very costly compared to RBF. Figure 9 depicts the difference between

Deep ANN and RBF in the computational cost of a single identification run using the YUKI algorithm, with a population of 20 and the maximum number of iterations is 100.

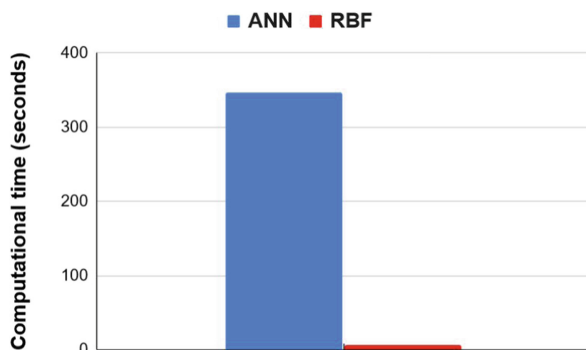


Fig. 9. Computation cost using Deep ANN and RBF.

8 Conclusion

In this paper, damage identification in steel plates is presented, using the inverse problem approach. The approach uses the boundary displacement response measured in the presence of an inner crack with different sizes and positions. The finite element method is used to simulate these boundary displacement responses. The inverse problem requires an iterative search with thousands of response evaluations, crack identification researchers investigate alternative solutions to FEM simulation, due to the very expensive computational cost. As well as suggest better-performing search algorithms that require a lower number of iterations.

The performances of Deep ANN and RBF networks for the inverse problem evaluation have been investigated in this work. Using the newly suggested YUKI algorithm. We found that Deep ANN is favourably placed to simulate the boundary displacement response, as it has good stability to unknown crack parameters compared to the RBF method, providing a more consistent prediction error. However, the computation time for RBF is significantly better, which may justify the use of this method.

Boundaries most close to damage are subjected to higher displacement than farther away boundaries. The use of the whole boundary displacement sensors is not favourable for the objective function, because that does not consider the above-mentioned fact, we investigated the segmentation of the boundaries and use cost functions that take into consideration the regional effect of the cracks, and found that the best results are found when considering the average error in all segment plus error in the segment corresponding to the minimum error. This approach will amplify the error in the wrong output, which helps reduce the ill-Posedness of this problem.

References

1. Amoura, N., Kebir, H., Benzerdjeb, A.: 3D crack identification using the Nelder-Mead Simplex algorithm combined with a random generation of crack positions. *Frattura e Integrità Strutturale* **16**(59), 243–255 (2022)
2. Amoura, N., Kebir, H., Rechak, S., Roelandt, J.: Axisymmetric and two-dimensional crack identification using boundary elements and coupled quasi-random downhill simplex algorithms. *Eng. Anal. Boundary Elem.* **34**, 611–618 (2010)
3. Al Thobiani, F., Khatir, S., Benaissa, B., Ghandourah, E., Mirjalili, S., Wahab, M. A.: A hybrid PSO and Grey Wolf Optimization algorithm for static and dynamic crack identification. *Theoret. Appl. Fract. Mech.* **118**, 103213 (2022)
4. Benaissa, B., Köppen, M., Wahab, M.A., Khatir, S.: Application of proper orthogonal decomposition and radial basis functions for crack size estimation using particle swarm optimization. *J. Phys. Conf. Ser.* **842**(1), 012014 (2017)
5. Khatir, S., Abdel Wahab, M., Tiachacht, S., Le Thanh, C., Capozucca, R., Magagnini, E., et al.: Damage identification in steel plate using FRF and inverse analysis. *Frattura ed Integrità Strutturale-Fracture and Structural Integrity* **58**, 416–433 (2021)
6. Khatir, S., Tiachacht, S., Benaissa, B., Le Thanh, C., Capozucca, R., Abdel Wahab, M.: Damage identification in frame structure based on inverse analysis. In: *Proceedings of the 2nd International Conference on Structural Damage Modelling and Assessment*, pp. 197–211 (2022)
7. Khatir, S., Wahab, M.A., Benaissa, B., Köppen, M.: Crack identification using eXtended IsoGeometric analysis and particle swarm optimization. In: *Fracture, Fatigue and Wear*, pp. 210–222 (2018)
8. Behtani, A., Tiachacht, S., Khatir, T., Khatir, S., Wahab, M.A., Benaissa, B.: Residual Force Method for damage identification in a laminated composite plate with different boundary conditions. *Frattura ed Integrità Strutturale* **16**, 35–48 (2022)
9. Amoura, N., Kebir, H., Rechak, S., Roelandt, J.: Numerical simulation of the behaviour of cracks in axisymmetric structures by the dual boundary element method. In: *Damage and Fracture Mechanics*, ed: Springer, pp. 435–443 (2009)
10. Samir, K., Idir, B., Serra, R., Brahim, B., Aicha, A.: Genetic algorithm based objective functions comparative study for damage detection and localization in beam structures. In: *Journal of Physics: Conference Series*, p. 012035 (2015)
11. Samir, K., Brahim, B., Capozucca, R., Wahab, M.A.: Damage detection in CFRP composite beams based on vibration analysis using proper orthogonal decomposition method with radial basis functions and cuckoo search algorithm. *Compos. Struct.* **187**, 344–353 (2018)
12. Benaissa, B., Belaidi, I., Hamrani, A.: Identifying defect size in two dimensional plates based on boundary measurements using reduced model and genetic algorithm. *J. Sci. Technol.* **2**, 7–12 (2017)
13. Gomes, G.F., Mendez, Y.A.D., da Silva Lopes Alexandrino, P., da Cunha, S.S., Ancelotti, A.C.: A review of vibration based inverse methods for damage detection and identification in mechanical structures using optimization algorithms and ANN. *Arch. Comput. Methods Eng.* **26**, 883–897 (2019)
14. Barai, S., Pandey, P.: Vibration signature analysis using artificial neural networks. *J. Comput. Civ. Eng.* **9**, 259–265 (1995)
15. Zang, C., Imregun, M.: Structural damage detection using artificial neural networks and measured FRF data reduced via principal component projection. *J. Sound Vib.* **242**, 813–827 (2001)
16. Abdeljaber, O., Avci, O., Kiranyaz, S., Gabbouj, M., Inman, D.J.: Real-time vibration-based structural damage detection using one-dimensional convolutional neural networks. *J. Sound Vib.* **388**, 154–170 (2017)

17. Stavroulakis, G.E., Engelhardt, M., Likas, A., Gallego, R., Antes, H.: Neural network assisted crack and flaw identification in transient dynamics. *J. Theor. Appl. Mech.* **42**, 629–649 (2004)
18. Stavroulakis, G., Antes, H.: Neural crack identification in steady state elastodynamics. *Comput. Methods Appl. Mech. Eng.* **165**, 129–146 (1998)
19. Khaleghi, M., Haghghat, E., Vahab, M., Shahbodagh, B., Khalili, N.: Fracture characterization from noisy displacement data using artificial neural networks. *Eng. Fract. Mech.* **271**, 108649 (2022)
20. Benaissa, B., Hocine, N.A., Khatir, S., Riahi, M.K., Mirjalili, S.: YUKI algorithm and POD-RBF for Elastostatic and dynamic crack identification. *J. Comput. Sci.* **55**(1851), 101451 (2021)
21. Benaissa, B., Ait Hocine, N., Belaidi, I., Hamrani, A., Pettarin, V.: Crack identification using model reduction based on proper orthogonal decomposition coupled with radial basis functions. *Struct. Multidiscip. Optim.* **54**(2), 265–274 (2016). <https://doi.org/10.1007/s00158-016-1400-y>
22. Stavroulakis, G., Antes, H.: Nondestructive elastostatic identification of unilateral cracks through BEM and neural networks. *Comput. Mech.* **20**, 439–451 (1997)
23. Buljak, V., Maier, G.: Proper orthogonal decomposition and radial basis functions in material characterization based on instrumented indentation. *Eng. Struct.* **33**, 492–501 (2011)
24. Arora, Y., Singhal, A., Bansal, A.: A study of applications of RBF network. *Int. J. Comput. Appl.* **94**(2), 17–20 (2014)
25. Goodfellow, I., Bengio, Y., Courville, A.: *Deep learning*. MIT press, Cambridge (2016)
26. LeCun, Y., Bengio, Y., Hinton, G.: *Deep learning*. *nature*, **521**, 436–444 (2015)
27. Hinton, G.E.: Learning multiple layers of representation. *Trends Cogn. Sci.* **11**, 428–434 (2007)
28. Sharma, O.: Deep challenges associated with deep learning. In: 2019 International Conference on Machine Learning, Big Data, Cloud and Parallel Computing (COMITCon), pp. 72–75 (2019)



Energy Dissipation Based Structural Condition Assessment Using Random Decrement Technique

Toan Pham-Bao^{1,2}(✉), Thao D. Nguyen^{1,2}, and Nhi Ngo-Kieu^{1,2}

¹ Laboratory of Applied Mechanics (LAM), Ho Chi Minh City University of Technology (HCMUT), 268 Ly Thuong Kiet Street, District 10, Ho Chi Minh, Viet Nam

baotoanbk@hcmut.edu.vn

² Vietnam National University Ho Chi Minh City, Linh Trung Ward, Thu Duc City, Ho Chi Minh City, Vietnam

Abstract. This study investigates the potential application of the random decrement (RD) technique for condition assessment in beam-like structure based on energy dissipation of material, when only acceleration responses are available for use. First, an analytical model of viscoelastic beam with various levels of energy dissipation was used, based on modal superposition principle, to obtain the response of systems to input force. Then, RD technique is employed to calculate to transform the random structural response into the free decay response. RD technique is only based output measurements, whereas other traditional methods need requirement of both input and output ones. In structural engineering, input ambient excitations (wind, earthquake and traffic load, etc.) are difficult to determine. Finally, a new feature established from the Power Spectral Density (PSD) of Randec signature, call the Displacement Loss Factor function (DLF), is used to assess structural condition. Numerical simulations of a linear beam loaded by white noise are used to verify the effectiveness of the method in assessing the structural condition.

Keywords: Energy dissipation · Random decrement · Power Spectral Density

1 Introduction

Nowadays, Damage Identification (DI) and Structural Health Monitoring (SHM) are becoming some of the most important issues in civil infrastructures, such as buildings and bridges [1]. Damage can cause a structure to produce irregular changes, generally demonstrated in vibration responses [2]. The vibration signals of the structure thus can be measured to consider the influence of damage on the mechanical parameters of the structure, as change in mechanical parameters leads to a variation in the vibrational characteristics of the mechanical system. The ability of SHM to perform assessment of the bridge during its operation is a great strength. However, the effect of the environment and traffic loads cannot be controlled or measured in a simple way [3]. Doebling et al. [4] conducted a literature review of the DI and SHM studies concerning dynamic properties.

From extracting irregularities (or features), damage can be identified in a structure. Traditional vibrational features, such as natural frequencies, damping and mode shapes, can also be used to update the physical parameters of models. While natural frequencies and mode shapes have been used extensively in detecting damage associated with a reduction in local stiffness of the structure, the use of damping to detect damage has not been supported, primarily due to the difficulty of damping measurement and analysis [5].

One of dynamics properties is energy dissipation of material which has been rarely applied to identify structural condition [6–8] because of the complex mechanism. In terms of mechanism, the damping represents the physical property that dissipates vibrational energy in the mechanical system [9]. Types of damping mechanisms include molecular dislocations, joint clamping pressure, viscosity of materials, interactions between fluids and structures, etc. [10]. In general, damping is basically divided into three main types such as material damping, structural damping, fluid damping [10]. Material damping is difficult to determine because it is caused by complicated interactions of molecule within the material. While it has been showed that the change of damping parameters caused by damage and deterioration can be more sensitive than natural frequencies, the accuracy of damping identification by measured vibration signal is not high [11]. If the factors affecting the damping are varied, the physical explanation of the damping change is very difficult. In addition, understanding about damping of real structures is not clear [12].

In this study, a new scheme for assessing structural condition employing transient loss factor identification using viscoelastic material model is presented. In addition to the elastic modulus E in Hooke's law, the viscous coefficient C as in Newton's law [13] is also used to represent the properties of the material. The viscous coefficient C is a novel parameter which shows material damping of structures [14, 15]. A feature called the Displacement Loss Factor function (DLF) is used to evaluate energy dissipation in the structure. The DLF is only determined from the power spectral density (PSD) of the output signal. In fact, the vibration response of the structure is often random by the ambient load. In order to limit the influence of unknown components in the dynamic response of the structure, random signal is converted to free decay signal containing only modal parameters through the Random Decrement (RD) technique [16]. Then DLF is extracted from PSD of Randec signatures.

2 Material and Method

The general linear relationship between stress and strain of a viscoelastic material [17] is described as follows:

$$\sum_{i=0}^n a_i \frac{d^i \sigma(t)}{dt^i} = \sum_{j=0}^m b_j \frac{d^j \varepsilon(t)}{dt^j} \quad n, m = 0, 1, 2, \dots \quad (1)$$

The material damping properties is simply described by the Kelvin-Voigt model which is used in some previous studies [18]. This model is performed in terms of a

combination in which an elastic spring is parallel with a viscous damper. Therefore, normal stress (σ) is relative with longitudinal strain (ε) as the following form:

$$\sigma(t) = E\varepsilon(t) + C \frac{d\varepsilon(t)}{dt} = E \left[\varepsilon(t) + \mu \frac{d\varepsilon(t)}{dt} \right] \tag{2}$$

where μ, E, C are damping factor, young modulus and viscous coefficient of materials, respectively. Governing equation of the Euler-Bernoulli beam associated with the Kelvin-Voigt model is expressed as bending vibration [19].

$$EJ(x) \left(\frac{\partial^4 w(x, t)}{\partial x^4} + \mu \frac{\partial^5 w(x, t)}{\partial x^4 \partial t} \right) + \rho A(x) \frac{\partial^2 w(x, t)}{\partial t^2} = f(x, t) \tag{3}$$

where w – horizontal displacement; J – inertia moment of cross-section; x – longitudinal coordinate; t – time; ρ – density of beam; A – cross-section area; f – external load.

In the modal analysis, the displacement function w of the beam [18] is found in the form as a linear superposition of N modal responses by Eq. (4).

$$w(x, t) = \sum_{r=1}^N X_r(x) T_r(t) \tag{4}$$

where $X_r(x)$ are r th shape functions that satisfy boundary conditions, and $T_r(t)$ are r th generalized displacements. Equation (4) is used to convert Eq. (3) to a set of N generalized equations as the following form:

$$\ddot{T}_r + \frac{C\omega_r^2}{E} \dot{T}_r + \omega_r^2 T_r = F_r(t) \tag{5}$$

where ω_r is the natural frequency and $F_r(t)$ is generalized load of the r th generalized coordinate. If F_r is a wideband load, the response of structure performs a zero-mean Gaussian process which consists of two components: deterministic part and stochastic part. The RD technique will limit the influence of stochastic part by averaging the time history segments of random signals determined by the trigger condition a as:

$$m_r(\tau) = E[T_r(t + \tau) | T_r(0) = a] = \frac{R_{T_r}(\tau)}{R_{T_r}(0)} a \tag{6}$$

where $E[\cdot]$ is defined as the conditional expected value, $R(\tau)$ is auto-correlation function of the displacement response and a is the trigger level. Because of the average in time domain, vibration response only obtains the deterministic part without stochastic part. Finally, the equivalent governing equation of structures can be derived from the stationary random vibration with the zero-mean load as follows:

$$\ddot{m}_r(t) + \frac{C\omega_r^2}{E} \dot{m}_r(t) + \omega_r^2 m_r(t) \approx 0 \tag{7}$$

Fourier transform (FT) of free decay response $m_r(t)$ in Eq. (7) is displacement spectrum $M_r(\omega)$ showed as:

$$M_r(\omega) = \frac{1/\omega_r^2}{\sqrt{\left[1 - \left(\frac{\omega}{\omega_r} \right)^2 \right]^2 + \left(\frac{C\omega}{E} \right)^2}} \tag{8}$$

Dimensionless displacement spectrum is presented by comparing the displacement spectrum with the maximum amplitude of the displacement PSD.

$$\frac{M_r}{M_{r,\max}}(\omega) \approx \sqrt{\frac{\left(\frac{C\omega_r}{E}\right)^2}{\left[1 - \left(\frac{\omega}{\omega_r}\right)^2\right]^2 + \left(\frac{C\omega}{E}\right)^2}} \quad (9)$$

In Eq. (9), C/E is prevented as energy dissipation of materials. In vibration of material with frequency ω , the loss factor η is defined as the ratio between the dissipated energy D and the initial strain potential Π .

$$\eta_r = \frac{D}{2\pi \Pi} = \frac{C\omega_r}{E} \quad (10)$$

Form Eq. (9) and (10), Displacement Loss Factor function (DLF) is calculated in frequency domain as:

$$DLF(\omega) = \frac{\left(1 - \left(\frac{\omega}{\omega_r}\right)^2\right)^2}{\left(\frac{M_{r,\max}}{M_r}\right)^2 - \left(\frac{\omega^2}{\omega_r^2}\right)} \quad (11)$$

DLF is simple to determine form PSD of output displacement. DLF is a novel feature to estimate dissipated energy based on the vibration signal of structures. This study will principally estimate the variation of the DLF with two material parameters E and C of the structures.

3 Exemplary Results

In order to investigate the proposed model, a viscoelastic beam subject to random load have been performed. Boundary condition of beam is simply supported. The basic parameters of the viscoelastic beam are show into Table 1.

Table 1. Parameters of the viscoelastic beam.

Dimension	Material density	Young Modulus	Loss factor
24.5 m x 20.6 m x 1.3 m	2663 kg/m ³	34 GPa	0.01

With the random load $f(x,t)$, the beam will operate with many different vibration mode as bending and torsion (Table 2) and the displacement response is also random (Fig. 1).

To estimate the changes of the DLF with material parameters of the beam structure, PSD of vibration response in material states (Table 3) with elastic modulus E_i and

Table 2. Natural frequencies of beam.

Mode	Frequency (Hz)
1 st bending	3.509
1 st torsion	5.817
2 nd torsion	11.664
2 nd bending	14.036
3 rd torsion	17.451

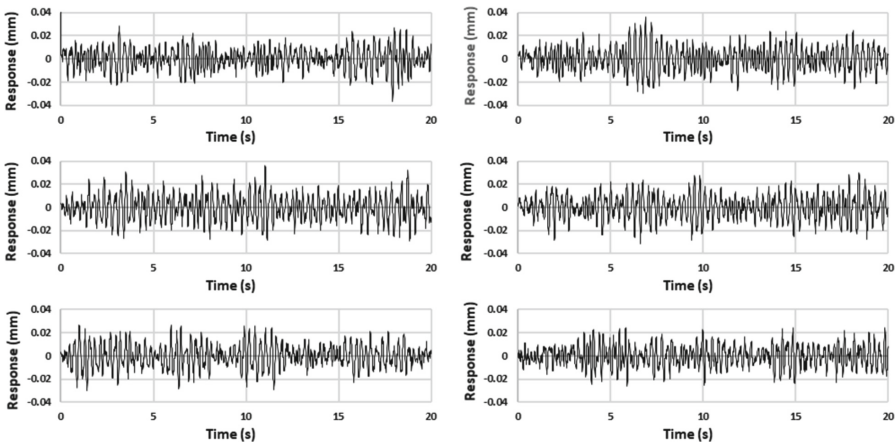


Fig. 1. History of random response.

viscous coefficient C_i have been performed (Fig. 2). When C increases, amplitudes of high frequency domain tend to decrease gradually in all position of beam. Besides, amplitudes at natural frequencies are mostly higher than ones at surrounding frequencies. The phenomenon of amplitude attenuation at high frequencies also occurs in positions with gradually decreasing modal stiffness on the beam.

In practice, the vibrational responses of engineering structures are affected by excitation by many external loads. The vibration response consists of two parts (a deterministic part and a stochastic part). The stochastic part will make the evaluation of the structural substance more complicated and imprecise. Therefore, estimating energy dissipation of material from PSD of the measured response will be affected by the stochastic part leading to create bias in the analysis results. In this study, the RD technique is used to minimize the effect of stochastic part in the dynamic response of the structures.

This technique was proposed based on the idea of a uniform mean to release a free response signature of a structure. This idea was performed by creating multiple sub-records of an extended output signal and adding them together. Threshold level is the most general criterion to identify trigger point of sub-records. The moment crossing the

Table 3. Description of material states

State	Young Modulus	Viscous coefficient
1	$E_1 = E$	$C_1 = C$
2	$E_2 = 0.9 E$	$C_2 = 1.2 C$
3	$E_3 = 0.8 E$	$C_3 = 1.4 C$
4	$E_4 = 0.7 E$	$C_4 = 1.6 C$
5	$E_5 = 0.6 E$	$C_5 = 1.8 C$
6	$E_6 = 0.5 E$	$C_6 = 2 C$

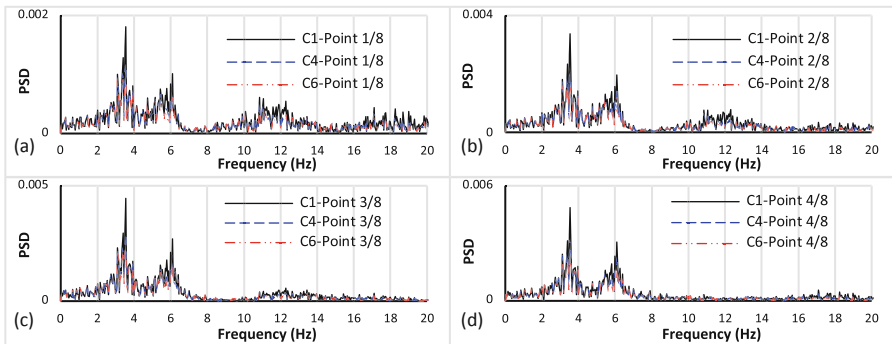


Fig. 2. PSD of response with different viscous coefficients: (a) point 1/8 of beam, (b) point 2/8 of beam, (c) point 3/8 of beam, (d) point 4/8 of beam

selected threshold of the signal is marked as the start of the sub-record to add up, thereby the average of the sub-records will remove the stochastic part from measured response.

An important factor of RD technique is the trigger condition. In general, it is positive to use a large number of trigger points, but time points with small value will suffer from large noise. Therefore, in order to balance between multiple starting points and high threshold levels, a trigger point in square root of two times the variance of the original signal is used [20]. Furthermore, another significant factor in using the RD technique is to decide the time length of segments. To apply time domain methods, the Randec signature must need a number of points enough to define the equational process. For applying modal domain methods, the Randec signature requires a sufficient number of points to perform complete decay process. Generally, this requirement is more important than that for time domain method [21]. Previously, the 10-s Randec signature for each 20-s vibration response is chosen (Fig. 3).

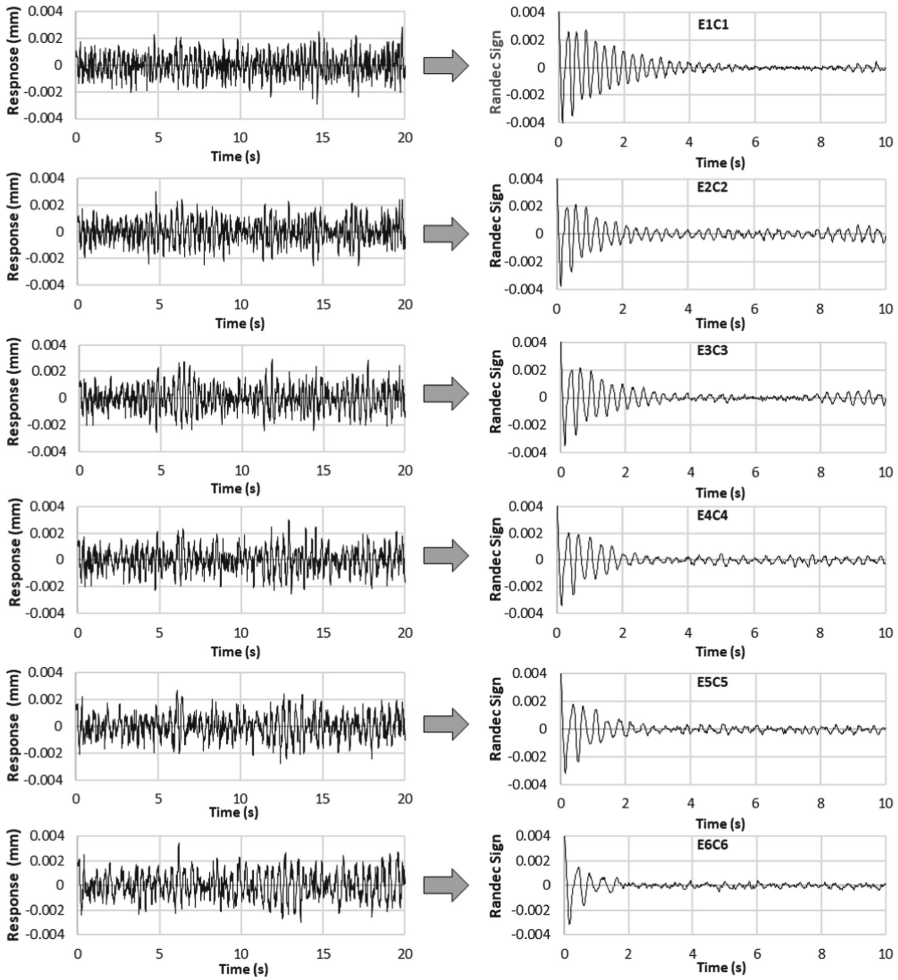


Fig. 3. Randec signature of random response with different material states

The Randec signature show the free-decay response of the structure by minimizing the stochastic part of signal. Therefore, the PSD of Randec signature carries the modal parameters of the structural vibration. DLF extracted from PSD of Randec signature (Fig. 4) will reflect material properties effectively.

Based on Fig. 4, the value of DLF increases with the energy dissipation of material (decreases of E and increases of C) in the frequency domain. Therefore, DLF is a novel feature in monitoring the material deterioration of structures. The average of the DLF at each material level is shown in Fig. 5. The DLF is change rapidly in positions with gradually increasing modal stiffness on the beam.

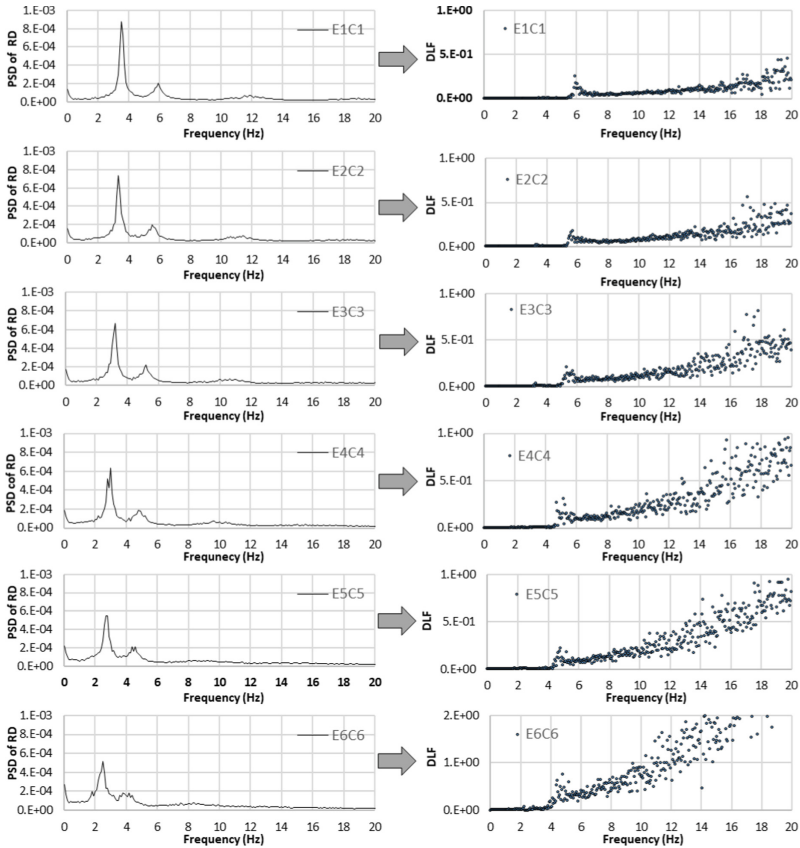


Fig. 4. PSD (left) and DLF (right) of RD with different material states

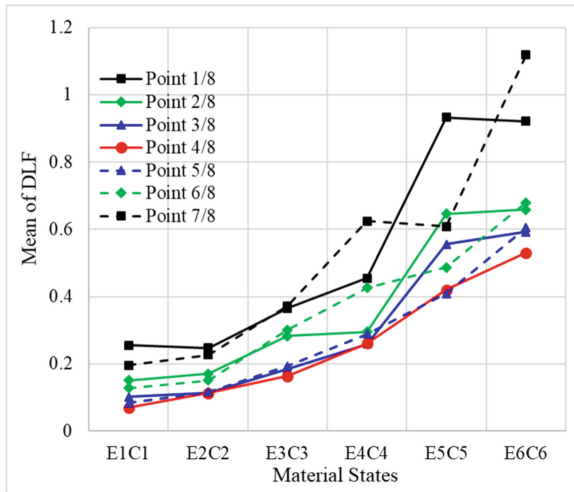


Fig. 5. The DLF value in other location of beam with different material states

4 Conclusion

In this study, the viscoelastic model has been used to investigate the material degradation more consistent with reality. With this model, the vibration amplitude of the high-order mode decrease when the material degradation increases.

This paper also presented the novel feature DLF to estimate the changes in the material property of structure. This DLF value is based only on the Randec signature of the output signal of the system, so it is without effects of the stochastic part of load.

The greater the degradation level of beam, the more increasing the DLF value in frequency domain. The higher the positions of beam have modal stiffness, the more rapidly the DLF value changes with material deterioration. The proposed method will be further developed to for health monitoring of beam-like structure such as bridge.

Acknowledgement. This research is funded by Vietnam National University Ho Chi Minh City (VNU-HCM) under grant number C2021–20–06. We acknowledge Ho Chi Minh City University of Technology (HCMUT), VNU-HCM for supporting this study.

References

1. Boller, C: Structural health monitoring—its association and use. In: In: Ostachowicz, W., Güemes, J. (eds.) *New Trends in Structural Health Monitoring*, pp. 1–79. Springer, Vienna (2013) https://doi.org/10.1007/978-3-7091-1390-5_1
2. Sinou, J.-J.: A review of damage detection and health monitoring of mechanical systems from changes in the measurement of linear and no-linear vibrations. *Mech. Vib. Measur. Effects Control* 643–702 (2009)
3. Li, S., Li, H., Liu, Y., Lan, C., Zhou, W., Ou, J.: SMC structural health monitoring benchmark problem using monitored data from an actual cable-stayed bridge. *Struct. Control. Health Monit.* 21(2), 156–172 (2014)

4. Doebling, S.W., Farrar, C.R., Prime, M.B., Shevitz, D.W.: Damage identification and health monitoring of structural and mechanical systems from changes in their vibration characteristics: a literature review (1996)
5. Cao, M.S., Sha, G.G., Gao, Y.F., Ostachowicz, W.: Structural damage identification using damping: a compendium of uses and features. *Smart Mater. Struct.* **26**(4), 043001 (2017)
6. Pham-Bao, T., Ngo-Kieu, N., Vuong-Cong, L., Nguyen-Nhat, T.: Energy dissipation-based material deterioration assessment using random decrement technique and convolutional neural network: a case study of Saigon bridge in Ho Chi Minh City, Vietnam, *Struct. Control Health Monitoring* **29**(7), (2022)
7. Pham-Bao, T., Nguyen-Nhat, T., Ngo-Kieu, N.: A novel approach to investigate the mechanical properties of the material for bridge health monitoring using convolutional neural network. *Struct. Infrastruct. Eng.* (2022)
8. Ngo-Kieu, N., Nguyen-Da, T., Pham-Bao, T., Nguyen-Nhat, T., Nguyen-Xuan, H.: Deep learning-based signal processing for evaluating energy dispersal in bridge structures. *J. Zhejiang Univ.-Sci. A* **22**(8), 672–680 (2021)
9. Beards, C.: *Structural Vibration: Analysis and Damping*. Arnold, London (1996)
10. De Silva, C.W.: *Vibration Damping, Control, and Design*. CRC Press, Boca Raton (2007)
11. Curadelli, R.O., Riera, J.D., Ambrosini, D., Amani, M.G.: Damage detection by means of structural damping identification. *Eng. Struct.* **30**, 3497–3504 (2008)
12. Tanaka, T.; Rehmat, S.E.; Matsumoto, Y., Abeykoon, J.D.: Damping properties of existing single-span prestressed concrete girder bridges with different service periods. In: 6 th International Conference on Structural Engineering and Construction Management, Kandy, Sri Lanka, pp. 15–22 (2015)
13. Chakraborty, B.C., Ratna, D.: *Polymers for Vibration Damping Applications*. Elsevier, US (2020)
14. Nguyen, T.D., Nguyen, H.Q., Pham, T.B., Ngo, N.K.: A novel proposal in using viscoelastic model for bridge condition assessment. In: Bui, T.Q., Cuong, L.T., Khatir, S. (eds.) *Structural Health Monitoring and Engineering Structures*. LNCE, vol. 148, pp. 331–341. Springer, Singapore (2021). https://doi.org/10.1007/978-981-16-0945-9_27
15. Nguyen, T.D., Nguyen, T.Q., Nhat, T.N., Nguyen-Xuan, H., Ngo, N.K.: A novel approach based on viscoelastic parameters for bridge health monitoring: a case study of Saigon bridge in Ho Chi Minh City-Vietnam. *Mech. Syst. Signal Process.* **141**, 106728 (2020)
16. Gul, M., Catbas, F.N.: Statistical pattern recognition for structural health monitoring using time series modeling: theory and experimental verifications. *Mech. Syst. Signal Process.* **23**(7), 2192–2204 (2009)
17. Mainardi, F.: *Fractional Calculus and Waves in Linear Viscoelasticity: An Introduction to Mathematical Models Translators*. World Scientific (2010)
18. Baz, AM.: *Active and passive vibration damping*. translators, John Wiley & Sons (2019)
19. Praharaj, R.K., Datta, N.: Dynamic response of Euler–Bernoulli beam resting on fractionally damped viscoelastic foundation subjected to a moving point load. *Proc. Inst. Mech. Eng. C J. Mech. Eng. Sci.* **234**(24), 4801–4812 (2020)
20. Asmussen, J.C.: *Modal Analysis Based on the Random Decrement Technique: Application to Civil Engineering Structures*. University of Aalborg, Denmark (1997)
21. Rodrigues, J., Brincker, R.: Application of the random decrement technique in operational modal analysis. *Aalborg Universitet*, 191–200 (2005)



An Analytical Model for Describing Tensile Behavior of FRCM

Yu Yuan and Gabriele Milani^(✉)

Department of Architecture, Built Environment and Construction Engineering (ABC),
Politecnico Di Milano, Piazza Leonardo da Vinci 32, 20133 Milan, Italy
gabriele.milani@polimi.it

Abstract. As a newly emerged strengthening material, FRCM (Fiber Reinforced Cementitious Matrix) has attracted the attention of many engineers and scholars due to the higher compatibility of the cementitious matrix with masonry structures compared to traditional organic matrix. Different from FRP (Fiber Reinforced Polymer) material that similarly can be externally applied onto the structures for strengthening, FRCM exhibits more complex failure modes due to the weaker performance of the matrix. To investigate the complex failure mechanism, the tensile test on FRCM coupon is a simple and intuitive method commonly used, in which the failure of both material and interface can be observed. In this article, an analytical model was proposed to reproduce the tensile behavior of FRCM, with the possibility to consider all the failure modes. A simplified mathematical model consisting of the components of the mortar layer, the fiber layer, and a zero-thickness interface gives the basis of force analysis, and from which the ODE system presenting the model behavior can be deduced and solved. This model was then validated against existing experimental results in terms of the global stress-strain relationships. It can be concluded that the proposed model is fast and stable, while able to reproduce the failure mode, global and local behavior of FRCM under tension.

Keywords: FRCM · Tensile test · Closed-form solution · Cracking

1 Introduction

For many existing masonry buildings, due to various damages caused by natural and human factors, as well as the poor seismic performance of the masonry structure itself, intervention and strengthening are often necessary. As a new strengthening strategy, the external application of composite materials to components can improve the load-bearing capacity and seismic performance of the structure without greatly increasing the weight of the structure and occupying space. Among them, FRCM (Fiber Reinforced Cement Matrix) has attracted attention in recent years in the area of masonry structure reinforcement. This is because, unlike the organic matrix used in FRP (Fiber Reinforced Polymer) strengthening systems, the inorganic matrix of FRCM ensures better compatibility with masonry materials, and facilitates the discharge of salt and moisture. For building heritages, an important advantage of FRCM is the reversibility of the interventions. An

important issue about the application of FRCM is the complex failure modes, not only failure will appear as the matrix-substrate debonding, but in the FRCM composite itself. That is, the mortar may crack, the fiber strip may slip inside the mortar, and even the fiber strip may break, due to the lower strength of the mortar matrix.

The tensile test is widely used as a simple and intuitive test [1–4], which can well characterize the various failure modes that FRCM may appear, although the test set-up and specimen preparation may have a large impact on the results. Therefore, in the case of limitations in comparing data from different experimental campaigns [2], the development of reasonable prediction models can be very meaningful, which can provide insights into explaining some experimental phenomena from a theoretical perspective. Numerical models have been developed specifically to describe the behavior of FRCMs under tension, such as modeling using finite element methods [4–6], or springs to characterize the interaction between materials [7]. In contrast, the model proposed in this paper has a faster calculation speed, and stable output due to the use of analytical solutions, while asking for only a few parameters.

To describe the FRCM coupon under classical tensile tests, a simplified mathematical model is established, including three parts, meaning the mortar layer, the fiber strip, and a zero-thickness interface. Three cases are separately considered to investigate the influence of failure for different components: 1) Case 1, which only considers the failure of mortar; 2) Case 2, which only considers the failure of the interface bond; 3) Case 3, in which both failures of mortar and interface will be considered. Then the situations where failures of both mortar and interface will appear can be discussed based on these two cases. The analytical approach is based on the closed-form solution of the ODE system derived from the equilibrium conditions of an infinitesimal part of the coupon, as well as the constitutive and geometric relationships. At different analysis moments and failures of components, different boundary conditions can be obtained to derive the closed-form solutions. This approach is then validated against existing experimental data for all cases considered. Good agreement can be found in terms of the global stress-strain relationship and bond strength. The occurrence of mortar cracking can also be presented by the model, however, due to the inhomogeneity of mortar mechanical properties and specimen geometry, manufacturing quality, etc., the location of cracks in the experiment cannot be exactly simulated.

2 The Analytical Model and Solutions

2.1 The Analytical Model

The analytical model is expected to describe the typical non-linear behavior of FRCM under tension. Based on the experimental phenomena, a simplified mathematical model was proposed, including three parts: (i) the mortar layer characterized by a perfectly elastic-brittle behavior; (ii) the fiber strip characterized by a fully elastic behavior throughout the analysis procedure; (iii) the zero-thickness interface characterized by a perfectly elastic-brittle shear stress-slip relationship which takes into consideration of the residual strength.

To assume that the material properties (mechanical and geometry) distributions along the width of the coupon are uniform, considering the symmetric loading conditions, we

can take only a quarter of the whole FRCM coupon for analysis at the beginning of the simulation as shown in Fig. 1 (a). Take an infinitesimal part of the FRCM for force analysis, according to the equilibrium condition we can write:

$$\begin{cases} t_f \frac{d\sigma_f}{dx} = \tau(s) \\ t_m \frac{d\sigma_m}{dx} = -\tau(s) \end{cases} \quad (1)$$

in which t_m is the thickness of the mortar layer, t_f is half of the thickness of the fiber strip. The tensile stress of mortar and fiber are denoted by σ_m and σ_f respectively. The shear stress along the mortar-fiber interface is denoted by $\tau(s)$, we assume an elastic-brittle behavior with a constant residual strength:

$$\begin{cases} \tau = K_i \cdot s \quad (s \leq \tau_m/K_i) \\ \tau = \tau_r \quad (s > \tau_m/K_i) \end{cases} \quad (2)$$

in which K_i is the initial elastic stiffness assumed for the interface, τ_m and τ_r are the maximum and residual shear strengths of the interface. And s is the difference of displacements between mortar (u_m) and fiber (u_f):

$$s = u_f - u_m \quad (3)$$

The constitutive laws of the materials at the elastic stage yield:

$$\begin{cases} \sigma_f = E_f \frac{du_f}{dx} \\ \sigma_m = E_m \frac{du_m}{dx} \end{cases} \quad (4)$$

in which E_m and E_f are Young's moduli of the mortar and fiber respectively. The ODE system can be obtained by combining Eq. (4) and Eq. (1).

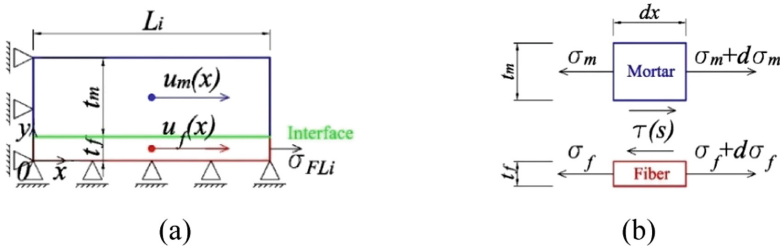


Fig. 1. The simplified mathematical model (a), and force analysis for the infinitesimals (b)

We will consider two moments to highlight in the global response the occurrence of unloading when crack generating:

- 1) Moment A, at which the tensile stress inside mortar reaches its maximum tensile strength;
- 2) Moment B, at which a crack appears at the same position mortar just gained its maximum strength, and the tensile stress at this position shifted to zero.

After the mortar cracks, we can take the uncracked mortar segment as a new object for analysis. And considering whether the model components enter the plastic stage, three cases might occur in each analyzed segment:

In Case 1, the interface behaves fully elastic until mortar cracking. Since it is assumed that the interface maintains elasticity before and after cracking, the same analytical method can be adopted for all the uncracked mortar segments under symmetrical conditions. At moment B, displacement translation will be performed to make the displacement of the new symmetric center (the center of the new uncracked segment) zero, thus making it possible to always take a quarter part of the segment for analysis.

In Case 2, the interface behaves fully plastic before mortar cracking. This situation may occur when the mortar length is too small, and the residual friction distributed along the interface is not able to provide enough energy to fracture the mortar. Thus, in Case 2, no further analysis will be performed, and the tensile procedure will be terminated when the fiber fractures. Two interface models with (Case 2-b) and without (Case 2-a) residual strength were considered in Case 2, to investigate the influence.

For Case 3, where both failures of mortar and interface will occur, the symmetric condition will no longer exist due to the interface entering partially before mortar cracking, and it is not possible for the failed interface to return elastic. The calculations will be more complex but still the same methodology to solve the ODE system. The simulation will be terminated when the fiber fractures, normally before this happens, Case 2 will appear for the mortar section without enough long length.

2.2 The Closed-Form Solutions

Case 1. In this case, we assume that the mortar matrix and the interface all behave as elastic before mortar cracks. We take the analysis for intact FRMC coupon as step $i = 1$; after the first crack appears in the middle, we denote the next analysis on the half segment as step $i = 2$, and so on. Combining Eq. (4) and Eq. (1), the following ODE system can be obtained:

$$\begin{bmatrix} \frac{du_f}{dx} \\ \frac{d\sigma_f}{dx} \\ \frac{du_m}{dx} \\ \frac{d\sigma_m}{dx} \end{bmatrix} = \begin{bmatrix} 0 & \frac{1}{E_f} & 0 & 0 \\ \frac{K_i}{t_f} & 0 & -\frac{K_i}{t_f} & 0 \\ 0 & 0 & 0 & \frac{1}{E_m} \\ -\frac{K_i}{t_m} & 0 & \frac{K_i}{t_m} & 0 \end{bmatrix} \begin{bmatrix} u_f \\ \sigma_f \\ u_m \\ \sigma_m \end{bmatrix} \tag{5}$$

The general solution of the ODE system can be obtained as below:

$$\begin{bmatrix} u_f \\ \sigma_f \\ u_m \\ \sigma_m \end{bmatrix} = C_1 \begin{bmatrix} 1 \\ 0 \\ 1 \\ 0 \end{bmatrix} + C_2 \left(\begin{bmatrix} 1 \\ 0 \\ 1 \\ 0 \end{bmatrix} x + \begin{bmatrix} 0 \\ E_f \\ 0 \\ E_m \end{bmatrix} \right) + C_3 \begin{bmatrix} -t_m\alpha \\ -t_m/t_f \\ t_m\beta \\ 1 \end{bmatrix} e^{\lambda_3 x} + C_4 \begin{bmatrix} t_m\alpha \\ -t_m/t_f \\ -t_m\beta \\ 1 \end{bmatrix} e^{\lambda_4 x} \tag{6}$$

in which:

$$\begin{cases} \lambda_3 = \sqrt{K_i(\frac{1}{E_m t_m} + \frac{1}{E_f t_f})} \\ \lambda_4 = -\sqrt{K_i(\frac{1}{E_m t_m} + \frac{1}{E_f t_f})} \\ \alpha = \sqrt{\frac{E_m t_m}{E_f t_f K_i(E_f t_f + E_m t_m)}} \\ \beta = \sqrt{\frac{E_f t_f}{E_m t_m K_i(E_f t_f + E_m t_m)}} \end{cases} \quad (7)$$

For determining the constants of integration, the boundary conditions of describing moment A are:

$$\begin{cases} u_f |_{x=0} = 0 \\ u_m |_{x=0} = 0 \\ \sigma_m |_{x=0} = f_{im} \\ \sigma_m |_{x=L_i} = 0 \end{cases} \quad (8)$$

in which L_i is the length of the quarter of the coupon under analysis, and we have $L_i = L/2^i$ for step i .

After displacement translation, for moment B we can write the following boundary conditions:

$$\begin{cases} u_f |_{x=0} = -u_{fL_i}^{iA} \\ u_f |_{x=L_i} = 0.5u_{fL_i}^{iA} \\ \sigma_m |_{x=0} = 0 \\ \sigma_m |_{x=L_i} = 0 \end{cases} \quad (9)$$

in which $u_{fL_i}^{iA}$ is the fiber displacement at the loading edge solved in moment i -A.

Case 2. In this case, we assume that the mortar will not break, while the interface will enter the plastic stage before the fiber fractures. Assume the local abscissa of the point at which the interface transforms from elastic to plastic stage is x_r , which will be assigned gradually from L_i to 0, to simulate the procedure of increasing interface slip until the fiber fractures.

For the elastic range ($0 \leq x \leq x_r$), the ODE system is the same as Eq. (5), which can be solved with different boundary conditions:

$$\left\{ \begin{array}{l} u_f|_{x=0} = 0 \\ u_m|_{x=0} = 0 \\ (u_f - u_m)|_{x=x_r} = s_e \\ \sigma_m|_{x=x_r} = \frac{\tau_r(L_i - x_r)}{t_m} \end{array} \right. \quad (10)$$

For the plastic range ($x_r < x \leq L_i$), the displacements of fiber and mortar at a certain point along the plastic range are:

$$u_f = u_f|_{x=x_r} + \int_{x_r}^x \frac{\sigma_f}{E_f} dx \quad (11)$$

in which σ_f is the tensile stress of fiber at x . The equilibrium condition of the plastic section gives:

$$\sigma_f = \sigma_f|_{x=x_r} + \frac{\tau_r(x - x_r)}{t_f} \quad (12)$$

Combining the constitutive laws of mortar and fiber, the integration of Eq. (11) gives the solutions along the plastic range:

$$\left\{ \begin{array}{l} u_f = \frac{f_{if}}{E_f} x + \frac{\tau_r}{E_f t_f} \left(\frac{1}{2} x^2 - L_i x \right) \\ \sigma_f = f_{if} - \frac{\tau_r(L_i - x)}{t_f} \\ u_m = \frac{\tau_r}{E_m t_m} \left(L_i x - \frac{1}{2} x^2 \right) \\ \sigma_m = \frac{\tau_r(L_i - x)}{t_m} \end{array} \right. \quad (15)$$

3 Validation

In this section, the experimental results of the FRCM coupon under the tensile test provided by Bertolesi et al. [4] were adopted to verify the reliability of the developed analytical model. In this experimental campaign carried out at the Polytechnic University of Milan, the FRCM coupon cast by cementitious mortar on the PBO fiber grid was tested, as well as the geometrical and mechanical properties of both two components, giving the possibilities to assume the parameters for validation as listed in Table 1.

It is now generally accepted that the constitutive behavior of FRCM composites in tension can be idealized as a trilinear relationship [5, 8]. In the first stage, the material is not cracked and the stiffness of the composite should ideally be the stiffness of the mortar. In the second stage, multiple cracks began to form, and the load-displacement (or stress-strain) curve oscillated multiple times. In the third stage, the cracks will propagate until the fibers fracture, the mortar layer has almost failed and the composite should ideally

Table 1. Parameters adopted to validate the present model.

E_m [MPa]	t_m [mm]	f_{tm} [MPa]	E_F [MPa]	f_{ff} [MPa]	t_F [mm]	B_F [mm]	L [mm]	τ_m [N/mm ²]	K [N/mm ³]	τ_f [N/mm ²]
6000	5	3.65	215900	3397	0.035	40	280	2.5	166.67	0.35

reproduce the elastic modulus of the dry fibers. The results in terms of the global coupon stress-strain curves obtained by the present model and experimental data are compared in Fig. 2. It can be concluded that the results generated by the present model are in good agreement with the experimental results in terms of trend and range, fitting into the generally recognized three-stages constitutive model. Similar ultimate strength and strain can be gained, as well as the beginning of the second stage, which should ideally be the moment mortar reaches its tensile strength.

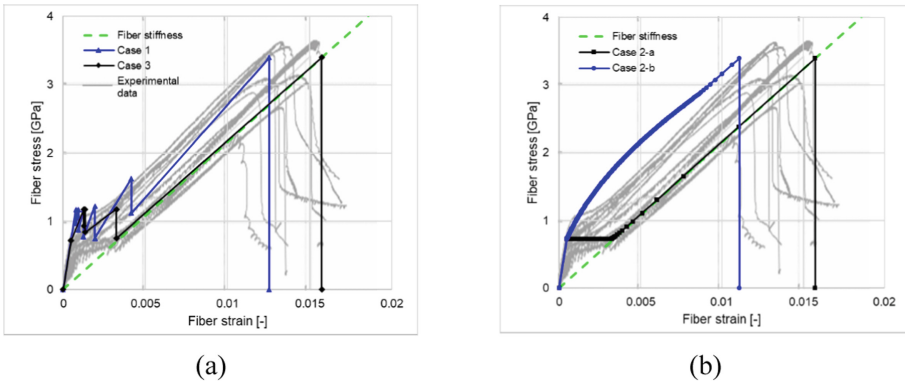


Fig. 2. The stress-strain relationships until fiber fracture for Cases 1 and 3 (a), and Case 2 (b) gained via the present model and experimental tests

The proposed analytical method can also provide the local behavior of FRCM under tension, including stress and displacement distributions of fibers and mortar along the length of the specimen. Due to the limitation of the length of the article, here only gives an example of the tensile stress distribution of the mortar until the specimen fails (the fibers fracture), as shown in Fig. 3. For Cases 1 and 3, the solid line represents the mortar stress at moment A (the mortar reaches its maximum tensile strength), while the dashed line represents moment B (the mortar breaks). While For case 2, the graphs in Fig. 3-c and Fig. 3-d show the distribution of mortar tensile stress with the increase of external force, the difference lies in the residual friction along the interface after interface failure. For Case 1 in Fig. 3-a, a clear symmetry pattern can be identified, thanks to the assumption of material and geometry symmetries, and the calculation process of constantly changing the symmetric center. For Case 3, the distribution of mortar stress is no longer symmetrical regarding the cracks, due to interface debonding that occurs first at the loading edge.

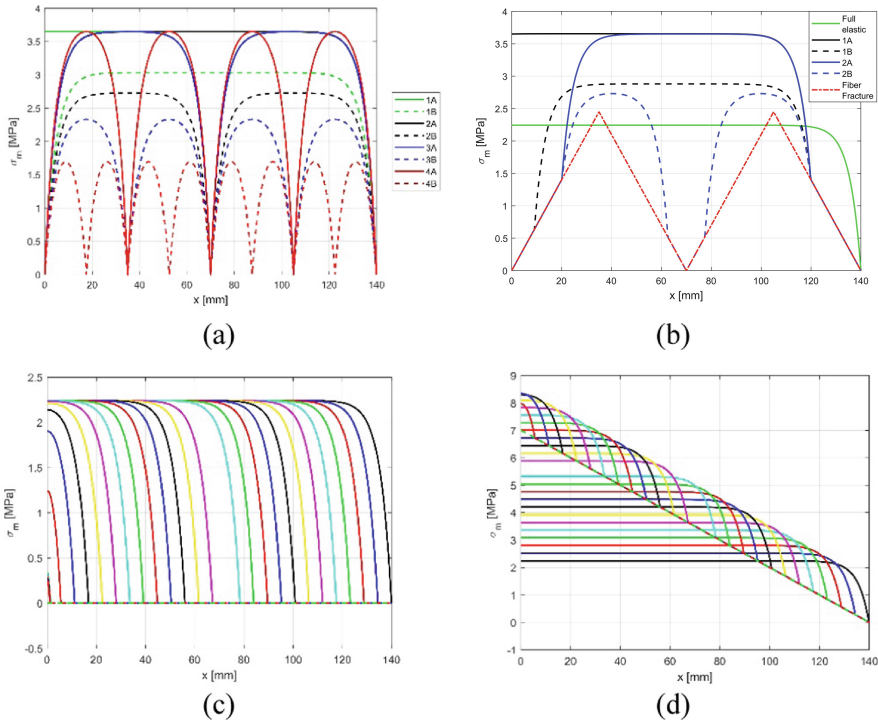


Fig. 3. Distribution of mortar tensile stress until fiber fracture for Case 1 (a), Case 3 (b), Case 2-a (c), and Case 2-b (d)

4 Conclusions

This study presents an analytical model which can consider all the failure modes of the FRCM coupon under tension. A classical mathematical model which consists of the mortar and fiber layers and zero-thickness interfaces was considered. A multi-segment linear relationship was chosen to describe the interface relationship, allowing us to gain the solutions analytically. This method can satisfactorily reproduce the tensile behavior of the FRCM coupon with little calculation effort and few parameters. The obtained results are in good agreement with the experimental results in terms of range and trend, fitting into the generally accepted trilinear constitutive law. Moreover, the local behavior of the entire system can be determined, as well as the locations of mortar cracking. But except for the one crack appearing at the center of the specimen, the locations of mortar cracking in the actual specimen is rather random due to internal flaws or eccentric loading.

Acknowledgments. Yu Yuan would like to acknowledge the financial support provided by the Chinese Scholarship Council (CSC) for performing her Ph.D. program at the Technical University of Milan, Italy.

References

1. de Felice, G., et al.: Mortar-based systems for externally bonded strengthening of masonry. *Mater. Struct.* **47**(12), 2021–2037 (2014). <https://doi.org/10.1617/s11527-014-0360-1>
2. D'antino, T., Papanicolaou, C.C.: Comparison between different tensile test set-ups for the mechanical characterization of inorganic-matrix composites. *Constr. Build. Mater.* **171**, 140–151 (2018). <https://doi.org/10.1016/j.conbuildmat.2018.03.041>
3. Arboleda, D., Carozzi, F.G., Nanni, A., Poggi, C.: Testing procedures for the uniaxial tensile characterization of fabric reinforced cementitious matrix (FRCM) composites. *J. Compos. Constr.* **20**, 04015063 (2016). [https://doi.org/10.1061/\(ASCE\)CC.1943-5614.0000626](https://doi.org/10.1061/(ASCE)CC.1943-5614.0000626)
4. Carozzi, F.G., Poggi, C.: Mechanical properties and debonding strength of Fabric Reinforced Cementitious Matrix (FRCM) systems for masonry strengthening. *Compos. B Eng.* **70**, 215–230 (2015). <https://doi.org/10.1016/j.compositesb.2014.10.056>
5. Bertolesi, E., Carozzi, F.G., Milani, G., Poggi, C.: Numerical modeling of Fabric Reinforce Cementitious Matrix composites (FRCM) in tension. *Constr. Build. Mater.* **70**, 531–548 (2014). <https://doi.org/10.1016/j.conbuildmat.2014.08.006>
6. Nerilli, F., Marfia, S., Sacco, E.: Micromechanical modeling of the constitutive response of FRCM composites. *Constr. Build. Mater.* **236**, 117539 (2020). <https://doi.org/10.1016/j.conbuildmat.2019.117539>
7. Grande, E., Milani, G.: Numerical simulation of the tensile behavior of FRCM strengthening systems. *Compos. B Eng.* **189**, 107886 (2020). <https://doi.org/10.1016/j.compositesb.2020.107886>
8. Hartig, J., Jesse, F., Schicktanz, K., Häußler-Combe, U.: Influence of experimental setups on the apparent uniaxial tensile load-bearing capacity of textile reinforced concrete specimens. *Mater. Struct.* **45**(3), 433–446 (2012). <https://doi.org/10.1617/s11527-011-9775-0>



Simplified Numerical Tool for a Fast Strength Estimation of Squared Masonry Columns Reinforced with FRP Jackets

Luis C. M. da Silva¹(✉), Ernesto Grande², and Gabriele Milani¹

¹ Department A.B.C, Politecnico Di Milano, Piazza Leonardo da Vinci 32, 20133 Milan, Italy
{luiscarlos.martinsdasilva,gabriele.milani}@polimi.it

² University Guglielmo Marconi, Rome, Italy
e.grande@unimarconi.it

Abstract. The work addresses the retrofitting of masonry columns with fiber reinforced polymers (FRP) jackets. Experimentation is still at a higher level and the study tries to enrich the set of available numerical models to estimate the capacity of squared masonry columns with a periodic arrangement. The numerical procedure assumes a strain-based incremental formulation relying on equilibrium, compatibility, and kinematic equations and precluding strenuous integration of FEs. An elastic-perfectly plastic response with a Mohr-Coulomb failure criteria has been assumed for both brick units and mortar joints. Failure of the FRP is governed by limited tensile strength and tearing (in the corners of the columns). An associated plastic flow-rule is followed. The numerical strategy has been validated with data from several experimental campaigns, with existing literature approaches and code-based formulas. A good agreement has been found and the strategy demonstrated fast (1–2 s).

Keywords: Masonry columns · FRP jackets · Masonry compressive strength · Retrofit masonry columns

1 Introduction

Most existing masonry constructions have been built to withstand vertical loads. Unreinforced masonry tends to exhibit low tensile strength and quasi-brittle response, which somehow has determined its employment in structural elements whose stability is governed by compressive stresses [1–3]. From a logical extension, masonry compressive strength is then of utmost importance when designing and assessing the structural safety of such buildings. European normative EN 1052–1 [4] include principles for the experimental determination of masonry compressive strength (perpendicular to bed joints).

The construction and testing of stacked masonry prisms, or even larger setups, is yet found in the literature to estimate this property [5], as it allows a good correlation with results from code-based tests [5, 6]. To cope with the associated experimentation costs (and corresponding time), several alternatives have been presented in the literature

to assess the masonry compressive strength. These may be grouped in semi-empirical, analytical, or numerical approaches; however, these need to be validated by experimental data.

Semi-empirical laws, as the ones presented by Haseltine [7] and more recently by Sarhat and Sherwood [8] are used in masonry code provisions [9, 10]. Limited information is retrieved on the masonry response, but those allow giving a rational and conservative basis for design. On this regard, the pioneering work of Hilsdorf [11] led to important experimental contributions that nurtured the onset of novel formulations. Hilsdorf proposed that an applied uniaxial compression stress leads to a tri-axial stress state within the masonry; latter exploited by McNary and Abrams [7] who reported a comprehensive testing program for the tri-axial characterization of units and mortar. Analytical approaches that consider the effect of both masonry components have been then developed. A valuable research work has been presented by Drougkas et al. [12], in which a mechanistic-based micro-model was proposed. Results were compared with experimental data on compressed masonry elements and a promising accuracy was found. More sophisticated analysis, such as those retrieved from continuous Finite element (FE) method, have been also explored and with good results. For instance, the works from Brencich et al. [13], Shrive and Jessop [14] and Pina-Henriques and Lourenco [15].

Nowadays, it is generally consensual – with experimental evidence – that masonry compressive failure is governed by the interaction between units and mortar. Again, it bears stressing that this was especially due to Hilsdorf [11] disruptive idea, whose formulation has been later improved by Khoo and Hendry [16] to solve the limitation of assuming that units and mortar have a similar strain at failure. Perhaps due to the existing solid background on masonry compressive behavior, one can explain the unravel of new and exciting techniques being applied to this aim, as for instance machine learning-based methods [17]. Although the behavior of masonry under pure compression is well documented, the assessment of strengthened elements still deserves more insight. A typical retrofitting strategy is the use of composite materials such as FRP (Fiber-Reinforced Plastics). FRP material systems are composed of fibres within a polymeric matrix, being possible to mention, for instance, the use of reinforced polymers made from glass (GFRP), carbon (CFRP) and aramidic fibers (AFRP).

The present research focuses on the structural performance of masonry columns. Its behavior can be easily improved by adequate strengthening, such as the use of innovative materials as FRPs. Data retrieved from experimental works allow the development of analytical and numerical models to compute the confined strength. Although the confined compressive strength of masonry columns is typically obtained either via conservative empirical laws or experimental campaigns, numerical analysis can be also an alternative. Complex FE models may allow to reproduce compressive failure considering localization of deformation and damage propagation (with spitting and shear cracks). Nonetheless, the computational time required blurs its practicability, hence are seldom used in practice. In such a context, the present work intends to demonstrate a mechanistic-based approach that allows computing the confined compressive strength of masonry columns. The numerical model can reproduce the nonlinear behavior of masonry and the failure of

units, mortar, and composite wrap (with a polymeric base, such as FRP, GFRP, etc.). To circumvent the latter underlined concern, the strategy allows obtaining a solution in a pair of seconds and will be made available to extend its use to engineering design practice.

2 Simplified Numerical Model for Squared Masonry Columns

A numerical model to compute the compressive strength of squared masonry columns is proposed in this section. The main theoretical assumptions will be addressed, which include both the case of unreinforced and reinforced squared masonry columns and for the case of a periodic arrangement.

2.1 Unreinforced Squared Masonry Columns

A good basis of work is already present in the literature to characterize the compressive behaviour of unreinforced masonry [15]. From the pioneering work by Hilsdorf [11], it is well accepted today that masonry compressive failure is mainly governed by the interaction between units and mortar. In specific, it relies on the evidence that the compressive strength of brick units is higher than the one of mortar joints; and, in converse, that the lateral expansion given by the Poisson's ratio is higher for mortar joints in respect to brick units. In this regard, when a masonry column is subjected to a compressive load, the bed mortar joints tend to expand laterally. To fulfil the compatibility conditions, such deformation is restrained by units owing its lower deformability, thence leading to a pure tri-axial compression state in mortar joints and a compression-tension-tension state in brick units. Such behaviour is presented in Fig. 1.

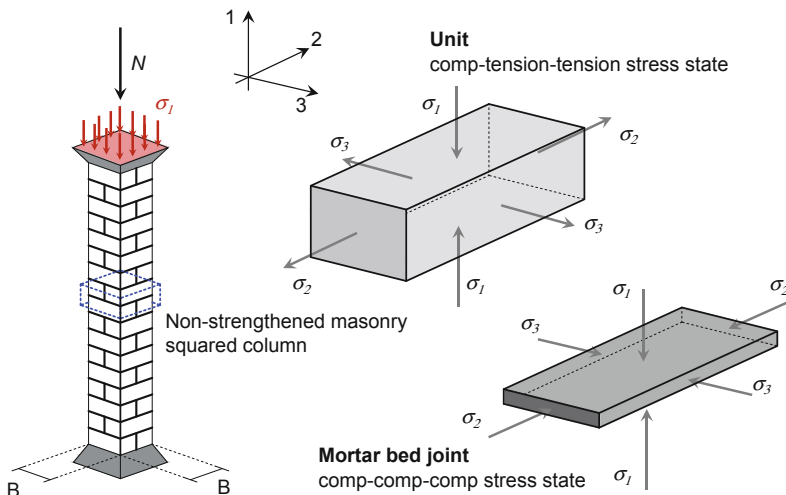


Fig. 1. Squared unreinforced masonry column and stress state in the masonry components.

2.2 FRP-Strengthened Squared Masonry Columns

Several experimental campaigns have been developed in literature in the use of modern and innovative interventions. In specific, the use of polymeric-based composites such as FRP (Fiber-Reinforced plastics) and GFRP (Glass-Fiber) are becoming a general solution. The adoption of such polymeric-based solutions allows increasing the ultimate capacity in terms of both strength and ultimate displacement.

Nonetheless, numerical works are still scarce and are typically based on complex micro-modelling approaches that have high cost in both modelling and processing stages [18]. Here, in order to decrease the required computational time costs, the numerical model is formulated accounting with the stress state addressed by Hilsdorf theory [11]. Regarding the latter, the model is enriched with kinematic compatibility conditions between masonry and the polymeric FRP wrap.

2.3 Constitutive Laws and Failure Criteria

A constitutive model based on an elastic-perfectly plastic assumption was considered for both masonry components. Failure of masonry components is governed by a Mohr-Coulomb behaviour. These assumptions are depicted in Fig. 2. In specific, the elastic limit for a given increment (i) is written such as:

$$f(\sigma_i) = \Delta\sigma_v^{(i)} - k = 0 \tag{1}$$

In which k defines the Mohr-Coulomb failure surface that, following the assumptions made, remains fixed in the stress space. For the polymeric-based and owing the high tensile strength and stiffness to weight ratio, an elastic behaviour with limited tensile strength was adopted:

$$\sigma_{FRP} = E\varepsilon_{FRP} \quad \text{such that} \quad \sigma_{FRP} \leq f_{t,FRP} \tag{2}$$

in which σ_{FRP} , ε_{FRP} , E_{FRP} , and $f_{t,FRP}$ are the tensile stress, tensile strain, Young’s modulus, and tensile strength of the polymeric base, respectively (Fig. 2).

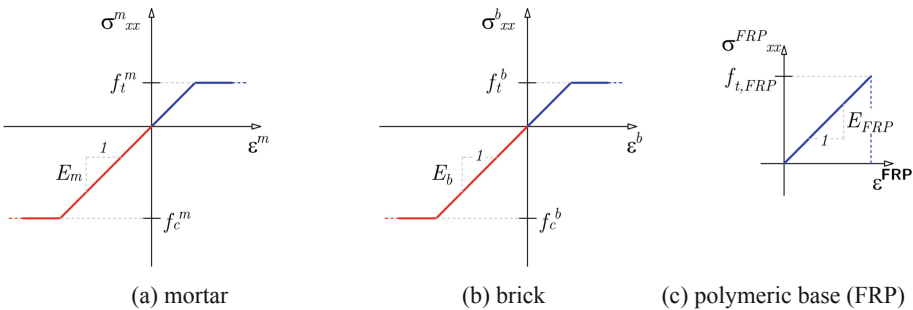


Fig. 2. Constitutive models for materials.

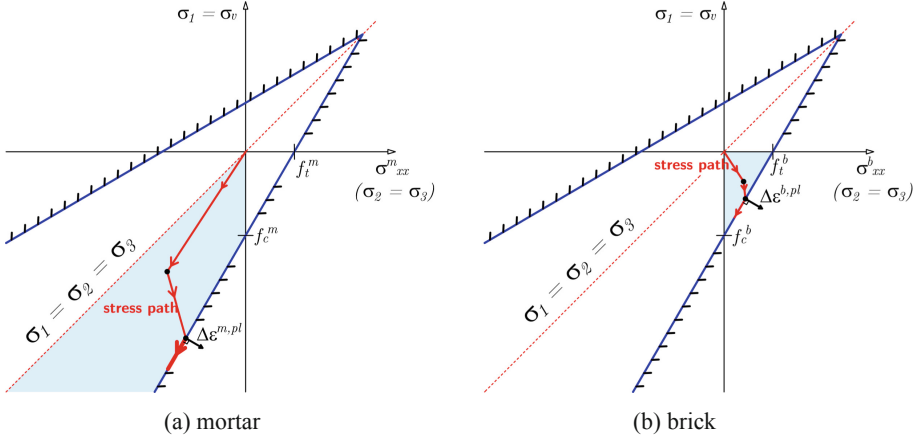


Fig. 3. Failure surface in the principal stress space (plane $\sigma_2 = \sigma_3$).

For both masonry components, an associated plastic flow rule has been assumed. In this regard, the plastic strain rate tensor for brick ($\Delta \varepsilon^{b,pl}$) and mortar ($\Delta \varepsilon^{m,pl}$) reads as:

$$\Delta \varepsilon^{(\cdot),pl} = \lambda_p^{(\cdot)} \frac{\partial f}{\partial \sigma_i} \quad i = 1, 2, 3 \text{ and } (\cdot) = b, m \quad (3)$$

in which $(\Delta \varepsilon^{(\cdot),pl})^T = [\Delta \varepsilon_{xx}^{(\cdot)}, \Delta \varepsilon_v^{(\cdot)}]$. For the present numerical model, only one failure surface $f(\sigma_i)$ is active for each masonry component as depicted in Fig. 3.

2.4 (a) Computational Details

A brief presentation on the used compatibility, constitutive, and equilibrium equations are given herein. The formulation is written in a way that allows solving, through a vertical incremental strain approach, the solution to the unknown variables of the system. In specific, the system has a total of fifteen unknowns that are given next and depicted in Fig. 4.

$$\left\{ \begin{array}{l} \text{brick} : \Delta \varepsilon_{xx}^b, \Delta \varepsilon_v^b, \Delta \sigma_{xx}^b, \Delta \lambda^b, \Delta \varepsilon_{xx}^{bpl}, \Delta \varepsilon_v^{bpl} \\ \text{mortar} : \Delta \varepsilon_{xx}^m, \Delta \varepsilon_v^m, \Delta \sigma_{xx}^m, \Delta \lambda^m, \Delta \varepsilon_{xx}^{mpl}, \Delta \varepsilon_v^{mpl} \\ \text{FRP} : \Delta \sigma_{FRP}, \Delta \varepsilon_{FRP} \\ \text{load} : \Delta \sigma_v \end{array} \right. \quad (4)$$

In which $\Delta \varepsilon_{xx}^b$ and $\Delta \varepsilon_{xx}^m$ are the horizontal elastic strain increments for brick and mortar; $\Delta \varepsilon_v^b$ and $\Delta \varepsilon_v^m$ are the vertical elastic strain increments for brick and mortar, respectively. Following an additive decomposition for strain terms, thence $\Delta \varepsilon_{xx}^{bpl}$, $\Delta \varepsilon_v^{bpl}$ are the corresponding plastic strain increments for brick; and $\Delta \varepsilon_{xx}^{mpl}$, $\Delta \varepsilon_v^{mpl}$ the corresponding plastic strain increments for mortar joints. The stress quantities are expressed using a similar notation, such that $\Delta \sigma_{xx}^b$ and $\Delta \sigma_{xx}^m$ are the horizontal stress in brick and

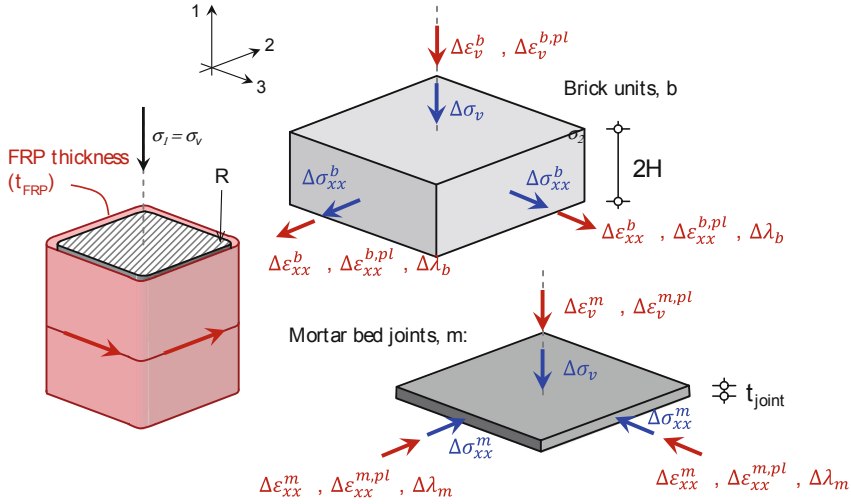


Fig. 4. Description of the geometric parameters and the stress-state components for the FRP-strengthened masonry column.

mortar bed joint, being $\Delta\lambda^b$ and $\Delta\lambda^m$ the corresponding plastic multipliers. The elastic strain and stress values in the FRP wrap are defined by $\Delta\sigma_{FRP}$ and $\Delta\varepsilon_{FRP}$, respectively.

Constitutive relations are defined for both brick and mortar according to:

$$[\Delta\varepsilon_{xx}^{(\cdot)}, \Delta\varepsilon_v^{(\cdot)}]^T = \frac{1}{E_{(\cdot)}} \begin{bmatrix} 1 - \nu_{(\cdot)} & -\nu_{(\cdot)} \\ -2\nu_{(\cdot)} & 1 \end{bmatrix} \begin{bmatrix} \Delta\sigma_{xx}^{(\cdot)} \\ \Delta\sigma_v^{(\cdot)} \end{bmatrix} \quad (\cdot) = b, m \quad (5)$$

In which the plastic relations for the masonry components are described through an associated plastic flow rule such that, following the assumptions ascribed in Sect. 2.3, one finds:

$$\begin{cases} \Delta\varepsilon_{xx}^{(\cdot),pl} = \Delta\lambda^{(\cdot)} \frac{f_c^{(\cdot)}}{f_t^{(\cdot)}} \\ \Delta\varepsilon_v^{(\cdot),pl} = -\Delta\lambda^{(\cdot)} \end{cases} \quad (6)$$

Compatibility relations between the bed joint and brick interface in the horizontal and vertical directions are, respectively, given as:

$$\Delta\varepsilon_{xx}^b + \Delta\varepsilon_{xx}^{b,pl} = \Delta\varepsilon_{xx}^m + \Delta\varepsilon_{xx}^{m,pl} \quad (7)$$

$$\Delta\varepsilon_v(2H + t) = 2H(\Delta\varepsilon_v^b + \Delta\varepsilon_v^{b,pl}) + t(\Delta\varepsilon_v^m + \Delta\varepsilon_v^{m,pl}) \quad (8)$$

and between the polymer wrap with the brick surface as:

$$\Delta\varepsilon_{xx}^b + \Delta\varepsilon_{xx}^{b,pl} = \Delta\varepsilon_{FRP} \quad (9)$$

The increment of stress in the masonry components is, for the current iteration i , given as:

$$\Delta\sigma_v^{(i)} = \frac{f_c^{(\cdot)}}{f_t^{(\cdot)}} \Delta\sigma_{xx}^{(\cdot)(i)} - f_c^{(\cdot)} - \sigma_v^{i-1} + \frac{f_c^{(\cdot)}}{f_t^{(\cdot)}} \sigma_{xx}^{(\cdot)(i-1)} \quad (10)$$

and for the polymeric wrap:

$$\Delta\sigma_{FRP} = E_{FRP}\Delta\varepsilon_{FRP} \quad (11)$$

Being the global equilibrium in the horizontal direction guaranteed if:

$$2HB\Delta\sigma_{xx}^b + tB\Delta\sigma_{xx}^m + t_{FRP}(2H + t)\sigma_{FRP} = 0 \quad (12)$$

The uncertainty of the mechanical properties of masonry components is generally significant. This is well document in experimental campaigns and, therefore, uncertainty is also modelled through a forward propagation approach. Coefficient of variation (Cov) values are eligible to be assigned to each mechanical parameter, for which the numerical model may provide results of a lower bound, a mean value, and an upper bound.

3 Experimental Data for Validation

The accuracy of the proposed numerical model is evaluated based on two experimental campaigns. In particular, the works from Faella et al. [19] and Krevaikas et al. [20] on the strengthening of squared masonry columns were selected. The results are provided in terms of ultimate capacity for both non-strengthened and strengthened cases, and values retrieved from the expressions of Eurocode 6 [10], ACI [9] and Italian code [21] are also presented.

The works selected from Faella et al. [19] gather tests on 28 clay-brick masonry squared columns confined by 1 or 2 layers of GFRP. The test series is indicated with the letter ‘B’ and are made with two different cross-sections equal to 380x380 mm² and to 250x250 mm², as indicated in Table 1. The masonry prisms were casted with weak mortar, composed by pozzolan, with low compression strength and that tries to reproduce a mortar type used in historical buildings in the Mediterranean area.

Table 1. Experimental tests from Faella et al. [19].

Test code	B (mm)	R (mm)	t _{mortar} (mm)	t _{layer,wrap} (mm)	n _{layers,wrap}	E _{FRP} (MPa)	f _{t,FRP} (MPa)
B#01UR	371.5	25	10	–	–	–	–
B#02UR	377.5	25	10	–	–	–	–
B#03UR	371	25	10	–	–	–	–
B#04G1	381.5	25	10	0.23	1	65000	1600
B#05G1	381	25	10	0.23	1	65000	1600
B#06G1	378.5	25	10	0.23	1	65000	1600
B#07G2	380.5	25	10	0.23	2	65000	1600
B#08G2	377.5	25	10	0.23	2	65000	1600

(continued)

Table 1. (continued)

Test code	B (mm)	R (mm)	t_{mortar} (mm)	$t_{\text{layer,wrap}}$ (mm)	$n_{\text{layers,wrap}}$	EFRP (MPa)	$f_{t,\text{FRP}}$ (MPa)
B#09G2	378.5	25	10	0.23	2	65000	1600
B#10UR	244	25	10	–	–	–	–
B#11UR	243.5	25	10	–	–	–	–
B#12UR	244	25	10	–	–	–	–
B#13G1	249	25	10	0.23	1	65000	1600
B#14G1	249.5	25	10	0.23	1	65000	1600
B#15G1	248.5	25	10	0.23	1	65000	1600
B#16G2	247.5	25	10	0.23	2	65000	1600
B#17G2	246.5	25	10	0.23	2	65000	1600
B#18G2	248.5	25	10	0.23	2	65000	1600
B#19UR	250	10	10	–	–	–	–
B#20UR	250	10	10	–	–	–	–
B#21G1	250	10	10	0.48	1	80700	2560
B#22UR	250	10	10	–	–	–	–
B#23UR	250	10	10	–	–	–	–
B#24UR	250	10	10	–	–	–	–
B#25G1	250	10	10	0.48	1	80700	2560
B#26G1	250	10	10	0.48	1	80700	2560
B#27G2	250	10	10	0.48	2	80700	2560
B#28G2	250	10	10	0.48	2	80700	2560

For brick units, and considering the experimental information available, an $E_b = 15000$ MPa, $\nu_b = 0.15$, $f_{cb} = 17.5$ MPa (CoV = 15%) and $f_{tb} = 1.75$ MPa (CoV = 15%) were assumed.

Similarly, for mortar it was considered $E_m = 1000$ MPa, $\nu_m = 0.3$, $f_{cm} = 1.027$ MPa (CoV = 15%), $f_{tm} = 0.1027$ MPa (CoV = 15%).

The works selected from Kreaikas et al. [20] gather tests on 8 clay-brick masonry squared columns confined by 1,2,3 or 5 layers of polymeric-wrap. In specific, the clay brick masonry was strengthened with a carbon and glass-based fiber polymer. The tests series are indicated with the letter 'C' and are made with a cross-section of 115×115 mm², as indicated in Table 2. For brick units, and considering the experimental information available, a $E_b = 15000$ MPa, $\nu_b = 0.15$, $f_{cb} = 23.5$ MPa (CoV = 15%) and $f_{tb} = 2.35$ MPa (CoV = 15%) were assumed. Similarly, for mortar it was considered $E_m = 300$ MPa, $\nu_m = 0.3$, $f_{cm} = 2.85$ MPa (CoV = 15%), $f_{tm} = 0.285$ MPa (CoV = 15%). The CoV values are assumed in this study.

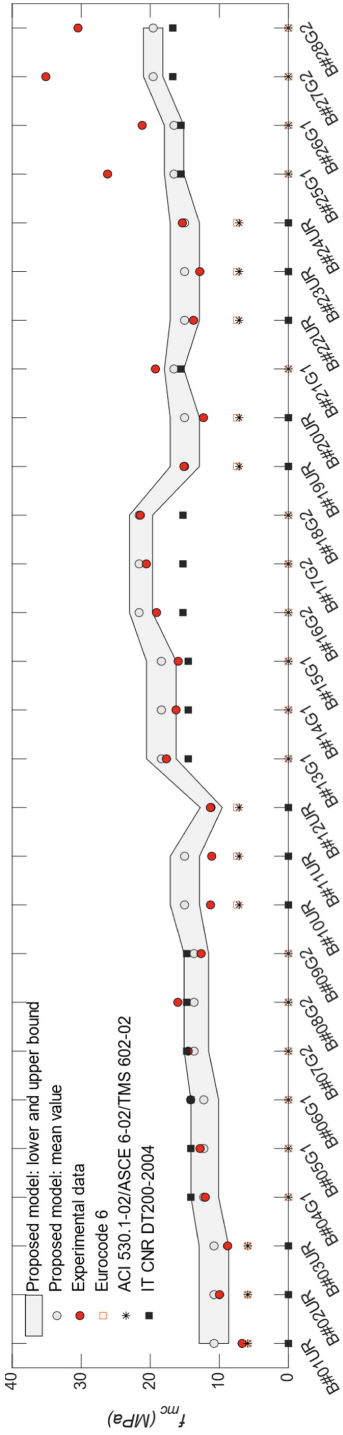
Table 2. Experimental tests from Krevaikas et al. [20].

Test code	B (mm)	R (mm)	t_{mortar} (mm)	$t_{\text{layer,wrap}}$ (mm)	$n_{\text{layers,wrap}}$	EFRP (MPa)	$f_{t,\text{FRP}}$ (MPa)
C1_1_R10	115	10	10	0.118	1	23000	3500
C1_1_R20	115	20	10	0.118	1	23000	3500
C2_1_R10	115	10	10	0.118	2	23000	3500
C2_1_R20	115	20	10	0.118	2	23000	3500
C3_1_R20	115	10	10	0.118	3	23000	3500
C3_1_R20	115	20	10	0.118	3	23000	3500
G5_1_R10	115	10	10	0.183	5	70000	2000
G5_1_R20	115	20	10	0.183	5	70000	2000

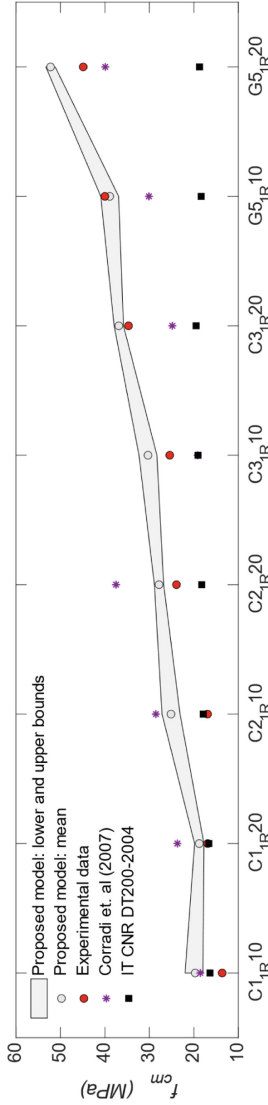
The results for the Faella et al. [19] and Krevaikas et al. [20] tests are provided in Fig. 5. Regarding the former, the experimental data fits well with the envelope of the proposed numerical model. Larger differences are yet found for the last four batches, i.e. for the squared column strengthened with Glass-fiber polymer. Nonetheless, the proposed model offers a conservative margin. Results from the Eurocode 6 [10] and ACI formulas [9] are too conservative for all the un-strengthened cases. On the other hand, the IT CNR DR 200 (2004) [21] leads to good estimations for the strengthened batches (when assuming the following parameters $\alpha_1 = 0.5$, $\alpha_2 = 1.0$ and $\alpha_3 = 1.0$).

Concerning the latter, the numerical results lead to good estimations with the data from Krevaikas et al. [20]. The larger discrepancy is related with the C21R10 batch (~26%).

In general, the model fits well, even in the absence of adequate measures for the COV values. In this case, the IT CNR DR 200 (2004) normative is too conservative (when assuming the following parameters $\alpha_1 = 0.5$, $\alpha_2 = 1.0$ and $\alpha_3 = 1.0$).



(a) Faella et al. (2011)



(b) Krevaiikas et al. (2005)

Fig. 5. Comparison between the numerical results against with experimental data.

4 Conclusions

The tensile low strength and quasi-brittle response characterizes the typical behavior of unreinforced masonries. These features somehow determined the employment of masonry in structural elements whose stability is governed by compressive stresses. Although the behavior of masonry under pure compression is well documented, the assessment of strengthened elements still deserves better comprehension. This need led to the development of a simple numerical model, based on the Hilsdorf's assumptions, which allows giving estimations on the capacity of squared masonry columns. Both un-strengthened and strengthened columns, i.e. with polymeric-based composites such as FRP (Fiber-Reinforced plastics) and GFRP (Glass-Fiber), are considered. The numerical model provides solutions within two seconds, and the results fit well with experimental data collected from clay-brick masonries. The importance of propagating uncertainty has been also demonstrated, especially since the compressive strength of brick units has generally a high CoV value. The numerical tool can be put at disposal to the community especially for retrofitting studies. Several improvements to the model can be also addressed, such as the adding of a cap in compression within the failure criteria for mortar joints, and the modification of the failure criteria for bricks, i.e. to a so-called Modified Mohr-Coulomb criteria.

References

1. Lourenço, P.B., Silva, L.C.: Computational applications in masonry structures: from the meso-scale to the super-large/super-complex. *Int. J. Multiscale Comput. Eng.* **18**(1), 1–30 (2020). <https://doi.org/10.1615/IntJMultCompEng.2020030889>
2. Funari, M.F., Silva, L.C., Mousavian, E., Lourenço, P.B.: Real-time structural stability of domes through limit analysis: application to St. Peter's Dome. *Int. J. Archit. Herit.*, 1–23 (2021). <https://doi.org/10.1080/15583058.2021.1992539>
3. Funari, M.F., Silva, L.C., Savalle, N., Lourenço, P.B.: A concurrent micro/macro FE-model optimized with a limit analysis tool for the assessment of dry-joint masonry structures. *Int. J. Multiscale Comput. Eng.* **20**(5), 65–85 (2022). <https://doi.org/10.1615/IntJMultCompEng.2021040212>
4. CEN. EN 1052–1. Methods of test for masonry – Part 1: Determination of compressive strength. Brussels, Belgium (1999)
5. Mojsilović, N.: Strength of masonry subjected to in-plane loading: a contribution. *Int. J. Solids Struct.* **48**(6), 865–873 (2011). <https://doi.org/10.1016/j.ijsolstr.2010.11.019>
6. Fortes, E.S., Parsekian, G.A., Fonseca, F.S.: Relationship between the compressive strength of concrete masonry and the compressive strength of concrete masonry units. *J. Mater. Civ. Eng.* **27**(9), 4014238 (2015). [https://doi.org/10.1061/\(ASCE\)MT.1943-5533.0001204](https://doi.org/10.1061/(ASCE)MT.1943-5533.0001204)
7. Haseltine, B.: International rules for masonry and their effect on the UK. *Mason. Int.* **1**(2), 41–43 (1987)
8. Sarhat, S.R., Sherwood, E.G.: The prediction of compressive strength of ungrouted hollow concrete block masonry. *Constr. Build. Mater.* **58**, 111–121 (2014). <https://doi.org/10.1016/j.conbuildmat.2014.01.025>
9. ACI, ACI 530.1–02. Commentary on specification for masonry structures. Manual of concrete practice. Detroit, USA (2004)
10. EN 1996–1–1, Eurocode 6: design of masonry structures. Part 1–1: general rules for reinforced and unreinforced masonry structures (2005)

11. Hilsdorf, H.K.: Investigation into the failure mechanism of brick masonry loaded in axial compression. *Designing, engineering and constructing with masonry products*. Gulf Publ. Co., pp. 34–41 (1969)
12. Drougkas, A., Roca, P., Molins, C.: Nonlinear micro-mechanical analysis of masonry periodic unit cells. *Int. J. Solids Struct.* **80**, 193–211 (2016). <https://doi.org/10.1016/j.ijsolstr.2015.11.004>
13. Brencich, A., Corradi, C., Gambarotta, L., Mantegazza, G., Sterpi, E.: Compressive strength of solid clay brick masonry under eccentric loading. In: *Proceeding of British Masonry Society*, pp. 37–46 (2002)
14. Shrive, N.G., Jessop, E.L.: An examination of the failure mechanism of masonry piers, prisms and walls subjected to compression. In: *Proceeding of British Ceramic Society*, pp. 30–110–7 (1982)
15. Lourenço, P.B., Pina-Henriques, J.: Validation of analytical and continuum numerical methods for estimating the compressive strength of masonry. *Comput. Struct.* **84**(29), 1977–1989 (2006). <https://doi.org/10.1016/j.compstruc.2006.08.009>
16. Khoo, C., HEndry, A.: A failure criterion for brickwork in axial compression. In: *Proceeding of the 3rd International Brick/Block Masonry Conference*, pp. 139–145 (1973)
17. Asteris, P.G., et al.: Masonry compressive strength prediction using artificial neural networks, pp. 200–224 (2019)
18. Scacco, J., Ghiassi, B., Milani, G., Lourenço, P.B.: A fast modeling approach for numerical analysis of unreinforced and FRCM reinforced masonry walls under out-of-plane loading. *Compos. Part B Eng.* **180**(107553) (2020). <https://doi.org/10.1016/j.compositesb.2019.107553>
19. Faella, C., et al.: Masonry columns confined by composite materials: experimental investigation. *Compos. Part B Eng.* **42**(4), 692–704 (2011). <https://doi.org/10.1016/j.compositesb.2011.02.001>
20. Krevaikas, T.D., Triantafillou, T.C.: Masonry confinement with fiber-reinforced polymers. *J. Compos. Constr.* **9**(2), 128–135 (2005). [https://doi.org/10.1061/\(ASCE\)1090-0268\(2005\)9:2\(128\)](https://doi.org/10.1061/(ASCE)1090-0268(2005)9:2(128))
21. CNR-DT200 R1/2012. Guide for design and construction of externally bonded FRP systems for strengthening existing structures : materials, RC and PC structures, masonry structures (2006)



Concurrent Multiscale Hybrid Topology Optimization for Light Weight Porous Soft Robotic Hand with High Cellular Stiffness

Musaddiq Al Ali^(✉), Masatoshi Shimoda, Brahim Benaissa, and Masakazu Kobayashi

Department of Advanced Science and Technology, Toyota Technological Institute, 2-12-1, Hisakata, Tenpaku-Ku, Nagoya 468-8511, Aichi, Japan
alali@toyota-ti.ac.jp

Abstract. This article's primary objective is to investigate the topological optimization of soft robotic grips, using hybrid topology optimization. For the goal of creating light weight and porous soft gripper designs. This task is constituted of two design problem, for which we developed a hybrid SIMP-ESO approach, where SIMP solves the macroscale and ESO solves the microscale optimization. We formulate the microstructure as the maximum allowable young moduli that can be achieved for high weight minimization for the microscale, considering the case of orthotropic materials. To examine the performance of the suggested method we evaluate several macro scale and microscale combinations. The results attained robust and 3D printable designs.

Keywords: Soft robotics · Porous structure · Multiscale · Hybrid topology optimization

1 Introduction

Soft robotics has been the subject of a strong interest in the last few years, both from researchers and industry. Roboticist is considered as a potentially whole new class of machines that perform better in the real world and are more versatile [1–4]. Soft robotics is intending to make robots that are, flexible, and soft like biological organisms. Like natural tissue, the main frame of a soft robot is distributing the energy to attain the action so it is deformed due to the action based on its reaction to the action fields rather than relying fully on linkage movements and gears as in traditional robotics. In the other words, it is seeking to expand the scope of robotics beyond the limited scope of dynamic rigid bodies. Designing an ultralightweight and stiff soft robotic gripping hand that attains gripping with a single actuation point is the main goal of this paper. This task is approached by adopting two aspects; the first one is implementing a structure that redistributes the strain energy to attain a precise prescribe displacement control. The second aspect is to make it a porous structure, to achieve extreme light weighting with maintaining high performance. Furthermore, the pore will be designed to have the maximum martial's property (i.e., axial and/or shear stresses resilience). In order to attain such structure, non-parametric

optimization is utilized in this research. One of the most efficient non-parametric optimization methods for attaining profound designs with the extremum of the user-defined objective is topology optimization. Through the discretization of the design space, this general technique applies conventional optimization algorithms to the topology of structures. In order to solve the optimization problem for static loading scenarios, load steps, design variables, responses, constraints, and objectives must be defined [5–8]. Associated with additive manufacturing, topologically optimized structures are shown robust design and showed good performance [9–11]. Furthermore, topology optimization gave the opportunity to create lightweight, highly functional structures.

In order to maximize structural performance to weight ratio while satisfying various design requirements, structural topology optimization seeks to identify the best and most reliable material distribution within the design domain. One of the earliest continuum topology optimization techniques for developing compliant systems was the homogenization approach. This method converts computationally expensive structural topology optimization problems into an effective multiscale optimization problem by introducing a material density function in each discretized element, which is made up of an infinite number of randomly distributed holes. The homogenization theory is used to determine the mechanical properties of materials.

There are two different approaches to adding microstructures: those based on rank laminate composites and those based on hollow microcells. In the former case, the homogenization equation can be solved analytically, whereas in the latter case, the homogenization problem is frequently solved using numerical techniques. With the homogenization method, theoretical structural performance can be mathematically constrained [12]. Ananthasuresh et al. [13] has extended the homogenization to perform compliant mechanisms designs. However, because the resulting mechanisms are not flexible enough, the results appear to be a mean compliance design rather than a compliant mechanism design. As a result, Nishiwaki et al. [14] developed a homogenization-based topology optimization method for the design of compliant mechanisms that includes flexibility. In their method and in order to effectively describe the flexibility, the creation of a multi-objective function using mutual mean compliance was used. SIMP (solid isotropic microstructure with penalization) has been used to design compliant mechanisms as a direct descendant of the homogenization method [15–18]. Additionally, the evolutionary structural optimization (ESO) method was developed on the straightforward tenet of gradually removing wasteful material from a structure in order to get the optimum structure conceivable.

The fundamental tenet of ESO is the elimination of the so-called “inefficient material” directly from the building in order to create the best design and it is firstly introduced by Min and Steven [19]. The cost function sensitivity is used to update the decision variables [20, 21]. Updates are based on the element sensitivity number that is generated by differentiating the objective function so that the elemental sensitivity and zero are identical for solid and soft elements, respectively. And as for SIMP, ESO was investigated for designing compliant mechanisms [22–25]. Due to the challenges in creating robust designs, the multiscale compliant mechanism has received little attention from researchers. In addition, due to the fluctuating effective properties for the grayscale elements at the start of the optimization process, the grayscale nature of such a problem

when it is optimized using the SIMP method significantly restricts attaining extrema. The research of Sivapuram et al. [26] suggested an improved compliant mechanism optimization using level-set method. The Binary element idea in zero-level-set method was shown to be effective for robust soft compliant mechanism design.

The idea of concurrent multiscale optimization of compliant mechanisms has not been investigated so far. Moreover, the hybrid method of SIMP and ESO has not been implemented in the concurrent design of the multiscale compliant mechanism. In this research, we investigate this idea of hybrid design methods of SIMP for macroscale and ESO for designing microscale to design porous displacement inverter, for robotic grip. We develop a dedicated finite element model to solve the homogenization for microstructure. We calculate the macrostructure using a different finite element model. The concurrent design function's sensitivity analysis is implemented through the adjoint approach, which significantly lowers the computational cost. We discussed in the second section the mathematical modelling of the multiscale problem. And in Sect. 3 we discuss the studied design cases. Finally, we conclude this study in Sect. 4.

2 The Mathematical Modelling of Concurrent Multiscale Hybrid Topology Optimization

In order to simultaneously optimize the objective function on both the macro \mathbf{x}_M and microscales \mathbf{x}_m , concurrent multiscale topology optimization was carried out. Two distinct finite element systems are used to discretize the macro and microscale design domains. For both systems in this paper, we used a bilinear structured mesh. According to Eq. (1), when is equal to 1, the corresponding element is a solid, while when it is zero, the element represents a void.

$$\mathbf{x}_M, \mathbf{x}_m = \begin{cases} 1 & \text{solid material} \\ 0 & \text{Void} \end{cases} \quad (1)$$

The utilization of a homogenization approach is required for concurrent design of multiscale problems for two reasons. The effective properties of the macrostructure must first be determined. The microscale objective function is use inverse homogenization to simultaneously create the macrostructure as well as the microstructure. Starting from the investigation for the evaluation of the effective elastic tensor by assuming that the Hooks law.

$$\boldsymbol{\sigma} = \mathbf{E}\boldsymbol{\varepsilon} \quad (2)$$

To evaluate overall (i.e., effective) elastic tensor \mathbf{E}_{ijkl}^H of the representative volume element (RVE) Eq. (3) is used:

$$\mathbf{E}^H = \frac{1}{|V|} \int_V \mathbf{E}_{ijqp} \left(\boldsymbol{\varepsilon}_{qp}^{0(kl)} - \boldsymbol{\varepsilon}_{qp}^{*(kl)} \right) dV \quad (3)$$

where \mathbf{E}_{ijqp} is the elastic tensor of the composite materials that consisting the RVE, $\boldsymbol{\varepsilon}_{qp}^{0(kl)}$ is the linearly independent unit strain test [27]. $\boldsymbol{\varepsilon}_{qp}^{*(kl)}$ is characteristic periodic

strain which is obtained by solving Eq. (4)

$$\int_{\Omega_m} \mathbf{E}_{ijqp} \boldsymbol{\epsilon}_{qp}^{*(kl)} \partial \gamma_n dV = \int_{\Omega_m} \mathbf{E}_{ijqp} \boldsymbol{\epsilon}_{qp}^{0(kl)} \partial \gamma_n dV \tag{4}$$

where $\partial \gamma_n$ is the arbitrary virtual displacement associated with unit strain case. Equation (3) is solved for the three cases of (i.e., $kl = 11, 22, 12$ respectively), within Eq. (4). On the other hand, the structure compliance in terms of the micro and macro design variables (\mathbf{x}_M and \mathbf{x}_m respectively) is given by:

$$C_{mech}(\mathbf{x}_M, \mathbf{x}_m) = \frac{1}{2} \sum_{i=1}^N \mathbf{U}_i^T \mathbf{K}_i(\mathbf{x}_M, \mathbf{x}_m) \mathbf{U}_i \tag{5}$$

where U_i and K_i represents the nodal displacement, and the stiffness matrix of the i th element with respect to the macrostructure of the N number of the elements. The stiffness matrix is taking the form [27]:

$$\mathbf{K} = \int_V \mathbf{B}^T \mathbf{E} \mathbf{B} dV \tag{6}$$

where \mathbf{E} is the element’s elastic tensor and \mathbf{B} is the strain displacement matrix. The elastic modulus of the microstructure \mathbf{E}_{ijqp} that is consisting of void and solid material is connected to the elastic tensor of the based solid material \mathbf{E}_0 as:

$$\mathbf{E}_{ijqp} = \mathbf{x}_m \mathbf{E}_0 \tag{7}$$

The effective elastic tensor of the microstructure \mathbf{E}^H that is calculated by implementing Eq. (3) is used to make the macroscale of the elemental elastic tensor \mathbf{E}_{macro} with a similar material interpolation scheme but with the difference of adopting the relaxed penalization of the macro design variables. The relaxation and penalization principles are utilized in SIMP in order to solve many problems that face the early version of it such as the non-existence and grayscale [28, 29]. However, these modifications are serious limitations for attaining design with global extrema of the traditional SIMP method [30–32]. This issue will be discussed later in the discussion section, so returning to the formulation part of the research, the elastic tensor \mathbf{E}_{macro} is formulated by penalizing the macro design variable \mathbf{x}_M to power ($p \geq \max[\frac{2}{1-\nu}, \frac{4}{1+\nu}]$) [33]. Here ν is the Poisson ratio of the solid materials. In this research p is chosen to be 3. The elastic modulus of the macrostructure is taking the final form of:

$$\mathbf{E}_{macro} = (1 - \alpha) \mathbf{x}_M^3 \mathbf{E}^H \tag{8}$$

where α is an infinitesimal value. By assuming that the actuator is subject to linear strain limits, a spring of stiffness K_{in} , and a force F_{in} at the input point A, the generalized model of the mechanically activated compliant mechanism problem is linearly implemented. As shown in Fig. 1, the goal is to maximize the displacement at the output point B.

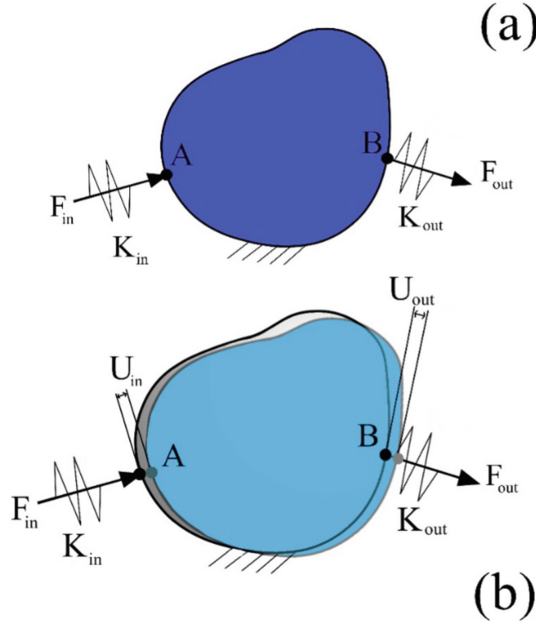


Fig. 1. The soft robotic gripper mechanism design problem

$$\begin{aligned}
 & \max_{\rho} : U_{out} \\
 & \text{s.t. } \{ \mathbf{K}\mathbf{U} = \mathbf{F} \\
 & \int_{\Omega_{dM}} \mathbf{x} d\Omega_{dM} \leq v, \mathbf{x} \in (0, 1] \quad \forall \mathbf{x} \in \Omega_{dM} \tag{9}
 \end{aligned}$$

The goal of is to attain porous soft gripper with maximizing the porous robustness to withstand the different loading condition. As such, in this research, we investigated the two cases of maximizing the bulk modulus and maximizing the shear modulus, of the microstructure. Therefore, the optimization is addressing also, the maximization of \mathbf{E}^H . The concurrent multiscale optimization algorithm will be:

$$\begin{aligned}
 & \text{find } \mathbf{x}_M, \mathbf{x}_m \quad (M = 1, 2, \dots, N_M; m = 1, 2, \dots, N_m) \\
 & \max_{\rho_M, \rho_m} : U_{out}(\mathbf{x}_M), \text{ Cellular stiffness} = \begin{cases} \text{Bulk modulus} = \mathbf{E}_{11}^H(\mathbf{x}_m) + \mathbf{E}_{22}^H(\mathbf{x}_m) \\ \text{Shear modulus} = \mathbf{E}_{33}^H(\mathbf{x}_m) \end{cases} \\
 & \text{s.t. } \left\{ \begin{aligned} & \mathbf{K}(\mathbf{x}_M)\mathbf{U} = \mathbf{F} \\ & \mathbf{E}^H = \frac{1}{|V|} \int_V \mathbf{E}_{ijqp}(\mathbf{x}_m) \left(\boldsymbol{\epsilon}_{qp}^{0(kl)} - \boldsymbol{\epsilon}_{qp}^{*(kl)} \right) dV \end{aligned} \right. \\
 & \int_{\Omega_{dM}} \mathbf{x}_M d\Omega_{dM} \leq v_M, \mathbf{x}_M \in (0, 1] \quad \forall \mathbf{x}_M \in \Omega_{dM}
 \end{aligned}$$

$$\int_{\Omega_{dm}} \mathbf{x}_m d\Omega_{dm} \leq v_m, \mathbf{x}_m = 0|1 \quad \forall \mathbf{x}_m \in \Omega_{dm} \tag{10}$$

Here, N_M and N_m stand for the macro- and microscale structures' corresponding element numbers. v_M and v_m are the volume fraction of the design variable \mathbf{x}_M and \mathbf{x}_m within the macro and micro design domains (Ω_{dM} and Ω_{dm} respectively).

2.1 Sensitivity Analysis and Optimization Method

The sensitivity analysis is given in equation, taking into account that the mechanical loading vector F is design independent in our linear analysis (11)

$$\frac{\partial C}{\partial \mathbf{x}} = \mathbf{U}_{in}^T \frac{\partial \mathbf{K}}{\partial \mathbf{x}} \mathbf{U}_{out} \tag{11}$$

while $\frac{\partial \mathbf{K}}{\partial \mathbf{x}}$ is only depending of the macroscale, therefore; the derivative of will take the form:

$$\frac{\partial \mathbf{K}}{\partial \mathbf{x}_M} = \int_{|\Omega_M|} \mathbf{B}^T \frac{\partial \mathbf{E}^H(\mathbf{x}_M)}{\partial \mathbf{x}_M} \mathbf{B} d\Omega_M \tag{12}$$

The microstructure objective function is independent of the macrostructure design variables \mathbf{x}_M , and only depending on the microstructure \mathbf{x}_m [34]. Therefore, the sensitivity of the homogenized material's elastic tensor $\frac{\partial \mathbf{E}^H(\mathbf{x}_m)}{\partial \mathbf{x}_m}$ is taking the form:

$$\frac{\partial \mathbf{E}^H(\mathbf{x}_m)}{\partial \mathbf{x}_m} = \frac{p}{|\Omega_m|} \int_{\Omega_m} (\mathbf{x}_m^{p-1}) \mathbf{E}_{ijqp}^0 (\boldsymbol{\epsilon}_{qp}^{0(kl)} - \boldsymbol{\epsilon}_{qp}^{*(kl)}) d\Omega_m \tag{13}$$

The macrostructure in this work is optimized with the SIMP approach, and the microstructure with the ESO method. This hybrid approach to optimization made it possible to produce solid and understandable design concepts while also drastically lowering the computing expense. The optimality criteria approach is also used to update the design variables[35, 35]. In order to ensure that solutions to the topology optimization problem exist and that the checkerboard problem doesn't emerge, a sensitivity filter is included to alter the sensitivities. $\hat{C}(\mathbf{x}_M)$ and $\hat{C}(\mathbf{x}_m)$ as follows:

$$\hat{C} = \frac{\partial C}{\partial \mathbf{x}_e} = \frac{1}{\mathbf{x}_e \sum_{f=1}^N H_f} \sum_{f=1}^N H_f \mathbf{x}_f \frac{\partial C}{\partial \mathbf{x}_f} \tag{14}$$

where H_f is the convolution operator to perform the modification, \mathbf{x}_e is the design variable at which the sensitivity is calculated, and \mathbf{x}_f [27, 27]. The H_f is defined as:

$$H_f = r - dist(e, f), \{f \in N | dist(e, f) \leq r\} \tag{15}$$

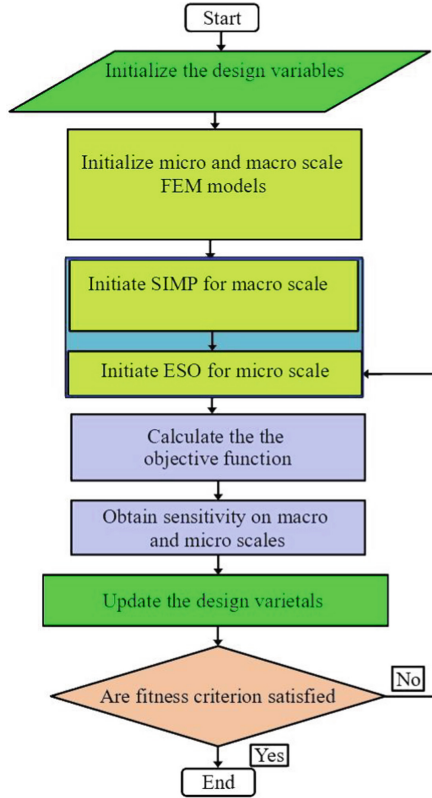


Fig. 2. Flowchart of concurrent multiscale optimization for soft gripper

After modifying the sensitivity, the following is a heuristic updating technique:

$$\mathbf{x}_e^{updated} = \begin{cases} \max(0, \mathbf{x}_e - \varepsilon) & \text{if } \mathbf{x}_e B_e^\omega \leq \max(0, \mathbf{x}_e - \varepsilon) \\ \max(0, \mathbf{x}_e + \varepsilon) & \text{if } \mathbf{x}_e B_e^\omega \geq \max(1, \mathbf{x}_e - \varepsilon) \\ \mathbf{x}_e B_e^\omega & \text{Otherwise} \end{cases} \quad (16)$$

where ε denotes a positive search step. Moreover, ω which is equal to 1/2 denotes a numerical damping coefficient, and B_e denotes the optimality condition:

$$B_e = -\frac{\partial C}{\partial \mathbf{x}_e} / L \frac{\partial V}{\partial \mathbf{x}_e} \quad (17)$$

where L here is a Lagrangian multiplier, and $\frac{\partial V}{\partial \mathbf{x}_e}$ is the volumetric topological derivative. The general algorithm for concurrent multiscale and hybrid topology optimization for soft robotic gripper is illustrated in Fig. 2.

3 Numerical Examples and Discussion

In this section, we are investigating several examples of soft gripper. The first model is having 80 and 80 mm in the x and the y directions (As shown in Fig. 3 (a)). The microstructure has 100 by 100 elements in the x and y directions. The volume fraction condition for microscale was 0.3, and 0.4 for the macroscale. For all cases, elastic tensor for solid material (\mathbf{E}_0) is given in Eq. (18).

$$\mathbf{E}_0 = \begin{bmatrix} 3 & 1 & 0 \\ 1 & 3 & 0 \\ 0 & 0 & 1 \end{bmatrix} \tag{18}$$

The first case of study is maximizing the bulk modulus [37] of the microscale ($\mathbf{E}_{11}^H + \mathbf{E}_{22}^H$ for 2D case). The microscale design is shown in Fig. 3 (b) and (c). The macroscale design is shown in Fig. 3 (d). To address the shear resistance maximization of the microscale, shear modulus (\mathbf{E}_{33}^H) is maximized for the problem mentioned earlier. The microscale design is shown in Fig. 3 (3) and (f). The macroscale design is shown in Fig. 3(g). The second macro design domain of 80 and 160 mm in the x and the y directions (As shown in Fig. 3 (h)). The gripper design results with maximizing the bulk modulus are shown in Figs. 3 (i), (j),and (k). For the case of maximizing the shear modulus, the results are presented in Figs. 3 (l), (m), and (n).

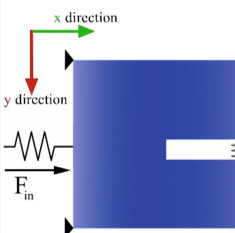
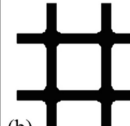
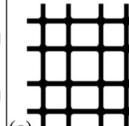


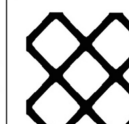

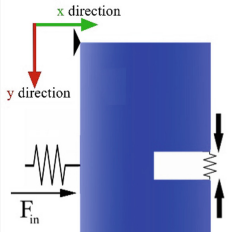
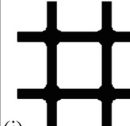
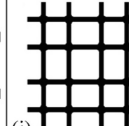
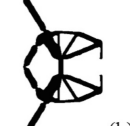

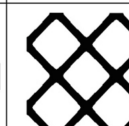

Initial Design Domain	Microcell Design	Microcell Design (2x2)	Design	Elastic Tensor
 <p>(a)</p>	 <p>(b)</p>	 <p>(c)</p>	 <p>(d)</p>	$\begin{bmatrix} 0.171 & 0.013 & 0 \\ 0.013 & 0.171 & 0 \\ 0 & 0 & 0.003 \end{bmatrix}$
	 <p>(e)</p>	 <p>(f)</p>	 <p>(g)</p>	$\begin{bmatrix} 0.094 & 0.088 & 0 \\ 0.088 & 0.094 & 0 \\ 0 & 0 & 0.100 \end{bmatrix}$
 <p>(h)</p>	 <p>(i)</p>	 <p>(j)</p>	 <p>(k)</p>	$\begin{bmatrix} 0.171 & 0.013 & 0 \\ 0.013 & 0.171 & 0 \\ 0 & 0 & 0.003 \end{bmatrix}$
	 <p>(l)</p>	 <p>(m)</p>	 <p>(n)</p>	$\begin{bmatrix} 0.094 & 0.088 & 0 \\ 0.088 & 0.094 & 0 \\ 0 & 0 & 0.100 \end{bmatrix}$

Fig. 3. Concurrent multiscale designs cases

In order to evaluate the computational cost of the suggested hybrid (SIMP-ESO) topology optimization method compared to the topology optimization using the SIMP method, we performed SIMP topology optimization for the second example (i.e., Fig. 3 (h)). The iteration numbers of the SIMP and hybrid (SIMP-ESO) methods are shown in Fig. 4. The results showed attaining robust design in a shorter time for the suggested hybrid method compared to the SIMP method (almost 3 times faster for the Hybrid topology optimization method).

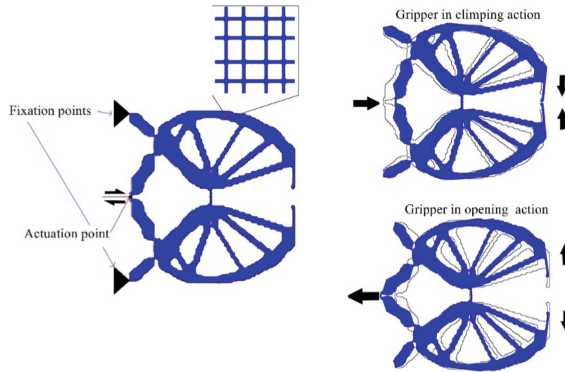


Fig. 4. Concurrent multiscale design of first numerical case of soft robotic in action

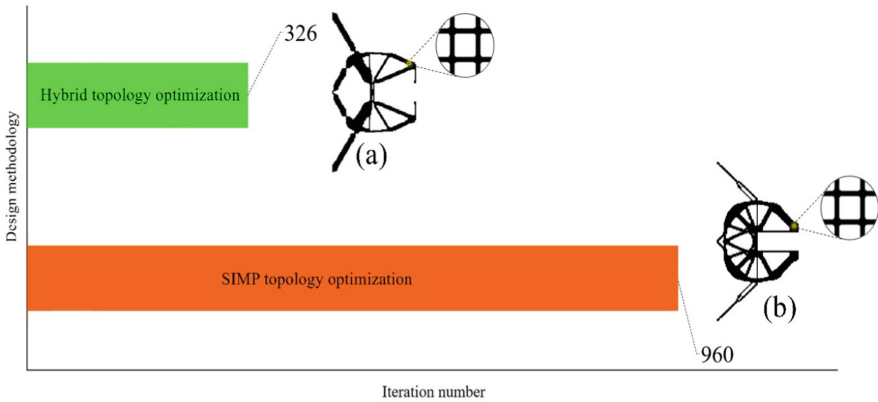


Fig. 5. The number of iterations for the hybrid topology optimization and SIMP method.

The output displacement (U_{out}) of our hybrid multiscale concurrent topology optimization (as shown in Fig. 5 (a)), also showed better results (1.2 times better) than using SIMP method alone (as shown in Fig. 5 (b)).

It is important to mention that Bendsoe and Sigmund [38] after performing a series of investigations with DOCO and the SIMP method, stated that when modeling the problem of the compliant mechanism using linear analysis (which is the analysis that is used in this research for all cases) often gives bad or useless designs compared to the results that

obtained with considering the nonlinear analysis instead. Moreover, they emphasized that for using linear analysis, in the best-case scenario, one only gets erroneous findings; in the worst-case scenario, the results are useless for a compliant mechanism. Consequently, it is imperative (As they stated) for designing compliant mechanisms with topology optimization, to adopt geometrically non-linear finite element modeling [38].

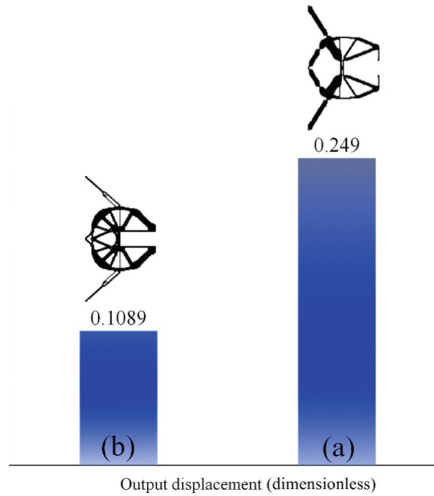


Fig. 6. The comparison of the output displacement for the suggested hybrid topology optimization and SIMP method.

The numerical examples that Bendsoe and Sigmund used, were built considering a simplistic gradient descent algorithm in mind (i.e., optimality criteria method (OCM)). The OCM's drawback is that it can fall into local extremum easily, therefore; careful attention to the gradient decent parameters is a must [20, 30]. Later several researchers make use of the method of moving asymptotes (MMA) [39, 40]. It is a general-purpose algorithm that can accommodate different kinds of optimization problems. It is based on a convex approximation that is appropriate for topology optimization, but the asymptote and move limitations have a significant impact on how effective it is [41]. Due to their nature, OCM and MMA methods are single-point search algorithms, which make them fall easily into local minima [42], especially with increasing the penalization power of the SIMP method. These points necessitate the investigation of the cause of nonlinear analysis promotion under further scrutiny. As such, after performing several investigations, our research has proved the first section of Bendsoe and Sigmund's statement, that the linearized modeling of maximizing the displacement as an objective function for attaining a compliant mechanism will give questionable design (as shown in Fig. 6 (b)).

In a previously performed research, a nonlinear finite element modeling of piezo-electric gripper was successfully attained [43]. And this is validating the second part of the statement of Bendsoe and Sigmund. However, in this research, we are showing robust design with good hinges formations (Fig. 6 (a)) in the case of hybrid topology

optimization. From the results, we deduce that the linear analysis is not the problem of not attaining good hinges for compliant mechanism design. Also, we extend our deduction that in the nonlinear analysis, the nonlinearity consideration is overcoming the huge alteration of the design variables by the penalization (and less severity in the mesh independency filters).

In Fig. 7, the Young modulus of elasticity is jumping as a function of third order so it will impact values of nodal displacements in the scope of linear elastic finite element analysis (especially with the use of bilinear element). As such, rigid elements (the design variables become unity) will aggregate around the hinges that should be existed. In non-linear analysis, the iterative methods are sensitive to the coupled analysis, therefore; the small fields (due to the low value of the penalized design variables) will appear strongly.

While in our hybrid multiscale topology optimization, the optimization is starting with a high value for the elastic tensors and then gradually decreases for all elements. This is put the macro design variables in a situation that is similar to modified Rational Approximation of Material Properties (RAMP) optimization. As such, the solution did not fall into local minima. Under these results, we deduce that the key element of the failure that the SIMP method is facing for the displacement control problems is in the method itself, and not in the objective or the finite element analysis. Moreover, the SIMP method can give great results if associated with some problem-related modifications, and parametrizations such as using ESO for concurrently designing the microscale in this research.

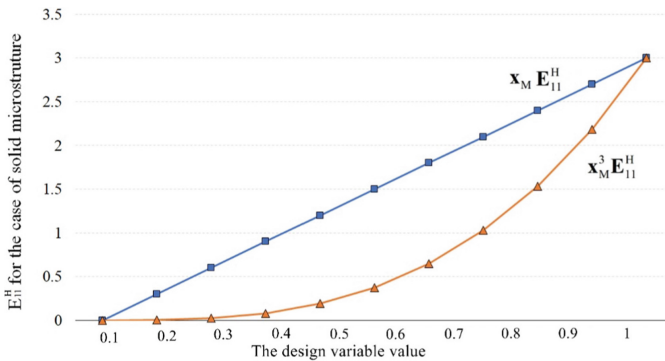


Fig. 7. The effect of the penalized design variable on the elemental young modulus of elasticity.

4 Conclusions

The numerical examples demonstrated that the microscale design responded well to the spatial configuration and the design domain’s boundary conditions on both macro and microstructure. In relation to macrostructure design, the spatial arrangements for the various scenarios showed an elaborated method for distributing strain energy on the macroscale. Microstructure, on the other hand, has shown optimized material distribution to maximize the moduli of elasticity in the case of optimizing the bulk modulus of

elasticity. For maximizing the shear modulus, the material distribution showed a good response to maximize the overall response especially the shear resistance (by increasing E33). Our hybrid approach of using SIMP for macroscale design and ESO for microscale design simultaneously allowed us to achieve good designs while also significantly reducing the computational cost. As a result, the suggested design process has the potential to create new, innovative, lightweight, porous soft robotic gripper designs that are both durable and elastically flexible.

References

1. Tavakoli, M., Batista, R., Sgrigna, L.: The UC soft hand: light weight adaptive bionic hand with a compact twisted string actuation system. In: *Actuators* (2015). <https://doi.org/10.3390/act5010001>
2. Al-Rubaiai, M., et al.: Nonlinear Modeling and Control of Polyvinyl Chloride (PVC) gel actuators. *IEEE/ASME Trans. Mechatronics* (2022). <https://doi.org/10.1109/TMECH.2022.3175445>
3. Al-Rubaiai, M., Tsuruta, R., Gandhi, U., Tan, X.: Distributed measurement of deformation magnitude and location with a pair of soft sensors. *Adv. Eng. Mater.* 2101146 (2022). <https://doi.org/10.1002/adem.202101146>
4. Al-Rubaiai, M.: *Enabling Soft Robotic Systems: New Solutions to Stiffness Tuning, Sensing, and Actuation Control*, Michigan State University (2021)
5. Al Alia, M., Sahibb, A.Y., Al Alic, M.: Teeth implant design using weighted sum multi-objective function for topology optimization and real coding genetic algorithm. In: 6th IIAE International Conference on Industrial Application Engineering 2018, The Institute of Industrial Applications Engineers, Japan, pp. 182–188 (2018). <https://doi.org/10.12792/iciae2018.037>
6. Al-Ali, M.A., Al-Ali, M.A., Takezawa, A., Kitamura, M.: Topology optimization and fatigue analysis of temporomandibular joint prosthesis, *World. J. Mech.* **7**, 323–339 (2017)
7. Abass, R.S., Al Ali, M., Al Ali, M.: Shape and topology optimization design for total hip joint implant. In: *World Congress Engineering 2019* (2019)
8. Al Ali, M., Al Ali, M., Sahib, A.Y., Abbas, R.S.: Design micro piezoelectric actuated gripper for medical applications. In: *Proceedings of the 6th IIAE International Conference on Industrial Applications Engineers, Japan*, pp. 175–180 (2018)
9. Tsukihara, R., Shimoda, M.: Free material orientation design for tailoring vibration eigenvalues of CFRP shell structures, *Trans. JSME* **87** (2021). (in Japanese)
10. Bendsøe, M.P., Kikuchi, N.: Generating optimal topologies in structural design using a homogenization method. *Comput. Methods Appl. Mech. Eng.* **71**, 197–224 (1988). [https://doi.org/10.1016/0045-7825\(88\)90086-2](https://doi.org/10.1016/0045-7825(88)90086-2)
11. Davoodi, E., et al.: Additively manufactured metallic biomaterials, *Bioact. Mater.* (2021)
12. Hassani, B., Hinton, E.: A review of homogenization and topology optimization I—homogenization theory for media with periodic structure. *Comput. Struct.* **69**, 707–717 (1998). [https://doi.org/10.1016/S0045-7949\(98\)00131-X](https://doi.org/10.1016/S0045-7949(98)00131-X)
13. Ananthasuresh, G.K., Kota, S., Gianchandani, Y.: Systematic synthesis of microcompliant mechanisms—preliminary results. In: *Proceedings of the 3rd National Conference on Application Mechine Robotics* (1993)
14. Nishiwaki, S., Frecker, M.I., Min, S., Kikuchi, N.: Topology optimization of compliant mechanisms using the homogenization method. *Int. J. Numer. Methods Eng.* **42**, 535–559 (1998)

15. Sigmund, O.: On the design of compliant mechanisms using topology optimization. *J. Struct. Mech.* **25**, 493–524 (1997)
16. Sigmund, O., Torquato, S.: Design of smart composite materials using topology optimization. *Smart Mater. Struct.* **8**, 365 (1999)
17. Huang, J., Ge, W., Yang, F.: Topology optimization of the compliant mechanism for shape change of airfoil leading edge (P). *ACTA Aeronaut. Astronaut. Sin. A B-* **28**, 988 (2007)
18. Maute, K., Frangopol, D.M.: Reliability-based design of MEMS mechanisms by topology optimization. *Comput. Struct.* **81**, 813–824 (2003). [https://doi.org/10.1016/S0045-7949\(03\)00008-7](https://doi.org/10.1016/S0045-7949(03)00008-7)
19. Xie, Y.M., Steven, G.P.: A simple evolutionary procedure for structural optimization. *Comput. Struct.* **49**, 885–896 (1993). [https://doi.org/10.1016/0045-7949\(93\)90035-C](https://doi.org/10.1016/0045-7949(93)90035-C)
20. Al Ali, M., Shimoda, M.: Investigation of concurrent multiscale topology optimization for designing lightweight macrostructure with high thermal conductivity. *Int. J. Therm. Sci.* **179**, 107653 (2022). <https://doi.org/10.1016/j.ijthermalsci.2022.107653>
21. Zhou, M., Rozvany, G.I.N.: On the validity of ESO type methods in topology optimization. *Struct. Multidiscip. Optim.* **21**(1), 80–83 (2001). <https://doi.org/10.1007/s001580050170>
22. Ansola, R., Vegueria, E., Canales, J., Tárrago, J.A.: A simple evolutionary topology optimization procedure for compliant mechanism design. *Finite Elem. Anal. Des.* **44**, 53–62 (2007). <https://doi.org/10.1016/j.finel.2007.09.002>
23. Huang, X., Xie, Y.M.: Evolutionary topology optimization of continuum structures with an additional displacement constraint. *Struct. Multidiscip. Optim.* **40**, 409–416 (2010). <https://doi.org/10.1007/s00158-009-0382-4>
24. Im, M.-G., Park, J.-Y., Han, S.-Y., et al.: A new topology optimization scheme based on BESO for electro-thermal-compliant mechanisms. In: *Proceedings of the 6th Australasian Congress on Applied Mechanics*, pp. 159–168 (2010)
25. Ansola, R., Vegueria, E., Maturana, A., Canales, J.: 3D compliant mechanisms synthesis by a finite element addition procedure. *Finite Elem. Anal. Des.* **46**, 760–769 (2010). <https://doi.org/10.1016/j.finel.2010.04.006>
26. Sivapuram, R., Dunning, P.D., Kim, H.A.: Simultaneous material and structural optimization by multiscale topology optimization. *Struct. Multidiscip. Optim.* **54**(5), 1267–1281 (2016). <https://doi.org/10.1007/s00158-016-1519-x>
27. Al Ali, M., Shimoda, M.: Toward multiphysics multiscale concurrent topology optimization for lightweight structures with high heat conductivity and high stiffness using MATLAB. *Struct. Multidiscip. Optim.* **65**, 1–26 (2022). <https://doi.org/10.1007/s00158-022-03291-0>
28. Bendsøe, M.P., Sigmund, O.: Material interpolation schemes in topology optimization. *Arch. Appl. Mech.* **69**, 635–654 (1999). <https://doi.org/10.1007/s004190050248>
29. Sigmund, O., Petersson, J.: Numerical instabilities in topology optimization: a survey on procedures dealing with checkerboards, mesh-dependencies and local minima. *Struct. Optim.* **16**, 68–75 (1998). <https://doi.org/10.1007/BF01214002>
30. Yan, S., Wang, F., Sigmund, O.: On the non-optimality of tree structures for heat conduction. *Int. J. Heat Mass Transf.* **122**, 660–680 (2018). <https://doi.org/10.1016/j.ijheatmasstransfer.2018.01.114m>
31. Ali, M., Shimoda, M.: Toward concurrent multiscale topology optimization for high heat conductive and light weight structure. In: Koshizuka, S. (ed.), *Conference on 15th World Congress on Computation Mechanics & 8th Asian Pacific Congress on Computation Mechanics, CIMNE, Yokohama*, pp. 1–12 (2022). <https://doi.org/10.23967/wccm-apcom.2022.118>
32. Dzierżanowski, G.: On the comparison of material interpolation schemes and optimal composite properties in plane shape optimization. *Struct. Multidiscip. Optim.* **46**, 693–710 (2012). <https://doi.org/10.1007/s00158-012-0788-2>
33. Bendsøe, M.P.: Optimal shape design as a material distribution problem. *Struct. Optim.* **1**, 193–202 (1989). <https://doi.org/10.1007/BF01650949>

34. Fujioka, M., Shimoda, M., Al Ali, M.: Concurrent shape optimization of a multiscale structure for controlling macrostructural stiffness. *Struct. Multidiscip. Optim.* **65**, 1–27 (2022). <https://doi.org/10.1007/s00158-022-03304-y>
35. Al Ali, M., Al Ali, M., Saleh, R.S., Sahib, A.Y.: Fatigue life extending for temporomandibular plate using non parametric cascade optimization. In: *Proceedings of the World Congress Engineering 2019*, pp. 547–553 (2019)
36. Abass, R.S., Al Ali, M., Al Ali, M.: Shape and topology optimization design for total hip joint implant. In: *Proc. World Congress Engineering (2019)*
37. Juvinall, R.C.: *Engineering Considerations of Stress, Strain, and Strength*. McGraw-hill, New York (1967)
38. Bendsoe, M.P., Sigmund, O.: *Topology Optimization: Theory, Methods, and Applications*. Springer, Heidelberg (2003). <https://doi.org/10.1007/978-3-662-05086-6>
39. Wang, L., Liang, J., Chen, W., Qiu, Z.: A nonprobabilistic reliability-based topology optimization method of compliant mechanisms with interval uncertainties. *Int. J. Numer. Methods Eng.* **119**, 1419–1438 (2019)
40. Zhan, J., Li, Y., Luo, Z., Liu, M.: Topological design of multi-material compliant mechanisms with global stress constraints. *Micromachines*. **12**, 1379 (2021)
41. Jiang, T., et al.: A first order method of moving asymptotes for structural optimization. *WIT Trans. Built Environ.* **14** (1970). <https://doi.org/10.2495/OP950101>
42. Benaissa, B., Hocine, N.A., Khatir, S., Riahi, M.K., Mirjalili, S.: YUKI Algorithm and POD-RBF for Elastostatic and dynamic crack identification. *J. Comput. Sci.* **55**, 101451 (2021). <https://doi.org/10.1016/j.jocs.2021.101451>
43. Al Ali, M., Al Ali, M., Sahib, A.Y., Abbas, R.S.: Design Micro-piezoelectric actuated gripper for medical applications. In: *Proceedings of the 6th IIAE International Conference on Applied Industrial Engineering 2018*. The Institute of Industrial Application Engineers, pp. 175–180 (2018). <https://doi.org/10.12792/iciae2018.036>



Reliability Assessment of Low-Rise Roof Structures Under Wind Loads in the Southern Region of Vietnam

Bac An Hoang^(✉)

University of Architecture Ho Chi Minh City (UAH), 196 Pasteur, District 3, Ho Chi Minh City, Vietnam

an.hoangbac@uah.edu.vn

Abstract. Low-rise buildings are common types of construction in the Southern region of Vietnam, which have from one to three stories and one or two sloped roofs. The roofs usually are covered with corrugated metal sheets roofs, and purlins are cold-formed steel. In this region, most people have limited economic conditions, and then they build houses by traditional methods based on experience. Therefore, many buildings do not comply with constructed standards, which will affect structural safety. This southern region is considered to be less affected by storms. However, in the rainy season (from August to December), high winds often appear and cause significant damage to the roofs of buildings. Therefore, in this study, the roof structure will be analyzed using the reliability theory. The author uses the Monte Carlo method to simulate random design parameters such as wind load, steel strength, and cross-sectional dimensions. The analysis results will show the safety level of the roof structure according to random variables. From this, the necessary recommendations are proposed to users and construction designers.

Keywords: Low-rise building · Reliability Theory · Wind load · Cold-formed steel · Vietnam

1 Introduction

Vietnam is a developing country with many economic difficulties, so low-rise housing is famous for living and working in rural areas or the periphery of cities. The typical house type is 1–2 stories, with one or a pitched roof. The roofs are usually covered with corrugated metal sheets and cold-formed steel (CFS) purlins. With such roof construction, they are affordable, durable, and low maintenance. Such low-rise houses are mostly built by local builders who do not have much knowledge of structural design.

In low-rise buildings with sloping roofs and large roof areas, the wind is one of the loads that significantly affect the safe working of the building [1]. According to [2, 3], storms have a lower impact on the southern region (Region IIA). Still, by the rainy season (August to December), statistics in recent years have thousands of houses damaged [4]. The damage caused by high winds to buildings in Vietnam has been studied by Giang

L.T [5]. With the assessment of wind storms as a frequent hazard for construction works, there have been many studies on this issue, such as the Institute of Building Science and Technology (IBST), which has proposed some storm prevention solutions for low-rise buildings [6]. However, these solutions may be appropriate only for storms with wind strength from 10 to 12 [7]. In Minh's research [7], it was stated that, due to the influence of climate change, storms are increasingly appearing with higher frequency than before, with unpredictable direction and increasing intensity. In recent years, storms with gusts of level 14 and above have been recorded in Vietnam [7]. Meanwhile, the Southern regions belong to Region IIA, wind speed of 132 km/h, and storm level of 12 [3]. The variations and trends of maximum wind speed in the period 1961–2007 were studied by Huang C.T [8].

Many studies have investigated the reliability of low-rise structures such as Ellingwood et al. [9] developed a fragility analysis method to assess the response of light-frame wood construction exposed to stipulated extreme windstorms and earthquakes. Lee et al. [10] presented a fragility assessment for roof sheathing in light frame constructions built-in high wind regions. Elshaer et al. [11] used Computational Fluid Dynamic (CFD) simulations to study the progressive stages of building damage for wind azimuth. M. Amini [12] presented a methodology for the reliability assessment of roof sheathing panels in low-rise structures for predicted wind pressure distributions. T. Acosta [13] investigated the prominent failure modes of educational facilities by using field observations. Prasad et al. [14] tested low-rise building models in the wind tunnel with flat, gabled, and hip roof configurations. From the overview studies, it is found that there is a need for more studies on the safety of the roof structure of low-rise buildings in the Southern region of Vietnam to have more warnings and instructions for builders to reduce future damages. Therefore, in this study, a method of evaluating the reliability of low-rise roof structures is proposed by Monte Carlo simulation. State function defined according to EC3 [15], its reliability simulation based on random effects of wind load, the influence of roof slope, cross-sectional size of purlins, steel strength, construction site location built in the southern region, characteristically Ho Chi Minh City.

2 Material and Methods

2.1 Load and Action

In this study, the roof structure of a typical low-rise building in the southern region (specifically, Ho Chi Minh City) is calculated according to Eurocode [15], and its safety is analyzed.

The loads used to design the structure were from Vietnam standard [3] and included:

- a) Dead load, which includes self-weight of the roof sheathing, purlin, and ceiling;
- b) Live load on the roof;
- c) Wind load: The formula determines the calculated value of the wind load static component W :

$$W = n.n_t.W_0.k.c \quad (1)$$

where: n - coefficient of wind load reliability; n_t - factor of wind load for various assumed service lifetime of structure; W_0 - the standard wind pressure; k - the height-dependent wind pressure variation factor; c - the aerodynamic factor;

From [3], $W_0 = 0.613V_0^2 \cdot 10^{-3}$ is the conventional figure for wind pressure. The statistical features and coefficient of variation (CV) of wind pressure have been simulated in [16] with mean $\mu_{W_t} = n_t \mu_{W_0}$ and the standard deviation is σ_{W_t} and $n_t = 0.83$ under the assumption that the building will last for 20 years.

2.2 Materials

Cold-formed steel for purlins and metal sheets, which has high strength and is lightweight and straightforward to install, is a suitable material for the roof structure. In Vietnam, commonly used is relatively high-strength steel ($f_y = 310 \div 400$ MPa, $f_u = 450 \div 540$ MPa) for instance G350–G450 [17].

2.3 Evaluation of System Reliability and Limit State Design

Finding the criteria for its limited state and evaluating the probability of failure p_f are the main goals of reliability theory. Thus, p_f can be written as follows:

$$p_f = P(U > B) \tag{2}$$

In which: U – load impact; B – structural strength.

Assuming randomness for variables U and B [18]. The reliability margin’s difference M then has a normal distribution:

$$M = B - U \tag{3}$$

And $\mu_M = \mu_B - \mu_U$, standard deviation (σ_M) and probability density ($f(m)$).

$$f(m) = \int_{-\infty}^{\infty} g(m + u)f(u)du \tag{4}$$

Thus, the probability of failure is given:

$$P_f = P(M < 0) = 1 - P_s = \int_{-\infty}^0 f(m)dm \approx \Phi(\beta) \tag{5}$$

The Monte Carlo approach generates a set of values for independent representations of $x_i, i = 1, 2, \dots, n$. It determines the safety margin [19] for the analysis of the probability of failure indicated by statement (4) (5), with the state function being complicated and having a large number of variables.

$$m = f(x_1, x_2, \dots, x_n) = f(\bar{x}) \tag{6}$$

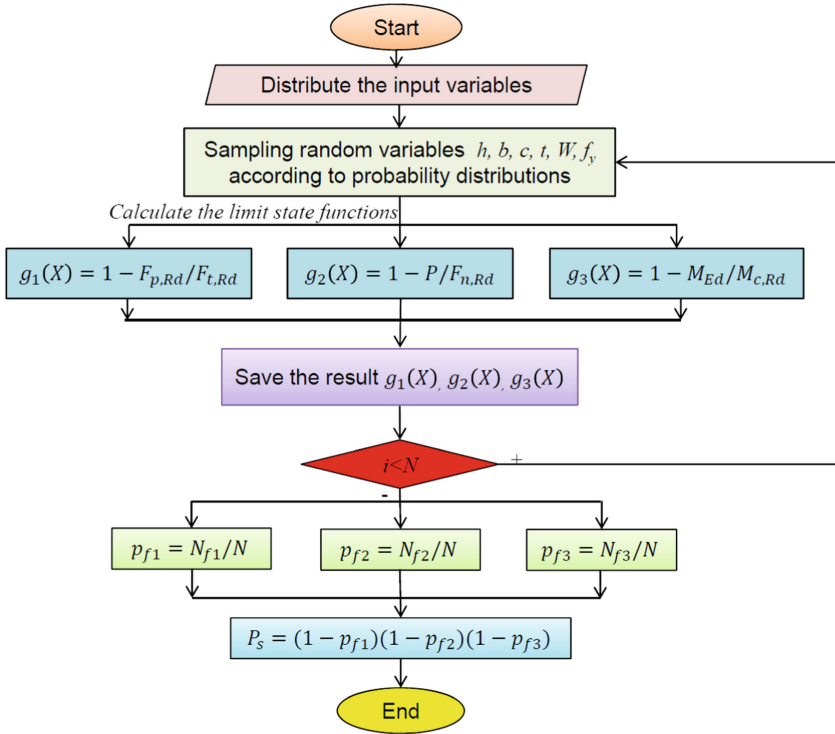


Fig. 1. Monte Carlo simulation flowchart

Consequently, the probability of failure is calculated:

$$P_f = 1 - P_s = P(M \leq 0) = \lim_{n \rightarrow \infty} \frac{k}{n} \tag{7}$$

where: n - the overall number of tests, k - the total of trials with $f(x) \leq 0$, P_s - reliability.

Consider the working cases of the roof structure to determine the limit state function and its failure probability:

a) Working of the joints between the roof and the end-wall under wind uplift: for anchoring the purlins, the use of dowels (12 mm rebars) that protrudes from the masonry was used to tie down the purlin to the masonry wall. Limit state function is the tensile strength of dowels:

$$g_1(X) = 1 - F_{p,Rd}/F_{t,Rd} \tag{8}$$

The probability of failure is P_{f1} .

b) Working of roof screws due to tensile forces, tensile strength significantly affected by screw properties and corrugated roof sheets. The area receiving wind pressure from the purlins and corrugated galvanized roof sheets is impacted by the screw spacing. The fastener spacing in the surveys ranged from 150 mm to 250 mm, with a mean of 200 mm separation. Limit state function is the tensile strength of screw:

$$g_2(X) = 1 - P/F_{n,Rd} \tag{9}$$

The probability of failure is P_{f2} .

c) Purlin working under load combination (wind uplift + static load). The limit state function is bending moment resistance:

$$g_3(X) = 1 - M_{Ed}/M_{c,Rd} \tag{10}$$

The probability of failure is P_{f3} .

From the failure probabilities of the above three cases, the failure probability of the roof structure is calculated as follows (Fig. 1):

$$P_s = 1 - P_f = (1 - P_{f1})(1 - P_{f2})(1 - P_{f3}) \tag{11}$$

The third class (RC1), in which the target of reliability index (β_1) is selected at 4.2 for the reference period $t_{ref} = 1$ year, can be applied to the roof structure, according to [20]. Following is how the reliability level for a particular remaining working life might be expressed:

$$\beta_{tref} = \Phi^{-1}\{[\Phi(\beta_1)]^{tr}\} \tag{12}$$

As a result, the roof structure’s lifetime should be considered $\beta \approx 3.34$ with $t_{tref}^{20} = 20$ years [16].

3 Numerical Example

3.1 Description of an Example

Consider a low-rise building with a double pitch roof, and the roof structure consists of purlin and corrugated galvanized roof sheets (Fig. 2). The building is located in the wind region II-A. Dimensions of building $H = 6.2$ m, $L = 7.8$ m, $B = 2 \times 7.8$ m, roof

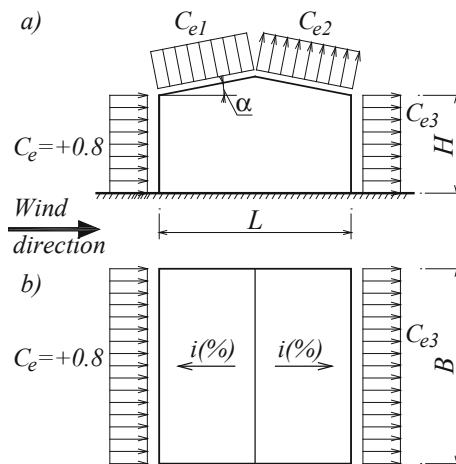


Fig. 2. Wind load on a low-rise building with pitch roof; $C_e, C_{e1} \div C_{e3}$ - aerodynamic factor

angle $\alpha = 11.31^\circ$ (roof slope is $i = 0.2$). Cold-formed channel purlin section C180 \times 50 \times 20 \times 1.5 (depth $h = 180$ mm, flange width $b = 50$ mm, lips $c = 20$ mm, thickness $t = 1.5$ mm), assume that the purlins are simply supported with span length, $L = 7.8$ m, equally spaced at 1.25 m. Impact load: self-weight of the roof structure. Material steel: $f_y = 350$ MPa, $E = 2.1 \times 10^5$ MPa, $\nu = 0.3$ (Fig. 3).

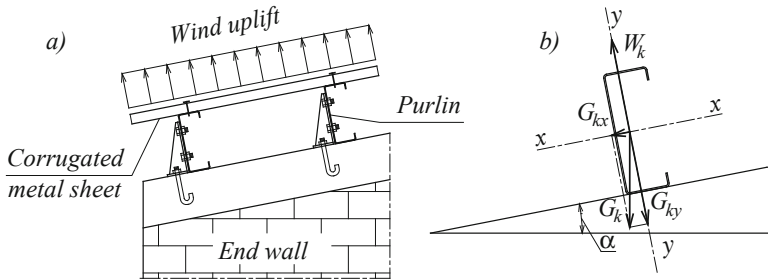


Fig. 3. The connection between metal sheet – purlin – end wall; load on purlin

3.1.1 Load and Static Analysis

The load combination, which included wind uplift and dead load, will be considered to design members.

Dead load:

Corrugated galvanized roof sheets (thickness=0.45mm),	
Self weight of sheet	= 0.0394 kN/m ² .
At a spacing of purlin is 1.25m,	= 0.0473 kN/m;
Self weight of purlin	= 0.0388 kN/m;
Total	$G_k = 0.08605$ kN/m

Wind load:

The calculated wind pressure to the roof:

$$W_1 = n \cdot n_f \cdot k \cdot W_0 \cdot c_{e1} = 1.2 \times 0.83 \times 0.93 \times 0.83 \times (-0.656) = -0.609 \text{ kN/m}^2.$$

At a spacing of 1.25m; $W_k = -0.609 \times 1.25 = 0.7613$ kN/m.

The total load is combined from dead load and wind load:

$$P_k = W_k - G_k \cos 11.31^\circ = -0.6558 \text{ kN/m}.$$

3.1.2 Verification of the Structural Elements According to Eurocode [15]

Verification of Bending following

Maximum span design moment	$M_{Ed} = 4.987$ kNm
Maximum shear force	$V_{Ed} = 2.557$ kN
Design moment resistance	$M_{c,Rd} = 7.212$ kNm
Check of span and single support	$M_{Ed} / M_{c,Rd} = 0.692 < 1$

Verification of screw loaded in tension

Pull-through resistance $F_{p,Rd} = 0.86 \text{ kN} < F_{t,Rd} = 5 \text{ kN}$
 $F_{p,Rd}/F_{t,Rd} = 0.172 < 1$

Verification strength of the bolted shear joint

The capacity of the connection $F_{n,Rd} = 13.92 \text{ kN} > P = 2.557 \text{ kN}$
 $P/F_{n,Rd} = 0.184 < 1$

3.2 Aspects of Random Variables Statistics

The mean (μ), standard deviation (σ) and coefficient of variation ($CV = \sigma/\mu$) are the characteristics of random variables in statistics, in which: standard deviation of the dimension of the purlin section $\sigma_{h,b,c,t} = (0.05 \div 0.3)\mu_{h,b,c,t}$, coefficient variation $CV_{h,b,c,t} = 0.05 \div 0.3$; the standard deviation of wind speed is increased from $\sigma_{V_0} = 0.9 \div 6.1 \text{ m/s}$, then CV_{V_0} is $0.024 \div 0.166$ [16] and correspondingly CV_{W_t} increases from $0.05 \div 0.3$; the standard deviation of the yield strength $CV_{f_y} = 0.05 \div 0.3$; roof slope according to values $i = 0.2, 0.25, 0.3, 0.4, 0.5$ (Table 1).

Table 1. Statistic parameters of random variables

S.no	Property	Random variables	Mean, μ	Std. Deviation, σ	CV	Probability Distribution
1	Yield strength, <i>MPa</i>	f_y	350	$(0.05 \div 0.3) \cdot \mu_{f_y}$	$0.05 \div 0.3$	Lognormal [21]
2	Section parameters, <i>mm</i>	h	180	$(0.05 \div 0.3) \cdot \mu_h$	$0.05 \div 0.3$	Normal [18]
		b	50	$(0.05 \div 0.3) \cdot \mu_b$	$0.05 \div 0.3$	Normal [18]
		c	20	$(0.05 \div 0.3) \cdot \mu_c$	$0.05 \div 0.3$	Normal [18]
		t	1.5	$(0.05 \div 0.3) \cdot \mu_t$	$0.05 \div 0.3$	Normal [18]
3	Wind pressure, <i>daN/m²</i>	$W_t = n_t W_0$	68.89	$(0.05 \div 0.3) \cdot \mu_{W_t}$	$0.05 \div 0.3$	Gumbel [18][16]
4	Roof slope	i ,		$0.2 \div 0.5$		

3.3 Structural Reliability Cases Estimation

Evaluate the working conditions of the roof by following cases: the connection of the purlin and end wall; the connection of the roof plate and purlin; the bending resistance of the purlin.

Finding that if the connection details are guaranteed according to the structure (safety working capacity with a margin of 0.184, 0.172, β index > 5.2 , does that mean $P_{f1} \approx P_{f2} \approx 0, P_{s1} \approx P_{s2} \approx 1$), now the reliability of the roof structure only depends on the working capacity of the purlin. The following section conducts a reliability analysis of purlins with random variables. The analysis results show that the most dangerous of purlin is the bending resistance, with a limit state function (10).

To investigate the reliability of the structure when considering the influence of the random factors in the following cases (Table 2):

Case 1: the influence of each dimensional quantity of the section and all the dimensional quantities of the cross-section simultaneously ($\sigma_h, \sigma_b, \sigma_c, \sigma_t$);

Case 2: due to variation of wind load (σ_{W0}).

Case 3: effect of the standard deviation of yield strength (σ_{fy});

Case 4: roof slope ratios $i=0.15, 0.2, 0.3, 0.4, 0.5$;

Case 5: Consider the simultaneous influence of cross-sectional dimensions ($\sigma_h, \sigma_b, \sigma_c, \sigma_t$), wind load (σ_{W0}), yield strength with roof slope $i = 0.2$;

Each case is surveyed with g_i (which varies with different M values), where $g_i = \mu_{M_i} / \mu_{M_{c,Rd}} \cdot \gamma_0 / \gamma_n$ is the ratio between the mean of M and mean of $M_{c,Rd}$, where $i = 1, 2, 3$ is the sequence number for the value of M_i has changes (Table 2).

Table 2. Cases of analysis

S.no	Survey cases		Coefficient of variation, CV			
			CV_h, CV_b, CV_c, CV_t	CV_{W0}	CV_{fy}	CV_i
1	Case 1:	$g_1 = 0.1$	$0.05 \div 0.3$			
		$g_2 = 0.2$	$0.05 \div 0.3$			
		$g_3 = 0.3$	$0.05 \div 0.3$			
2	Case 2:	$g_1 = 0.1$		$0.05 \div 0.3$		
		$g_2 = 0.2$		$0.05 \div 0.3$		
		$g_3 = 0.3$		$0.05 \div 0.3$		
3	Case 3:	$g_1 = 0.1$			$0.05 \div 0.3$	
		$g_2 = 0.2$			$0.05 \div 0.3$	
		$g_3 = 0.3$			$0.05 \div 0.3$	

(continued)

Table 2. (continued)

S.no	Survey cases		Coefficient of variation, CV			
			CV_h, CV_b, CV_c, CV_t	CV_{W_0}	CV_{f_y}	CV_i
4	Case 4:	$g_3 = 0.3$				0.15, 0.2, 0.3, 0.4, 0.5
5	Case 5:	$g_1 = 0.1$	$0.05 \div 0.3$	$0.05 \div 0.3$	$0.05 \div 0.3$	0.2
		$g_2 = 0.2$	$0.05 \div 0.3$	$0.05 \div 0.3$	$0.05 \div 0.3$	0.2
		$g_3 = 0.3$	$0.05 \div 0.3$	$0.05 \div 0.3$	$0.05 \div 0.3$	0.2

Used the MATLAB program to assess the system reliability by implementing a Monte Carlo simulation, with $N = 10^5$ samples (Figs. 1).

4 Result and Discussion

The analysis results reliability of the purlin have the density of wind load (W_0), depth (h), flange width (b), lip (c), thickness (t), yield strength (f_y), roof slopes (i), safety margin M , reliability P_s , and probability of failure P_f , reliability index β . Figure 4,

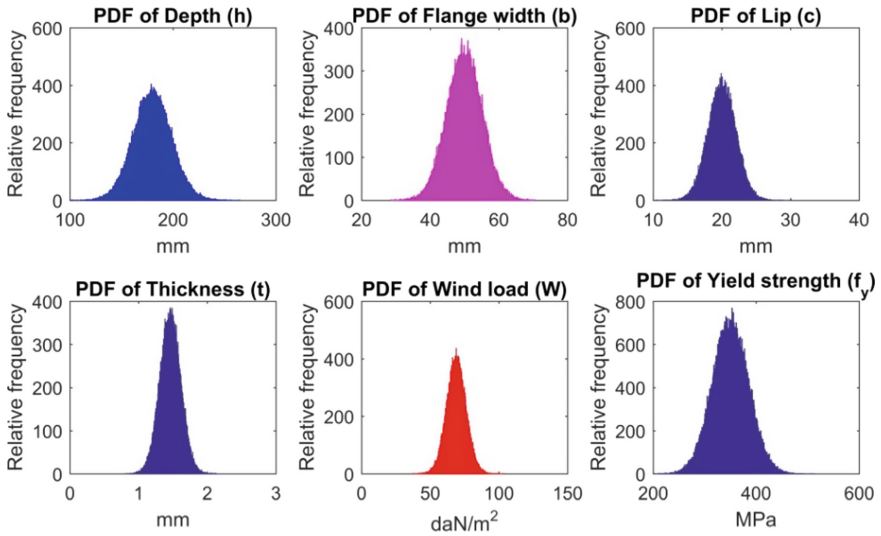


Fig. 4. Probability density function (PDF) of Yield strength (f_y), Wind pressure (W_0), Depth (h), Flange width (h), Lip (c), Thickness (t)

5 presented the density of random variables of case 5 with the coefficient variation of parameters $CV = 0.1$, $g_3 = 0.3$, roof slope $i = 0.2$

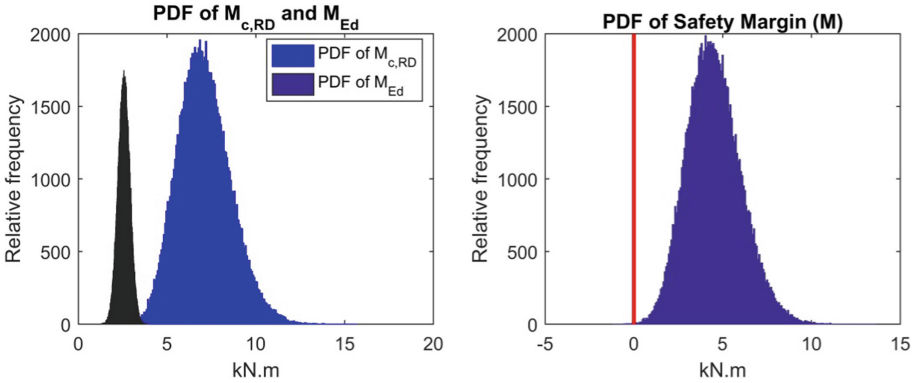


Fig. 5. PDF of Moment resistance ($M_{c,RD}$) and Moment (M_{Ed}); PDF of Safety margin (M)

Table 3a. Characteristics of reliability of case 1 with variable CV_h

S.no	Characteristic reliability		Coefficient variation of depth, CV_h					
			0.05	0.1	0.15	0.2	0.25	0.3
1	$g_{1h} = 0.1$	$P_s =$	0.95320	0.79770	0.71172	0.66080	0.62845	0.60504
		$\beta =$	1.67671	0.83343	0.55842	0.41465	0.32775	0.26641
2	$g_{2h} = 0.2$	$P_s =$	0.99996	0.97190	0.89738	0.82026	0.78057	0.74127
		$\beta =$	3.92834	1.90949	1.26678	0.91636	0.77411	0.64726
3	$g_{3h} = 0.3$	$P_s =$	1.00	0.99797	0.96842	0.91612	0.83613	0.81484
		$\beta =$	> 5.2	2.87386	1.85813	1.37942	0.97868	0.89587

Notes: β from 5.2 then $P_s = 0.9999999 \approx 1$

Table 3a, b, c, and Fig. 6 display the evaluated results, where, reliability index (β), reliability (P_s) due to the influence of each cross-sectional dimensions such as h (Table 3a), b (Table 3b), c (Table 3c), t (Table 3d), and all four parameters h, b, c, t (Table 4) for three cases of the safety margins. Sort by order of influence on the reliability of purlins is depth h , flange width b , lips c , thickness t . The influence of the factors depends on the safety margin (M). Ratio $g_1 = 0.9$ and $CV = 0.05$, the reliability of purlins is very low with $\beta = 0.86514$, $P_s = 0.806$; $g_2 = 0.8$ and $CV = 0.05$, the reliability of purlins are pretty low, is $\beta = 2.0697$ and $P_s = 0.98$; $g_3 = 0.3$ and $CV = 0.05$, the reliability of purlins are on average $\beta = 3.09$, $P_s = 0.999$; when CV from 0.1 the reliability of purlins is very low in all cases.

Tables 4 and Fig. 8 show the reliability results of purlins under variations of parameters of the cross-section that reliability of purlin is very low and not acceptable: CV_{Dim}

Table 3b. Characteristics of reliability of case 1 with variable CV_b

S.no	Characteristic reliability		Coefficient variation of flange width, CV_b					
			0.05	0.1	0.15	0.2	0.25	0.3
1	$g_{1b} = 0.1$	$P_s =$	1.00000	0.99515	0.96110	0.90530	0.85170	0.80995
		$\beta =$	> 5.2	2.58634	1.76360	1.31236	1.04375	0.87771
2	$g_{2b} = 0.2$	$P_s =$	1.00000	1.00000	1.00000	0.99190	0.97175	0.94600
		$\beta =$	> 5.2	> 5.2	> 5.2	2.40438	1.90716	1.60725
3	$g_{3b} = 0.3$	$P_s =$	1.00000	1.00000	1.00000	0.99824	0.98948	0.97348
		$\beta =$	> 5.2	> 5.2	> 5.2	2.91825	2.30727	1.93460

Table 3c. Characteristics of reliability of case 1 with variable CV_c

S.no	Characteristic reliability		Coefficient variation of lips, CV_c					
			0.05	0.1	0.15	0.2	0.25	0.3
1	$g_{1c} = 0.1$	$P_s =$	1.00000	0.99890	0.97905	0.93830	0.89150	0.84965
		$\beta =$	> 5.2	3.06181	2.03451	1.54066	1.23454	1.03493
2	$g_{2c} = 0.2$	$P_s =$	1.00000	1.00000	1.00000	0.98745	0.96870	0.94485
		$\beta =$	> 5.2	> 5.2	4.88652	2.23986	1.86202	1.59685
3	$g_{3c} = 0.3$	$P_s =$	1.00000	1.00000	1.00000	0.99962	0.99763	0.99227
		$\beta =$	> 5.2	> 5.2	> 5.2	3.36697	2.82464	2.42126

Table 3d. Characteristics of reliability of case 1 with variable CV_t

S.no	Characteristic reliability		Coefficient variation of thickness, CV_t					
			0.05	0.1	0.15	0.2	0.25	0.3
1	$g_{1t} = 0.1$	$P_s =$	0.85425	0.69950	0.63945	0.60355	0.58145	0.57150
		$\beta =$	1.05484	0.52296	0.35699	0.26255	0.20560	0.18019
2	$g_{2t} = 0.2$	$P_s =$	0.99225	0.88740	0.78260	0.72935	0.68065	0.65695
		$\beta =$	2.42048	1.21282	0.78100	0.61085	0.46952	0.40415
3	$g_{3t} = 0.3$	$P_s =$	0.99978	0.96275	0.88906	0.82142	0.77724	0.73980
		$\beta =$	3.52065	1.78349	1.22155	0.92080	0.76291	0.64273

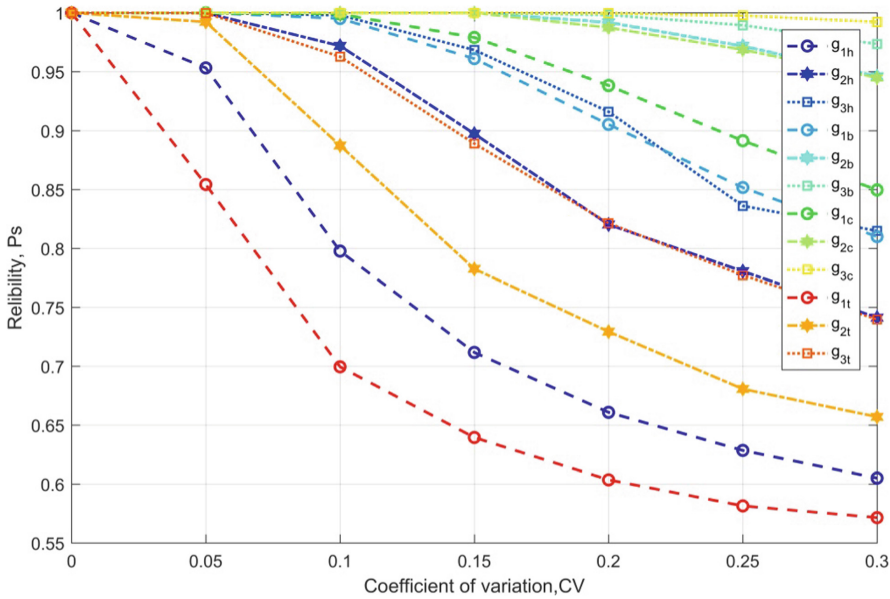


Fig. 6. The reliability of the purlin according to the variations of dimensions cross-section Notes: $g_{ij} - i=1,2,3$ for g_1, g_2, g_3 ; j - is the index for random variables h, b, c, t , respectively;

Table 4. Reliability characteristics of case 1 with variable CV_{Dim}

S.no	Reliability characteristics		Coefficient variation of dimmensions, CV_{Dim}					
			0.05	0.1	0.15	0.2	0.25	0.3
1	$g_{1Dim} = 0.1$	$P_s =$	0.8065	0.62716	0.55404	0.49720	0.46216	0.4366
		$\beta =$	0.8651	0.32434	0.13588	-0.0070	-0.0949	-0.1594
2	$g_{2Dim} = 0.2$	$P_s =$	0.9807	0.83592	0.71304	0.63116	0.57340	0.5256
		$\beta =$	2.0697	0.97783	0.56229	0.33493	0.18504	0.06441
3	$g_{3Dim} = 0.3$	$P_s =$	0.9990	0.93664	0.82200	0.72804	0.65376	0.5964
		$\beta =$	3.0902	1.52716	0.92301	0.60690	0.39549	0.2440

Notes: $g_{iDim} - i = 1, 2, 3$ for g_1, g_2, g_3 ; Dim - is the index showing the simultaneous consideration of the random variables of the cross-section

$= 0.05$, with $g_{1Dim} = 0.1$, $\beta = 0.865$ and $P_s = 0.806$; $g_{2Dim} = 0.2$, $\beta = 2.069$ and $P_s = 0.98$; $g_{3Dim} = 0.3$, $\beta = 3.09$ and $P_s = 0.999$; when CV_{Dim} from 0.5, the reliability drops to very low.

Tables 5 and Fig. 8 show the reliability results of purlins when considering the influence of wind load with three cases of safety margin. That the reliability of the purlin is relatively low:

Table 5. Reliability characteristics of case 2 with variable CV_W

S.no	Reliability characteristics		Coefficient variation of wind load, CV_W					
			0.05	0.1	0.15	0.2	0.25	0.3
1	$g_{1W} = 0.1$	$P_s =$	0.96370	0.81750	0.72250	0.67225	0.63630	0.61950
		$\beta =$	1.79534	0.90588	0.59028	0.44613	0.34859	0.30417
2	$g_{2W} = 0.2$	$P_s =$	1.00	0.98880	0.93020	0.86680	0.81495	0.77625
		$\beta =$	4.50122	2.28352	1.47728	1.11139	0.89629	0.75959
3	$g_{3W} = 0.3$	$P_s =$	1.00	0.99993	0.99447	0.97228	0.93670	0.89838
		$\beta =$	> 5.2	3.81066	2.54081	1.91540	1.52768	1.27235

- Ratio $g_{1W} = 0.1$, $CV_o = 0.05 \div 3$ then $\beta = 1.795 \div 0.3041$ and $P_s = 0.963 \div 0.619$, purlin is unsafe;
 - Ratio $g_{2W} = 0.2$, $CV_W = 0.05$, the reliability of the purlin is guaranteed with $\beta = 4.5$ and $P_s = 1$, when CV_W is from 0.05, the purlin is unsafe;
 - Ratio $g_{3W} = 0.3$, $CV_W = 0.05, 0.1$, the reliability of purlins is guaranteed with $\beta = > 5.2, 3.81$ respectively with $P_s = 1, 0.9999$, when CV_W from 0.1, the reliability of purlins is low, no guarantee of safety.

Table 6. Reliability characteristics of case 3 with variable CV_{fy}

S.no	Reliability characteristics		Coefficient variation of yield strength, CV_{fy}					
			0.05	0.1	0.15	0.2	0.25	0.3
1	$g_{1fy} = 0.1$	$P_s =$	0.99700	0.91610	0.81970	0.75940	0.70955	0.67720
		$\beta =$	2.74778	1.37931	0.91422	0.70437	0.55207	0.45988
2	$g_{2fy} = 0.2$	$P_s =$	1.00	0.99760	0.97150	0.92160	0.87610	0.83205
		$\beta =$	>5.2	2.82016	1.90331	1.41592	1.15571	0.96230
3	$g_{3fy} = 0.3$	$P_s =$	1.00	1.00	0.99914	0.98859	0.93870	0.90063
		$\beta =$	>5.2	4.94013	3.13580	2.27639	1.54395	1.28517

Tables 6 and Fig. 8 show the reliability results of purlins when considering the effect of yield strength that:

Ratio $g_{1fy} = 0.1$, reliability of purlin very low with $\beta = 2.747 \div 0.459$ and $P_s = 0.997 \div 0.677$;
 $g_{2fy} = 0.2$, $CV_{fy}=0.05$, the reliability of the purlin is $\beta \geq 5.2$ and $P_s = 1$, when CV_W is from 0.05, the purlin is unsafe;

$g_{3fy} = 0.3$, $CV_{fy} = 0.05, 0.1$, the reliability of purlins is guaranteed with $\beta \geq 5.2$, 4.94 respectively with $P_s = 1$, when CV_{fy} from 0.1, the reliability of purlins is low, no safe.

Table 7. Reliability characteristics of case 4 with variations of slope ratio i and wind load

S.no	Reliability characteristics		Coefficient variation of wind load, CV_W					
			0.05	0.1	0.15	0.2	0.25	0.3
1	$i = 0.15$	$P_s =$	1.00	0.99988	0.99000	0.96120	0.91828	0.87484
		$\beta =$	>5.2	3.67270	2.32635	1.76478	1.39359	1.14957
2	$i = 0.2$	$P_s =$	1.00	0.99993	0.99447	0.97228	0.93670	0.89838
		$\beta =$	>5.2	3.81066	2.54081	1.91540	1.52768	1.27235
3	$i = 0.3$	$P_s =$	1.000	0.99996	0.99664	0.98120	0.95044	0.91310
		$\beta =$	>5.2	3.94440	2.71041	2.07919	1.64913	1.36009
4	$i = 0.4$	$P_s =$	1.000	1.00	0.99980	0.99716	0.98416	0.96320
		$\beta =$	>5.2	5.41880	3.54008	2.76570	2.14843	1.78909
5	$i = 0.5$	$P_s =$	1.000	1.00	1.00	1.00	0.99988	0.99916
		$\beta =$	>5.2	>5.2	>5.2	4.75342	3.67270	3.14165

Table 7 and Fig. 7 show the β index, P_s of purlins with slopes ratio $i = 0.15, 0.2, 0.3, 0.4, 0.5$ corresponding to pitch angle is $\alpha = 8.53^\circ, 11.3^\circ, 14.04^\circ, 19.25^\circ, 24.23^\circ$, the safety margin for durability are all taken as $g_3 = 0.3$. As the slope of the roof increases, the aerodynamic coefficient c decreases, leading to a decrease in the wind load on the roof, so the purlin of the roof has reliability.

Considering the CV_W from 0.0 to 0.1, the reliability of the purlin reduces slowly; When $CV_W = 0.1$, purlins are still reliable with $\beta = 3.672$ and $P_s = 0.99988$ for roof slope ratios;

$CV_W = 0.15$, the roof has a slope ratio $i = 0.15 \div 0.3$, and purlins have decreasing reliability $\beta = 2.71 \div 2.32$ and $P_s = 0.9944 \div 0.99$; the roof has a slope ratio $i = 0.4, 0.5$, and the purlins are safe with $\beta = 3.54 \div > 5.2$ and $P_s = 0.9998$;

CV_W increases from 0.2 \div 0.3, only roofs with slope ratio $i = 0.5$ then purlins are safe; for the remaining slopes, purlins have decreasing reliability $\beta = 2.76 \div 1.14$ corresponding to $P_s = 0.997 \div 0.874$ working of purlin is not reliable.

Notes: g_{1W} - reliability of case 1 due to wind load (W); g_{1fy} - reliability of case 1 due to yield strength; g_{1Dim} - reliability of case 1 due to cross-sectional dimensions; g_1 - reliability of case 1 due to simultaneous influence of factors.

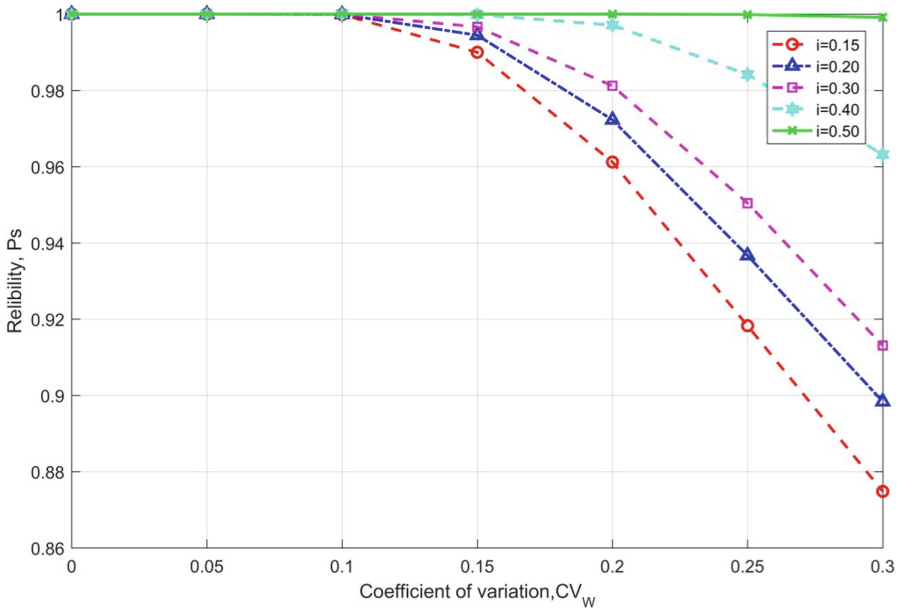


Fig. 7. Effect of roof slope ratios and wind load variation on purlin reliability

Table 8. Reliability characteristics of case 5 with variable CV

S.no	Reliability characteristics		Coefficient variation, CV					
			0.05	0.1	0.15	0.2	0.25	0.3
1	$g_1 = 0.1$	$P_s =$	0.76730	0.60357	0.53187	0.48210	0.45148	0.42944
		$\beta =$	0.72998	0.26259	0.07996	-0.0448	-0.1042	-0.1778
2	$g_2 = 0.2$	$P_s =$	0.96356	0.79704	0.67432	0.60532	0.55076	0.50340
		$\beta =$	1.79358	0.83109	0.45187	0.26714	0.12758	0.00852
3	$g_3 = 0.3$	$P_s =$	0.99804	0.90532	0.78572	0.69632	0.62284	0.55760
		$\beta =$	2.88453	1.31247	0.79166	0.51385	0.31295	0.14489

Table 8 and Fig. 8 show the reliability characteristics of purlins when considering the simultaneous influence of factors (h, b, c, t, W, f_y) and roof slope ratio $i = 0.2$. The results express the impact levels of factors on the reliability of purlins, sorted in ascending order of yield strength, wind load, and then cross-sectional size. The reliability of purlins is very low even with a reserve of 30% bending moment resistance (g_3), with $CV = 0.05$, $\beta = 2.884$, and $P_s = 0.998$, not guaranteed.

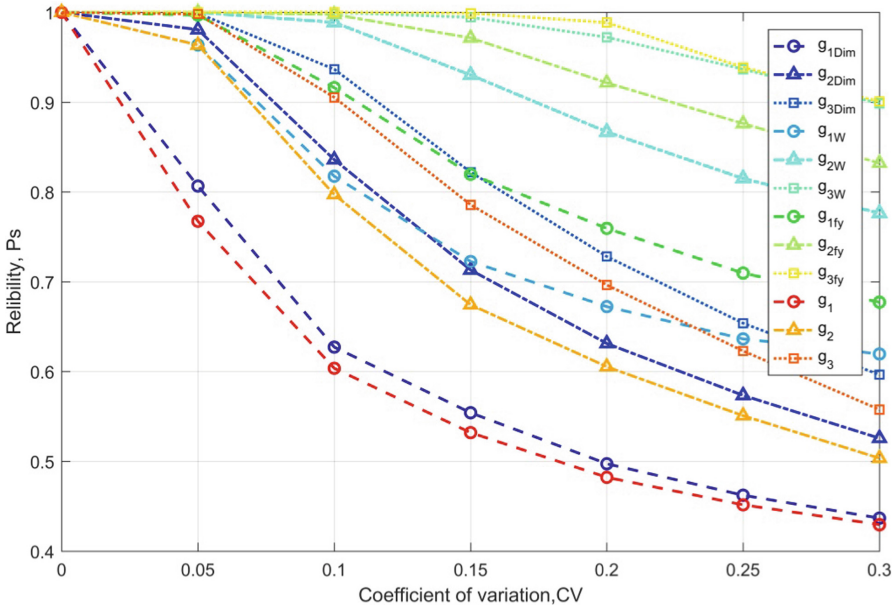


Fig. 8. The reliability of purlins when considering the simultaneous effects of random factors

5 Conclusions

In this study, the safety of the roof structure in the southern region was evaluated concerning various random parameters, including the purlin section properties, wind load, yield strength, and roof slope. The results of statistical characteristics of these parameters are developed in Sects. 3 and 4.

The main factor that sets the roof at risk is wind load, which shows that under unexpected climate change conditions, uncertain wind speed changes result in significant wind pressure changes. In order to accurately justification for wind loads and structural calculations, the designer should consider the roof’s slope and utilize the additional coefficients like Minh. N.D [7] suggested 1.1 to 1.15.

The analysis also shows that if the connection between purlins and roof structure, between screws and roofing corrugated iron ensures the correct structure, they have high reliability and guarantee. The reliability of the roof structure depends on the reliability of the purlin capacity.

Established the state function as the condition of moment capacity of the purlin, then determined the relationship between the reliability and the margin of safety due to the influence of the random variables by using the Monte Carlo simulation.

In addition, the analysis of other factors such as low-rise roof shape (slope, roof elevation, Etc.), load types (wind dynamics, live loads, Etc.), connections in the roof structure, shape of other forms of purlins (Z-shaped, top-hat, Etc.), other working conditions such as shear resistance, stability, Etc. of purlins will also be analyzed.

To maintain the safety of society, state management organizations must have more research, rules, and directions on how to plan and develop low-rise buildings in various locations.

References

1. Ekanayake, B.J: Wind-Induced Damages on Roofs: Sri Lankan Case (2020)
2. QCVN: Vietnam building code. QCVN 02:2009/BXD, Natural Physical & Climatic Data for Construction (2009)
3. TCVN. Vietnam Standard. TCVN 2737–1995, Loads and Effects - Design Standard. Construction Publishing House (1995)
4. S. R. of Vietnam. National report on disaster reduction in Vietnam. Kobe-Hyogo, Japan (2004)
5. Giang, L.T.: Damage caused by strong wind & wind loads standard for building in Viet Nam. Tokyo (2005)
6. Xuan Chinh, N.: Technical Guide – Preventing and minimizing damage to houses due to storms. Hanoi (2008)
7. Dai Minh, N.: Experience of the Philippines in dealing with Super Typhoon Haiyan and storm prevention solutions for low-rise buildings in our country. *Sci. Technol. Mag.* **2** (2014)
8. Huong, C.T.: Variations and trend of maximum wind speed in Vietnam during 1961–2007 (in Vietnamese). *J. Sci. - Univ. Nat. Technol.* **3** (2010)
9. Ellingwood, B., Rosowsky, D., Li, Y., Kim, J.: Fragility assessment of light-frame wood construction subjected to wind and earthquake hazards. *J. Struct. Eng. - J STRUCT ENG-ASCE* **130** (2004)
10. Lee, K.H., Rosowsky, D.V.: Fragility assessment for roof sheathing failure in high wind regions. *Eng. Struct.* **27**(6), 857–868 (2005)
11. Elshaer, A., Abdallah, H., Bitsuamlak, G.: Progressive collapse of low-rise buildings under wind loads (2018)
12. Amini, M., Kasal, B.: Reliability assessment of roof sheathing performance in light wood frame structures subjected to wind pressure **1** (2010)
13. Acosta, T.S.: Risk assessment of low-rise educational buildings with wooden roof structures against severe wind loadings. *J. Asian Archit. Build. Eng.* **21**, 973–985 (2021)
14. Prasad, D., Uliate, T., Ahmed, M.R.: Wind loads on low-rise building models with different roof configurations. *Int. J. Fluid Mech. Res.* **36**, 231–242 (2009)
15. Eurocode. Eurocode 3 - Part 1–3: General rules - Supplementary rules for cold-formed members and sheeting (2004)
16. Hoang, B.A.: Safety evaluation of billboards when considering the random effects of design parameters in the Southern Region of Vietnam. In: *Structural Health Monitoring and Engineering Structures*, pp. 313–329 (2021)
17. China steel and Nippon steel Vietnam joint-stock company. Product manual: Cold rolled steel coils (2020)
18. Rzhantsyn, A.: *Theory of Design of Reliable Structures*. Stroyizdat, Moscow (1978)
19. Holický, M.: *Reliability analysis for structural design* (2009)
20. Standard, E.: *Eurocode 0 - Basis of structural design*. Eurocode 0 (2002)
21. Bartlett, F.M., Dexter, R.J., Graeser, M.D., Jelinek, J.J., Schmidt, B.J., Galambos, T.V.: Updating standard shape material properties database for design and reliability. *Eng. J.* (2003)



A Practical Review of Prairie Dog Optimization Algorithm in Solving Damage Identification Problems in Engineering Structures

Lan Ngoc-Nguyen^{1,2}(✉), Hoa-Tran^{1,2}, Samir Khatir¹, Huu-Quyét Nguyen², Thanh Bui-Tien², and Magd Abdel Wahab¹

¹ Soete Laboratory, Faculty of Engineering and Architecture, Ghent University, Ghent, Belgium
ngoclan.nguyen@ugent.be

² Faculty of Civil Engineering, University of Transport and Communications, Hanoi, Vietnam

Abstract. Up to now, the field of Structure Health Monitoring (SHM) is always a topic of interest to many researchers around the world. One of the core types of research in SHM is to apply and validate different state-of-art scientific and technological advances, especially optimization algorithms (OA), to improve the damage detection capability of the SHM system. Among the different OAs, natural-inspired OAs have emerged to be widely preferred due to their robustness and high level of accuracy thanks to their redundancy of being trapped in local minima. The non-stop evolution of natural-inspired OAs has led to the discovery of many advanced algorithms in the last twenty years, though many of them have not been assessed in solving the more complex optimization problems, notably in civil engineering structures. In this study, the authors will review the effectiveness and practicality of a recently introduced optimization algorithm called the Prairie Dog Optimization algorithm (PDO) in solving damage identification problems of engineering structures. To evaluate its efficiency, the PDOA algorithm will be compared with some other natural-inspired algorithms such as Cuckoo Search (CS), and Genetic Algorithm (GA) in a damage detection case of a bridge structure in Vietnam.

Keywords: Nature-inspired optimization algorithms · Prairie Dog Optimization · Damage identification · Swarm intelligence

1 Introduction

During the exploitation process, engineering structures such as bridges and dams usually have to endure many different loads, varying from the vehicular loads to the ambient and possible catastrophic loads from natural disasters, which may affect the structure's operation as well as their service life. Structural inspection to detect damage and provide warnings and reparation is usually carried out periodically or only unexpectedly when structural damage has already occurred. Therefore, early damage identification helps the structure to work not only safely and efficiently but also significantly reduces the overall maintenance cost of the structures. Much research has been conducted in the last two

decades which focuses on the techniques to improve the efficacy of structural damage detection in structural health monitoring [1–9].

Of all the currently used techniques for damage detection, optimization algorithms (OAs) have proven to be among the most effective tools which are able to not only locate the position of failure but also identify the level of failure in the structure effectively. For instance, Nguyen-Ngoc et al. [10] proposed a hybrid method combining the Particle Swarm Optimization algorithm (PSO) and Artificial Neural Network (ANN) to detect structural damage of a truss bridge structure. PSO is used to optimize the weight of the ANN network, which provides a high level of accuracy in solving the damage detection problem of the given case study. Ho et al. [11] combined the Marine Predator algorithm with a feedforward neural network to detect failures of a laboratory-free-free beam and a full-scale bridge deck model. The result shows that the proposed method accurately detects the single and multiple structural damages with a low computational cost required. The neural network is also used by Khatir et al. [12] with Arithmetic Optimization Algorithm (AOA) to detect damages in a composite plate. The proposed method outperforms the other traditional method in detecting structural failures in a shorter amount of time. Zenzen et al. [13] applied the bat algorithm with the frequency response function (FRF) to identify damages on beam-like and truss structures with a high level of effectiveness. The above researches are just one of the many successful applications of optimization algorithms in solving structural damage detection problems. However, not all OAs are effective in solving this kind of problem, especially for complex structures. It is essential to review beforehand the practicality of an OA before it can be applied to a specific type of structure.

In this study, the practicality of a recently proposed OA- Prairie Dog Optimization algorithm (PDO), which is inspired by the behavior of Prairie Dog in the wild, is performed. The algorithm is proven to be effective in dealing with mathematical problems; however, its effectiveness in solving damage identification problems in structure will be validated in this study, notably in a case study of a real-life truss bridge span. Hypothesis damages are generated on the structure model by adjusting the stiffness of the respective truss elements. The accuracy and efficiency of PDO are compared and discussed with other well-known OAs: Cuckoo Search (CS) and Genetic Algorithm (GA).

2 Methodology-Prairie Dog Optimization

The PDO algorithm was first introduced in 2022 by Absalom et al. [14], which simulates the habits of the prairie dog – a family of rodent, non-carnivorous species that mainly inhabited the deserts of Northern America. In order to survive in one of the most wilderness areas on Earth, the prairie dogs have developed multiple survival characteristics traits such as strong arms, long-nailed toes, and short-distance fast runner, which enable them to run and escape from the predators by hiding in their connected burrows [15]. Prairie dogs also live in a communal colony consisting of many coterie-families of small groups of prairie dogs, which help them to survive more effectively by foraging as a group and avoiding predators through group communication through different kinds of sounds, notably the foraging call and the alarming sound when a predator threat is nearby. The mathematical model of PDO consists of two main phases: Exploration and

exploitation, which are inspired by the foraging, burrow building, and their response to the source of communications respectively.

Phase 1: Exploration

In the exploration phase, the mathematical model is constructed based on the foraging and burrow-digging activities of prairie dogs to initiate the search in the optimization problem space. In real life, when an existing food source is no longer suitable to feed the whole colony, prairie dogs will search for a new food source that is presumably more abundant than the previous one. A system of burrows is then constructed near the new food source to create hiding places for the different coterie. The updated position of the foraging food source is mathematically modeled as in the Eq. (1) below:

$$PD_{i+1,j+1} = GB_{i,j} - 0.1 \times (GB_{i,j} \times \Delta + \frac{PD_{i,j} \times \text{mean}(PD_{n,m})}{GB_{i,j} \times (ub_j - lb_j) + \Delta}) - (1 - \frac{rPD_{i,j}}{GB_{i,j}}) \times \text{Levy}(n) \quad (1)$$

where $PD_{i,j}$ indicates the position of the j th dimension of the i th prairie dog in a coterie, GB is the global best position obtained, rPD is a random position of prairie dog generated, m and n are the numbers of coterie and prairie dogs in a colony, respectively ub and lb are the upper and lower boundary of the optimization problem, Δ is a small number indicates the difference between the prairie dogs, $\text{Levy}(n)$ is a Levy distribution [16].

When a food source is located, the prairie dogs start to construct burrows nearby. The number of burrows is identified based on the digging strength of the prairie dogs, which shall be reduced with the increased number of iterations. The updated position of the burrow constructed is given in equation number (2) as follows:

$$PD_{i+1,j+1} = GB_{i,j} \times rPD \times 1.5 \times k \times \left(1 - \frac{iter}{Maxiter}\right)^{2 \frac{iter}{Maxiter}} \times \text{Levy}(n) \quad (2)$$

where $iter$ and $Maxiter$ are the current iteration and the maximum number of iterations, respectively, $k = -1$ when the current iteration is an odd value and $k = 1$ when the current iteration is an even value, the introduction of k is to add the stochastic property to the exploration phase.

Phase 2: Exploitation

The exploitation phase is simulated based on the two unique responses of prairie dogs when communicating for food foraging or for predator warning. When the communication is about the food, the colony shall converge at the location of the food source. When the communication is to warn about the presence of predators, the nearest individual will hide in the burrows while the others await from their burrows, waiting for the possible coming alarm to decide if they should hide or not. The exploitation phase of PDO is modeled in Eqs. (3) and (4) as follows:

$$PD_{i+1,j+1} = GB_{i,j} - \mu \times (GB_{i,j} \times \Delta + \frac{PD_{i,j} \times \text{mean}(PD_{n,m})}{GB_{i,j} \times (ub_j - lb_j) + \Delta}) - (1 - \frac{rPD_{i,j}}{GB_{i,j}}) \times \beta \quad (3)$$

$$PD_{i+1,j+1} = GB_{i,j} \times rPD \times 1.5 \times \left(1 - \frac{iter}{Maxiter}\right)^{2 \frac{iter}{Maxiter}} \times \beta \quad (4)$$

where μ is a small number indicating the quality of the food source, β is a random number between 0 and 1.

It is to be noted that the phases of exploration and exploitation phases are decided based on the number of iterations: For exploration, when $iter \leq \frac{Maxiter}{4}$, foraging activities will be executed, and when $\frac{Maxiter}{4} \leq iter \leq \frac{Maxiter}{2}$, the burrow digging is performed. For exploitation, when $\frac{Maxiter}{2} \leq iter \leq \frac{3 \times Maxiter}{4}$, the prairie dogs' response to food signal will be conducted and finally when $\frac{3 \times Maxiter}{4} \leq iter \leq Maxiter$, the burrow digging is performed.

The flowchart of PDO is shown in Fig. 1 as follows:

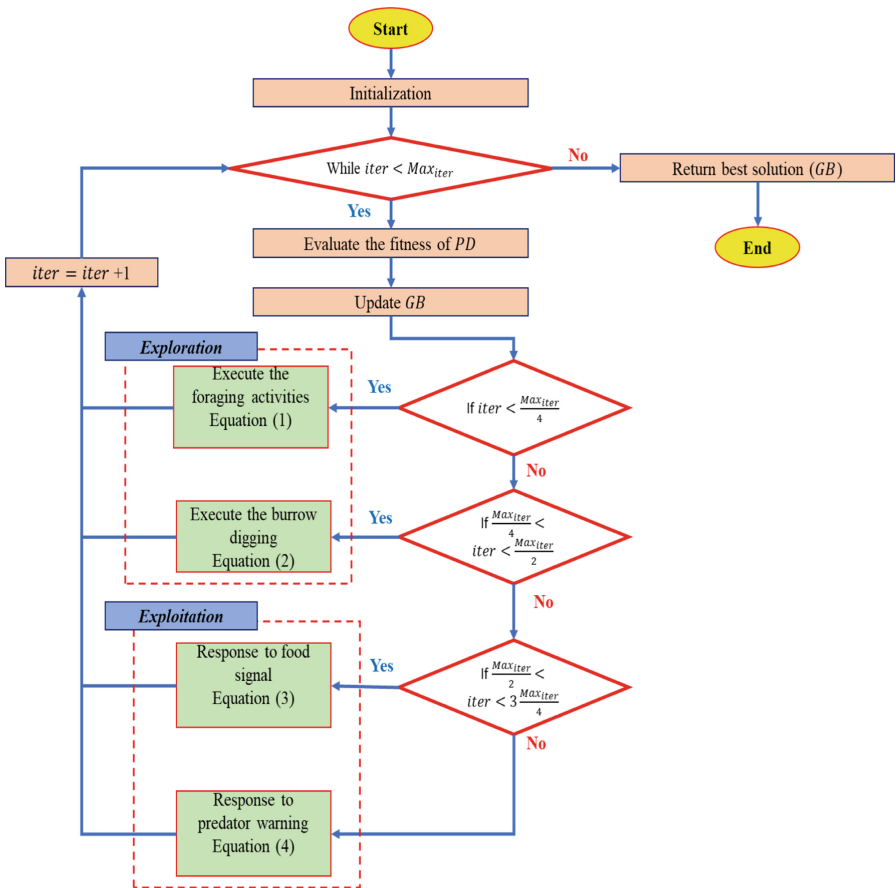


Fig.1. Flowchart of PDO algorithm

3 Practical Review for Damage Identification-Nam O Bridge

3.1 Case Study Introduction

To review the practicality of the PDO algorithm in solving damage identification problems of structures, a real-life case study of a railway bridge is selected. The chosen bridge is the Nam O railway bridge, which is in Da Nang province, Vietnam. The bridge lies on the main North-South Railway Line, which is the busiest and the most important transportation railway route in Vietnam. The bridge consists of four simply supported spans of 75 m in length equally. The load-bearing superstructure is made of steel with different section types connected by the truss bolts. For this research, only the first span will be considered for the validation of the optimization algorithm (Fig. 2).



Fig. 2. Nam O railway bridge

3.2 Finite Element Model

The Finite Element (FE) model of the considered bridge span is constructed using MATLAB toolbox Stab1l [17], which was developed by KU Leuven for structural modeling and analysis. The constructed model consists of 45 nodes and 146 beam elements of 06 degrees of freedom (DOF) originally: three translational displacements and three rotational displacements in the Cartesian coordinate space. The material properties of the bridge model are assumed to be the same for all the truss components with the following: Young's modulus = 196 GPa, Poisson's ratio = 0.3, and density = 7850 kg/m³. In this model, non-structural components of the bridge are considered as additional loads (Fig. 3).

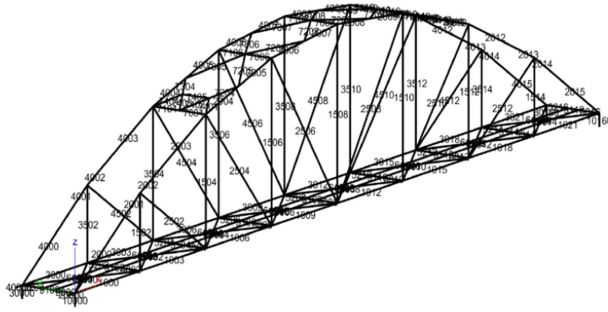


Fig. 3. FE model of the truss arch span

To validate the correctness of the FE model, experimental measurement of the bridge was carried out in 2017 to obtain the dynamic properties of the real-life bridge. During the measurement, two main excitation sources were considered: the ambient wind load and the free vibration of the superstructure after a train passed. 32 vibration-sensitive points—all located at the truss joint positions along the span are considered for the modal testing. High sensitivity accelerometers typed PCB393B12 (ranging from 965 to 1083 mV/m/s²) with the magnet base are attached to the mentioned position for the response signal acquisition. A measurement grid was performed for the vibration measurement of the span, as shown in Fig. 4 below.

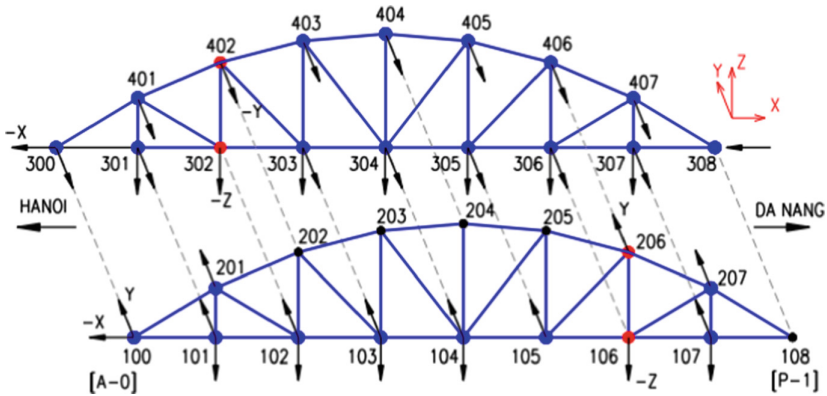


Fig. 4. Measurement grid of the first span. Blue: roving points; Red: reference points [18].

Once the vibration measurement finishes, the raw data is collected and analyzed using the modal identification program MACEC [19]. Fast Fourier Transform (FFT) converts the signal from the time domain to the frequency domain. The obtained signal is then filtered to remove noise and distortion by a fifth-order Chebyshev Type I filter with a lowpass frequency of 20 Hz. Subspace Stochastic Identification (SSI) [20] is then employed for the system identification of the operational modal analysis (OMA) of the bridge to obtain the dynamic properties, notably the natural frequencies and the mode shapes of the measured bridge span. Once the measurement results are obtained,

model updating is performed to correlate the initial FE model with the measured one. The updating parameters are the Young’s modulus of the different truss elements and the stiffness of the additional spring under the bearings. The model updating of the structure is detailed in [18]. Table 1 show the result of model updating for the first 05 natural modes of the bridge.

Table 1. Natural frequencies and modal assurance criterion (MAC) value before and after model updating

No	Measured frequency (Hz)	Initial FE model’s frequency (Hz)	Updated FE model’s frequency (Hz)	Initial MAC values	Updated MAC values
1	1.45	1.18 (18.6%)	1.47 (1.4%)	0.87	0.96
2	3.11	2.76 (11.3%)	3.14(1.0%)	0.85	0.92
3	3.28	3.11(5.2%)	3.32(1.2%)	0.86	0.95
4	4.62	3.79 (17.7%)	4.80 (3.7%)	0.63	0.94
5	6.05	3.94(34.9%)	6.96 (13.0%)	0.66	0.91

3.3 Validation of Damage Identification Using PDO

In this section, to validate the practicality and effectiveness of PDO in solving damage identification problems of the considered bridge structure, two hypothesis damage scenarios are generated on the FE model of the bridge span. Damage is simulated by reducing the stiffness of the truss member according to the percentage level of damage (Fig. 5):

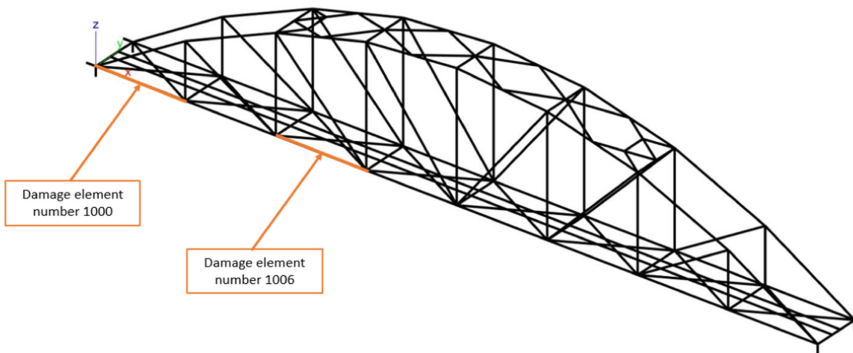


Fig. 5. Damage elements of Nam O bridge

- First scenario: 25% damage level is introduced to the truss element number 1000 of the model.
- Second scenario: 25% and 42% damage levels are introduced to the truss elements number 1000 and 1006 of the model accordingly.

The objective function for the two scenarios above is denoted in Eq. (5) as follows:

$$\text{ObjectiveFunction} = \sum_{i=1}^5 \left(f_i - \tilde{f}_i \right)^2 / \tilde{f}_i^2 + \sum_{i=1}^5 [1 - \text{MAC}(\Psi_i - \tilde{\Psi}_i)] \quad (5)$$

where $f_i, \tilde{f}_i, \Psi_i, \tilde{\Psi}_i$ are the natural frequencies and mode shapes of the simulated and measured values for considered 05 mode shapes of the bridge span. PDO is applied to optimize the above objective function with the initialization consisting of 150 population sizes and 50 iterations. To evaluate the effectiveness of PDO, the algorithm is compared against two other well-known optimization algorithm-Cuckoo Search (CS) and Genetic Algorithm (GA). The results obtained are shown in the two Figures below:

For the first damage scenario:

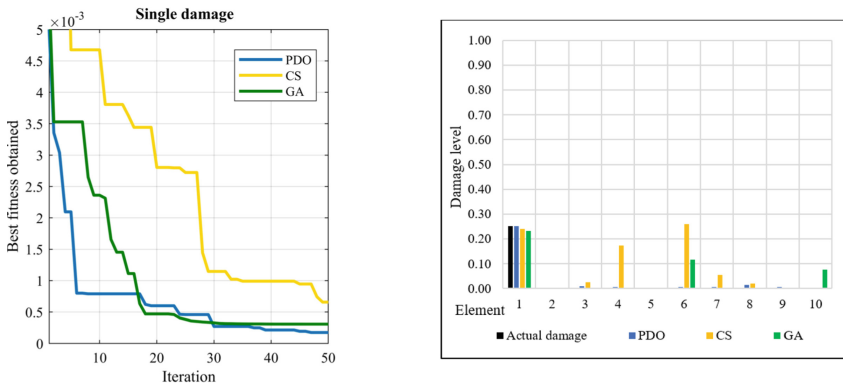


Fig. 6. Convergence of fitness function (left) and damage detection result for the first scenario(right)

For the second damage scenario:

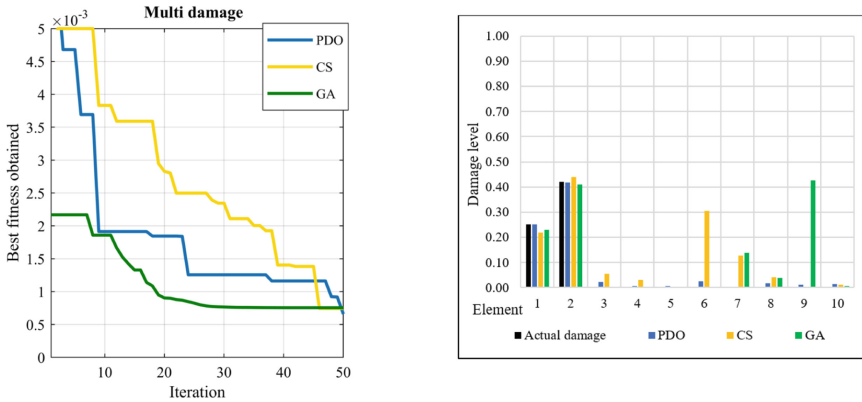


Fig. 7. Convergence of fitness function (left) and the damage detection result of the second scenario (right)

From Fig. 6 and Fig. 7, we can see that in the first damage scenario, PDO has a faster and better convergence rate than CS and GA. While all the three considered are able to quantify the damage at the first element (the element number 1000 in the model) quite closely with PDO has the higher accuracy, CS and GA provide false damage location with false damage locations at elements 4,6 and 7 for CS and elements 6 and 10 for GA. In the second damage scenario, the slope for the convergence of PDO is also better than CS and GA. False damages are also appeared at the faux location in the case of CS and GA, while PDO identifies correctly both the location and level of damage. The results of the two scenarios show that PDO can detect and quantify structural damage with a higher level of accuracy in comparison with CS and GA.

4 Conclusion

In this paper, a practical review of a recently developed optimization algorithm-PDO in solving the damage identification problem of engineering structures is performed. PDO has proven its superiority in solving mathematical and engineering problems in its original work. To validate its effectiveness and practicality, a case study of a truss bridge span is considered. Two damage scenarios are generated individually on the baseline FE model of the bridge by modifying the stiffness of the respective truss members. To test its accuracy, the proposed PDA is compared with two other well-known algorithm-GA and CS. The obtained results show that the proposed algorithm can locate and identify structural damages with a higher level of accuracy than the compared algorithms, thus confirming its practicality in dealing with the damage detection problems of bridge structures. In future research, PDO can be improved to further improve its efficiency, as well as its application in more complex structures such as large-scale infrastructures like bridges, dams, skyscrapers, etc.

Acknowledgments. The authors acknowledge the financial support of VLIR-UOS TEAM Project, VN2018TEA479A103, 'Damage assessment tools for Structural Health Monitoring of Vietnamese infrastructures', funded by the Flemish Government. This work is also funded by Vin-group and supported by Innovation Foundation (VINIF) under project code VINIF.2021.DA00192.

References

1. Corbally, R., Malekjafarian, A.: A data-driven approach for drive-by damage detection in bridges considering the influence of temperature change. *Eng. Struct.* **253**, 113783 (2022)
2. Chen, H.-P.: Structural health monitoring of large civil engineering structures (2018)
3. Ko, J.M., Ni, Y.Q.: Technology developments in structural health monitoring of large-scale bridges. *Eng. Struct.* **27**(12), 1715–1725 (2005)
4. Hajjalizadeh, D.: Deep-learning-based drive-by damage detection system for railway bridges. *Infrastructures* **7**(6), 84 (2022)
5. Cho, S., et al.: Structural health monitoring of a cable-stayed bridge using wireless smart sensor technology: data analyses. *Smart Struct. Syst.* **6**(5_6):461–480 (2010)
6. Khatir, S., et al.: A new robust flexibility index for structural damage identification and quantification. *Eng. Failure Anal.* **129**, 105714 (2021)
7. Hackmann, G., Guo, W., Yan, G., Sun, Z., Chenyang, L., Dyke, S.: Cyber-physical codesign of distributed structural health monitoring with wireless sensor networks. *IEEE Trans. Parallel Distrib. Syst.* **25**(1), 63–72 (2013)
8. Bui-Tien, T., Bui-Ngoc, D., Nguyen-Tran, H., Nguyen-Ngoc, L., Tran-Ngoc, H., Tran-Viet, H.: Damage detection in structural health monitoring using hybrid convolution neural network and recurrent neural network. *Frattura ed Integrità Strutturale* **16**(59), 461–470 (2022)
9. Khatir, S., Tiachacht, S., Thanh, C.-L., Tran-Ngoc, H., Mirjalili, S., Wahab, M.A.: A robust FRF damage indicator combined with optimization techniques for damage assessment in complex truss structures. *Case Stud. Construct. Mat.* e01197 (2022)
10. Nguyen-Ngoc, L., et al.: Damage detection in structures using particle swarm optimization combined with artificial neural network. *Smart Struct. Syst.* **28**(1), 1–12 (2021)
11. Viet Ho, L., et al.: A hybrid computational intelligence approach for structural damage detection using marine predator algorithm and feedforward neural networks. *Comput. Struct.* **252**, 106568 (2021)
12. Khatir, S., Tiachacht, S., Le Thanh, C., Ghandourah, E., Mirjalili, S., Wahab, M.A.: An improved artificial neural network using arithmetic optimization algorithm for damage assessment in FGM composite plates. *Comp. Struct.* **273**, 114287 (2021)
13. Zenzen, R., Belaidi, I., Khatir, S., Wahab, M.A.: A damage identification technique for beam-like and truss structures based on FRF and bat algorithm. *Comptes Rendus Mécanique* **346**(12), 1253–1266 (2018)
14. Ezugwu, A.E., Agushaka, J.O., Abualigah, L., Mirjalili, S., Gandomi, A.H.: Prairie dog optimization algorithm. *Neural Comput. Appl.* 1–49 (2022)
15. Hoogland, J.L.: *The Black-Tailed Prairie Dog: Social Life of a Burrowing Mammal*. University of Chicago Press, Chicago (1995)
16. Yang, X.S., Deb, S.: Cuckoo search via Levy flights. In: 2009 World congress on nature & biologically inspired computing (NaBIC) (2009)
17. François, S., et al.: Stabli: An educational matlab toolbox for static and dynamic structural analysis. *Comput. Appl. Eng. Educ.* **29**(5), 1372–1389 (2021)

18. Tran-Ngoc, H., Khatir, S., De Roeck, G., Bui-Tien, T., Nguyen-Ngoc, L., Abdel Wahab, M.: Model updating for NAM o bridge using particle swarm optimization algorithm and genetic algorithm. *Sensors* **18**(12), 4131 (2018)
19. Edwin, R., Mattias, S., De Roeck, G.: Macec 3.3. A Matlab toolbox for experimental and operational modal analysis. User Manual, Leuven (2014)
20. Peeters, B., De Roeck, G.: Reference-based stochastic subspace identification for output-only modal analysis. *Mech. Syst. Signal Process.* **13**(6), 855–878 (1999)



2D Mixed Polygonal Finite Elements for Fluid Computation – An Overview

T. Vu-Huu¹ and Thanh Cuong-Le²(✉)

¹ Faculty of Civil Engineering, Vietnam Maritime University, 484 Lach Tray Str, Hai Phong, Vietnam

truongvh.ctt@vimar.edu.vn

² Faculty of Civil Engineering, Ho Chi Minh City Open University, Ho Chi Minh City, Vietnam
cuong.lt@ou.edu.vn

Abstract. The polygonal finite element method (PFEM) is one of the most well-known and reliable numerical techniques used to solve various engineering issues. And in the last decade, the development of PFEM for fluid flow computation issues has been the subject of several noteworthy research. Therefore, it could quickly mention several PFEM developments, mainly a novel mixed polygonal finite element (PFE). They are specifically mixed polygonal finite elements, such as the low-order mixed PFE - Pe_1Pe_0 , the equal-order mixed PFE - Pe_1Pe_1 , and the high-order PFE - MINI Pe . Consequently, the primary objective of this work is to provide an overview of recent advancements in PFEM for fluid flow calculation issues. In this paper, the techniques used to enhance the PFEs for fluid flow problems are detailed and compiled.

Keywords: Polygonal finite element method (PFEM) · Fluid flow computation

1 Introduction

In recent years, PFEM has become well-known as one of the most reliable numerical approaches with a high degree of flexibility and other desired benefits. For instance, the features of Voronoi diagrams and the advantage of using mesh generation techniques to build arbitrary element forms are discussed [1]. A further benefit of PFEM is that it is more accurate than its triangular and quadrilateral pioneers without requiring a sizeable total mesh size [1]. It indicates that PFEs may deliver superior solutions compared to quadrilateral elements or triangles.

It is well-known that the Navier–Stokes (N-S) equations, functions of fluid velocity and pressure (\mathbf{u}, p), may be utilised to simulate fluid flows mathematically. So, the first approach used to create novel PFEs is the very well-known mixed scheme method (MSM - see Refs. [2]) since it allows for the simultaneous combination of both variables of fluid velocity and pressure (\mathbf{u}, p) inside the same discretisation system. To further complicate matters, MSM allows for introducing a wide range of new variables (e.g., heat or energy transfer, etc.), most of which are dependent on the original ones.

In addition, it was understood that for element geometries with more than four sides, appropriate first-order shape functions did not exist. Therefore, the second core technique relies on actual foundation shape functions that may be applied to polygons. These shape functions are derived from basic concepts in perspective geometry, which is given by the system of Wachspress presented in Refs.. Rational functions are used to generate linear relationships within shape functions for elements with more than four nodes. By using rational functions, linear relations are able to derive within-shape functions for any polygons.

Furthermore, a novel stabilisation strategy is applied to deal with the potential instability issue of MSM. This technique, which is based on the work of Bochev et al. (2004) and is an enhanced projection approach, enables one to eliminate the residual term of the stabilisation process while maintaining the global system's symmetry [3]. It allows the local stabilisation term of each element to adjust automatically to the varying forms and sizes throughout the whole discrete polygonal domain.

The following sections provide the whole detailed context for building innovative PFEs. Section 2 presents the idea of mixed PFEs. Then, the shape functions of PFEs are detailed in Sect. 3. Besides, Sect. 3 shows the advanced stabilisation method for PFEs. The conclusions and some future works are given in the Sect. 5.

2 2D Polygonal Finite Elements

2.1 Polygol Definition

Polygons, as everyone knows, are made by joining together n straight lines to form a 2D object. See 0 for an illustration of several common types of regular polygons, including triangles, quadrilaterals, pentagons, hexagons, etc. A polygon's name figures out how many sides it has and its number of edges, vertices, and nodes (Fig. 1).

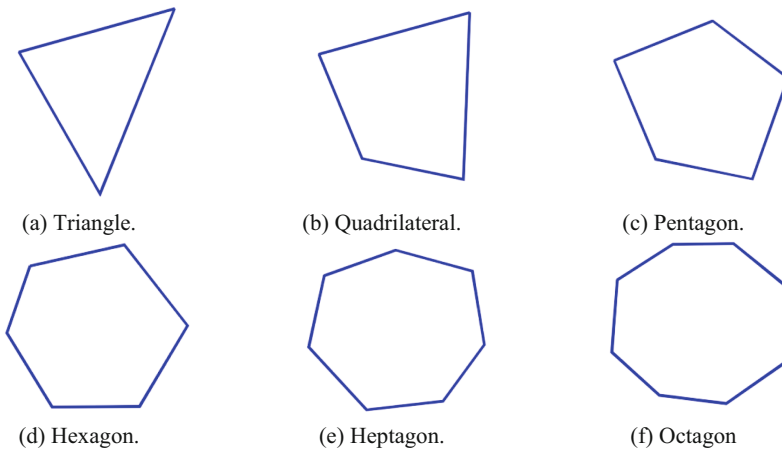


Fig.1. Samples of polygons.

2.2 Low-Order PFE (Pe_1Pe_0)

Cameron Talischi et al. introduced this PFE in 2014, see Ref. [1]. It is called a low order with the chosen approximation spaces defined over the domain’s convex polygonal partitions that naturally satisfy the inf-sup condition. It does not admit spurious pressure modes or exhibit locking. The pressure field is constant within each element, while the velocity is represented by the standard iso parametric transformation of a linearly-complete basis, see 0 (Fig. 2).

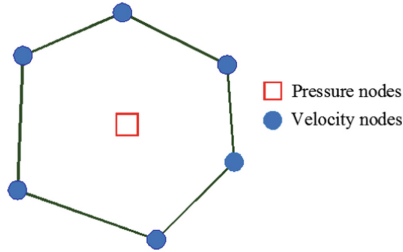


Fig. 2. The mixed low-order polygonal scheme, Pe_1Pe_0 [1].

This PFE has a conspicuous restriction: the instability performance on the triangular and quadrilateral meshes [1]. It means that Pe_1Pe_0 cannot satisfy the inf-sup condition in the case of such families of mesh.

2.3 Equal-Order PFE (Pe_1Pe_1)

A fresh equal-order mixed scheme of polygons, Pe_1Pe_1 , for the pair of pressure and velocity on the convex polygons, was created in 2020 to alleviate the limitations of Pe_1Pe_0 [4]. This implies that, as shown in 0, both the velocity field and the pressure field may be expressed in terms of polygonal basis shape functions. When compared to the current low-order mixed system of polygons, Pe_1Pe_0 , where the pressure field is governed by element-wise constant functions, this is the most notable difference (Fig. 3).

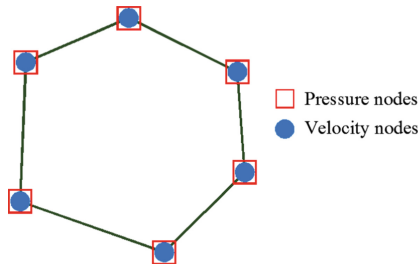


Fig. 3. A mixed equal-order mixed polygonal scheme, Pe_1Pe_1 , [4].

The benefit of this PFE is the ability to compute with any mesh family. In addition, the fluid pressure performance of this PFE exceeds that of the current Pe_1Pe_0 .

2.4 A High-Order PFE (MINIPe)

Another novel advanced high-order mixed PFE for fluid flow problems was introduced in 2019; see 0. First, polygonal basis functions are collected to model the pressure field in this PFE. Then, polygonal basis functions and a polygonal bubble function are used to calculate the velocity approximatively (Fig. 4).

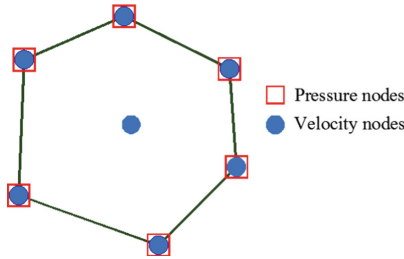


Fig. 4. A high-order mixed scheme of the MINIPe, [5].

3 Polygonal Shape Functions

3.1 Wachpress Basis Shape Functions

The Wachpress system of polygonal shape functions have the following intriguing properties:

- Characteristics of the Kronecker delta include: $\phi_i(\mathbf{x}_j) = \delta_{ij}$;
- Polygonal domain with a smooth C^∞ interior and a smooth C^0 border;
- Advantages of being linear: $\sum_{i=1}^n \phi_i(\mathbf{x})\mathbf{x}_i = \mathbf{x}$;
- The partitional unity: $\sum_{i=1}^n \phi_i(\mathbf{x}) = 1$; positive: $\phi_i(\mathbf{x}) \geq 0$;
- When subjected to an affine transformation, Wachpress coordinates remain unchanged, $\alpha : \mathbb{R}^2 \rightarrow \mathbb{R}^2$ is applied to the points $\mathbf{x}_1, \mathbf{x}_2, \dots, \mathbf{x}_n$ and \mathbf{x} of the element Ω_e .

Thus, the basis function $\phi_i(\alpha\mathbf{x}, \alpha\mathbf{x}_1, \alpha\mathbf{x}_2, \dots, \alpha\mathbf{x}_n) = \phi_i(\mathbf{x}, \mathbf{x}_1, \mathbf{x}_2, \dots, \mathbf{x}_n)$ of the i^{th} vertex of a polygon $\Omega^e \in \mathfrak{S}$ is established with counter-clockwise ordering as:

$$\phi_i^e = \frac{\varphi_i}{\sum_{j=1}^{n_{ne}} \varphi_j} = \frac{\varphi_i}{\psi} \quad \text{with} \quad \varphi_i = \frac{S(\mathbf{x}_{i-1}, \mathbf{x}_i, \mathbf{x}_{i+1})}{S(\mathbf{v}, \mathbf{x}_{i-1}, \mathbf{x}_i)S(\mathbf{v}, \mathbf{x}_i, \mathbf{x}_{i+1})} \quad (1)$$

where, $S(\mathbf{x}_a, \mathbf{x}_b, \mathbf{x}_c)$ represents the area of the triangle $[\mathbf{x}_a, \mathbf{x}_b, \mathbf{x}_c]$, see 0 (a). Besides, one may use a Wachpress coordinator that considers the perpendicular lengths between an internal point \mathbf{v} and the polygon's edges, see 0 (b). In 0 (b), $h_i(\mathbf{x})$ denotes the perpendicular distance of \mathbf{v} to the edge \mathbf{e}_i ; then parameter $\mathbf{p}_i(\mathbf{x})$ is defined by the quotient

of \mathbf{n}_i and $h_i(\mathbf{x})$. And, \mathbf{n}_i is the outward normal vector of the edge $\mathbf{e}_i = [\mathbf{x}_i, \mathbf{x}_{i+1}]$. Then, the shape functions become:

$$\phi_i^e = \frac{\varphi_i}{\psi} = \frac{\tilde{\varphi}_i}{\sum_{j=1}^{n_{ne}} \tilde{\varphi}_j} \text{ with } \tilde{\varphi}_i = \det(\mathbf{p}_{i-1}, \mathbf{p}_i) \tag{2}$$

and the gradients are:

$$\nabla \phi_i^e = \phi_i^e \left[\vartheta_i - \sum_{j=1}^{n_{ne}} \varphi_j^e \vartheta_j \right] \text{ where } \vartheta_i = \mathbf{p}_{i-1} + \mathbf{p}_i \tag{3}$$

Therefore, the set of shape functions for every convex polygon may be generated by Eqs. (2) - (3) (Fig. 5).

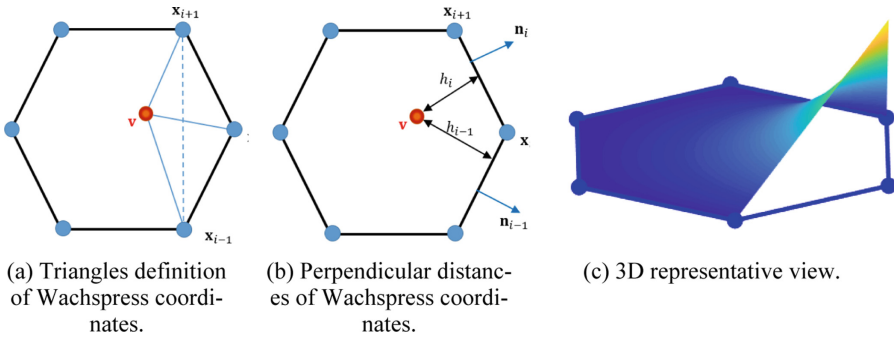


Fig. 5. Wachspress polygonal shape function for a hexagon.

3.2 Bubble Shape Function of Polygons

The definition of the bubble shape function for a convex polygon, developed by the work of Malsch and Dasgupta, is presented here. See 0 to see how the bubble shape function has a value of 1 at an inner node and zero at the border. A function $A(\mathbf{x})$ that can get from the ratio of products of Eq. (1) or Eq. (2) as (Fig. 6):

$$A(\mathbf{x}) = \frac{1}{\psi} = \frac{1}{\tilde{\psi}}. \tag{4}$$

Then, as Eq. (4), $B(\mathbf{x})$ is given by:

$$B(\mathbf{x}) = \|\mathbf{x} - \mathbf{x}_b\|_{\Omega^e}^2 \tag{5}$$

where \mathbf{x}_b is the centroidal coordinates in Ω^e . Hence, the indication of the bubble shape function $\phi_b^e \in \mathbf{B}^h$ is:

$$\phi_b^e = \frac{1}{1 + \|\mathbf{x} - \mathbf{x}_b\|_{\Omega^e}^2 \tilde{\psi}} \tag{6}$$

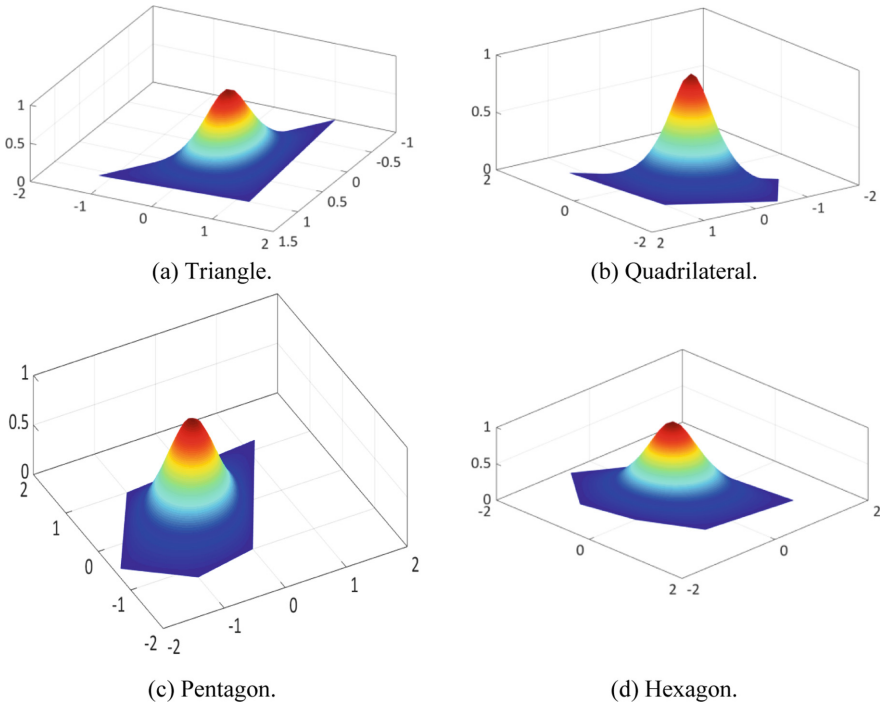


Fig. 6. The demonstration of bubble shape function.

and its gradient is:

$$\nabla \phi_b^e = \frac{\|\mathbf{x} - \mathbf{x}_b\|_{\Omega^e}^2 \nabla \tilde{\psi} + \nabla \|\mathbf{x} - \mathbf{x}_b\|_{\Omega^e}^2 \tilde{\psi}}{\left(\|\mathbf{x} - \mathbf{x}_b\|_{\Omega^e}^2 \tilde{\psi} + 1\right)^2}. \tag{7}$$

4 Stabilisation Method

The projection technique developed by Bochev et al. [3] is improved to eliminate the residual term of the stabilisation process and maintain global system symmetry. As a bonus, this stabilising for the polygonal discretisations is simple and perfect for any shape and size of convex polygons. The adjustment starts with the operator $\Pi_h : L^2(\Omega) \rightarrow R_0$ with the chosen test function of pressure $q \in L_0^2$. Then, $\Pi_h q = q_h \in R_0$ when and only when:

$$\int_{\Omega} \left(\Pi_h q - q_h\right) d\Omega = 0. \tag{8}$$

This approach is modified so that it can handle the challenge of the arbitrary shape of an element in the polygon mesh. It is well-known that a simple method of local averaging

may be used to calculate a pressure projection [2]:

$$\prod_h q|_{\Omega_e} = \frac{1}{|\Omega_e|} \int_{\Omega_e} q_h d\Omega_e, \quad \forall \Omega_e \in \mathfrak{S}_h. \tag{9}$$

Substituting the standard test functions to a polygonal mesh, $\{\psi_i\}_{i=1}^{n_{ne}}$, by a the local term, $q_h|_{\Omega_e} = \sum_{i=1}^{n_{ne}} q_i \psi_i$, into Eq. (9), we get [6]:

$$\prod_h q|_{\Omega_e} = \frac{\sum_{i=1}^{n_{ne}} q_i^e}{n_{ne}}. \tag{10}$$

Equation (10) shows that the projected pressure is the mean of the vertex values of polygons. In fact, the local stabilisation matrix, c_e , of elements on the polygonal mesh is found by solving Eq. (8) and (9):

$$\begin{aligned} c_e(q_h, p_h) &= \frac{1}{v} \int_{\Omega_e} (q_h - \prod q_h) (p_h - \prod p_h) d\Omega \\ &= \sum_{i,j=1}^{n_{ne}} \frac{1}{v} q_i \int_{\Omega_e} \left(\psi_i - \frac{1}{n_{ne}} \right) \left(\psi_j - \frac{1}{n_{ne}} \right) d\Omega q_j, \end{aligned} \tag{11}$$

for all $\Omega_e \in \mathfrak{S}_h$. In this case, the ψ_i and ψ_j do not disappear on Ω_e . Assembling the global stabilisation matrix **C** for PFE from contribution matrices c_e is, therefore:

$$\mathbf{C} = \underset{e=1}{\overset{n_e}{\mathbf{A}}} \sum_{i,j=1}^{n_{ne}} \frac{1}{v} \int_{\Omega_e} \left(\psi_i - \frac{1}{n_{ne}} \right) \left(\psi_j - \frac{1}{n_{ne}} \right) d\Omega, \tag{12}$$

where **A** is the assembly operator, e is the e^{th} element, n_e is the total number of the elements in the domain \mathfrak{S}_h .

5 Conclusions and Future Works

This study concludes by providing an overview of the strategies employed to improve the PFEs for fluid flow simulations throughout the last decade. Specifically, they are mixed polygonal finite elements, such as low-order mixed PFE - Pe_1Pe_0 , equal-order mixed PFE - Pe_1Pe_1 , and high-order PFE - MINIPe. The advanced techniques which are applied to construct the present PFEs are the mixed scheme method, the polygonal shape functions of Wachpress, the bubble shape function for convex polygons given by Malsch and Dasgupta, the stabilisation technique offered by Bochev et al. Besides, although the current novel mixed PFEs have success in fluid flow computations, they only pause in the 2D problems. Hence, one of the further priority works is the application to 3D problems. Then another future task would be the other higher-order PFEs using novel quadratic serendipity shape functions suggested by Rand et al. in 2014. Finally, the next task could be the fluid-structure interaction computations.

References

1. Talischi, C., et al.: Polygonal finite elements for incompressible fluid flow. *Int. J. Numer. Meth. Fluids* **74**(2), 134–151 (2014)
2. Elman, H.C., Silvester, D.J., Wathen, A.J.: *Finite Elements and Fast Iterative Solvers: With Applications in Incompressible Fluid Dynamics*. Oxford University Press (2014)
3. Bochev, P.B., Dohrmann, C.R., Gunzburger, M.D.: Stabilization of low-order mixed finite elements for the Stokes equations. *SIAM J. Numer. Anal.* **44**(1), 82–101 (2006)
4. Vu-Huu, T., et al.: An equal-order mixed polygonal finite element for two-dimensional incompressible Stokes flows. *Eur. J. Mech.-B/Fluids* **79**, 92–108 (2020)
5. Vu-Huu, T., et al.: A high-order mixed polygonal finite element for incompressible Stokes flow analysis. *Comput. Methods Appl. Mech. Eng.* **356**, 175–198 (2019)
6. Dohrmann, C.R., Bochev, P.B.: A stabilized finite element method for the Stokes problem based on polynomial pressure projections. *Int. J. Numer. Meth. Fluids* **46**(2), 183–201 (2004)

Author Index

A

Abdelouahed, Chbihi, 138
Adnane, ElJersifi, 138
Agliata, Rosa, 161
Al Ali, Musaddiq, 220, 265
Amoura, Nasreddine, 220
Azem, Said, 127

B

Behtani, Amar, 171, 186
Benaissa, Brahim, 171, 186, 220, 265
Bettucci, E., 82
Bettucci, Elisa, 70
Bui-Tien, Thanh, 296

C

Capozucca, R., 82
Capozucca, Roberto, 48, 59, 70
Cuong-Le, Thanh, 307

D

da Silva, Luis C. M., 253
Doan, Xuan Hung, 24

G

Grande, Ernesto, 253

H

Hassan, Bouaouine, 138
Heshmati, Amirhossein, 114
Hoang, Bac An, 279
Hoa-Tran., 296
Hocine, Nourredine Aït, 127

Hojdys, Łukasz, 149
Hua, Yiwei, 210

J

Jafari-Talookolaei, Ramazan-Ali, 93

K

Kahouadji, Amar, 171
Khatir, A., 82
Khatir, Abdelwahhab, 48, 70
Khatir, S., 82
Khatir, Samir, 35, 70, 93, 114, 171, 186, 220, 296
Khatir, Tawfiq, 186
Kobayashi, Masakazu, 265
Krajewski, Piotr, 149
Kwicien, Arkadiusz, 149

L

Lach, Michał, 149
Larijani, Yasin Faghih, 35

M

Magagnini, E., 82
Magagnini, Erica, 48, 59, 70
Milani, Gabriele, 199, 210, 244, 253
Munafò, Placido, 161

N

Nawal, Semlal, 138
Ngoc-Nguyen, Lan, 296
Ngo-Kieu, Nhi, 234
Nguyen, Duong Huong, 24
Nguyen, Huong-Duong, 1
Nguyen, Huu-Quyêt, 296

Nguyen, Nhu Mai Thi, [24](#)
Nguyen, Quoc Bao, [24](#)
Nguyen, Thao D., [234](#)
Nguyen, Tran- Hieu, [1](#)
Nguyen, Viet Phuong, [24](#)

P

Pace, Giuseppe, [59](#)
Pashaei, Mohammad-Hadi, [93](#)
Pham, Duy Hoa, [24](#)
Pham-Bao, Toan, [234](#)

R

Redjala, Sonya, [127](#)
Riahi, Mohamed Kamel, [186](#)
Rostamian, Yaser, [35](#)

S

Saadatmorad, Morteza, [93](#), [114](#)
Sanae, Naamane, [138](#)

Serpilli, Michele, [161](#)
Shimoda, Masatoshi, [265](#)
Slimani, Mohand, [171](#), [186](#)

T

Talookolaei, Ramazan-Ali Jafari, [114](#)
Tiachacht, Samir, [171](#), [186](#)

V

Valvo, Paolo S., [114](#)
Viskovic, Alberto, [149](#)
Vu, Anh-Tuan, [1](#)
Vu-Huu, T., [307](#)

W

Wahab, Magd Abdel, [296](#)

Y

Yuan, Yu, [199](#), [244](#)